

THE DEVELOPMENT AND APPLICATION OF NANOHOOPS AS NOVEL
FLUORESCENT PROBES FOR BIOLOGICAL APPLICATIONS

by

TERRI CHRISTINE LOVELL

A DISSERTATION

Presented to the Department of Chemistry and Biochemistry
and the Graduate School of the University of Oregon
in partial fulfillment of the requirements
for the degree of
Doctor of Philosophy

September 2020

DISSERTATION APPROVAL PAGE

Student: Terri Christine Lovell

Title: The Development and Application of Nanohoops as Novel Fluorescent Probes for Biological Applications

This dissertation has been accepted and approved in partial fulfillment of the requirements for the Doctor of Philosophy degree in the Department of Chemistry and Biochemistry by:

Michael Haley	Chairperson
Ramesh Jasti	Advisor
Vickie De Rose	Core Member
Bruce Branchaud	Core Member
Annie Zemper	Institutional Representative

and

Kate Mondloch	Interim Vice Provost and Dean of the Graduate School
---------------	--

Original approval signatures are on file with the University of Oregon Graduate School.

Degree awarded September 2020

© 2020 Terri Christine Lovell

DISSERTATION ABSTRACT

Terri Christine Lovell

Doctor of Philosophy

Department of Chemistry and Biochemistry

September 2020

Title: The Development and Application of Nanohoops as Novel Fluorescent Probes for Biological Applications

Fluorescent molecules are imperative for the detection of diseases and observation of complex biological processes in living systems. A wide variety of small molecule fluorophores are available, however they each come with their limitations. An entirely new scaffold with enhanced photophysical properties, tunability, and chemical stability would be advantageous. Herein, we present our efforts in designing and applying nanohoops as novel fluorophores for biological applications.

Chapter I reviews commonly used small molecule fluorophores and how to tune their photophysical properties using physical organic chemistry concepts. Chapter II describes how to enhance the brightness of nanohoops to make them suitable for biological imaging. Chapter III demonstrates how to shift the fluorescence of nanohoops further red, which is desirable for cellular imaging. Chapter IV reports the first intracellular targeted nanohoop for live cell imaging. Lastly, Chapter V describes our efforts to broadly apply nanohoops as novel fluorophores for protein and DNA labelling. This dissertation describes the pronounced strides made towards developing nanohoops as novel fluorophores for biotechnology.

This dissertation includes previously published and unpublished co-authored

material.

CURRICULUM VITAE

NAME OF AUTHOR: Terri Christine Lovell

GRADUATE AND UNDERGRADUATE SCHOOLS ATTENDED:

University of Oregon, Eugene
Memorial University of Newfoundland, St. John's

DEGREES AWARDED:

Doctor of Philosophy, Chemistry, 2020, University of Oregon
Master of Science, Polymer Science, 2016, University of Oregon
Bachelor of Science, Chemistry, 2015, Memorial University of Newfoundland

AREAS OF SPECIAL INTEREST:

Synthetic Organic Chemistry
Chemical Biology
Physical Organic Chemistry

PROFESSIONAL EXPERIENCE:

Teaching Assistant, Department of Chemistry and Biochemistry and Materials
Science Institute, University of Oregon, Eugene 2016-2020

Research and development Intern II, Thermo Fisher Scientific, Eugene, Oregon,
2015-2016

GRANTS, AWARDS, AND HONORS:

Knight Campus Transitioning Scholar Fellowship, University of Oregon, 2020

Canadian Chemistry Conference and Exhibition Oral Presentation Award,
Canadian Society for Chemistry, 2019

Undergraduate Student Research Award (Declined), Natural Sciences and
Engineering Research Council, 2015

Science Communication Presentation Award, Chemical Institute of Canada–
Science Atlantic, 2015

Undergraduate Student Research Award, Natural Sciences and Engineering
Research Council, 2014

Hebron Diversity Award, Memorial University of Newfoundland, 2014

Summer Organic Chemistry Conference Undergraduate Presentation Award,
Memorial University of Newfoundland, 2014

Hebron Diversity Award, Memorial University of Newfoundland, 2013

Vice President's List, Memorial University of Newfoundland, 2011

Entrance Scholarship, Memorial University of Newfoundland, 2011

PUBLICATIONS:

Lovell, T. C.; Fosnacht, K. G.; Colwell, C. E.; Jasti, R. Effect of Curvature and Placement of Donor and Acceptor Units in Cycloparaphenylenes: A Computational Study. *Submitted*.

Lovell, T. C.; Garrison, Z. R.; Jasti, R. Synthesis, Characterization and Computational Investigation of Bright Orange-emitting Benzothiadiazole [10]Cycloparaphenylene. *Angew. Chem.* **2020**, *59*, 14363-14367.

Schaub, T. A.*; Prantl, E.; Kohn, J.; Marshall, C.; Leonhard, E. J.; Lovell, T. C.; Zakharov, L.; Brozek, C.; Waldvogel, S.; Grimme, S.; Jasti, R. Exploration of the Solid-State Sorption Properties of Shape-Persistent Macrocyclic Nanocarbons as Bulk Materials and Small Aggregates. *J. Am. Chem. Soc.* **2020**, *142*, 8763–8775.

Lovell, T. C.*; Colwell, C. E.*; Zakharov, L. N.; Jasti, R. Symmetry Breaking and the Turn-on Fluorescence of Small, Highly Strained Carbon Nanohoops. *Chem. Sci.* **2019**, *10*, 3786–3790.

ACKNOWLEDGMENTS

I would like to thank Professor Ramesh Jasti for his continued support and guidance throughout my PhD. I am thankful that he allowed me to have intellectual freedom to pursue ideas that were outside of organic chemistry. It greatly enhanced my growth as an independent scientist and critical thinker. Thank you Professor Mike Haley, Professor Vickie DeRose, Professor Bruce Branchaud and Professor Annie Zemper. I am grateful to have such a supportive committee with boundless input.

I have had a lot of important mentors who have contributed to my growth at the University of Oregon. Thank you to Dr. Brittany White for guiding me when I joined the Jasti lab. Thank you to Dr. Tobias Schaub for helping me grow as a researcher during his Postdoc. Thank you to the current members of the Jasti Lab Ruth Maust, Claire Otteson, Tavis Price, Julia Fehr, James May, Tara Clayton and Hannah Hashimoto. A special thank you to Zach Garrison, an undergraduate student who worked with me for two years. It was a pleasure to have a student with such enthusiasm and curiosity. I would like to acknowledge past members of the Jasti Lab Dr. Evan Darzi, Dr. Penghao Li, Dr. Brittany White, Dr. Tobias Schaub, Dr. Jeff Van Raden, Dr. Erik Leonhardt and Dr. Curtis Colwell who all assisted me in their own unique way during my time at UO.

I must thank my collaborators, who made this thesis possible. Professor Xiaolin Nan, Julia Shangguan, Dr. Fehmi Civitci, and Dr. John Kenison for their efforts on two-photon imaging. Randall Armstrong for his work in flow cytometry. Professor Michael Pluth and Sarah Bolton for their work on cellular imaging. Furthermore, Rachael Cunningham and Emily Sutton who taught me bioconjugation analysis techniques and cell culture. Additionally, Dr. Mike Strain and Dr. Nanette Jarenwattananon for their

NMR expertise and Dr. Lev Zakharov for crystallography data. We would be nowhere without the chemistry support staff, especially Janet Macha.

I was fortunate to have many people support me before coming to the University of Oregon for my PhD. I would like to thank the staff of the Master's Industrial Internship Program, especially Lynde Ritzow, Stacey York, and Casey Check, who supported me endlessly during my Master's. My co-workers at Thermo Fisher Scientific, particularly Eric Welch, Adam York, Scott Sweeney, Andrew Dix, Judie Berlier, Doug Smith, Hannah Hart, and Doug Anderson, who made my time in industry fun and helped me discover my love of fluorophores. I would like to thank Professor Graham Bodwell, Professor Christopher Rowley and Professor Sunil Pansare for their mentorship during my undergraduate degree. Furthermore, I would like to acknowledge my high school chemistry teacher, Mr. Tony Hynes, for getting me excited and captivated by chemistry at a young age.

A lot of friends have supported me along the way, but I would like to send a special thanks to Tobi, Lisa, Thais, Claire, and Doug. I am forever grateful for our adventures and your exceptional friendship. Adam and Stacey York were exceptional support in my professional and career development. Additionally, along with their daughters Charlotte and Amelia York, they were an amazing support system in Eugene and a home away from home.

I would like to acknowledge my family in Newfoundland. A special thanks to my parents Debbie and Faron Lovell, my brother Jason Lovell, and sister-in-law Kelly Lovell for supporting me throughout my graduate career. They have spent many nights on the phone with me helping me through the challenges that come with obtaining a PhD and

living in a different country over 4000 miles away. I am grateful for my adorable puppy Chloe, who loves me unconditionally and always cheered me up when I was stressed or sad.

Finally, I would like to thank my fiancé Curtis Colwell for his endless love and support. You have given so much emotional and intellectual support, I could not have made it through without you. You are the light of my life.

Dedicated to my grandparents Laverne and Larry Lawrence and Joseph and Vonnie Lovell.

TABLE OF CONTENTS

Chapter	Page
I. COMMON FLUORESCENT DYES USED FOR BIOLOGICAL APPLICATIONS	1
1.1 Introduction.....	1
1.1.1 The Process of Fluorescence	2
1.2 Synthesis of fluorescent scaffolds	3
1.2.1 Coumarins	4
1.2.2 Cyanine.....	5
1.2.3 Xanthenes (Fluorescein and Rhodamine)	6
1.2.4 BODIPY	9
1.2.5 Perylene.....	10
1.2.6 Cycloparaphenylene.....	11
1.3 Tuning the emission of fluorophores.....	13
1.3.1 Electron withdrawing and electron donating groups for altering molecular orbitals	14
1.3.2 Extending Conjugation.....	21
1.3.3 Heteroatoms incorporation.....	23
1.4 Enhancing quantum yield of fluorophores.....	24
1.5 Enhancing the photostability of fluorophores	26
1.6 Conclusions	28
1.7 Bridge to next chapter.....	28
II. TUNING AND ENHANCING THE FLUORESCENCE EMISSION OF CYCLOPARAPHENYLENES.....	30
2.1 Introduction	30
2.2 Synthesis	33
2.3 Photophysical properties	35
2.4 Conclusions	38
2.5 Experimental Detail.....	38
2.5.1 General Experimental Details and Synthesis	38

Chapter	Page
2.5.2 Photophysical Characterization	68
2.5.3 Electrochemical Analysis	71
2.5.4 Calculations	75
2.6 Bridge to Chapter III.....	82
III. RED-SHIFTING THE FLUORESCENCE EMISSION OF	
CYCLOPARAPHENYLENES.....	83
3.1 Introduction	83
3.2 Synthesis	85
3.3 Photophysical properties	87
3.4 Computational analysis.....	89
3.5 Conclusions	90
3.6 Experimental section.....	91
3.6.1 General experimental details and synthesis.....	91
3.6.2 Photophysical characterization	97
3.6.3 C ₆₀ Binding Constant	99
3.6.4. Electrochemical Analysis	100
3.6.5. Computational Calculations	101
3.6.7 StrainViz calculations	107
3.7 Bridge to Chapter IV.....	108
IV. <i>IN-VIVO</i> IMAGING OF AN INTRACELLULAR TARGETED	
CYCLOPARAPHENYLENE.....	109
4.1 Introduction	109
4.2 Synthesis	112
4.3 Photophysical Properties.....	113
4.4 Cytotoxicity and <i>in-vivo</i> Imaging	114
4.5 Conclusions	117
4.6 Experimental Section.....	117
4.6.1 General experimental details and synthesis.....	117
4.6.2 Photophysical characterization	124
4.6.3 Cell Imaging Experiments.....	125

Chapter	Page
4.7 Bridge to Chapter V	126
V. BIOCONJUGATION OF CYCLOPARAPHENYLENES TO BIOMOLECULES	
FOR IMMUNOCHEMISTRY AND <i>IN VITRO</i> IMAGING.....	127
5.1 Introduction	127
5.2 Synthesis of a CPP with conjugation handle.....	128
5.3 Conjugation of NHS-PEG _x -CPPs to amine functionalized DNA.....	130
5.3 Conjugation of NHS-PEG _x -CPPs to proteins.....	133
5.4 Synthesis of biotin-CPP and antibody labeling.....	134
5.5 Conclusions and future work.....	135
5.6 Experimental detail.....	135
5.6.1 Synthesis and general experimental detail	135
5.6.2 Cell Studies.....	147
5.7 Concluding Remarks.....	149
REFERENCES CITED	150

LIST OF FIGURES

Figure	Page
1.1. Jabłoński diagram illustrating the process of fluorescence.....	3
1.2. Synthesis of 7-hydroxy and 7-aminocoumarins through Pechmann condensation, Knoevenagel condensation and Buchwald-Hartwig cross coupling.	5
1.3. Synthesis of cyanine dyes.	6
1.4. Synthesis of fluorescein.	7
1.5. Rhodamine synthesis.	8
1.6. Synthesis of symmetric and asymmetric BODIPYs.....	10
1.7. Synthesis of water soluble perylene dye.	11
1.8. Synthesis of CPPs and water soluble CPP.....	13
1.9. Orbital stabilization and destabilization from addition of electron withdrawing and electron donating groups.	14
1.10. Coumarin HOMO and LUMO orbital densities and fluorescence tuning by incorporating EWGs and EDGs. ⁷⁶	16
1.11. HOMO and LUMO orbital densities of fluorescein and rhodamine and fluorescence tuning by incorporating EDGs.....	17
1.12. HOMO and LUMO orbital densities of BODIPY and fluorescence tuning by incorporating EWGs and EDGs.	18
1.13. HOMO and LUMO orbital densities of PDI and fluorescence tuning by incorporating EWGs and EDGs.	20
1.14. Red-shifting of CPPs through incorporation of electron accepting units within the CPP backbone.....	20
1.15. Red-shifting of fluorescence through conjugation extension of the π -system.	22
1.16. Unique red-shifting of CPPs through increasing bending effect and decreasing torsion angles.	23
1.17. Heteroatom incorporation to tune fluorescence of rhodamine and BODIPY.	24
1.18. Quantum yield enhancement through structure rigidification and minimizing TICT.	25

Figure	Page
1.19. Sulfonation to increase quantum yields and synthesis.....	26
1.20. Fluorination and attachment of TSQs to enhance photostability.	27
2.1 a) Structure of an armchair carbon nanotube (CNT) and its relation to [n]cycloparaphenylenes; b) HOMO (left) and excited state (right) S ₁ ' orbitals of [12]CPP and c) HOMO (left) and excited state (right) S ₁ ' orbitals of [5]CPP. Orbitals have been calculated using CAM-B3LYP/STO-3G level of theory. d) <i>meta</i> [n]CPPs with broken symmetry in this work.	31
2.2. Building block synthetic approach to <i>m</i> [6]-, <i>m</i> [7]-, <i>m</i> [8]-, <i>m</i> [10]- and <i>m</i> [12]CPP.....	34
2.3. Modified synthetic strategy for <i>m</i> [5]CPP.	35
2.4. (a) Absorbance and emission spectra of <i>m</i> [<i>n</i>]CPPs; (b) HOMO (left) and S ₁ ' (right) orbital depiction of [5]CPP and <i>m</i> [5]CPP, demonstrating change in orbital symmetry. Calculated using CAM-B3LYP/STO-3G level of theory; (c) absorbance, extinction coefficient (ϵ), emission and quantum yield (Φ) of <i>m</i> [5]- <i>m</i> [8]-, <i>m</i> [10]- and <i>m</i> [12]CPP and brightness comparison of <i>m</i> [<i>n</i>]CPPs and [<i>n</i>]CPPs.....	36
2.5. Extinction coefficient determination of <i>m</i> [5]CPP at the a) absorbance maxima and b) HOMO→LUMO transition.....	68
2.6. Extinction coefficient determination of <i>m</i> [6]CPP at the a) absorbance maxima and b) HOMO→LUMO transition.....	68
2.7. Extinction coefficient determination of <i>m</i> [7]CPP at the a) absorbance maxima and b) HOMO→LUMO transition.....	68
2.8. Extinction coefficient determination of <i>m</i> [8]CPP at the a) absorbance maxima and b) HOMO→LUMO transition.....	69
2.9. Extinction coefficient determination of <i>m</i> [10]CPP at the absorbance maxima.	69
2.10. Extinction coefficient determination of <i>m</i> [12]CPP at the absorbance maxima.	69
2.11. <i>m</i> [5]CPP Single irreversible oxidation (DCM) E = 0.47 V.	72
2.12. <i>m</i> [6]CPP Oxidation (DCM) E _{1/2} = 0.50 V and 0.68 V.	72
2.13. <i>m</i> [7]CPP Oxidation (DCM) E _{1/2} = 0.65 V and 0.81 V.	73

Figure	Page
2.14. <i>m</i> [8]CPP Oxidation (DCM) $E_{1/2} = 0.69$ V and 0.85 V.	73
2.15. <i>m</i> [10]CPP Oxidation (DCM) $E_{1/2} = 0.80$ V and 0.91 V.	74
2.16. <i>m</i> [12]CPP Oxidation (DCM) $E_{1/2} = 0.86$ V and 0.95 V.	74
2.17. Comparison of HOMO and LUMO energy levels of [<i>n</i>]CPPs (yellow) and <i>m</i> [<i>n</i>]CPPs (green). Calculated using B3LYP/6-31G(d,p) level of theory.	75
2.18. <i>m</i> [5]CPP Calculated absorption (red lines) compared to experimental absorption (black trace) results and table of calculated transitions.	76
2.19. <i>m</i> [6]CPP Calculated absorption (red lines) compared to experimental absorption (black trace) results and table of calculated transitions.	77
2.20. <i>m</i> [7]CPP Calculated absorption (red lines) compared to experimental absorption (black trace) results and table of calculated transitions.	78
2.21. <i>m</i> [8]CPP Calculated absorption (red lines) compared to experimental absorption (black trace) results and table of calculated transitions.	79
2.22. <i>m</i> [10]CPP Calculated absorption (red lines) compared to experimental absorption (black trace) results and table of calculated transitions.	80
2.23. <i>m</i> [12]CPP Calculated absorption (red lines) compared to experimental absorption (black trace) results and table of calculated transitions.	81
3.1. [10]CPP, furthest red-emitting nano hoops, and novel BT[10]CPP.	85
3.2. Synthesis of BT[10]CPP, linear BT system III.3, and attempted synthesis of BT[8]CPP.	86
3.3. a) Experimental absorbance (solid line) and emission (dashed line) of BT[10]CPP and comparison to [10]CPP and III.3 in dichloromethane. b) BT[10]CPP \supset C ₆₀ space filling model and c) BT[10]CPP fluorescence quenching by C ₆₀	88
3.4. HOMO and S1' of [10]CPP, BT[10]CPP and [10]CPTacq calculated at CAM- B3LP/6-31G* with dichloromethane as the solvent.	90
3.5. Fluorescence of BT[10]CPP in various solvents, excited at 334 nm.	97

3.6. Absorbance versus concentration for extinction coefficient determination of BT[10]CPP at the a) absorbance maximum and b) HOMO→LUMO transition and c) extinction coefficient of III.3.....	98
3.7. Experimental (circles) and fitted (dashed lines) triplicate data of the integrated fluorescence intensity vs absorbance of compound III.3 (grey) and standards anthracene (blue) and quinine sulfate (orange) used to determine quantum yield. ...	98
3.8. Fluorescence titration and binding curve of C ₆₀ and [10]CPP or BT[10]CPP in toluene. a) [10]CPP (5.52×10^{-7} mol/L) in the presence of C ₆₀ (5.00×10^{-5} mol/L) and b) BT[10]CPP (3.91×10^{-7} mol/L) in the presence of C ₆₀ (3.89×10^{-5} mol/L).	100
3.9. BT[10]CPP single reversible oxidation (DCM) E = 0.78 V.	101
3.10. III.3 single reversible oxidation (DCM) E = 1.14 V and reduction (DCM) E = - 2.00 V.	101
3.12. Calculated absorption spectrum and electronic transitions for BT[10]CPP.	103
3.13. Calculated absorption spectrum and electronic transitions for BT[8]CPP.	104
3.14. Calculated fluorescence spectrum and electronic transitions for [10]CPP.	105
3.15. Calculated fluorescence spectrum and electronic transitions for BT[10]CPP.	106
3.16. Calculated fluorescence spectrum and electronic transitions for [10]CPTcaq.	107
3.17. Strain-Viz calculations of a) BT[10]CPP, b) BT[8]CPP, c) [10]CPP and d) [8]CPP.	108
4.1. Advantages and challenges with common small molecules fluorophores and carbon nanomaterials. CPPs as a promising novel fluorescent scaffold at the intersection of small molecules and nanomaterials.	111
4.2. Synthesis of lysosome targeted nano hoop.	113
4.3. Cytotoxicity studies of morpholine- <i>m</i> [6]CPP and NHS- <i>m</i> [6]CPP in HeLa cells over 1 hour. Neither CPP compound shows significant cytotoxicity up to 50 μM.	115

Figure	Page
4.4. Colocalization of morpholine- <i>m</i> [6]CPP and NHS- <i>m</i> [6]CPP in live HeLa cells. a) morpholine- <i>m</i> [6]CPP, b) LysoTracker™ Deep Red, c) overlay. d) morpholine- <i>m</i> [6]CPP, e) MitoTracker™, f) overlay. g) NHS- <i>m</i> [6]CPP b) LysoTracker™ Deep Red, c) overlay.....	116
4.5. HeLa cell uptake of morpholine- <i>m</i> [6]CPP at 4, 27 and 37 °C to investigate uptake mechanism. Uptake is strongly hindered at 4°C incubation, demonstrating an energy dependent mechanism of nanohoop uptake into cells.	117
4.6. Absorbance versus concentration×pathlength for extinction coefficient determination of a) morpholine- <i>m</i> [6]CPP and b) alkyne- <i>m</i> [6]CPP in DMSO.	125
5.1. Different functional groups used for conjugation of biomolecules and reporter molecules.	128
5.2. Synthesis of benzyl alcohol functionalized CPP towards an NHS ester-CPP for bioconjugation.....	129
5.3. Synthesis of NHS ester-CPP for bioconjugation.....	130
5.4. Synthesis of NHS-PEG ₄ -[12]CPP for bioconjugation.	130
5.5. Gel analysis of nanohoop-DNA conjugates.....	131
5.6. a) Gel analysis of nanohoop-DNA conjugations with constant hoop final concentration or constant DNA concentration. b) analysis of duplex formation of nanohoop-ssDNA conjugate and complementary ssDNA.	132
5.7. TPF imaging of DNA-nanohoop conjugates.....	133
5.8. TPF imaging of Con A-nanohoop conjugates in different media.	134
5.9. One-photon fluorescence imaging of Con A-nanohoop conjugates and degree of labelling.	134
5.10. Synthesis and TPF imaging of biotin-nanohoop.	135

LIST OF TABLES

Table	Page
2.1. Triplicate quantum yield data, excited at the absorbance maxima.....	70
2.2. Triplicate quantum yield data, excited at HOMO→LUMO transition.....	70
2.3. HOMO→LUMO absorbance maxima and extinction coefficients.....	70
2.4. Fluorescence lifetimes and calculated decay rates.	71
2.5. Oxidation potentials of <i>m</i> [<i>n</i>]CPPs.....	71
2.6. First oxidation peak of <i>m</i> [<i>n</i>]CPPs.....	72
2.7. Calculated HOMO→LUMO absorption for <i>m</i> [<i>n</i>]CPPs.	75
2.8. Single point energies of compounds used in homodesmotic reactions and calculated strain.....	82
2.9. Calculated strain energy in <i>m</i> [<i>n</i>]CPPs, <i>ipso</i> carbon deviation, and dihedral angle. [<i>n</i>]CPP values in brackets. ¹²¹ It is noted that the strain for each aryl ring in <i>m</i> [<i>n</i>]CPPs are not equivalent due to asymmetry. <i>ipso</i> carbon deviations are for phenylenes opposite to the <i>meta</i> phenylene in the nano hoop.....	82
3.1. Average extinction coefficient and error of BT[10]CPP at absorbance maximum and HOMO→LUMO transition and III.3.....	98
3.2. Triplicate quantum yields, average quantum yield and error of BT[10]CPP and III.3.	98
3.3. Fluorescence lifetimes of BT[10]CPP and III.3 and calculated decay rates ⁹⁰ of BT[10]CPP.....	99
4.1. Photophysical properties of alkyne- <i>m</i> [6]CPP and morpholine- <i>m</i> [6]CPP in DMSO and comparison to parent <i>m</i> [6]CPP in CH ₂ Cl ₂	114
4.2. Average extinction coefficient and error of morpholine- <i>m</i> [6]CPP and alkyne- <i>m</i> [6]CPP.....	125
4.3. Triplicate quantum yields, average quantum yield and error of morpholine- <i>m</i> [6]CPP and alkyne- <i>m</i> [6]CPP.....	125

CHAPTER I

COMMON FLUORESCENT DYES USED FOR BIOLOGICAL APPLICATIONS

This chapter was written by myself with input from Professor Ramesh Jasti and Professor Bruce P. Branchaud.

Chapter II includes co-authored material with excerpts from work published in *Chemical Science*. The excerpts were written by myself with assistance from Dr. Curtis E. Colwell. The experimental work included from the published material was performed by myself or Dr. Curtis E. Colwell. Dr. Lev N. Zakharov provided crystal structure analysis of one of the final products discussed in the experimental section. Professor Ramesh Jasti provided editorial assistance.

Chapter III includes co-authored material with excerpts from work published in *Angewandte Chemie International Edition*. The excerpts were written by myself. The experimental work included from the published material was performed by myself with assistance from Zachary R. Garrison under my direction. Professor Ramesh Jasti provided editorial assistance.

Chapter IV includes unpublished co-authored material. The excerpts were written by myself with assistance from Sarah G. Bolton. The experimental work included was performed by myself with assistance from Sarah G. Bolton and Dr. Yu Zhao under my direction. Professor Ramesh Jasti and Professor Michael D. Pluth provided experimental input.

Chapter V includes unpublished co-authored material. The excerpts were written by myself with editorial assistance from Professor Ramesh Jasti. The experimental work included was performed by myself with assistance from Julia Shangguan, Dr. Fehmi Civitci, and Dr. John Kenison. Experimental guidance was provided by Professor Xiaolin Nan and Professor Ramesh Jasti.

1.1 Introduction

Albert Coons realized the utility of fluorescent molecules for biological applications when he labelled antibodies with fluorescein isothiocyanate.¹ Since then,

fluorophores have been extensively used in countless biological applications. They are attached to biological molecules to interrogate living systems, provide guidance for surgery, and identify and monitor diseases. Furthermore, fluorophores are a necessary component of many diagnostic kits, such as those used for diagnosing coronavirus (COVID-19). Interrogating disease progression requires simultaneous monitoring of multiple entities. Therefore, observing complex biological processes is intimately connected to the rational design and synthesis of bright stable fluorescent molecules.

Currently, the synthetic dyes that are commercially available are comprised of four common cores: coumarins, cyanines, xanthenes and BODIPYs. This chapter focuses on the four main scaffolds and newer perylene and cycloparaphenylene scaffolds. Synthetic methods to access these fluorophores and how to optimize their fluorescent properties are explored. The focus is on not just the trends, but the fundamental physical organic chemistry concepts that lead to the fluorescent properties. These fundamentals offer a holistic understanding of fluorescence in these fluorophores.

1.1.1 The Process of Fluorescence

The first account of fluorescence was in 1845 by Sir John Herschel while working with the antimalarial drug quinine, which showed a “celestial blue colour” in certain light.² It was not until 1852 when Sir George Stokes used quinine to work out the process of fluorescence.³ This process is shown in the Jabłoński diagram in **Figure 1.1**.⁴ A photon is absorbed resulting in an excited state (S_1 , S_2 , etc; **Figure 1.1 i**). The factors that describe this process are absorption maximum (λ_{\max}) and extinction coefficient (ϵ). The extinction coefficient describes how well a molecule absorbs light. It is wavelength dependent and usually reported in $M^{-1}cm^{-1}$. Extinction coefficients of common fluorophores start at $12,000 M^{-1}cm^{-1}$, and fluorophores with high extinction coefficients reach $200,000 M^{-1}cm^{-1}$.⁵ Upon excitation, energy is lost through rapid relaxation to the first singlet excited state (S_1 ; **Figure 1.1 ii**). Fluorescence is the process where a molecule emits a photon upon returning to the ground state from the excited state ($S_1 \rightarrow S_0$; **Figure 1.1 iii**). The key factors that describe this process are the emission maximum (λ_{em}), quantum yield (ϕ), and fluorescence lifetime (τ). Fluorescence efficiency is defined by the quantum yield, which is the ratio of photons emitted to photons absorbed. The

fluorescence lifetime is the average time between excitation and emission and is related to the relative rates of fluorescence and competing nonradiative processes. As an alternative to fluorescence, the molecule may return to the ground state by a nonradiative pathway (**Figure 1.1 iv**) such as vibrational excitation, photoinduced electron transfer, or Förster resonance energy transfer.⁶ Furthermore, the excited state molecule could convert to the triplet state through intersystem crossing (**Figure 1.1 v**) followed by radiative (**Figure 1.1 vi**) or nonradiative (**Figure 1.1 iv**) decay. Additional metrics to evaluate a fluorophore are Stokes shift and brightness. The difference in energy between the absorption and emission maxima of the same electronic transition is termed the Stokes shift. A large Stokes shift is desirable for many biological applications so the incident light does not interfere with the emission collection increasing the noise. The brightness is the quotient of extinction coefficient and quantum yield ($\epsilon \times \phi$). High brightness is desirable for a large signal to noise ratio and, therefore, lower detection limit. These fluorophore properties are a direct result of their molecular structure, which are altered through structural manipulation to suit the needs of a specific applications.

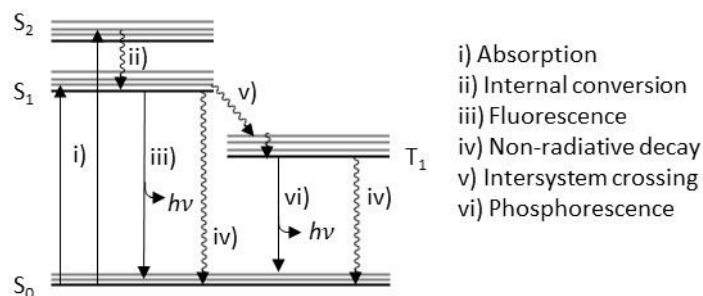


Figure 1.1. Jablonski diagram illustrating the process of fluorescence.

1.2 Synthesis of fluorescent scaffolds

Fluorescent properties of a molecule are a direct result of their molecular structure. Therefore, synthetic organic chemistry allows fine tuning of photophysical properties. Described below is a history of the improvements in synthetic methodologies for the production of fluorescent dyes.

1.2.1 Coumarins

Coumarins, discovered by Vogel in 1820, are the oldest common fluorescent scaffold.^{7,8} Coumarins are naturally occurring in many plants as a chemical defense to combat predators. This scaffold is highly exploited in the perfumes and cosmetics industry, but their most relevant role is in natural products, organic chemistry and medicinal chemistry.⁹

Coumarins are typically synthesized by Pechmann or Knoevenagel condensation (**Figure 1.2**). The synthesis of common coumarin 4-methyl-7-hydroxy-coumarin (**I.1, 4-MU**) is achieved by Pechmann condensation of resorcinol and ethyl acetoacetate (**Figure 1.2**). Fluorinated¹⁰ 7-hydroxycoumarin (**I.3, Pacific Blue™**) is also efficiently prepared using the Pechmann condensation.¹¹ The Pechmann condensation can be performed using alternative, safer, green catalysts like Amberlyst-15 and Dowex50WX4 beads. This synthesis is so simple undergraduates synthesize coumarins in their second-year chemistry lab.^{12,13} Additionally, coumarins can be synthesized from Knoevenagel condensation of salicylaldehydes and ethyl acetoacetate or dialkyl malonates in the presence of base **I.2**.¹⁴ Highly functionalized coumarins such as **I.3** are synthesized in reasonable yields using the Knoevenagel condensation.¹⁵ However, preparation of 7-aminocoumarins using these routes is more difficult and requires protection of the aniline nitrogen to afford an N-alkylated 7-aminocoumarin. A more recent advancement in the synthesis of 7-aminocoumarins is the use of Buchwald-Hartwig cross coupling. This approach easily converts a 7-hydroxy group (**I.5**) to an unsubstituted primary aniline (**I.6**).¹⁶

The most common coumarin used as a biological dye is **4-MU** with a $\lambda_{\max} = 360$ nm and $\lambda_{\text{em}} = 450$ nm (Stokes shift = 90 nm) in aqueous media at pH 10. It has a lower extinction coefficient of $17,000 \text{ M}^{-1}\text{cm}^{-1}$, quantum yield of 0.63, and brightness of $11,000 \text{ M}^{-1}\text{cm}^{-1}$.¹¹ 7-hydroxycoumarins are most fluorescent when deprotonated, but they are not fully deprotonated unless they are in basic media of $\text{pH} \geq 10$. The pKa of the hydroxyl group can be changed through halogenation.¹⁰ Additionally, switching the hydroxyl group for an amino group reduces pH dependence.

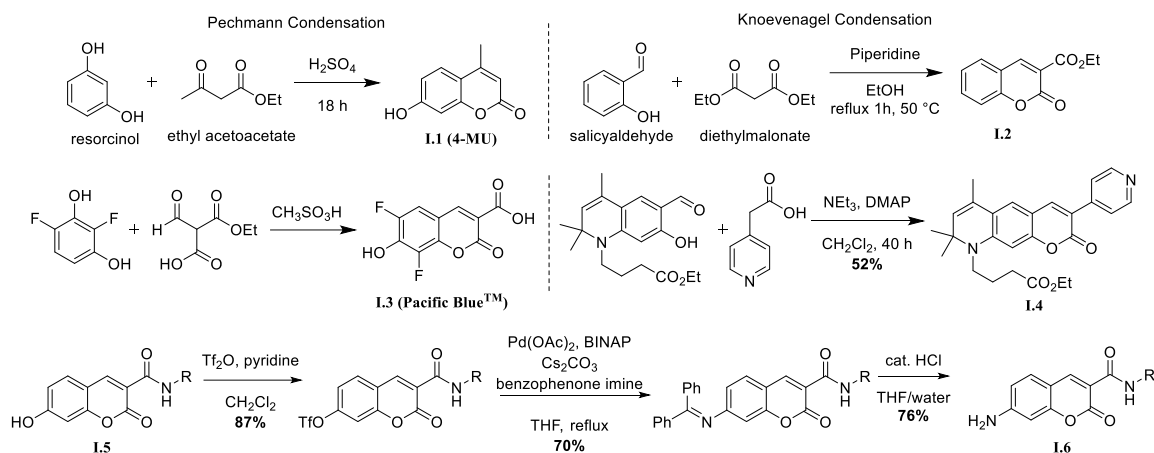


Figure 1.2. Synthesis of 7-hydroxy and 7-aminocoumarins through Pechmann condensation, Knoevenagel condensation and Buchwald-Hartwig cross coupling.

The resulting 7-aminocoumarin scaffold does not exhibit significant pH sensitivity.¹⁶ 7-amino-4-methylcoumarin (AMC) in methanol has a λ_{max} of 351 nm and λ_{em} of 430 nm. The ϵ is very close to **4-MU** at $18,000 \text{ M}^{-1}\text{cm}^{-1}$. However, it is slightly brighter than **4-MU** with a quantum yield of 0.75 and brightness of $14,000 \text{ M}^{-1}\text{cm}^{-1}$.⁵ Coumarin emission ranges from 430 nm to 650 nm.^{5,17}

1.2.2 Cyanine

Cyanine (Cy) dyes were first synthesized in 1856 and are comprised of nitrogen heterocyclic subunit(s) linked by a poly methine bridge. The number of carbons in the methine bridge is denoted in the name (ie Cy3, Cy5, etc.). Several cyanine dyes are produced in nature. Betanin is responsible for the color of red beets and Muscaurin I is responsible for the red color in the iconic white-spotted red toadstool mushroom.^{18,19} Initially, cyanines were mainly used as DNA stains due to weak fluorescence in solution, until intercalation into RNA or double stranded DNA (dsDNA) where fluorescence dramatically increases.^{20,21} It was not until 1993, when cyanine dyes were synthesized with sulfonate groups (to enhance solubility) and bioconjugation handles, that they were used as labeling reagents.²²

Cyanines are synthesized through condensation of quaternary heterocyclic salts with an activated methyl group (**I.7**) and an orthoester ($\text{CH}(\text{OEt})_3$, **Figure 1.3, I.8**).^{18,23} Cy5 dyes are synthesized through this same condensation reaction, but with a different

orthoester to give **I.9**. Alternatively, the central methine moiety can be supplied through a Vilsmeier-type reaction where cyanine **I.10** is obtained in reasonable yields through one-pot synthesis of 2,3,3-trimethyl-3*H*-indole in dimethylformamide (DMF) shown in **Figure 1.3**.^{18,24} Protonation of DMF results in Vilsmeier-like reagent **I.11** supplying the methine moiety. Syntheses have been further refined to use hemicyanine intermediate **I.12**, to deliver symmetric and asymmetric cyanines (such as **I.13**) in higher yield.^{22,25,26}

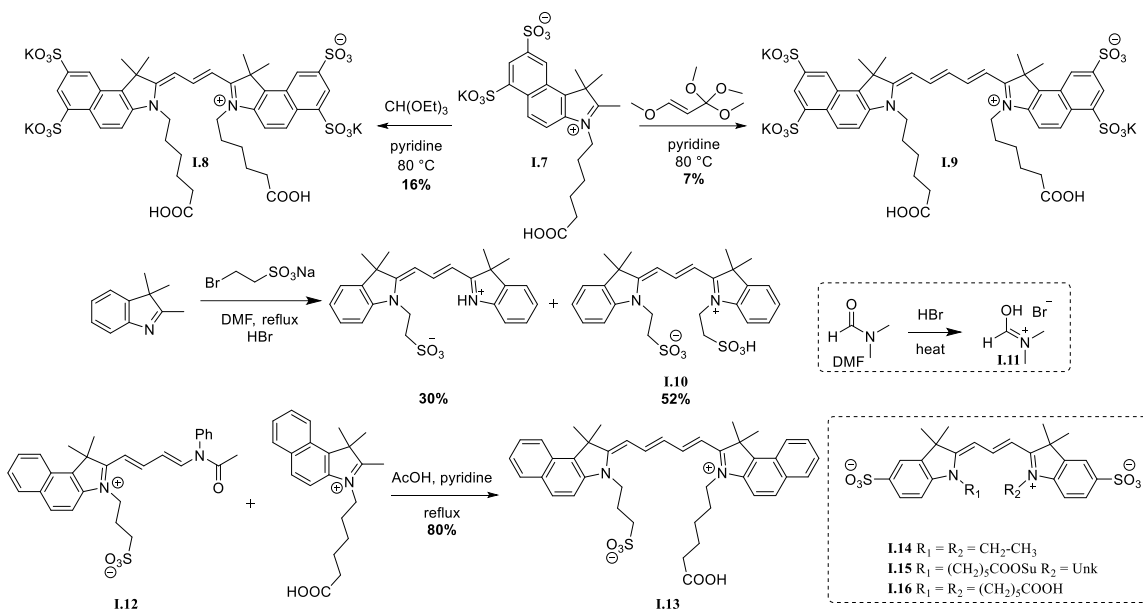


Figure 1.3. Synthesis of cyanine dyes.

Cyanine dyes have large extinction coefficients, on the order of $10^5 \text{ M}^{-1}\text{cm}^{-1}$, and a wide range of possible fluorescence. Cy3 **I.14** has a $\lambda_{\text{max}} = 554 \text{ nm}$ and $\lambda_{\text{em}} = 568 \text{ nm}$ (Stokes shift = 14 nm) in PBS (pH 7) with a high extinction coefficient of $130,000 \text{ M}^{-1}\text{cm}^{-1}$.⁵ While several papers cite the quantum yield of **I.14**^{5,11} and **I.15**²⁷ to be 0.14 in PBS, the primary reference did not measure their quantum yields. Instead, **I.16** was reported to have a quantum yield of 0.04 and extinction coefficient of $150,000 \text{ M}^{-1}\text{cm}^{-1}$.²² Its brightness is therefore between $6,000\text{-}18,000 \text{ M}^{-1}\text{cm}^{-1}$, depending on the quantum yield reported. Cyanine emissions range from 575 nm to 808 nm.^{22,23}

1.2.3 Xanthenes (Fluorescein and Rhodamine)

Fluorescein was first synthesized in 1871²⁸ and was the first antibody label for immunofluorescence.¹ Fluorescein is one of the most widely used fluorophores in biological and medicinal research. It has also found its way to use in ophthalmology as a stain to detect corneal defects.

Fluorescein is in equilibrium between two possible states, the open fluorescent form **I.17** and the non-fluorescent lactone **I.18**. It is most fluorescent in the open dianion form. Fluoresceins were initially synthesized through condensation of resorcinol and phthalic anhydride with zinc chloride at high temperatures. A better method was introduced where the condensation is performed in neat acid, such as methanesulfonic acid, at lower temperatures (**Figure 1.4**).²⁹ Another innovation introduced was improvement in product purification. Purification is achieved through conversion of fluorescein **I.19** to the more easily purified diacetate lactam **I.20**, then converted back to fluorescent **I.19**.

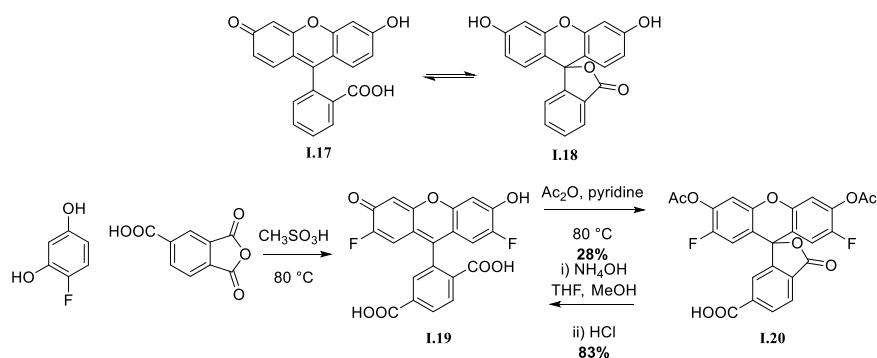


Figure 1.4. Synthesis of fluorescein.

Unsubstituted fluorescein **I.17** has $\lambda_{\text{max}} = 490$ nm and $\lambda_{\text{em}} = 514$ nm, with a resultant Stokes shift of 24 nm. At pH 9, **I.17** has an extinction coefficient of $93,000 \text{ M}^{-1}\text{cm}^{-1}$ and a quantum yield of 0.95. The resulting brightness of $88,000 \text{ M}^{-1}\text{cm}^{-1}$ is brighter than the coumarins or cyanines discussed above. Fluorescein emission ranges from 525 nm to 566 nm.³⁰

The amino analogue of fluorescein is termed rhodamine. These analogues have lower pH-sensitivity and better photostability. Tetramethyl rhodamine (TMR) **I.21** was initially synthesized through condensation of phthalic anhydride with 3-

(dimethylamino)phenol at high temperatures.³¹ Even with a Lewis acid catalyst (ZnCl_2) low yields are obtained.³² Additionally, a mixture of isomers is obtained and only a limited number of phenols are compatible with this method.³³ Accordingly, functionalized rhodamines are mostly sold as isomeric mixtures and are expensive. Lavis and coworkers utilized the Buchwald-Hartwig cross-coupling, similar to the method used to make amino coumarins above, to synthesize isomerically pure rhodamine dyes from fluorescein derivatives.³³ Fluorescein **I.17** was triflated and converted to spiro lactam **I.22**, followed by Buchwald-Hartwig amination to afford tetraethyl rhodamine **I.23**. This synthesis yielded isomerically pure rhodamines in much higher yields than previous methods. In 2016, Levin and coworkers found optimized conditions to synthesize isomerically pure TMR **I.21** in high yields from **I.24** and 3-(dimethylamino)phenol in an oxygen atmosphere. Unlike the Buchwald-Hartwig amination approach, this method could be employed to make rhodamines with cyclic fused amines like **I.26** in 87% yield.³⁴

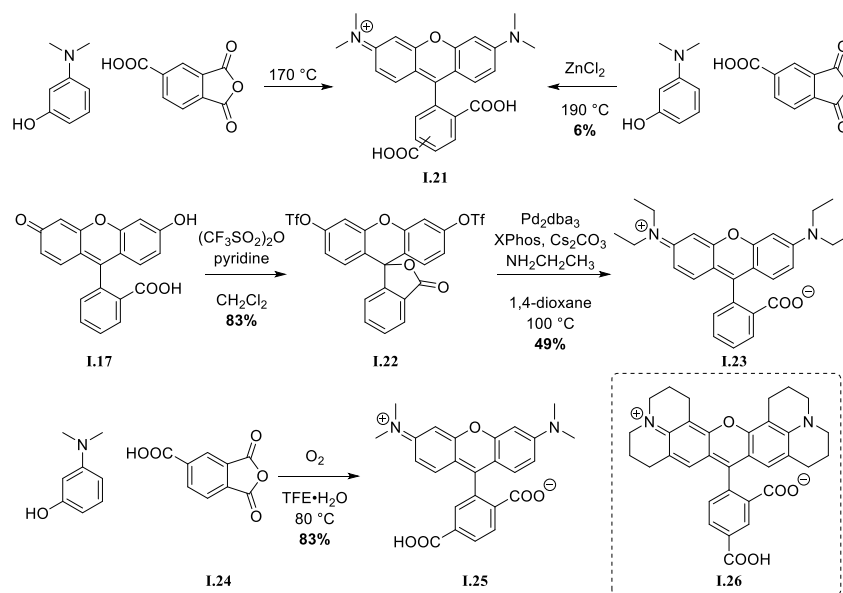


Figure 1.5. Rhodamine synthesis.

Rhodamines exhibit fluorescein-like optical properties. Rhodamine 110 (amine version of **I.17**) has a $\lambda_{\text{max}} = 496 \text{ nm}$ and $\lambda_{\text{em}} = 517 \text{ nm}$, with a resultant Stokes shift of 21 nm at pH 7.5. The extinction coefficient is $74,000 \text{ M}^{-1}\text{cm}^{-1}$ and quantum yield is 0.92,

resulting in a brightness of $68,000 \text{ M}^{-1}\text{cm}^{-1}$. Substitution of the nitrogen changes the photophysical properties (discussed below), where TMR **I.23** has a $\lambda_{\text{max}} = 540 \text{ nm}$ and $\lambda_{\text{em}} = 565 \text{ nm}$ (Stokes shift = 25 nm) and quantum yield of 0.68. Rhodamine emission ranges from 525 nm to 764 nm .^{35,36}

1.2.4 BODIPY

BODIPY dyes were first synthesized in 1968 by Treibs and Kreuzer.³⁷ BODIPY is an abbreviation for boron dipyrromethene. BODIPY dyes are known for environmentally independent fluorescence, small Stokes shift and lipophilicity. It was not until 1988 when Molecular Probes® published a patent for use as a biomolecular label that interest grew in BODIPY dyes.³⁸

The initial BODIPY synthesis was realized by intermolecular condensation of 2,4-dimethyl-pyrrol to give a mixture of BODIPY **I.27** and **I.28**.³⁷ This process was improved by using optimized conditions and glutaric anhydride in place of acetic anhydride to yield BODIPY **I.29**.³⁹ This doubled the yield and resulted in a free carboxylic acid for possible biomolecule conjugation. Alternatively, other activated carboxylic acid derivatives could replace acid anhydrides, such as acid chlorides.⁴⁰ To install aromatic moieties at the *meso*-position, pyrroles and aromatic aldehydes can be used. 2-methylpyrrol reacts with 4-iodobenzaldehyde to give intermediate **I.30**, which is oxidized using *p*-chloranil and complexed to give BODIPY **I.31**.⁴¹ However, the oxidation step limits the tolerated functional groups on the aromatic unit. While these methods are suitable to access symmetric BODIPY dyes they are not efficient for preparing asymmetric BODIPYs. Asymmetric BODIPY dyes are accessed through preparation of ketopyrroles followed by condensation with a different pyrrole.^{42–44} For example, Vilsmeier-Haack reaction of **I.32** followed by hydrolysis affords ketopyrrole **I.34**. Condensation of **I.34** with 2,4-dimethylpyrrole and complexation with $\text{BF}_2 \cdot \text{OEt}_2$ gives asymmetric BODIPY **I.35**.⁴³ Additionally, this method can also provide a higher yielding route to symmetric BODIPYs. The unsubstituted BODIPY core was not synthesized until 2009 due to instability resulting from the high nucleophilicity of the pyrrole carbons.^{45–47}

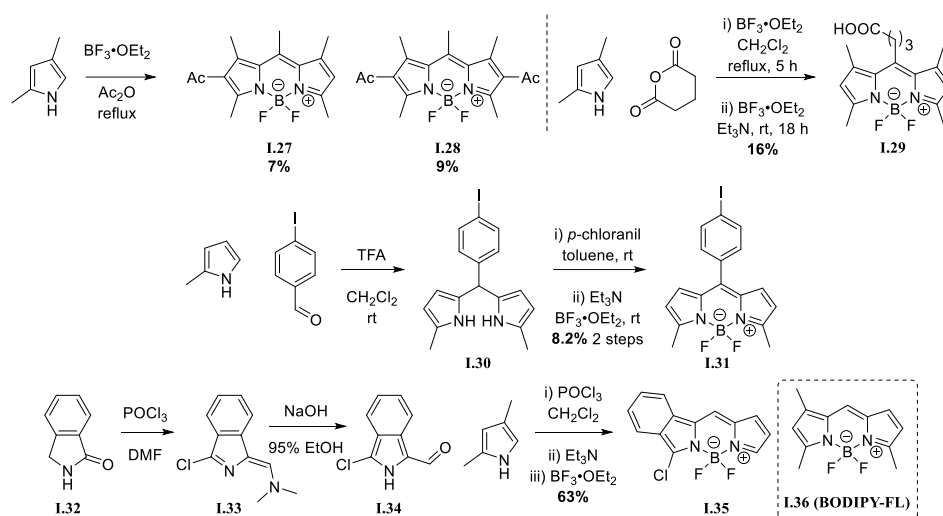


Figure 1.6. Synthesis of symmetric and asymmetric BODIPYs.

BODIPY dyes have high extinction coefficients and quantum yields. BODIPY-FL **1.36** has an extinction coefficient of $91,000 \text{ M}^{-1}\text{cm}^{-1}$ and a quantum yield of 0.94 in methanol, making them the brightest ($86,000 \text{ M}^{-1}\text{cm}^{-1}$) scaffold discussed thus far.⁵ However, BODIPYs possess the smallest Stokes shifts. BODIPY-FL has a $\lambda_{\text{max}} = 505 \text{ nm}$ and $\lambda_{\text{em}} = 511 \text{ nm}$, which is a Stokes shift of only 6 nm. BODIPY emission ranges from 500 nm to 710 nm.⁴⁸

1.2.5 Perylene

Perylene is a rylene dye, which were first synthesized in 1913 and have been widely used as industrial colorants.⁴⁹ However, fluorescent potential was not realized until almost 50 years later due to insolubility. Furthermore, they were not explored for biological purposes until 45 years later in 2004 when the first water soluble rylene dye **1.42** was synthesized.

Unlike previous scaffolds, perylenes are not synthesized through condensation reactions. Instead, **1.37** is oxidized with vanadium oxide to afford a dicarboxylic anhydride, which is converted to the dicarboxylic imide **1.38** with ammonia. Oxidative coupling of two molecules of **1.38** affords the perylene tetracarboxylic diimide **1.39**. Hydrolysis with concentrated sulfuric acid at $220 \text{ }^\circ\text{C}$ affords the dianhydride **1.40**.⁵⁰ **1.40** is available in large quantities for under \$1 per gram. As a result, this is the common starting point in perylene dye synthesis. The bay region of **1.40** is chlorinated and

converted to perylene diimide (PDI) **I.41**. Nucleophilic aromatic substitution of **30** with phenol affords the o-aryl substituted PDI, which is treated with concentrated sulfuric acid to yield the final water-soluble PDI **I.42**.⁵¹ Progress in PDI functionalization has been covered elsewhere.⁵² While many monofunctional water-soluble rylene dyes have been prepared^{53–55}, we cannot find examples of them attached to biomolecules like antibodies or DNA.

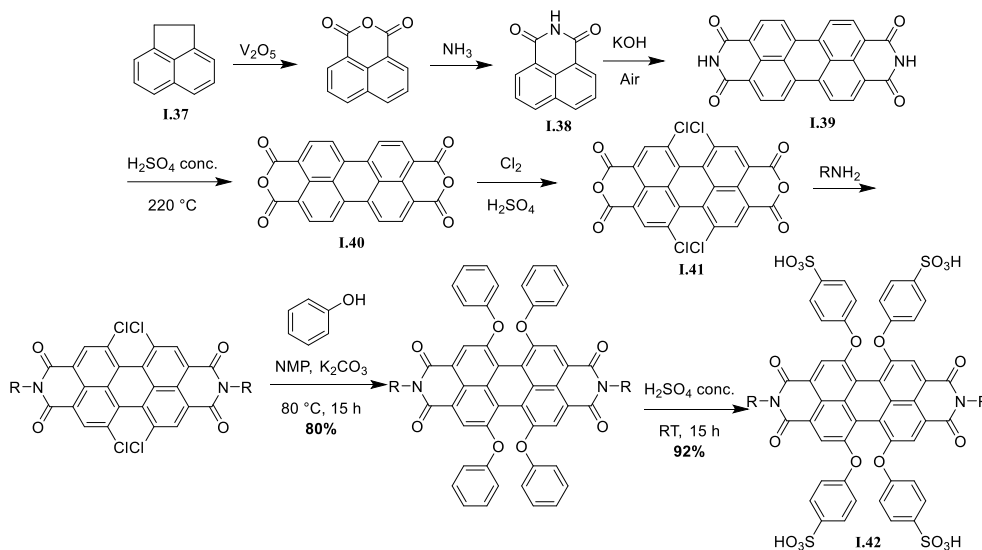


Figure 1.7. Synthesis of water soluble perylene dye.

While unfunctionalized perylene dyes have quantum yields that reach unity in organic solvents, water soluble versions are not as bright. **I.42** has a $\lambda_{\text{max}} = 541$ nm and $\lambda_{\text{em}} = 619$ nm (Stokes shift = 78 nm) in water. The extinction coefficient is $27,800 \text{ M}^{-1}\text{cm}^{-1}$ and quantum yield of 0.58, resulting in a brightness of $16,000 \text{ M}^{-1}\text{cm}^{-1}$.⁵¹ Perylene emission ranges from 530 nm to 750 nm.⁵⁶

1.2.6 Cycloparaphenylene

[*n*]cycloparaphenylenes (CPPs) were first synthesized by Jasti and Bertozzi in 2008 in an effort to prepare carbon nanotubes with precise structure.^{57–61} These strained macrocyclic structures, often referred to as carbon nano hoops, are composed of all *para*-linked phenylenes and can be considered as a short carbon nanotube slice.

CPPs were initially synthesized through lithiation additions, cross-couplings, and aromatization using lithium naphthalenide. The challenge with the preparation of these molecules is the large amount of strain in these bent aromatic molecules. As such, a 3,6-*syn*-dimethoxy-cyclohexa-1,4-diene unit (seen in **I.43**) is used as a “masked” aromatic unit to obtain the curvature needed to make the macrocyclic precursor. **I.43** is obtained through lithiation of diodobenzene and double addition into benzoquinone. Borylation of **I.43** affords coupling partner **I.44**. Unstrained macrocyclic precursors are made through Suzuki reaction of curved intermediates **I.43** and **I.44** to give macrocycles **I.45**, **I.46** and **I.47**. The final CPPs were obtained through aromatization with lithium naphthalenide.⁵⁷ Since the initial synthesis, the synthetic methods have been greatly improved. A notable improvement was when the “building-block” approach was initiated. Going through building-block **I.51** allowed the synthesis of unsymmetric curved pieces such as **I.52**. With this, the phenyl groups could be assembled much quicker and allowed the formation of the macrocyclic precursors more controllably.⁶² One land-mark improvement was the use of triethylsilyl protecting groups (TES) instead of methoxy groups.⁶⁰ This allowed stereoselective additions to make curved building blocks like **I.43** more efficiently. Arguably the biggest advancement in CPP synthesis is milder aromatization conditions using tin(II)chloride.⁶⁰ This made the synthesis significantly more functional group tolerant and higher yielding.^{63–66} With these improvements, even functionalized CPPs can be prepared on the gram-scale.⁶⁷

Characteristics of CPPs are their high extinction coefficients, large effective Stokes shift and high quantum yields for larger sizes. All CPPs have a $\lambda_{\text{max}} = 350$ nm and λ_{em} range from 450-587 nm, which is a Stokes shift ranging from 100 nm to 237 nm. [12]CPP has an extinction coefficient of $140,000 \text{ M}^{-1}\text{cm}^{-1}$ and a quantum yield of 0.80, making it the brightest ($110,000 \text{ M}^{-1}\text{cm}^{-1}$) fluorophore discussed thus far. However, their photophysical properties have mainly been explored in organic solvents. Nevertheless, disulfonate[8]CPP, **I.53**, is an example of CPPs in a biological context, which does retain its brightness in aqueous media.⁶⁶ Cycloparaphenylene emissions range from 450 nm to 570 nm.^{64,68}

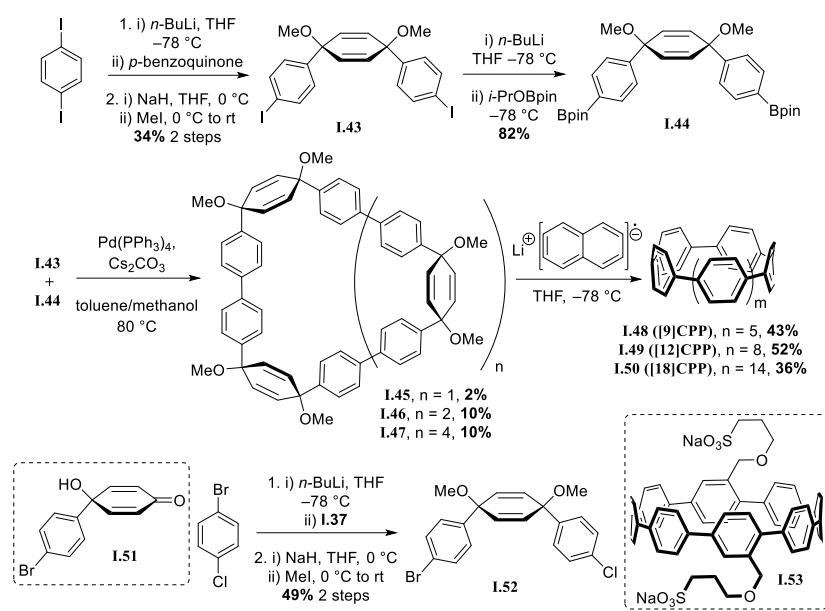


Figure 1.8. Synthesis of CPPs and water soluble CPP.

1.3 Tuning the emission of fluorophores

Monitoring complex biological systems requires simultaneous observation of multiple entities. Therefore, fluorophores with varying emission wavelengths that span the color spectrum are required. Additionally, particular colors are desirable for certain applications. For example, red-emitting fluorophores are desirable in biological imaging applications because tissues scatter and absorb less light at longer wavelengths.⁶⁹ Longer wavelength (lower energy) light is also less damaging to cells. Therefore, controllably manipulating fluorophore optical properties is crucial. While there are many reviews on fluorophores that list variants of common scaffolds and their fluorescent properties, they do not discuss the underlying reason for these trends. Here, we provide rational using fundamental physical organic chemistry concepts. We seek to provide a better understanding to researchers that seek to tune fluorescent dye optical properties. Fluorophore emission is tuned through changing the energy levels of the frontier molecular orbitals (FMO), which include the highest occupied molecular orbital (HOMO) and lowest unoccupied molecular orbital (LUMO). The narrower the HOMO-LUMO gap the more red the emission wavelength. While we do note this energy gap is determined by multiple factors^{70,71}, for simplicity we focus on the HOMO and LUMO densities on each position and how electron withdrawing groups (EWG), electron

donating groups (EDG) and extended π -conjugation affect these atomic orbitals. This description is accurate for most dyes because emission is the result of a transition from the lowest lying excited state (usually the LUMO) to the HOMO. However, this simplification does not accurately describe absorbance since absorbance can happen via many transitions, not just the HOMO to LUMO transition. Lastly, we note that EDG and EWG affect FMO distribution, but looking at orbital distribution in the parent molecule does allow prediction of substituent effects.

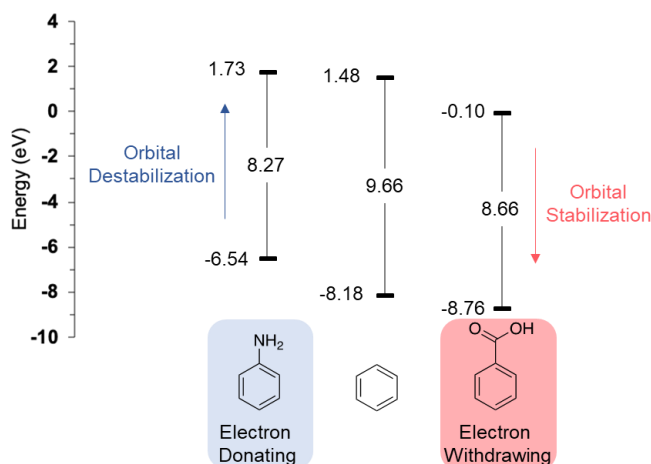


Figure 1.9. Orbital stabilization and destabilization from addition of electron withdrawing and electron donating groups.

1.3.1 Electron withdrawing and electron donating groups for altering molecular orbitals

Common methods to change the HOMO and LUMO levels to red-shift (bathochromic shift) the emission are addition of electron donating groups (EDGs) and electron withdrawing groups (EWGs). In the simple case of benzene (**Figure 1.10**), addition of electron donating groups destabilize (raise) the HOMO and LUMO, whereas electron withdrawing groups have a stabilizing (lower) effect.^{70,72REF} Addition of donor or acceptor groups to positions where only one FMO is localized allows electronic modulation of this FMO level, without affecting the other. This results in a change of the HOMO-LUMO gap and, therefore, fluorescence.⁷¹ Hammett parameters are commonly used to describe the withdrawing or donating ability of a substituent and the resultant photophysical properties. However, Hammett parameters do not provide a holistic picture

of substituent effects on conjugated systems.⁷³ Hyperconjugation and hypervalency effects are not encompassed in Hammett parameters, which are important influencers on the photophysical properties of conjugated molecules. Therefore, qualitative molecular orbital theory is used to understand the photophysical properties of conjugated molecules. The atomic contributions to the HOMO and LUMO for each scaffold are shown in **Figures 1.10-1.13**.

For coumarin, significant LUMO electron density resides on the 4-position with minimal HOMO density. Therefore, adding EWG on the 4-position should stabilize (decrease) the LUMO significantly, decreasing the energy gap (ie. red-shift fluorescence).⁷¹ Substituting the methyl group in **I.54** for a CF₃ (**I.55**) results in a shift from 442 nm for **I.54** to 480 nm. The CF₃ has a significant effect on the LUMO of **I.55**, while a minimal effect on the HOMO, therefore its emission is further red than that of **I.54**. Addition of a carboxylic acid (**I.56**) in the 4-position in place of the methyl group of **I.54** causes a red-shift of over 50 nm. The emission is further red-shifted than **I.55** because the carboxylic acid is conjugated with the rest of the scaffold (see extending conjugation section). A methyl ester in the 4-position, as in **I.57**, elicits a further red-shift in the fluorescence versus the carboxylic acid derivative **I.56**. Substituting the 3-position (**I.58**) with a carboxylic acid or methyl ester (**I.59**) does not influence the emission because the EWG is affecting the HOMO and LUMO equally. Therefore, no resultant change of the energy gap.

The 6-position has HOMO contributions while having no LUMO contributions, therefore donors decrease the HOMO-LUMO gap. Addition of weakly π donating fluorine atoms on **I.3** slightly red-shifts the fluorescence of **I.60**. Halogens have competing inductive and resonance effects, however, they act as weak π -donors. Enhancing the donating ability of the nitrogen in amino coumarins also red-shifts the fluorescence. Formation of a heterocycle as in **I.61** improves hyperconjugation and the fluorescence is shifted to 551 nm and is further shifted to 575 nm with fused system **I.62**. In summary, red-shifting the coumarin scaffold is achieved by putting strong EDGs on the 7-position, EWGs on the 4-position.

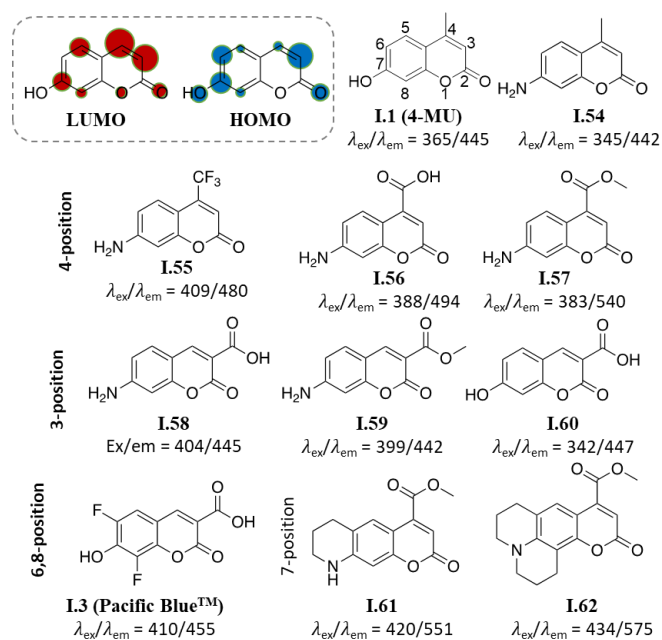


Figure 1.10. Coumarin HOMO and LUMO orbital densities and fluorescence tuning by incorporating EWGs and EDGs.⁷⁴

The HOMO and LUMO orbital densities of fluorescein and rhodamine are shown in **Figure 1.11**. The photophysical properties of fluorescein are more difficult to tune than rhodamine because substitution of the phenolic oxygen yields the non-fluorescent lactone form. Therefore, the main way to modulate the fluorescence of fluorescein is through halogenation. Fluorination (**I.64**) and chlorination (**I.65**) of **I.63** elicits a modest bathochromic shift. Iodination and bromination (**I.66**) causes a further 10 nm shift. However, the overall effect results in a mere 41 nm shift in fluorescence from **I.63**. The lack of tunability of fluorescein resulted in amination of the xanثone core to produce the rhodamine scaffold.

Rhodamine 110, **I.67**, has an emission of 517 nm. When the donating ability of the amine is increased through addition of methyl groups the fluorescence is shifted to 531 nm (**I.68**) and 576 nm (**I.21**). Heterocycle formation (**I.69**) provides optimal nitrogen lone pair conjugation with the π -system, therefore red-shifting the fluorescence to 588 nm. In summary, red-shifting xanثone dye fluorescence is achieved by halogenation of fluorescein or increasing the donating ability of rhodamine nitrogens.

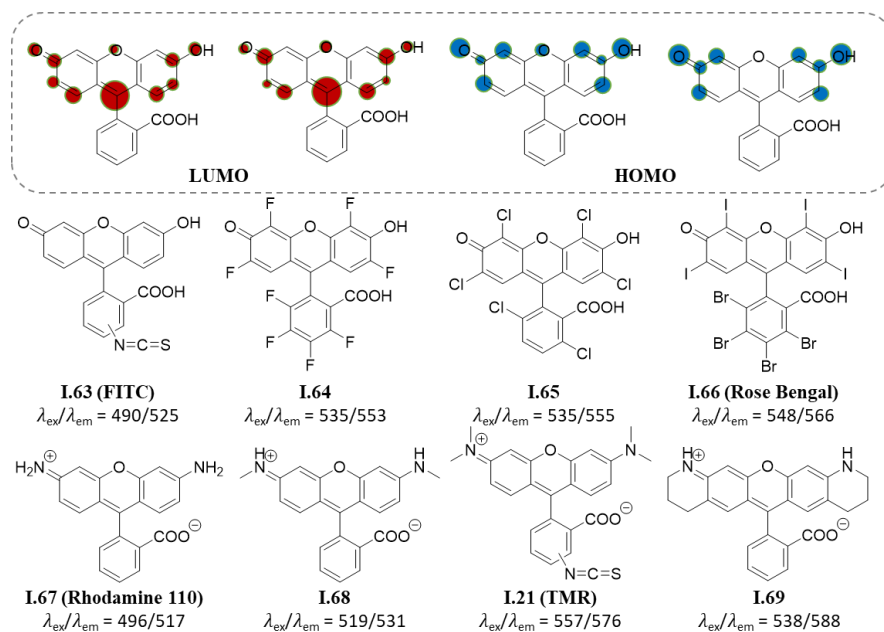


Figure 1.11. HOMO and LUMO orbital densities of fluorescein and rhodamine and fluorescence tuning by incorporating EDGs.

The tuning of BODIPY fluorescence has not been well understood in the past,⁴⁰ however the fluorescence follows expected trends when using an FMO analysis. There is more HOMO orbital contribution on the 3- and 5-position, indicating that EDGs in these positions would result in a red-shift in fluorescence. Two EDGs in the 3- and 5-positions in **I.71** red-shifts the fluorescence from unsubstituted BODIPY **I.70**.⁴⁷ This effect is more obvious when electron donating ability is increased. Switching chlorides of **I.72** to methoxy groups (**I.73**) only slightly red-shifts the fluorescence. This is more dramatically shifted with substitution of one (**I.74**) or two (**I.75**) amines.

The BODIPY scaffold has HOMO density on the 2- and 6-positions and no significant LUMO contributions. Substituting an ethyl group on the 2-position as shown in **I.77** red-shifts the fluorescence compared to **I.76**. The fluorescence is further shifted when substituting both the 2- and 6-positions with methyl (**I.78**) or ethyl groups (**I.79**). Substitution with bromide (**I.80**) shows a 42 nm bathochromic shift in fluorescence relative to **I.86**. Furthermore, fusing cyclic structures on the 2- and 6-positions shifts the fluorescence more (**I.81**) due to better hyperconjugation.⁷⁵ However, if the cyclic structure is fused to positions with LUMO density like **I.82** the same red-shifting as **I.81** is not observed. There are a few structures that appear to stray from the expected trends.

I.83 and **I.84** have withdrawing groups on positions with mainly HOMO density, yet the fluorescence is red-shifted versus the unfunctionalized version **I.86**. However, when considering the optimized geometry of the molecule, the nitro group of **I.83** is parallel with the π -system and therefore is in conjugation. The resultant π -system extension results in the observed red-shift (see extending conjugation section). This is also true for sulfonate **I.84**.

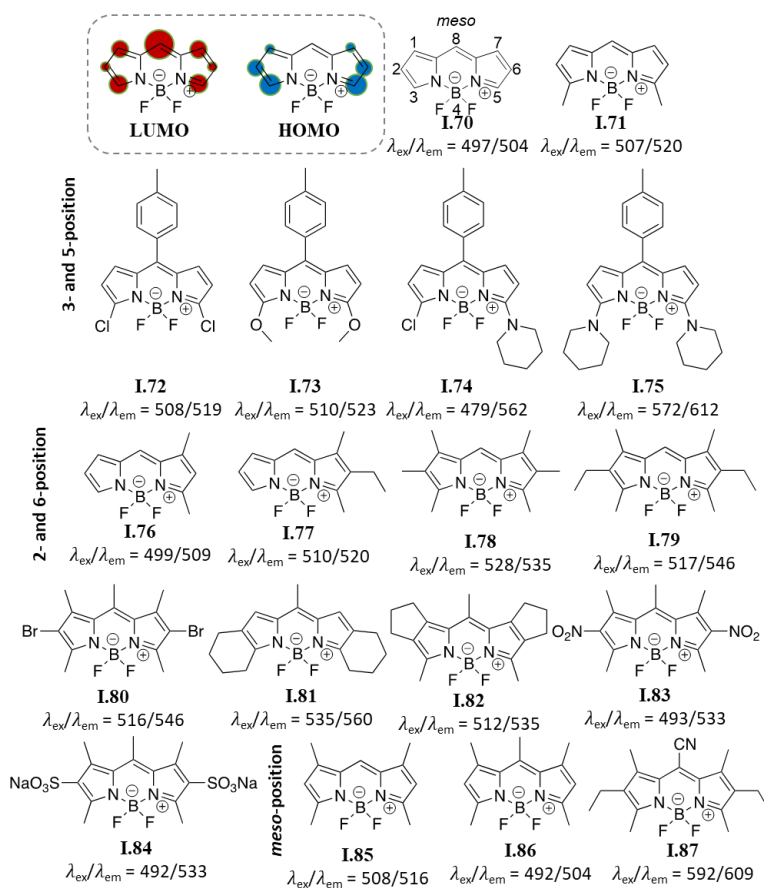


Figure 1.12. HOMO and LUMO orbital densities of BODIPY and fluorescence tuning by incorporating EWGs and EDGs.

As stated earlier, the more the BODIPY core is functionalized the further red it will emit. However, if EDG are added to positions where the LUMO mainly resides then the fluorescence is blue-shifted (hypsochromic shift). This is illustrated with **I.85** and **I.86**. **I.86** is more highly functionalized than **I.85**, but there is an EDG in the *meso*-

position, which destabilizes the LUMO resulting in a blue-shift relative to **I.85**. This reinforces the importance of considering orbital contribution on each position.

It is postulated that *meso*-position alkylation and arylation does not affect the fluorescence, however, this is not the case. The *meso*-position shows exclusively LUMO contribution. Therefore, adding EWG to the *meso*-position as in **I.87** red-shifts the fluorescence by over 60 nm compared to **I.79**. In summary, red-shifting the BODIPY scaffold is achieved by putting strong EDGs on the 3-, 5-, 2-, and 6-positions and strong EWGs on the *meso*-position.

No significant orbital separation is observed on the PDI scaffold (**Figure 13**). The nitrogen atoms are located on a nodal plane of the HOMO and LUMO, therefore, substitution of the imide does not significantly change the optical properties.⁴⁹ The bay region has slightly more HOMO density, therefore, this may be the only viable region to add EDGs. When switching hydrogen (**I.88**⁷⁶) in this region for better donors like **I.89** and **I.90** the fluorescence shifts by almost 80 nm.⁷⁷ Even better donors such as **I.91** and **I.92** cause shifts over 100 nm.⁷⁸ Although, one has to be mindful of the bay substituents. If the groups are too large it will result in a twisting of the PDI core, potentially leading to a hypsochromic shift.⁴⁹ Other “push-pull” variants of rylene structures lacking one diimide exist, but are not covered here.⁷⁹

The *ortho*-position shows mainly LUMO contribution, therefore EWGs should red-shift the fluorescence. However, cyano substitution in those positions (**I.93**) causes a blue-shift.⁸⁰ TD-DFT calculations predict **I.93** emission to be 5 nm red-shifted versus **I.88** and the fluorescence transition is LUMO→HOMO for both. Some have speculated a rational, but lack of experimental studies does not allow a conclusive verdict.⁴⁹ Red-shifting the PDI scaffold is achieved by putting strong EDGs in the bay-positions.

Cyanine and CPPs are not affected by electron donating and electron withdrawing group incorporation onto their scaffold since their HOMO and LUMO orbitals are evenly distributed. For CPPs, instead electron accepting moieties (or units) must be incorporated into the backbone.

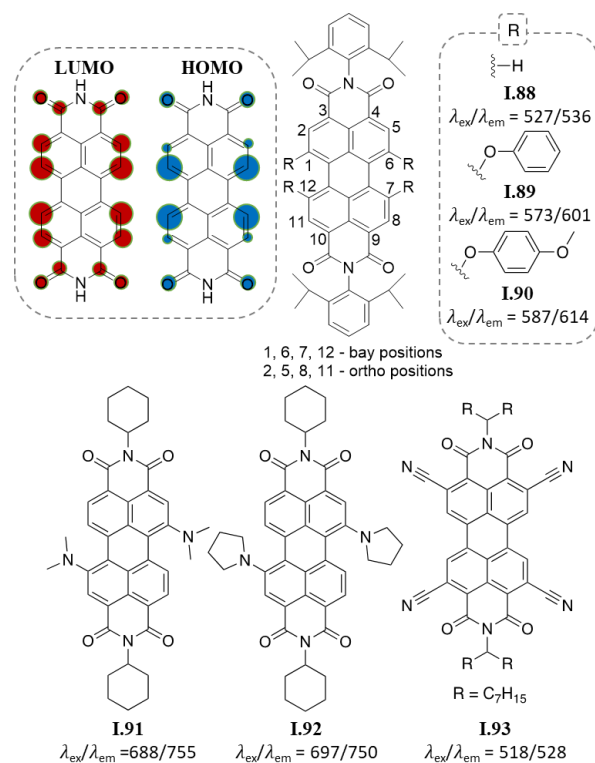


Figure 1.13. HOMO and LUMO orbital densities of PDI and fluorescence tuning by incorporating EWGs and EDGs.

A tetracyanoanthraquinone unit incorporated into the CPP backbone (**I.95**) shifts the fluorescence of [10]CPP **I.94** dramatically by 176 nm to 642 nm. Unfortunately, the quantum yield diminishes to almost zero.⁸¹ However, we have shifted the fluorescence of the nano hoops while retaining the quantum yield (**Chapter III**).

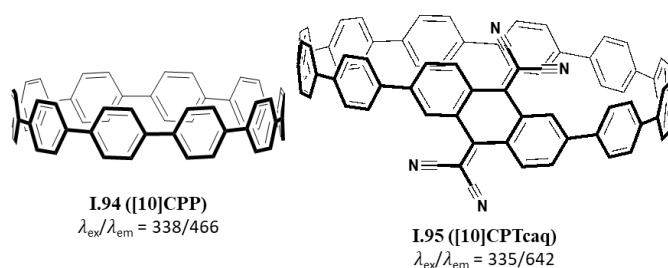


Figure 1.14. Red-shifting of CPPs through incorporation of electron accepting units within the CPP backbone.

1.3.2 Extending Conjugation

The other common method to red-shift the emission of fluorophores is through π -conjugation extension, which stabilizes the LUMO and destabilizes the HOMO by adding additional atomic orbitals. This is usually achieved through addition of arylene or ethenylene substituents.

Addition of benzofusions on coumarin shifts the fluorescence to 570 nm (**I.96**) or 623 nm (**I.97**), depending where they are fused.⁸² Alternatively, aryl ethenylene moieties can shift the emission as well (**I.98**). There have also been coumarin-cyanine hybrids (**I.99**) synthesized that shift the fluorescence to 663 nm.¹⁷

Red-shifting the emission of cyanine is mainly achieved through conjugation extension. Either the methylene bridge is extended or aryl fusions are added to the phenyl ring. Cy3 **I.100** has an emission of 575 nm, extension of the bridge to Cy5 **I.101** shifts the fluorescence to 677 nm.²² Further bridge extension to Cy7 **I.102** affords emission at 789 nm. Unfortunately, extension of the bridge and red-shifting the fluorescence of the cyanine scaffold comes at the cost of diminished quantum yields. Addition of benzofusions to Cy3 and Cy5 shifts the fluorescence 27 nm to the red (**I.103** vs **I.100** and **I.104** vs **I.101**).²³

Additional benzofusions on fluorescein and rhodamine yield naphthofluorescein and naphthorhodamine, which shift the emission by 154 nm to 668 nm (**I.105**– **I.107**).^{83,84} However, the pKa of naphthofluorescein **I.107** is 8, meaning at physiological pH it is not in the highly fluorescent dianion form, limiting its usage.⁵

Addition of aryl ethenylene groups on the BODIPY scaffold can dramatically shift the spectral properties (**I.108**– **I.110**). The more aryl ethenylenes incorporated, the more the fluorescence is red-shifted.⁴⁸ Combining EDG and extending BODIPY conjugation can shift the emission to 780 nm, which is in the near-infrared.⁸⁵ Furthermore, conjugation can be extended off the pyrroles (**I.111** or **I.112**).⁸⁶ However, addition of aryl or ethenylene substituents at the meso-position of the BODIPY does not result in significant red-shifting. This is because the π -system in the *meso*-position is perpendicular to the π -system of the BODIPY core, therefore, is not in conjugation with the rest of the molecule (**I.113** versus **I.71** and **I.111** versus **I.112**).⁸⁶

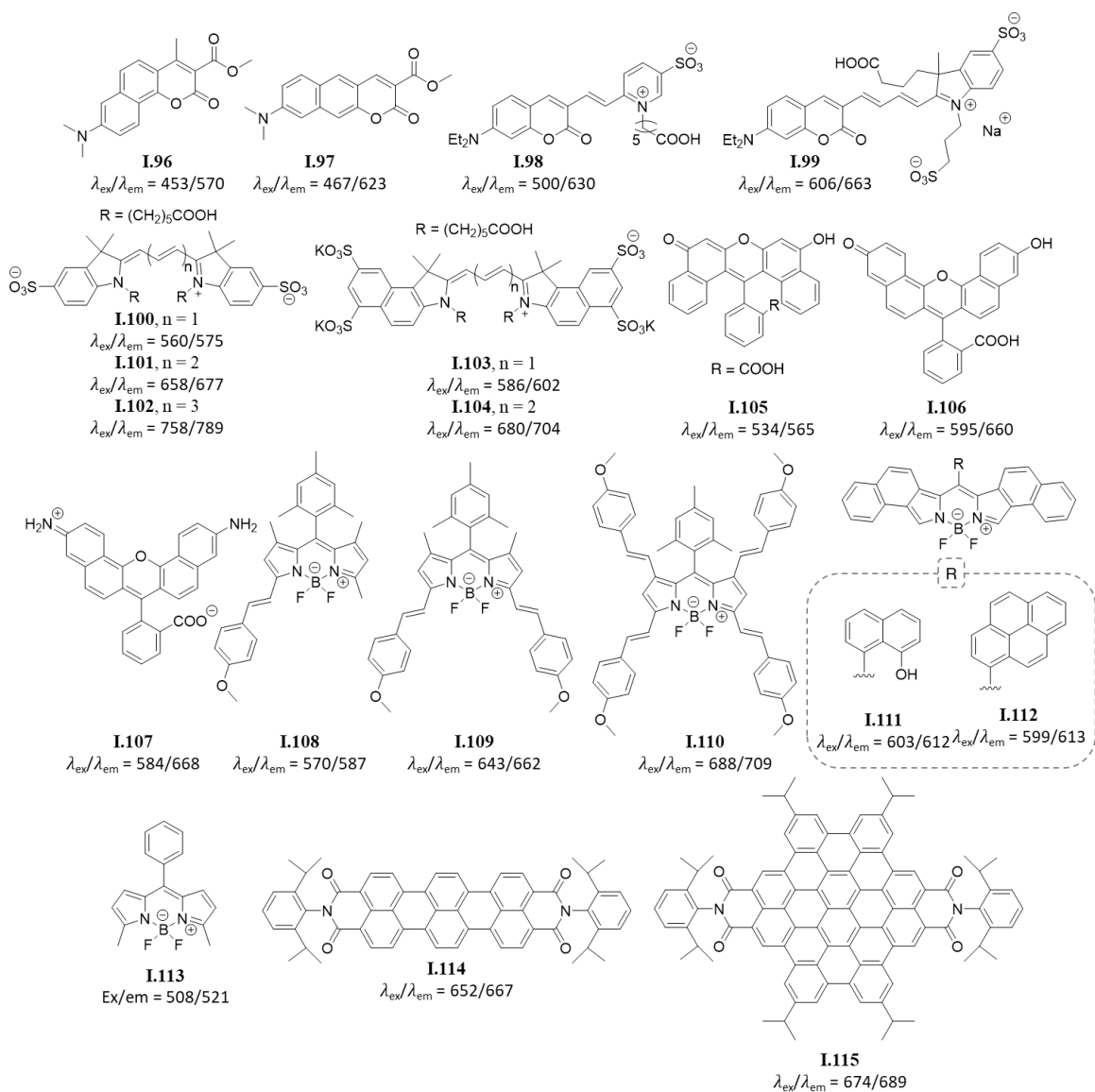


Figure 1.15. Red-shifting of fluorescence through conjugation extension of the π -system.

Red-shifting of perylene is easily achieved through extension of the aromatic core. Perylene **I.88** emits at 536 nm and addition of a naphthalene to the core gives terrylene **I.114** which emits at 667 nm.⁵⁶ Spectral shifting is also achieved via additional aryl fusions on the terrylene core (**I.114** vs **I.115**).⁵⁶

Cycloparaphenylenes are an interesting case. In the other examples, to increase conjugation aryl or ethynylene substituents were added to the core scaffold. However, for cycloparaphenylenes decreasing the number of aryl (phenyl) rings red-shifts the fluorescence. For example, [12]CPP (**I.116**) emits at 450 nm, whereas [7]CPP (**I.117**)

emits at 587 nm. For these strained aromatic macrocycles, the important factors controlling the HOMO and LUMO levels are the torsion angle of neighboring phenylenes and phenylene bending (**Figure 1.16**).⁸⁷ The smaller the CPP the more bent the phenylene rings become, resulting in destabilization of the HOMO and stabilization of the LUMO. As CPP size is reduced, the torsion angle between neighboring benzene rings decreases. This results in an increase in π -conjugation, therefore, stabilizing the LUMO and destabilizing the HOMO. Together, bending and torsion effects result in a red-shift in fluorescence as the CPP size decreases.

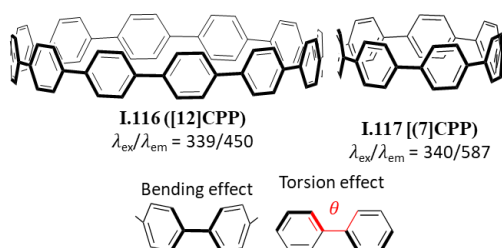


Figure 1.16. Unique red-shifting of CPPs through increasing bending effect and decreasing torsion angles.

1.3.3 Heteroatom incorporation

An alternative approach to red-shifting the fluorescence of fluorescein, rhodamine, and BODIPY is heteroatom incorporation in the core. In the BODIPY case, a large amount of LUMO density is on the *meso*-position. Incorporation of nitrogen in the *meso*-position affords aza-BODIPY **I.119**. The fluorescence of BODIPY **I.118** is shifted from 585 nm to 680 nm.⁸⁸ Here, the electronegative atom lowers the LUMO significantly, which is responsible for the red-shift seen. Heteroatom substitution in the xanthone core however, is different.

Many state aromaticity and/or electronegativity predicts the HOMO-LUMO gap, however neither one accurately predicts it alone. Consider the HOMO-LUMO gap of furan, thiophene, and pyrrole. The narrowest HOMO-LUMO gap (most red) is thiophene followed by furan, then pyrrole. Stanger and coworkers suggest the less aromatic the unit, the more red it would be⁸⁹. Based on aromaticity, we expect furan to be the most red followed by thiophene, then pyrrole. Others in the fluorophore field say the less electronegative the heteroatom, the redder the dye will emit. Using electronegativity

alone, we would expect thiophene to be the reddest, followed by pyrrole, followed by furan. These trends do not match and neither predict what is observed experimentally.

Aromaticity is a better predictor of the HOMO-LUMO gap, but the factor that is overlooked when looking solely at aromaticity are the p orbital levels of the atom. Thiophene has a 3p orbital, whereas furan has a 2p orbital. The 3p orbital is more diffuse and higher in energy, resulting in a narrower HOMO-LUMO gap than furan.⁹⁰ Therefore, the best way to predict HOMO-LUMO gap when switching heteroatoms is by using aromaticity to first predict a trend and then adjusting that trend by comparing the FMOs of the atoms (3p vs 2p).

These rules/principles explain the fluorescent trends of Rhodamine 110 **I.67**, carborhodamine 110 **I.120** and Si-rhodamine 110 **I.121**. Replacement of the xanthone oxygen with a carbon results in a less aromatic moiety, therefore red-shifting the fluorescence to 577 nm. Switching carbon for silicon still yields a non-aromatic moiety, however silicon has higher energy p-orbitals (HOMO) and lower energy d-orbitals (LUMO) resulting in a further red-emitting fluorophore at 609 nm.

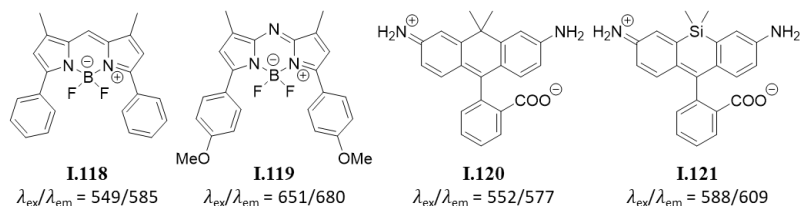


Figure 1.17. Heteroatom incorporation to tune fluorescence of rhodamine and BODIPY.

1.4 Enhancing quantum yield of fluorophores

The quantum yield is a key factor in determining fluorophore brightness. Molecules that are not sufficiently bright are limited in their applications. The main approaches to increase the quantum yield are structural rigidification, minimizing twisted internal charge transfer, and sulfonation.

Fluorophores with significant conformational flexibility undergo modes of vibrations upon excitation, resulting in non-radiative energy loss and, therefore, low quantum yields. One method to reduce non-radiative energy loss is fluorophore scaffold rigidification. This approach has been very successful for the cyanine scaffold. The

quantum yield of cyanine dyes is quenched by photoinduced isomerization and intersystem crossing.⁹¹ Rigidification of the polymethine bridge results in a minimization of the non-radiative pathways and, therefore, an increase in quantum yield. Rigidification of cyanine **I.122** results in a 10 fold enhancement in quantum yield for **I.123**.⁹²

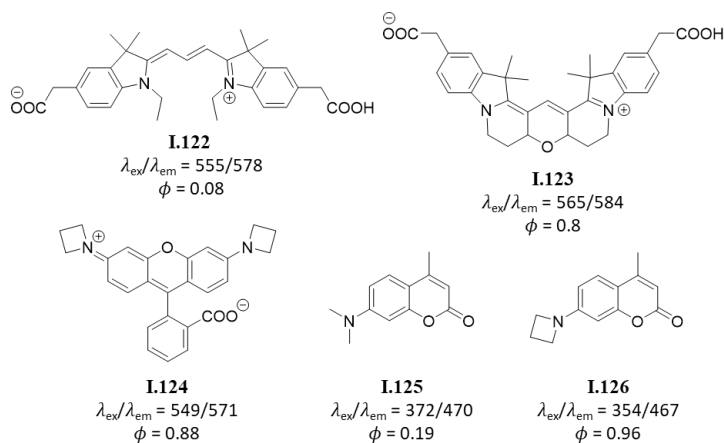


Figure 1.18. Quantum yield enhancement through structure rigidification and minimizing TICT.

Another non-radiative pathway that decreases the quantum yield is formation of a twisted internal charge transfer (TICT) state. This is seen with Rhodamine 110 **I.67** and TMR **I.21**. **I.67** has a quantum yield of 0.88, alkylation red-shifts the fluorescence, but is accompanied by a large decrease in quantum yield (0.41 for **I.21**). To mitigate TICT, Lavis and coworkers appended different sized nitrogen rings on rhodamine.⁹³ They found a 4-membered heterocycle (azetidiny-rhodamine **I.124**) more than doubled the quantum yield of TMR **I.21** going from 0.41 to 0.88. The quantum yield is the same as the non-alkylated rhodamine **I.67**, but red-shifted by 50 nm. It was also effective for the amino coumarin scaffold. Dimethylamino coumarin **I.125** has a quantum yield of 0.19 and substitution of the dimethyl amino for an azetidiny ring affords **I.126** with a quantum yield of 0.96.

Not surprisingly, since the CPPs are made of entirely carbon and hydrogen, CPPs require different methods to enhance the quantum yields. This is discussed in **Chapter II**.

Even if the quantum yield is high in a cuvette, many times the quantum yield is significantly quenched when the fluorophore is conjugated to biologically relevant

molecules like proteins. This is due to interactions between dye molecules resulting in intermolecular dye-dye quenching. A remedy for this quenching is sulfonation of the dyes. Sulfonation makes the molecules negatively charged, decreasing the propensity of aggregation. Sulfonation can also increase dye brightness in aqueous media, presumably due to increased solubility resulting in decreased aggregation induced quenching.^{94,95} AMCA **I.127**-streptavidin conjugate has a quantum yield of 0.25. Sulfonation of the scaffold to give Alexa Fluor 350 **I.128**-streptavidin conjugate has a quantum yield of 0.55, more than double **I.127**.⁹⁴ The classic, and surprisingly still popular, sulfonation method is refluxing the fluorophore in fuming sulfuric acid.⁹⁶ This method is very harsh, dangerous, and usually provides the sulfonated fluorophore in low yields. Sulfonation of the benzene ring of a 7-amino-4-methylcoumarin proceeds in 23% yield.⁹⁶ While sulfonation is a valuable method, alternative approaches are needed. A surprisingly underreported sulfonation method employs the use of sodium sulfite.⁹⁷⁻¹⁰⁰ This method is an nucleophilic addition reaction of sodium sulfite to an alkyl halide like **I.129** to give **I.130** in 94% yield.⁹⁸ This strategy is inexpensive and immensely safer than routes using fuming sulfuric acid or sulfonating reagents such as 1,3-propanesultone.

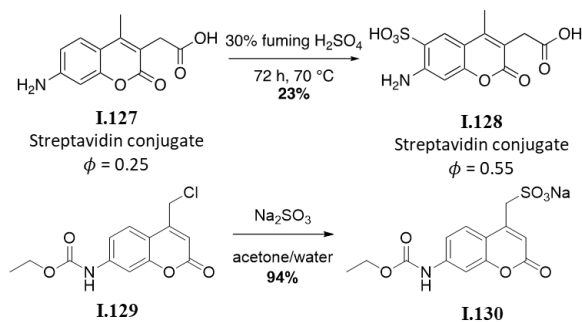


Figure 1.19. Sulfonation to increase quantum yields and synthesis.

1.5 Enhancing the photostability of fluorophores

Bright photostable fluorophores are essential for high resolution bioimaging. The quality of cell images obtained highly depends on the number of photons detected, which is referred to as the “photon budget”. This determines the amount of information that can be obtained and therefore, it is important to have a high photon budget. Photoinduced degradation of fluorophores, photobleaching, results in a termination of fluorescence and

therefore reduces the photon budget. A major photobleaching pathway involves intersystem crossing to the triplet state followed by oxidation. Therefore, the two main methods used to enhance photostability is decreasing reactivity to reactive oxygen species (ROS) and shortening the triplet-state lifetime.

The most common approach to decrease reactivity with ROS is fluorination. Substitution of a hydrogen with a fluorine atom prevents addition of oxygen. Fluorination of fluorescein decreases bleaching by half. For example, 17% of fluorescein fluorescence **I.63** is lost after 33 minutes of irradiation, but only 8% of fluorinated **I.82** fluorescence was lost.²⁹ The photostability of the fluorinated fluoresceins improves as the number of fluorines increases. This was also applied to coumarins and cyanines (**Figure 1.20**, **I.132** and **I.133**).^{10,101} Additional modifications to improve photostability include azetidine incorporation in rhodamine as shown in **I.124**.⁹³ However, the exact reason as to why that helps improve photostability is unknown.¹⁰²

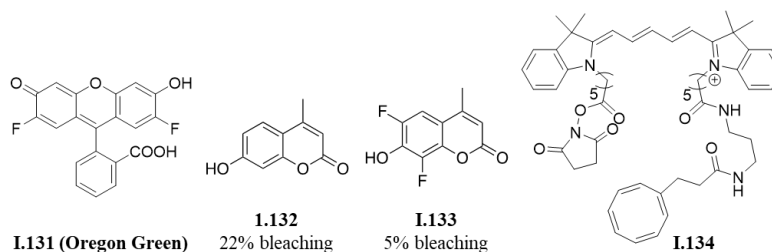


Figure 1.20. Fluorination and attachment of TSQs to enhance photostability.

The other approach to increase photostability is to limit intersystem crossing to the triplet state. The addition of small-molecule triplet state quenchers (TSQs) can mitigate photobleaching. The most common additives are cyclooctatetraene (COT), 4-nitrobenzyl alcohol (NBA), and 6-hydroxy-2,5,7,8-tetramethylchroman-2-carboxylic acid (Trolox).^{103–105} Unfortunately, these TSQs are poorly soluble in aqueous media, membrane impermeable and toxic, which limits their usage *in vivo*. To circumvent this, Blanchard and coworkers covalently linked TSQs to Cy5. Comparison of the parent Cy5 showed 90% photobleaching, compared to <20% of Cy5-TSQ **I.134**.¹⁰⁴ This covalent approach allows the TSQ to be soluble in solution and is more compatible with live cell imaging.

1.6 Conclusions

Fluorophores play a critical role in biology and biochemistry. Small molecule fluorophores are advantageous because precise manipulation of their structure alters their photophysical properties. Fluorophore emission is red-shifted through incorporation of donor and acceptor moieties, extending conjugation, and for some heteroatom incorporation. Analysis of the frontier molecular orbitals of the parent dye scaffold enables photophysical prediction as a result of structural change. However, it is important to not only use Hammett parameters, but to consider hyperconjugation and pi-donating effects of inductive withdrawers like halogens. The quantum yield of classic fluorescent scaffolds are increased through structural rigidification, minimizing twisted internal charge transfer, and sulfonation. Finally, their photostability is increased through minimizing reactivity with reactive oxygen species and shortening the triplet-state lifetime. With innovations in organic chemistry we expect new fluorophores with enhanced photophysical properties to be synthesized. Furthermore, with the advancements in fluorescence imaging capabilities and techniques there is room for newer fluorophore scaffolds. Cyloparaphenylenes are unique small molecules with promise as bright, stable alternatives to the classic scaffolds. However, these molecules are still in their infancy.

With the fundamental physical organic chemistry concepts described, we anticipate that the development of new fluorophores can move away from a trial-and-error basis. Melding all the desirable fluorophore properties into one molecule is difficult. Modifications to make fluorophores brighter and red-shifted often result in structures that are insoluble and cell impermeable limiting their applications. Therefore, fluorophore development that works towards the incorporation of all of these properties is needed. The availability of better fluorophores will allow better interrogation of biological systems and therefore unveil new discoveries.

1.7 Bridge to next chapter

This chapter explores the synthesis and photophysical properties of common and newer fluorophores. The ability to interrogate biological systems is intimately connected

to the availability of bright, photostable reporter molecules. Cycloparaphenylenes have untapped potential as a novel fluorescent scaffold for biological applications, but they are still in their infancy. The next chapter describes how to improve the quantum yield of CPPs to improve their photophysics for biological imaging.

CHAPTER II

TUNING AND ENHANCING THE FLUORESCENCE EMISSION OF CYCLOPARAPHENYLENES

From Lovell, T. C.[‡]; Colwell, C. E.[‡]; Zakharov, L. N.; Jasti, R. Symmetry breaking and the turn-on fluorescence of small, highly strained carbon nanohoops. *Chem. Sci.* **2019**, *10*, 3786-3790. [‡]These authors contributed equally.

This chapter includes co-authored material with excerpts from work published. The excerpts were written by myself with assistance from Dr. Curtis E. Colwell. The experimental work included from the published material was performed by myself and Dr. Curtis E. Colwell. Dr. Lev N. Zakharov provided crystal structure analysis of one of the final products discussed in the experimental section. Professor Ramesh Jasti provided editorial assistance.

[*n*]Cycloparaphenylenes (CPPs), or “carbon nanohoops,” are unique conjugated macrocycles with radially oriented π -systems similar to those in carbon nanotubes. The centrosymmetric nature and conformational rigidity of these molecules lead to unusual size-dependent photophysical characteristics. Their unique properties make these molecules promising novel fluorescent probes for biology. However, not all size CPPs are bright enough for this application. A new nanohoop family is reported, referred to as *meta*[*n*]cycloparaphenylenes, where a single carbon–carbon bond is shifted by one position in order to break the centrosymmetric nature of the parent CPPs. This symmetry breaking leads to bright emission in the smaller nanohoops, which are typically non-fluorescent due to optical selection rules. This joint synthetic, photophysical, and theoretical study provides further design principles to manipulate the optical properties of this growing class of molecules with radially oriented π -systems.

2.1 Introduction

Carbon nanomaterials have been intensely studied in materials science, physics, and biology due to their outstanding strength, enhanced conductivity, biocompatibility,

and near-infrared absorption and emission.^{106–110} The arrangement of the carbon atoms in these materials along with the size of the structure play a key role in the observed properties. As such, achieving atomic-level control in the preparation of carbon nanomaterials is a grand challenge in the field nanoscience. Over the last several years, in an effort to prepare carbon nanotubes with precise structure, the syntheses of the $[n]$ cycloparaphenylenes (CPPs) (**Figure 1a**) were developed.^{57–61} These strained macrocyclic structures, often referred to as carbon nano hoops, are composed of all *para*-linked phenylenes and can be thought of as a short slice of a carbon nanotube (**Figure 1a**). These structures, unlike typical carbon nanomaterials, can be manipulated with atomic precision since they are prepared using stepwise organic synthesis. Moreover, these materials and related derivatives have shown advantageous optoelectronic properties for potential applications ranging from organic electronics,^{111,112} to supramolecular sensing,^{113–115} to bioimaging.⁶⁶

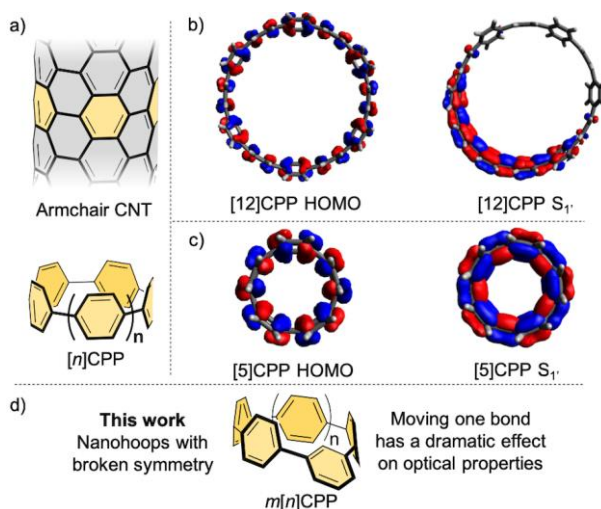


Figure 2.1 a) Structure of an armchair carbon nanotube (CNT) and its relation to $[n]$ cycloparaphenylenes; b) HOMO (left) and excited state (right) $S_{1'}$ orbitals of [12]CPP and c) HOMO (left) and excited state (right) $S_{1'}$ orbitals of [5]CPP. Orbitals have been calculated using CAM-B3LYP/STO-3G level of theory. d) *meta*[n]CPPs with broken symmetry in this work.

Interestingly, the nano hoops possess size dependent optical properties that stand in stark contrast to related materials such as acyclic oligophenylenes or even semiconducting quantum dots. Whereas most materials show a red-shifting fluorescence emission with increasing size, the CPPs have a red-shifting fluorescence with decreasing

size. For example, [12]CPP emits at 450 nm whereas [8]CPP emits at 533 nm.⁶⁸ Concomitant with this red-shifting fluorescence is an accompanying decreasing quantum yield as the nanohoop size decreases. For example, [12]CPP has a quantum yield of 81% whereas the smallest CPPs, [5]- and [6]CPP, are completely non-emissive.^{116–118} Another very unique feature of the CPP optics is that the major absorption is entirely independent of the diameter with a maximum at 340 nm for all CPPs.^{87,119}

These unique photophysical properties spurred investigation into theoretical explanations of these phenomena. The absorption phenomena has been explained by Yamago and co-workers¹¹⁹ wherein the major absorption is dominated by transitions that are similar in energy (i.e. HOMO→LUMO+1 or LUMO+2 and HOMO–1 or HOMO–2→LUMO) amongst all sized CPPs and the HOMO→LUMO transition is forbidden due to symmetry. Similarly, detailed theoretical work by Tretiak and co-workers suggested that CPPs with more than seven phenyl rings are emissive due to exciton localization in an S_1' excited state in which the centrosymmetry is broken, seen in **Figure 1b** for [12]CPP.¹²⁰ Since this localization and symmetry breaking does not happen in the smaller sizes (**Figure 1c**), these structures become non-emissive as the transition is forbidden by symmetry. These works suggest that disrupting the centrosymmetric nature of the molecular orbitals is a strategy that could be employed to alter the photophysical properties of the nanohoops. This basic concept was theoretically explored by Tretiak wherein they postulated that inserting different acenes into the CPP backbone would break the excited state symmetry.¹²¹

Inspired by these works, we report the synthesis, characterization, and analysis of a new class of carbon nanohoops wherein one phenyl ring is linked in the *meta*-position (**Figure 1d**). This minor change in linkage, or “kink”, acts to break the conjugation of the nanohoop, therefore altering the symmetry of the molecular orbitals without significantly decreasing the inherent strain in the molecule. The *meta*-nanohoops, termed *meta*[*n*]CPPs (*m*[*n*]CPPs), are compared to the [*n*]CPP series to further understand what effect this small structural perturbation of the hoop has on the photophysical properties and to provide experimental evidence corroborating Tretiak’s theoretical prediction.¹²⁰ Additionally, tuning the photophysical properties of this growing class of structures is critical for exploiting them as novel scaffolds in biological imaging,⁶⁶ supramolecular

sensing^{113,122,123} as well as novel optoelectronic materials.^{124,125} Herein, we report the general synthesis of an entire series of *m*[*n*]CPPs, carbon nanohoops with broken symmetry, and a detailed study of their photophysical properties.

2.2 Synthesis

The preparation of these fully conjugated and highly bent macrocycles is a synthetic challenge due to the large amount of intrinsic strain in the target molecules. The most strained target compound, ***m*[5]CPP**, is calculated to have 102 kcal/mol of strain (*vide infra*). Fortunately, methods for the synthesis of [*n*]CPPs can be adapted, wherein the strain is incorporated using cyclohexadienes as curved masked phenylenes. Building blocks **II.1–II.7** can easily be accessed on the gram scale using methods previously developed (**Figure 2.1**).^{61,126} By combining these building blocks through selective lithiations followed by diastereoselective additions, or Suzuki Miyaura cross couplings, advanced intermediates **II.8–II.12** were readily prepared (see 2.5.1 for more detail). Following this, relatively unstrained macrocycles **II.13–II.17** were prepared via Suzuki-Miyaura cross coupling of intermediates **II.8–II.12** and 1,3-dibromobenzene or 1,3-benzenediboronic acid bis(pinacol) ester in moderate yields ranging from 10–45%. The triethylsilyl protecting groups were removed and the cyclohexadienes were unmasked via reductive aromatization to yield ***m*[6]-**, ***m*[7]-**, ***m*[8]-**, ***m*[10]-**, and ***m*[12]CPP** in fairly good yields. As proposed, upon synthesis of ***m*[6]CPP**, we immediately noticed bright green fluorescence, which is not observed in the parent [6]CPP. Characterization by NMR (¹H and ¹³C), IR, mass spectrometry, and X-ray crystallography (for ***m*[6]CPP**) confirmed structural assignment. A telling piece of characterization data for the product is the chemical shift of the inward pointing proton present on the *meta*-connected phenylene. As the nanohoop shrinks, the proton is forced further into the shielding cones of the flanking phenylenes. This results in the signal shifting upfield from 7.12 ppm for ***m*[12]CPP** to 5.62 ppm for ***m*[6]CPP**. Characterization by cyclic voltammetry resulted in redox chemistry similar to that of [*n*]CPPs.

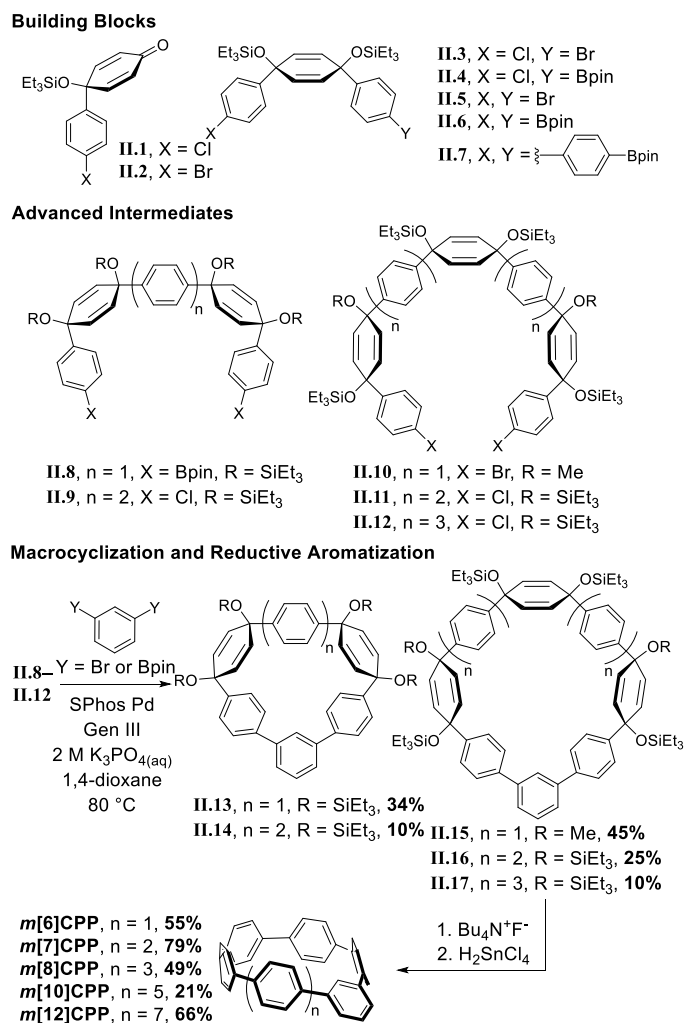


Figure 2.2. Building block synthetic approach to *m*[6]-, *m*[7]-, *m*[8]-, *m*[10]- and *m*[12]CPP.

The synthesis of the most strained *m*[5]CPP required a slightly different strategy (**Figure 2.3**). Here, the *meta*-functionalized benzene was incorporated into ketone precursor **II.18**. Lithiation of **II.3** and addition to ketone **II.18**, followed by protection with triethylsilyl chloride affords advanced intermediate **II.19**. Miyaura borylation gives the bisboronate **II.20** in good yield. Oxidative homocoupling⁶¹ then smoothly transforms **II.20** to the challenging macrocycle **II.21** in 42% yield under mild conditions. Deprotection and reductive aromatization yielded *m*[5]CPP. Again, we noticed immediately that this very strained *meta*-nanohoop is fluorescent whereas the parent [5]CPP is non-emissive. With a series of these highly strained CPP analogues in hand, the influence of symmetry breaking on the properties of these materials was explored.

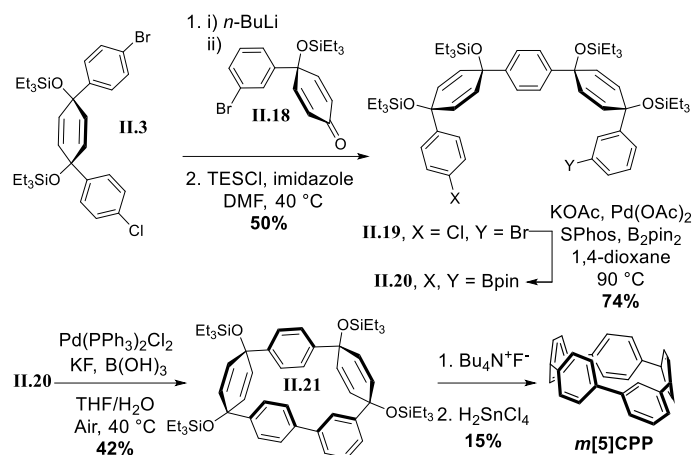


Figure 2.3. Modified synthetic strategy for *m*[5]CPP.

2.3 Photophysical properties

The photophysical properties of these molecules are particularly exciting. Similar to CPPs, the *m*[*n*]CPPs have a common absorption maximum around 328 nm (**Figure 2.4a**) from HOMO–1→LUMO and HOMO→LUMO+1 transitions (**Figures 2.18–2.23**). However, in this series there is a red-shifting second absorption as the size of the hoop decreases (visible as a peak for *m*[6]–*m*[8]CPP and a shoulder to the main absorption at 328 nm for *m*[10]- and *m*[12]CPP), which is the HOMO→LUMO absorption. The extinction coefficient of the higher energy transition is larger than that of the lower energy transition in all cases (**Figure 2.4c** and **Table 2.3**). The series shows decreasing, but never vanishing, fluorescence ranging from 429–534 nm and quantum yields ranging from 0.01 for *m*[5]CPP to 0.77 for *m*[12]CPP (**Figure 2.4a** and **2.4c**). Fluorescent lifetimes of all *m*[*n*]CPPs are around 3 ns (**Table 2.4**), which is different than the [*n*]CPP series with lifetimes ranging from 2–18 ns.

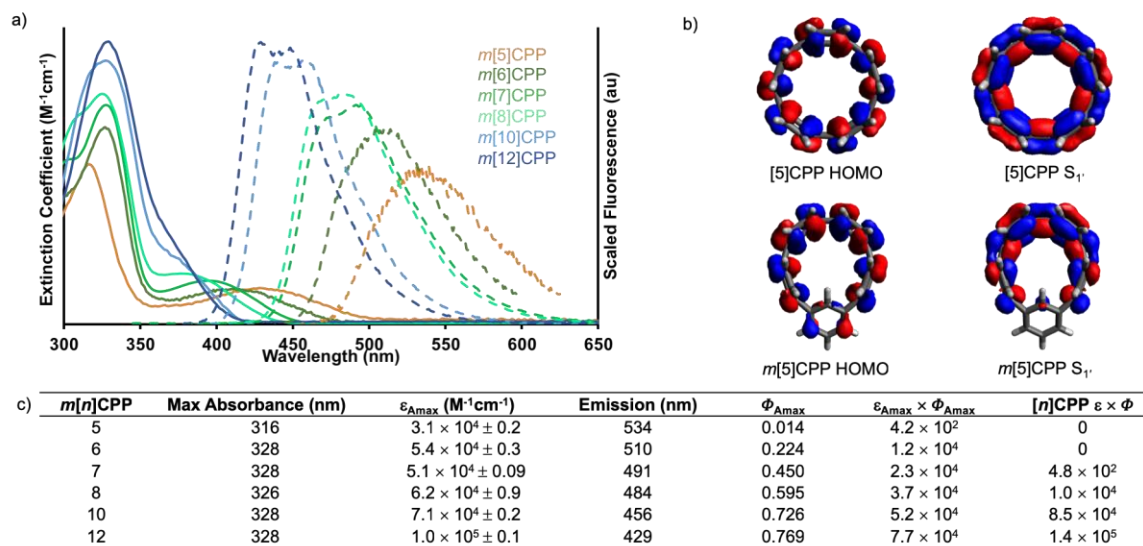


Figure 2.4. (a) Absorbance and emission spectra of $m[n]$ CPPs; (b) HOMO (left) and $S_{1'}$ (right) orbital depiction of [5]CPP and $m[5]$ CPP, demonstrating change in orbital symmetry. Calculated using CAM-B3LYP/STO-3G level of theory; (c) absorbance, extinction coefficient (ϵ), emission and quantum yield (Φ) of $m[5]$ – $m[8]$ -, $m[10]$ - and $m[12]$ CPP and brightness comparison of $m[n]$ CPPs and $[n]$ CPPs.

Density functional theory calculations and a comparison to the $[n]$ CPPs were used to explain the photophysical phenomena further. As mentioned earlier, HOMO→LUMO transition of $[n]$ CPPs is Laporte forbidden due to conservation of orbital symmetry of the ground and excited state. The CPPs are therefore excited through HOMO→LUMO+1 and HOMO→LUMO+2 or HOMO–1→LUMO and HOMO–2→LUMO. From these states, internal conversion to a spatially localized $S_{1'}$ state occurs. Here, the larger $[n]$ CPPs ($n \geq 8$) exhibit exciton localization over about seven of the phenylenes (**Figure 2.1b**). When exciton localization occurs, the symmetry is different than the ground state, allowing the $S_{1'}$ →HOMO transition. When $n \leq 7$ there is complete orbital delocalization over the whole $S_{1'}$ excited state structure (**Figure 2.1c**), therefore the ground state symmetry is conserved. In these cases, the $S_{1'}$ →HOMO transition is Laporte forbidden, resulting in undetectable fluorescence for [5]CPP and [6]CPP and only weak fluorescence for [7]CPP.

Our calculations show that changing a single phenylene from *para* to *meta* does in fact change the orbital symmetry of the π -system. **Figure 2.4b** demonstrates the difference in orbital symmetry between the HOMO and relaxed excited state of $m[5]$ CPP

compared to [5]CPP. The symmetry broken nanohoops show a dramatic increase in intensity for both the HOMO→LUMO and $S_{1'} \rightarrow \text{HOMO}$ transitions. This is apparent from a tenfold increase in the extinction coefficient and oscillator strength of the HOMO→LUMO transition when comparing ***m*[5]CPP** with an extinction coefficient of $6.0 \times 10^3 \text{ M}^{-1}\text{cm}^{-1}$ and oscillator strength of 0.1217 to [5]CPP possessing an extinction coefficient of $4.5 \times 10^2 \text{ M}^{-1}\text{cm}^{-1}$ and oscillator strength of 0.0015.¹¹⁶ The change in orbital symmetry also results in a “turn on” in fluorescence of the smaller sizes.

Like [*n*]CPPs, the quantum yield of *m*[*n*]CPPs decreases with decreasing size. However, the transition is at no point forbidden by symmetry as is the case for [*n*]CPPs. As such, the reduction in quantum yield is attributed to strain effects. It has been reported previously that curving a conjugated system, such as *p*-phenylenes¹²⁷ or pyrene,¹²⁸ reduces the quantum yield respective to the increase in strain. For *m*[*n*]CPPs, the decrease in quantum yield indicates an increase in the rate of non-radiative decay (k_{nr}) as the fluorescence lifetime was found to be relatively constant across all *m*[*n*]CPPs measured (**Table 2.4**). In CPPs, the lifetime increases as the diameter decreases and the $S_{1'} \rightarrow \text{HOMO}$ transition is forbidden due to centrosymmetry. In contrast, introducing a *meta* phenylene allows $S_{1'} \rightarrow \text{HOMO}$ transitions across the entire series of *m*[*n*]CPPs.

To truly assess the aptitude of the *m*[*n*]CPPs to serve as enhanced fluorophores compared to their [*n*]CPPs analogues, we turn to their brightness, which is the product of the extinction coefficient and quantum yield. Nanohoops ***m*[5]–*m*[8]CPPs** have an obvious increase in brightness over their *para*-counterparts, seen in **Figure 2.4c**. For example, [8]CPP was previously used as a fluorescent probe with a brightness of $10,000 \text{ M}^{-1}\text{cm}^{-1}$.⁶⁶ Now, ***m*[6]CPP** has a comparable brightness of $12,000 \text{ M}^{-1}\text{cm}^{-1}$, but is synthetically far easier to access. This edge is lost at larger sizes wherein ***m*[10]-** and ***m*[12]CPPs** are still brighter than many commercial fluorophores like DAPI,^{30,129,130} AMC,¹³¹ and rhodamine 110,^{5,30} but not quite as bright as [10]-¹³² and [12]CPP.^{132,133} We anticipate that this is relevant to the biological applications of nanohoops as new types of biocompatible fluorophores and novel fluorescent sensing materials.⁶⁶

2.4 Conclusions

The connectivity of carbon atoms, size, and symmetry all play critical roles in determining the properties of carbon nanomaterials. Rarely can these variables be systematically probed in a precise manner. Bottom-up synthetic strategies allow for the examination of these fundamental questions in an unambiguous manner. By rational design, a series of $m[n]$ CPPs were prepared wherein a single carbon-carbon bond is moved over by one position from the parent carbon nanohoop structures ($[n]$ CPPs). Shifting a CPP's phenylene from *para* to *meta* was proven as an efficient means to activate the previously forbidden absorption and emission transitions by breaking orbital symmetry, resulting in a fluorescence turn-on of the smaller nanohoops. The enhancement of fluorescence was accompanied by a blue-shift of these transitions proportional to a decrease in strain of about 20%. Advantageously, smaller nanohoops, which are more easily accessed by synthesis, can now be rendered fluorescent.

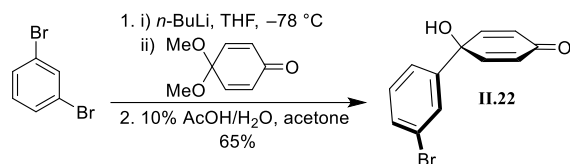
2.5 Experimental Detail

2.5.1 General Experimental Details and Synthesis

All glassware was flame dried and cooled under an inert atmosphere of nitrogen unless otherwise noted. Moisture sensitive reactions were carried out under nitrogen atmosphere using Schlenk and standard syringe/septa techniques. Tetrahydrofuran, dichloromethane, dimethylformamide and 1,4-dioxane were dried by filtration through alumina according to the methods describes by Grubbs.¹³⁴ Silica column chromatography was conducted with Zeochem Zeoprep 60 Eco 40-63 μm silica gel. Automated flash chromatography was performed using a Biotage Isolera One. Recycling gel permeation chromatography (GPC) was performed using a Japan Analytical Industry LC-9101 preparative HPLC with JAIGEL-1H/JAIGEL-2H columns in series using CHCl_3 . Thin Layer Chromatography (TLC) was performed using Sorbent Technologies Silica Gel XHT TLC plates.

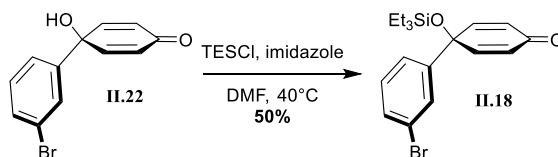
Developed plates were visualized using UV light at wavelengths of 254 and 365 nm. ^1H NMR spectra were recorded at 500 MHz or 600 MHz on a Bruker Advance-III-HD NMR spectrometer. ^{13}C NMR spectra were recorded 150 MHz on a Bruker Advance-III-HD NMR spectrometer. All ^1H NMR spectra were taken in CDCl_3 (referenced to TMS, δ 0.00 ppm) or $\text{DMSO}-d_6$ (referenced to residual DMSO, δ 2.50 ppm). All ^{13}C NMR

spectra were taken in CDCl₃ (referenced to chloroform, δ 77.16 ppm) or DMSO-*d*₆ (referenced to DMSO, δ 39.52 ppm). Mass spectra were obtained from the University of Illinois at Urbana-Champaign Mass Spectrometry Lab using EI, ESI, ASAP, or MALDI or from University of Oregon CAMCOR using ASAP. HRMS was attempted for all compounds, but when not successful, LRMS is reported. Absorbance and fluorescence spectra were obtained in a 1 cm Quartz cuvette with dichloromethane using an Agilent Cary 100 UV-Vis spectrometer and a Horiba Jobin Yvon Fluoromax-4 Fluorimeter. Fluorescent quantum yield was measured in dichloromethane at room temperature using a Hamamatsu absolute PL quantum yield measurement system. Fluorescence lifetimes were measured in dichloromethane using a Horiba Jobin Yvon Tempro Fluorescence Lifetime System. A LUDOX® prompt was used and decay curves were fit to a single exponential function. Electrochemical experiments were performed using a Biologic SP-50 potentiostat with a Ag wire reference electrode, Pt wire counter electrode, and glassy carbon working electrode under nitrogen atmosphere in 100 mM solutions of Bu₄NPF₆ in DCM with ferrocene as a reference. All reagents were obtained commercially unless otherwise noted. Compounds *para*-benzoquinone mono-methyl ketal¹³⁵, **II.23**⁶¹, **II.32**¹²⁶, PPh₃ Pd Gen III and SPhos Pd Gen III¹³⁶ were prepared according to literature procedure.



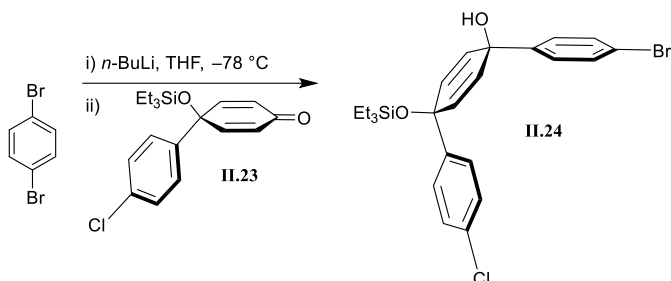
II.22. 1,3-dibromobenzene (4.3 mL, 35.7 mmol, 1.1 equiv) was added to a 500 mL round bottom flask equipped with a stir bar. The reaction flask was capped with a septa, evacuated and refilled with nitrogen. Tetrahydrofuran (51 mL) was cannulated to the reaction flask, which was cooled to -78 °C over 30 min. *n*-BuLi (13.6 mL, 34.1 mmol, 1.05 equiv, 2.5 M in hexanes) was added to the reaction mixture dropwise over 10 min. This was followed by the dropwise addition of *para*-benzoquinone monomethyl ketal (4.6 mL, 32.4 mmol, 1 equiv) and the reaction stirred at -78 °C for 1 h. The reaction was quenched with deionized water (20 mL) at -78 °C and warmed to room temperature. The product was extracted with ethyl acetate (3 x 20 mL) and washed with brine (30 mL). The organic layers were dried over sodium sulfate, decanted and concentrated to yield the

protected product as a slightly yellow solid. The protected product was dissolved in a minimal amount of acetone (20 mL) and a 10% acetic acid solution in water (20 mL) was added. This was stirred at room temperature for 1 h. The reaction was quenched with a saturated solution of sodium bicarbonate (50 mL). The product was extracted with ethyl acetate (3 x 20 mL), washed with brine (20 mL), dried over sodium sulfate and concentrated to yield the crude product as an orange solid. The product was purified by trituration with hexanes and ethanol to give **II.22** as an off white solid (5.588 g, 65% 2 Steps). IR (neat) 1659, 1610 cm^{-1} ; ^1H NMR (600 MHz, Chloroform-*d*) δ 7.67 (t, $J = 1.9$ Hz, 1H), 7.46 (d, $J = 7.9$ Hz, 1H), 7.37 (d, $J = 7.9$ Hz, 1H), 7.25 (t, $J = 7.9$ Hz, 1H), 6.87 (d, $J = 10.0$ Hz, 2H), 6.23 (d, $J = 10.0$ Hz, 2H), 3.04 (s, 1H). ^{13}C NMR (151 MHz, Chloroform-*d*) δ 185.60, 150.34, 140.99, 131.53, 130.45, 128.54, 127.19, 124.04, 123.09, 70.58. HRMS (ESI-TOF) (m/z): $[\text{M}+\text{H}]^+$ calculated for $\text{C}_{12}\text{H}_{10}\text{BrO}_2$, 264.9864; found, 264.9871.

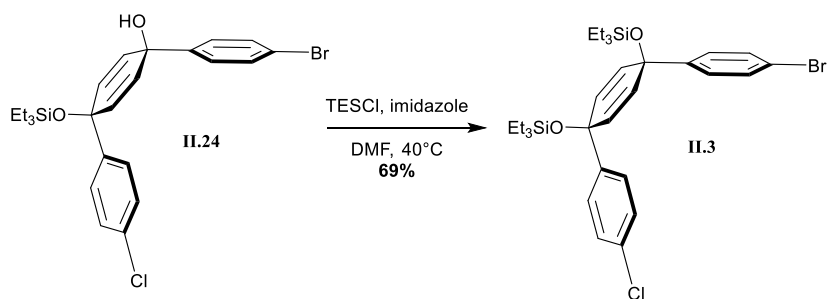


II.18. **II.22** (5.588 g, 26.7 mmol, 1 equiv) and imidazole (5.74 g, 84.3 mmol, 4 equiv) were added to a 250 mL round bottom flask equipped with a stir bar and septum. Dimethylformamide (105 mL) was added to the flask followed by triethylsilyl chloride (4.2 mL, 89.8 mmol, 1.2 equiv). The reaction mixture was heated to 40 °C in an oil bath and stirred overnight. The reaction mixture was cooled to room temperature and quenched with a saturated solution of sodium bicarbonate (30 mL). The product was extracted with ethyl acetate (3 x 100 mL) and washed with 5% lithium chloride solution in water (3 x 100 mL). The organic layers were dried over sodium sulfate and concentrated to yield the crude product as a yellow oil. The product was purified by automated flash silica gel chromatography (0% to 10% ethyl acetate in hexanes) to give **II.18** as a slightly yellow oil (4.0 g, 50%). IR (neat) 2954, 2875, 1670, 1631 cm^{-1} ; ^1H NMR (600 MHz, Chloroform-*d*) δ 7.60 (t, $J = 1.9$ Hz, 1H), 7.42 (ddd, $J = 7.9, 2.0, 1.0$ Hz, 1H), 7.34 (ddd, $J = 7.9, 1.8, 1.1$ Hz, 1H), 7.21 (t, $J = 7.9$ Hz, 1H), 6.79 (d, $J = 10.0$ Hz, 2H), 6.24 (d, $J = 10.0$ Hz, 2H), 0.98 (t, $J = 8.0$ Hz, 9H), 0.66 (q, $J = 7.9$ Hz, 6H). ^{13}C

NMR (151 MHz, CDCl₃) δ 185.59, 151.35, 142.46, 131.10, 130.25, 128.60, 126.93, 124.08, 122.88, 72.70, 6.90, 6.22. HRMS (ESI-TOF) (m/z): [M+H]⁺ calculated for C₁₈H₂₄BrO₂Si, 379.0729; found, 379.0732.

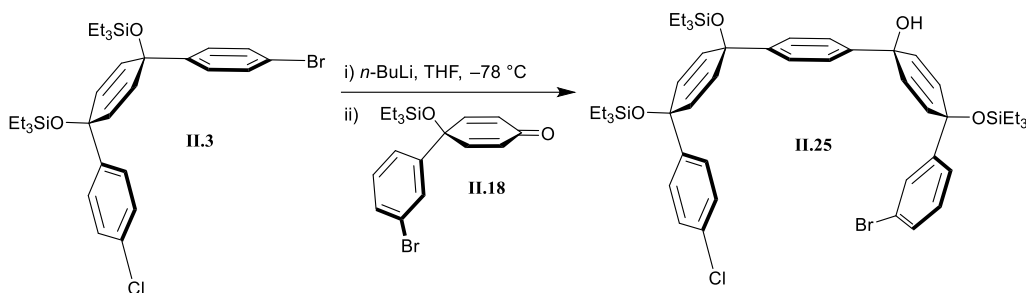


II.24. 1,4-dibromobenzene (3.9 g, 16 mmol, 1.1 equiv) was added to a 100 mL round bottom flask equipped with a stir bar and septa. The flask was evacuated and filled with nitrogen. Tetrahydrofuran (23 mL) was added to the flask and this was cooled for 30 min at -78 °C. *n*-BuLi (6.5 mL, 16 mmol, 1.05 equiv, 2.4 M in hexanes) was added dropwise over 5 min. **II.23** (4.6 mL, 15 mmol, 1 equiv) was added to the reaction flask dropwise and the reaction was stirred for 1 h at -78 °C. The reaction was quenched with deionized water (40 mL) while at -78 °C and warmed to room temperature. The product was extracted with ethyl acetate (3 x 70 mL) and washed with brine (3 x 40). The organic layers were dried over sodium sulfate, decanted and concentrated to yield the crude product **II.24** as a yellow oil. The product was used as is for the next reaction.

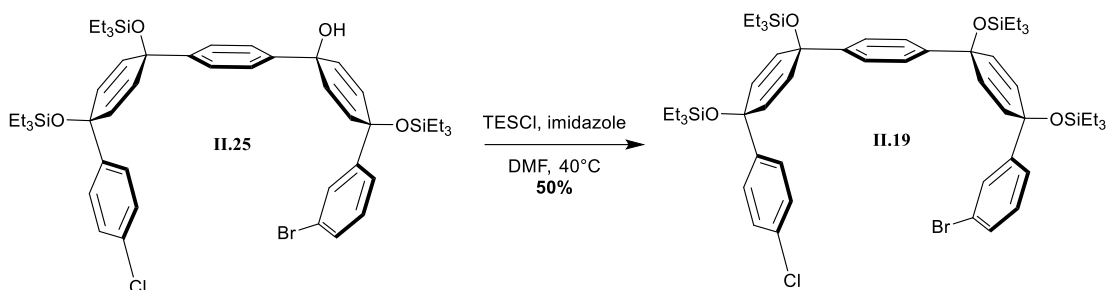


II.3. Crude **II.24** and imidazole (2.3 g, 25 mmol, 4 equiv) were added to a 250 mL round bottom flask equipped with a stir bar and septum. Dimethylformamide (75 mL) was added to the flask followed by triethylsilyl chloride (3.0 mL, 18 mmol, 1.2 equiv). The reaction mixture was heated to 40 °C in an oil bath and stirred overnight. The reaction mixture was cooled to room temperature and quenched with a saturated solution of

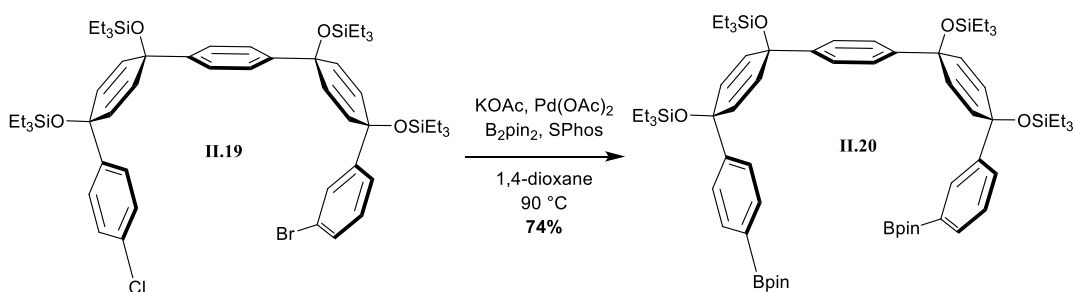
sodium bicarbonate (30 mL). The product was extracted with ethyl acetate (3 x 60 mL) and washed with 5% lithium chloride solution in water (30 mL) and brine (30 mL). The organic layers were dried over sodium sulfate and concentrated to yield the crude product as a yellow oil. The product was purified by automated flash silica gel chromatography (0% to 3% ethyl acetate in hexanes) to give **II.3** as a white solid (6.3 g, 69% 2 steps). IR (neat) 2952, 2871, 1483, 1401 cm^{-1} ; ^1H NMR (600 MHz, Chloroform-*d*) δ 7.38 (d, $J = 8.3$ Hz, 2H), 7.23 (d, $J = 0.9$ Hz, 4H), 7.17 (d, $J = 8.3$ Hz, 2H), 5.95 (s, 4H), 0.95 – 0.89 (m, 18H), 0.59 (qd, $J = 8.0, 2.5$ Hz, 12H). ^{13}C NMR (151 MHz, Chloroform-*d*) δ 144.97, 144.41, 133.11, 131.46, 131.37, 131.25, 128.31, 127.60, 127.24, 121.29, 71.10, 71.04, 7.02, 6.41. HRMS (EI) (m/z): $[\text{M}]^+$ calculated for $\text{C}_{30}\text{H}_{42}\text{BrClO}_2\text{Si}_2$, 604.1595; found, 604.1594.



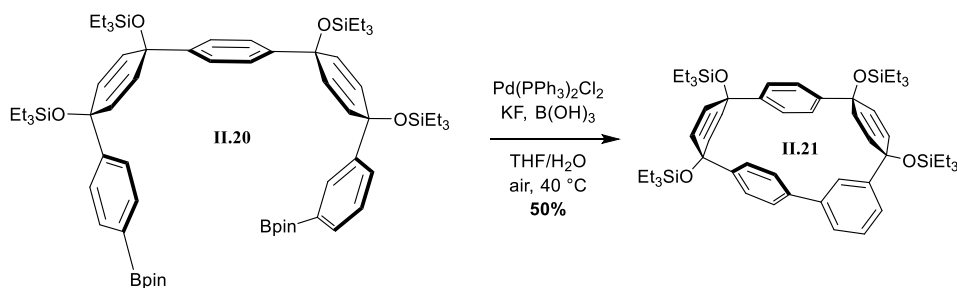
II.25. **II.3** (1.5 g, 2.5 mmol, 1.1 equiv) was added to a 25 mL one-neck round bottom flask equipped with a stir bar and septa. The flask was evacuated and filled with nitrogen. Tetrahydrofuran (27 mL) was added to the flask and it was cooled for 30 min at $-78\text{ }^\circ\text{C}$. *n*-BuLi (1.0 mL, 2.6 mmol, 1.05 equiv, 2.5 M in hexanes) was added dropwise over 3 min. **II.18** (0.72 mL, 2.5 mmol, 1 equiv) was added to the reaction flask dropwise and the reaction was stirred for 1 h at $-78\text{ }^\circ\text{C}$. The reaction was quenched with deionized water (10 mL) while at $-78\text{ }^\circ\text{C}$ and deionized water (5 mL) was added again when the ice bath was removed. The product was extracted with ethyl acetate (3 x 20 mL) and washed with brine (3 x 20 mL). The organic layers were dried over sodium sulfate and concentrated to yield the crude product **II.25** as a colorless oil. The product was not purified.



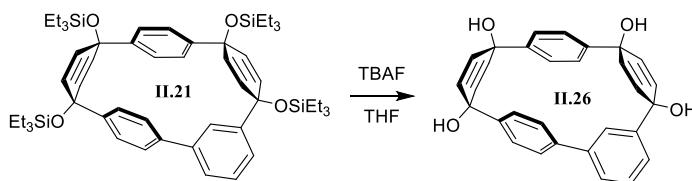
II.19. Crude **II.25** and imidazole (0.67 g, 9.9 mmol, 4 equiv) were added to a 100 mL round bottom flask equipped with a stir bar and septum. Dimethylformamide (10 mL) was added to the flask followed by triethylsilyl chloride (0.5 mL, 3.0 mmol, 1.2 equiv). The reaction mixture was heated to 40 °C in an oil bath and stirred overnight. The reaction mixture was cooled to room temperature and quenched with a saturated solution of sodium bicarbonate (20 mL). The product was extracted with ethyl acetate (3 x 100 mL) and washed with 5% lithium chloride solution in water (3 x 50 mL). The organic layers were dried over sodium sulfate and concentrated to yield the crude product as a yellow oil. The product was purified by automated flash silica gel chromatography (0% to 5% ethyl acetate in hexanes) to give **II.19** as a white solid (1.25 g, 50% 2 steps). IR (neat) 2953, 2874, 1457, 1405 cm^{-1} ; ^1H NMR (600 MHz, Chloroform-*d*) δ 7.47 (dd, $J = 1.5$ Hz, 1H), 7.34 (dd, $J = 7.9, 1.9$ Hz, 1H), 7.25 – 7.22 (m, 6H), 7.21 – 7.17 (m, 3H), 7.08 (t, $J = 7.9$ Hz, 1H), 6.02 (d, $J = 10.9$ Hz, 2H), 6.00 (d, $J = 9.9$ Hz, 2H), 5.91 (d, $J = 3.9$ Hz, 2H), 5.90 (d, $J = 3.5$ Hz, 2H), 0.97 – 0.89 (m, 38H), 0.66 – 0.60 (m, 12H), 0.57 (q, $J = 7.8$ Hz, 13H). ^{13}C NMR (151 MHz, Chloroform-*d*) δ 148.41, 144.95, 144.83, 144.70, 131.91, 131.77, 131.06, 130.98, 130.14, 129.60, 129.14, 128.18, 127.28, 125.76, 125.70, 124.29, 122.35, 71.23, 71.15, 7.05, 7.03, 6.46, 6.41. HRMS (ESI-TOF) (m/z): $[\text{M}+\text{Na}]^+$ calculated for $\text{C}_{54}\text{H}_{80}\text{BrClNaO}_4\text{Si}_4$, 1041.3903; found, 1041.3909.



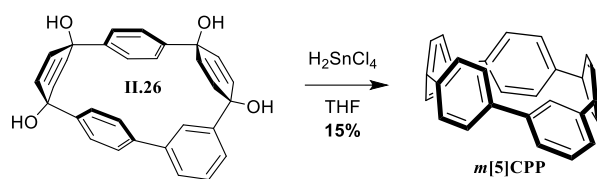
II.20. Potassium acetate (KOAc) (634.8 mg, 6.5 mmol, 6.6 equiv) that had been stored in an oven was added to a 25 mL round bottom flask equipped with a stir bar. **NOTE:** KOAc is extremely hygroscopic and the reaction is water sensitive, therefore it must be dried in an oven and weighed quickly while hot. The KOAc and flask were flame-dried again under vacuum until all apparent moisture was removed. Palladium(II) acetate (1.1 mg, 0.0049 mmol, 0.05 equiv), SPhos (50.3 mg, 0.12 mmol, 0.125 equiv), bis(pinacolato)diboron (994.8 mg, 3.9 mmol, 4 equiv) and **II.19** (1.0 g, 0.98 mmol, 1 equiv) were added to the flask, which was placed under vacuum for 1 h with stirring. The flask was purged with nitrogen and evacuated 3 times. 1,4- dioxane (3.3 mL) was purged with nitrogen for 1 h prior and added to the round bottom flask at room temperature. The round bottom flask was placed in an oil bath while it heated up to 90 °C. The reaction mixture changed from yellow to orange to red to a very dark red. The reaction was stirred at 90 °C overnight. Ethyl acetate (EtOAc) was added to the reaction mixture, which was filtered through a fritted suction funnel with 2 cm Celite[®]. The flask was rinsed several times with EtOAc and sonicated. The filtrate was transferred to a 250 mL flask and concentrated to yield a white waxy solid. This was rinsed with ethanol and suctioned through a Büchner funnel to yield **II.20** as a white solid (843.1 mg, 74%). IR (neat) 2953, 2875, 1357, 1317 cm⁻¹; ¹H NMR (600 MHz, Chloroform-*d*) δ 8.01 (s, 1H), 7.70 (d, *J* = 8.0 Hz, 2H), 7.68 (d, *J* = 8.4 Hz, 1H), 7.33 (d, *J* = 7.7 Hz, 2H), 7.29 (d, *J* = 7.9 Hz, 1H), 7.25 – 7.22 (m, 3H), 7.20 (d, *J* = 8.3 Hz, 2H), 6.02 (d, *J* = 9.8 Hz, 2H), 5.95 (d, *J* = 10.0 Hz, 2H), 5.93 (s, 4H), 1.34 (s, 12H), 1.30 (s, 12H), 0.96 – 0.88 (m, 36H), 0.65 – 0.54 (m, 24H). ¹³C NMR (151 MHz, CDCl₃) δ 149.19, 145.31, 145.06, 144.72, 134.69, 133.60, 132.55, 131.64, 131.58, 131.37, 131.13, 128.62, 127.43, 125.61, 125.54, 125.15, 83.72, 83.61, 71.53, 71.36, 71.29, 71.25, 24.90, 24.88, 7.10, 7.06, 6.47, 6.45, 6.43. HRMS (ESI-TOF) (*m/z*): [M+Na]⁺ calculated for C₆₆H₁₀₄B₂NaO₈Si₄, 1181.6892; found, 1181.6926.



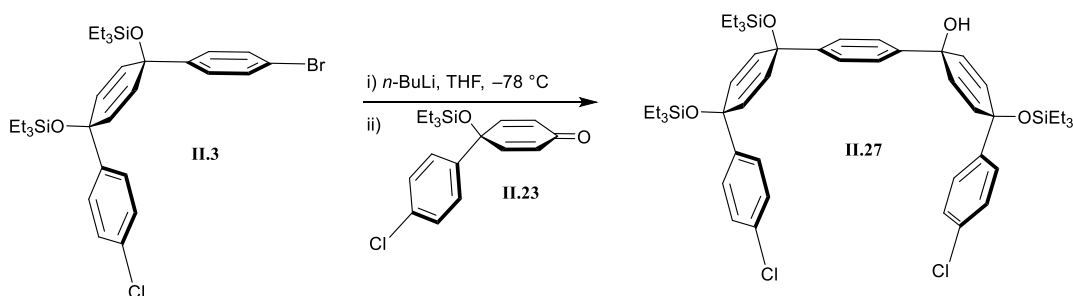
II.21. Diboronic ester **II.20** (400 mg, 0.417 mmol, 1.00 equiv) was added to a round bottom flask followed by bis(triphenylphosphine)palladium(II) dichloride (59 mg, 0.083 mmol, 0.2 equiv) and boric acid (129 mg, 2.09 mmol, 5.00 equiv). The solids were dissolved in tetrahydrofuran (200 mL) and the mixture was stirred vigorously for 10 min. Potassium fluoride (24 mg, 0.417 mmol, 1.00 equiv) dissolved in water (20 mL) was added to the mixture. The reaction was stirred at 40 °C open to the atmosphere overnight. The next day, the mixture was filtered through Celite[®] washing with EtOAc, dried over sodium sulfate, and concentrated to give the crude product as an orange oil. The product was purified by automated flash silica gel chromatography (0% to 30% dichloromethane in hexanes) to yield **II.21** as a white solid (190 mg, 50%). IR (neat) 2953, 2874, 1457, 1412 cm⁻¹; ¹H NMR (500 MHz, Chloroform-*d*) δ 7.65 (d, *J* = 6.6 Hz, 1H), 7.43 – 7.35 (m, 2H), 7.12 (d, *J* = 6.7 Hz, 2H), 6.92 (d, *J* = 6.7 Hz, 2H), 6.88 (d, *J* = 6.8 Hz, 2H), 6.58 (d, *J* = 6.9 Hz, 2H), 6.47 (s, 1H), 6.40 (d, *J* = 8.3 Hz, 2H), 6.12 (d, *J* = 8.3 Hz, 2H), 5.96 (d, *J* = 8.5 Hz, 2H), 5.86 (d, *J* = 8.5 Hz, 2H), 1.01 (t, *J* = 7.9 Hz, 9H), 0.97 (t, *J* = 7.9 Hz, 9H), 0.87 (t, *J* = 8.0 Hz, 9H), 0.84 (t, *J* = 7.9 Hz, 9H), 0.72 (q, *J* = 7.9 Hz, 6H), 0.64 (q, *J* = 7.9 Hz, 6H), 0.50 (q, *J* = 7.9 Hz, 6H), 0.46 (q, *J* = 7.9 Hz, 6H). ¹³C NMR (126 MHz, CDCl₃) δ 145.63, 143.99, 143.87, 143.13, 141.22, 141.11, 134.02, 132.79, 132.74, 131.05, 130.66, 128.60, 126.93, 126.75, 125.79, 125.61, 123.22, 122.78, 72.88, 72.53, 72.02, 71.46, 7.12, 7.03, 6.96, 6.95, 6.46, 6.44, 6.41, 6.40. HRMS (ESI-TOF) (*m/z*): [M+Na]⁺ calculated for C₅₄H₈₀NaO₄Si₄, 927.5031; found, 927.5050.



II.26. **II.21** (33 mg, 0.036 mmol, 1 equiv) was dissolved in THF (0.9 mL). Tetra-*n*-butylammonium fluoride (0.22 mL, 0.22 mmol, 6 equiv, 1 M in tetrahydrofuran) was added and the reaction was stirred for 1 h. The reaction was quenched with water (1 mL) and the THF was removed by distillation. The resulting mixture was filtered to afford **S5** as a white solid that was rinsed with water and dichloromethane. The product was not purified further.

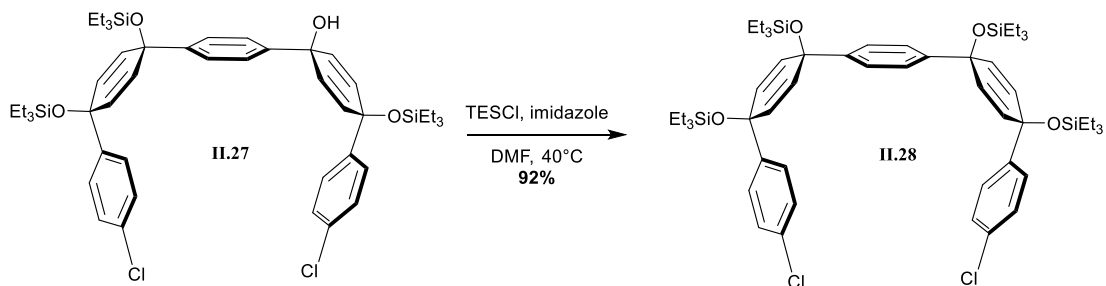


***m*[5]CPP.** Crude **II.26** was dissolved in tetrahydrofuran (0.36 mL). A solution of tin(II) dichloride dihydrate (18 mg, 79 μmol , 2.2 eq) and concentrated hydrochloric acid (12 μL , 150 μmol , 4.2 eq) in THF (710 μL) was added and the reaction was stirred for 1 h at room temperature. A 1 M concentrated solution of NaOH (1 mL) was added and the mixture was extracted with dichloromethane (3 x 3 mL). The organic layers were concentrated and the product. The product was purified by preparative thin layer chromatography on alumina (50% dichloromethane in hexanes) to yield ***m*[5]CPP** as a yellow solid (2.0 mg, 15% 2 steps). ^1H NMR (500 MHz, Chloroform-*d*) δ 7.40 – 7.31 (m, 15H), 7.06 (d, $J = 8.7$ Hz, 4H), 4.80 (s, 1H). ^{13}C NMR (151 MHz, Chloroform-*d*) δ 145.23, 142.82, 140.79, 139.05, 136.69, 135.38, 129.88, 128.64, 128.33, 127.54, 126.71, 121.18. HRMS (ASAP) (m/z): $[\text{M}+\text{H}]^+$ calculated for $\text{C}_{30}\text{H}_{21}$, 381.1643; found, 381.1642.

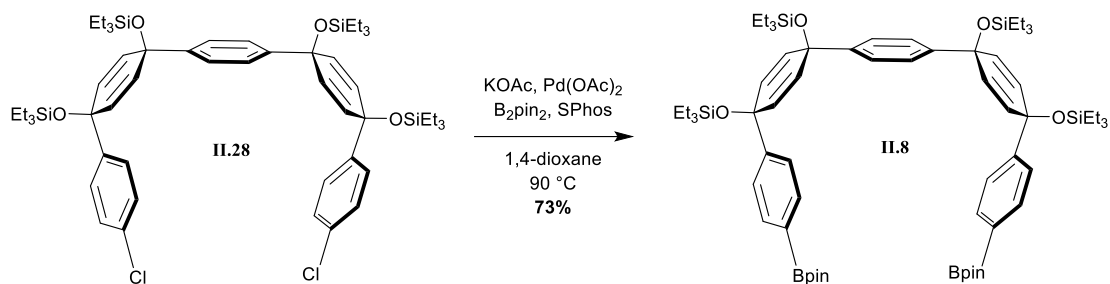


II.27. **II.3** (6.0972 g, 10.1 mmol, 1.1 equiv) was added to a 100 mL round bottom flask equipped with a stir bar and septa. The flask was evacuated and filled with nitrogen. Tetrahydrofuran (15 mL) was added to the round bottom flask and was cooled for 30 min at -78 $^{\circ}\text{C}$. *n*-BuLi (4.2 mL, 10.6 mmol, 1.05 equiv, 2.5 M in hexanes) was added dropwise. **II.23** (3.12 mL, 10.1 mmol, 1 equiv) was added to the reaction flask dropwise and the reaction was stirred for 1 h at -78 $^{\circ}\text{C}$. The reaction was quenched with deionized water (15 mL) at -78 $^{\circ}\text{C}$ and warmed to room temperature. The product was extracted with ethyl acetate (3 x 40 mL) and washed with brine (30 mL). The organic layers were

dried over sodium sulfate and concentrated to yield the crude product **II.27** as a colorless oil. The product was not purified.

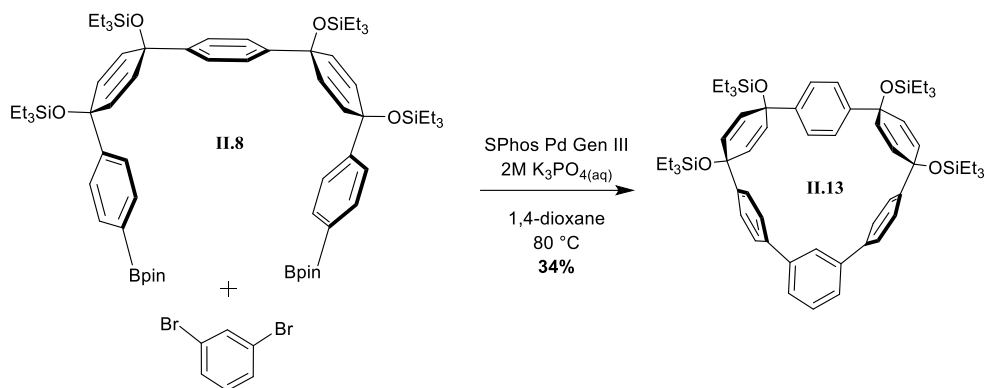


II.28. Crude **II.27** (8.67 g, 10.1 mmol, 1 equiv) and imidazole (2.74 g, 40.2 mmol, 4 equiv) were added to a 250 mL round bottom flask and was equipped with a stir bar and septum. Dimethylformamide (50 mL) was added to the flask followed by triethylsilyl chloride (2.0 mL, 12.1 mmol, 1.2 equiv). The reaction mixture was heated to 40 °C in an oil bath and stirred overnight. The reaction mixture was cooled to room temperature and quenched with a saturated solution of sodium bicarbonate (50 mL). The product was extracted with ethyl acetate (3 x 100 mL) and washed with 5% lithium chloride solution in water (3 x 100 mL). The organic layers were dried over sodium sulfate and concentrated to yield the crude product as a yellow oil. The product was purified by automated flash silica gel chromatography (0% to 15% ethyl acetate in hexanes) to give **II.28** as a white solid (9.0 g, 92% 2 steps). IR (neat) 2952, 2874, 1481, 1456, 1405 cm^{-1} ; ^1H NMR (600 MHz, Chloroform-*d*) δ 7.24 (s, 4H), 7.22 (d, $J = 8.4$ Hz, 4H), 7.19 (d, $J = 8.4$ Hz, 4H), 6.01 (d, $J = 10.1$ Hz, 4H), 5.91 (d, $J = 10.1$ Hz, 4H), 0.94 (t, $J = 7.9$ Hz, 18H), 0.91 (t, $J = 7.9$ Hz, 18H), 0.62 (q, $J = 7.9$ Hz, 12H), 0.57 (q, $J = 8.0$ Hz, 12H). ^{13}C NMR (151 MHz, Chloroform-*d*) δ 144.98, 144.63, 132.91, 131.68, 131.17, 128.15, 127.31, 127.23, 125.73, 71.18, 71.13, 7.05, 7.03, 6.46, 6.40. HRMS (ESI-TOF) (m/z): $[\text{M}+\text{Na}]^+$ calculated for $\text{C}_{54}\text{H}_{80}\text{Cl}_2\text{NaO}_4\text{Si}_4$, 997.4409; found, 997.4455.

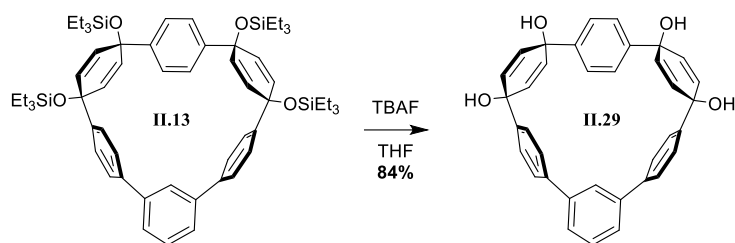


II.8. Potassium acetate (KOAc) (1.1 g, 12 mmol, 6.6 equiv) that had been stored in an oven was added to a 25 mL round bottom flask equipped with a stir bar. **NOTE:** KOAc is extremely hygroscopic and it is important to have none or very little moisture in the reaction, therefore it must be weighed very quickly while it is warm. The KOAc and flask were flame-dried again under vacuum until all apparent moisture was removed.

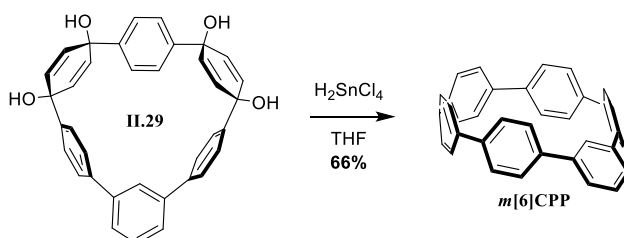
Palladium(II) acetate (20 mg, 0.09 mmol, 0.05 equiv), SPhos (91 mg, 0.2 mmol, 0.13 equiv), bis(pinacolato)diboron (1.8 g, 7 mmol, 4 equiv) and **II.28** (1.7 g, 1.2 mmol, 1 equiv) were added to the flask and was put under vacuum for 1 h with stirring. The flask was purged with nitrogen and evacuated 3 times. 1,4-dioxane (6 mL) was sparged with nitrogen for 1 h, added to the round bottom flask at room temperature and the mixture was stirred for 5 min. The flask was placed in an oil bath and heated to 90 °C. The color of the reaction mixture changed from yellow to orange to red to a very dark red. The reaction was stirred at 90 °C over 2 nights. EtOAc was added to the reaction mixture. This was filtered through Celite[®] in a fritted suction funnel. The reaction flask was rinsed several times with EtOAc with sonication. The filtrate was transferred to a 250 mL round bottom flask and concentrated to yield a white waxy solid. This was rinsed with ethanol and filtered using a Büchner funnel to yield **8** as a white solid (1.51 g, 73%). IR (neat) 2954, 2876, 1610, 1361 cm⁻¹; ¹H NMR (600 MHz, Chloroform-*d*) δ 7.69 (d, *J* = 8.2 Hz, 4H), 7.32 (d, *J* = 8.2 Hz, 4H), 7.22 (s, 4H), 5.98 (d, *J* = 10.2 Hz, 4H), 5.94 (d, *J* = 10.2 Hz, 4H), 1.33 (s, 24H), 0.95 – 0.90 (m, 36H), 0.63 – 0.56 (m, 24H). ¹³C NMR (151 MHz, Chloroform-*d*) δ 149.17, 144.91, 134.65, 131.61, 131.22, 125.68, 125.16, 83.68, 71.60, 71.25, 24.88, 7.07, 6.45. HRMS (ESI-TOF) (*m/z*): [M+Na]⁺ calculated for C₆₆H₁₀₄B₂NaO₈Si₄, 1181.6892; found, 1181.6871.



II.13. *m*-dibromobenzene (0.06 mL, 0.08 mmol, 1 equiv), **II.8** (666.5 mg, 0.058 mmol, 1.2 equiv) and SPhos Pd Gen III (38.1 mg, 0.0048 mmol, 0.1 equiv) were added to a 50 mL round bottom flask equipped with a stir bar. The flask was evacuated for 5 min and purged with nitrogen 5 times. 1,4-dioxane and a solution of 2 M K_3PO_4 were sparged with nitrogen for over 1 h prior to use. The round bottom flask was equipped with a septa and 1,4-dioxane (160 mL) was added to the round bottom flask and the solution was sparged for 20 min. The round bottom flask was heated to 80 °C for 10 min and K_3PO_4 (16 mL, 2 M in deionized water) was added. The reaction was stirred at 80 °C overnight. The reaction mixture was cooled to room temperature. It was filtered through a fritted suction funnel filled with Celite[®]. The round bottom flask was rinsed with dichloromethane and filtered through the Celite[®] plug. The filtrate was added to a separatory funnel along with deionized water (10 mL) and the product was extracted (3 x 30) with dichloromethane. The organic layer was washed with brine (20 mL), dried over sodium sulfate and concentrated to yield an orange oil. The product was purified by automated flash silica gel chromatography (5% to 45% dichloromethane in hexanes) to yield the product **II.13** as a white solid (193 mg, 34%). IR (neat) 2952, 2874, 1457, 1403, 1237 cm^{-1} ; 1H NMR (600 MHz, Chloroform-*d*) δ 7.55 (dd, $J = 7.5, 1.9$ Hz, 2H), 7.48 – 7.44 (m, 5H), 7.30 (d, $J = 8.3$ Hz, 4H), 6.93 (s, 4H), 6.24 (t, $J = 1.9$ Hz, 1H), 6.13 (d, $J = 10.1$ Hz, 4H), 5.72 (d, $J = 10.1$ Hz, 4H), 0.97 (t, $J = 7.9$ Hz, 18H), 0.93 (t, $J = 7.9$ Hz, 18H), 0.69 (q, $J = 7.9$ Hz, 12H), 0.58 (q, $J = 7.9$ Hz, 12H). ^{13}C NMR (151 MHz, $CDCl_3$) δ 144.92, 144.77, 143.15, 142.47, 141.76, 131.48, 131.43, 128.80, 128.69, 128.06, 125.99, 125.81, 125.73, 125.35, 122.39, 71.19, 70.58, 7.15, 7.04, 6.97, 6.80, 6.61, 6.50, 6.48, 6.42. HRMS (ESI-TOF) (m/z): $[M+Na]^+$ calculated for $C_{60}H_{84}NaO_4Si_4$, 1003.5344; found, 1003.5375.

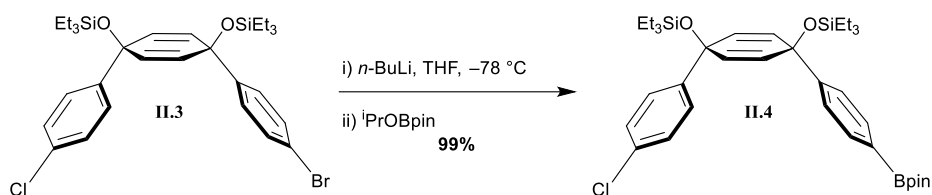


II.29. Tetrahydrofuran (1.05 mL) was added to **II.13** (102.9 mg, 0.1 mmol, 1 equiv) and the vial was equipped with a stir bar and septa. Tetra-*n*-butylammonium fluoride (1.05 mL, 1 mmol, 10 equiv, 1 M in tetrahydrofuran) was added to the reaction flask and this was stirred for 2 h at room temperature. The reaction was quenched with deionized water (5 mL), filtered in a Büchner funnel and washed with deionized water and dichloromethane to yield **II.29** as a white solid (46 mg, 84%). IR (neat) 3370, 3187, 1408 cm^{-1} ; ^1H NMR (600 MHz, $\text{DMSO-}d_6$) δ 7.60 (dd, $J = 7.6, 1.9$ Hz, 2H), 7.51 (t, $J = 7.6$ Hz, 1H), 7.47 (d, $J = 8.0$ Hz, 4H), 7.33 (d, $J = 7.9$ Hz, 4H), 6.88 (s, 4H), 6.17 (t, $J = 2.0$ Hz, 1H), 6.07 (d, $J = 9.9$ Hz, 4H), 5.65 (d, $J = 9.8$ Hz, 4H). ^{13}C NMR (151 MHz, DMSO) δ 145.94, 144.97, 142.45, 142.38, 131.85, 131.53, 129.54, 128.78, 126.26, 125.54, 122.79, 68.63, 68.09, 23.53, 19.70, 13.98. HRMS (ESI-TOF) (m/z): $[\text{M}+\text{Na}]^+$ calculated for $\text{C}_{36}\text{H}_{28}\text{NaO}_4$, 547.1885; found, 547.1869.



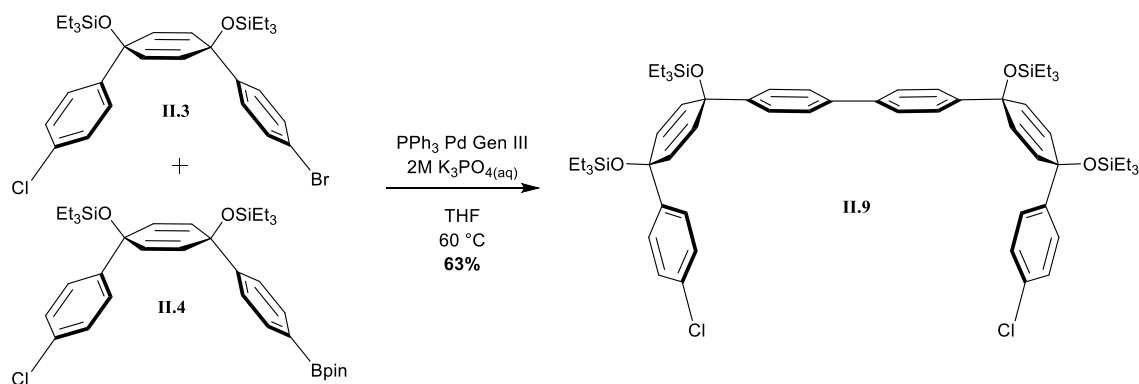
***m*[6]CPP.** $\text{SnCl}_2 \cdot \text{H}_2\text{O}$ (180.6 mg, 0.80 mmol) was added to a 100 mL round bottom flask equipped with a stir bar and septum. Tetrahydrofuran (20 mL) was added to the flask followed by hydrochloric acid (0.13 mL, 1.6 mmol, 12 M). This was stirred at room temperature for 30 min. H_2SnCl_2 solution (2.1 mL, 0.09 mmol, 2.2 equiv, 0.04 M) was added to the scintillation vial containing **II.29** (20.3 mg, 0.04 mmol, 1 equiv) and was stirred for 1 h at room temperature. The reaction was quenched with saturated sodium bicarbonate (5 mL). The filtrate was transferred to a separatory funnel and the product was extracted with dichloromethane (5 x 7 mL). The organic layers were washed with

brine (10 mL), dried over sodium sulfate and concentrated to give the crude product as a green solid. The product was purified by automated flash alumina column chromatography (10% to 45% dichloromethane in hexanes) to yield **m[6]CPP** as a green solid (12 mg, 66%). IR (neat) 2921, 2851, 1661, 1261 cm^{-1} ; ^1H NMR (600 MHz, Chloroform-*d*) δ 7.45 – 7.38 (m, 19H), 7.15 (d, J = 8.6 Hz, 4H), 5.62 (t, J = 1.9 Hz, 1H). ^{13}C NMR (151 MHz, CDCl_3) δ 142.79, 139.53, 139.04, 137.43, 136.42, 136.38, 129.45, 128.99, 128.08, 127.85, 127.58, 127.20, 122.20, 77.25, 77.03, 76.82. HRMS (ASAP-TOF) (m/z): $[\text{M}+\text{H}]^+$ calculated for $\text{C}_{36}\text{H}_{25}$, 457.1956; found, 457.1956.

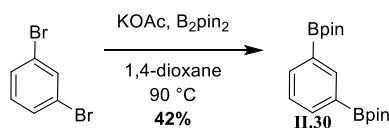


II.4. **II.3** (5 g, 8.25 mmol, 1.0 eq) was added to a 100 mL round bottom flask equipped with a stir bar. The reaction flask was capped with a septa and the flask was evacuated and refilled with nitrogen. Tetrahydrofuran (48 mL) was added to the reaction flask and the mixture was cooled for 30 min at $-78\text{ }^\circ\text{C}$. *n*-BuLi (3.5 mL, 8.7 mmol, 1.05 eq, 2.5 M in hexanes) was added to the reaction mixture dropwise. This was followed by the dropwise addition of 2-Isopropoxy-4,4,5,5-tetramethyl-1,3,2-dioxaborolane (3.4 mL, 16.5 mmol, 2 eq) and the reaction was stirred at $-78\text{ }^\circ\text{C}$ for 1 h. The reaction was quenched with deionized water (30 mL) at $-78\text{ }^\circ\text{C}$ and the reaction mixture was warmed to room temperature. The product was extracted with ethyl acetate (3 x 50 mL) and washed with brine (3 x 20 mL). The organic layers were dried over sodium sulfate, decanted into a round bottom flask and concentrated to yield a slightly yellow oil. Ethanol (20 mL) was added to the oil and was sonicated, producing a white precipitate. The product **II.4** was isolated by suction filtration to yield a white solid (5.3 g, 99%). IR (neat) 2955, 2874, 1399, 1359, 1321 cm^{-1} ; ^1H NMR (500 MHz, Chloroform-*d*) δ 7.72 (d, J = 7.8 Hz, 2H), 7.32 (d, J = 7.9 Hz, 2H), 7.24 (d, J = 8.8 Hz, 2H), 7.22 (d, J = 8.7 Hz, 2H), 5.99 (d, J = 10.0 Hz, 2H), 5.92 (d, J = 10.0 Hz, 2H), 1.34 (s, 12H), 0.93 (t, J = 8.0 Hz, 9H), 0.91 (t, J = 7.9 Hz, 9H), 0.61 (q, J = 8.0 Hz, 6H), 0.57 (q, J = 7.7 Hz, 6H). ^{13}C NMR (126 MHz, CDCl_3) δ 148.90, 144.59, 134.73, 132.91, 131.60, 131.24, 128.21, 127.27, 125.15, 83.79,

71.45, 71.15, 24.88, 7.03, 6.45, 6.41. HRMS (ESI-TOF) (m/z): [M+Na]⁺ calculated for C₃₆H₅₄BClNaO₄Si₂, 675.3240; found, 675.3246.

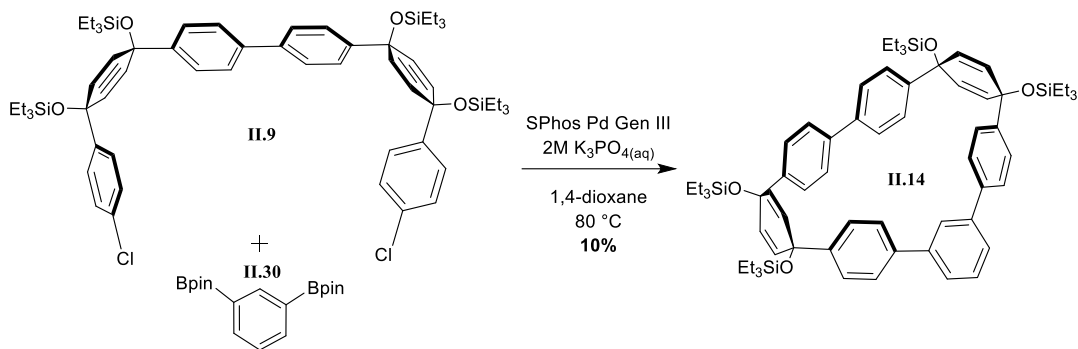


II.9. **II.3** (1.00 g, 1.65 mmol, 1 equiv), **II.4** (1.18 g, 1.82 mmol, 1.1 equiv) and PPh₃ Pd Gen III (31 mg, 0.050 mmol, 0.03 equiv) dissolved in tetrahydrofuran (16 mL) and warmed to 60 °C. K₃PO₄ (1.6 mL, 2 M in deionized water) was added and the reaction was left overnight. The next day, the reaction was filtered through Celite[®], dried over sodium sulfate and the solvent was removed under reduced pressure to yield an oil. The product was purified by automated flash silica column chromatography (0% to 30% dichloromethane in hexanes) to yield **II.9** as a white solid (1.1 g, 63%). IR (neat) 2951, 2873, 1490, 1456, 1401 cm⁻¹; ¹H NMR (500 MHz, Chloroform-d) δ 7.50 (d, J = 8.2 Hz, 4H), 7.37 (d, J = 8.5 Hz, 4H), 7.28 (d, J = 8.3 Hz, 4H), 7.23 (d, J = 8.5 Hz, 4H), 6.03 (d, J = 10.0 Hz, 4H), 5.96 (d, J = 9.8 Hz, 4H), 0.94 (t, J = 7.9 Hz, 36H), 0.61 (q, J = 8.1 Hz, 24H). ¹³C NMR (126 MHz, CDCl₃) δ 144.90, 144.66, 139.59, 132.97, 131.78, 131.16, 128.23, 127.33, 126.76, 126.24, 71.27, 71.16, 7.05, 7.04, 6.47, 6.43. HRMS (ESI-TOF) (m/z): [M+Na]⁺ calculated for C₆₀H₈₄Cl₂NaO₄Si₄, 1073.4722; found, 1073.4722.



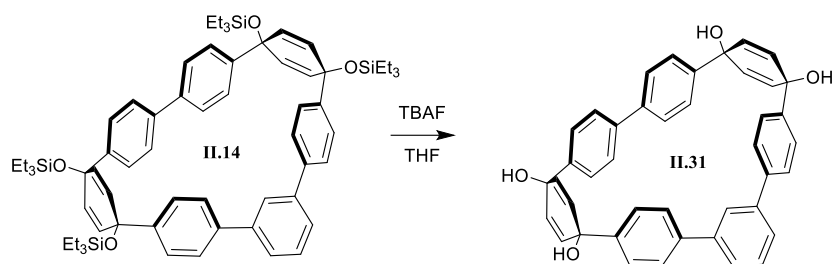
II.30. 1,3-dibromobenzene (5.0 mL, 9.8 g, 41 mmol, 1 equiv), Pd(dppf)₂Cl₂ (169 mg, 0.21 mmol, 0.005 equiv) and bis(pinacolato)diboron (25 g, 99 mmol, 2.4 equiv) were added to a round bottomed flask. Oven dried hot KOAc (27 g, 270 mmol, 6.6 equiv) was added and the solids were placed under vacuum. The flask was refilled with nitrogen, 1,4-dioxane

(40 mL) was added, and the reaction was warmed from room temperature to 90 °C. The reaction was stirred at this temperature overnight. The next day, the reaction was filtered through Celite[®] washing with ethyl acetate (80 mL) and the solvent of the filtrate was removed under reduced pressure until crystallization occurred. The crystals were collected by filtration and washed with cold ethanol to yield **II.30** as a white solid (5.8 g, 42%). IR (neat) 2977, 1602, 1303 cm⁻¹; ¹H NMR (500 MHz, Chloroform-*d*) δ 8.28 (s, 1H), 7.90 (d, *J* = 7.4 Hz, 2H), 7.37 (t, *J* = 7.4 Hz, 1H), 1.34 (s, 24H). ¹³C NMR (126 MHz, CDCl₃) δ 141.23, 137.62, 127.04, 83.73, 24.88. HRMS (ESI-TOF) (*m/z*): [M+H]⁺ calculated for C₁₈H₂₉B₂O₄, 331.2252; found, 331.2244.

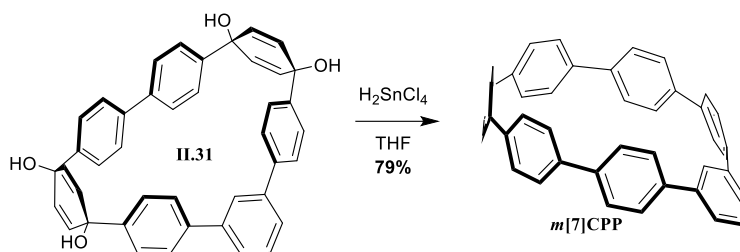


II.14. **II.9** (157 mg, 0.475 mmol, 1 equiv), **II.9** (500 mg, 0.475 mmol, 1 equiv), and Sphos Pd Gen III (37 mg, 0.048 mmol, 0.1 equiv) were dissolved in 1,4-dioxane (240 mL) and heated to 80 °C. K₃PO₄ (24 mL, 2 M in deionized water) was added and the reaction was stirred overnight. The reaction mixture was filtered through Celite[®] and the solvent was removed under reduced pressure to yield a golden oil. The product was purified by automated flash silica column chromatography (0% to 100% dichloromethane in hexanes) to yield a white solid. The solid was purified by recycling gel permeation chromatography to yield **II.14** as a white solid (50 mg, 10%). IR (neat) 2954, 2875, 1085 cm⁻¹; ¹H NMR (600 MHz, Chloroform-*d*) δ 7.58 (dd, *J* = 7.5, 1.8 Hz, 2H), 7.50 (m, 2H), 7.40 (d, *J* = 8.4 Hz, 4H), 7.26 (d, *J* = 8.4 Hz, 4H), 7.23 (d, *J* = 8.3 Hz, 4H), 7.04 (d, *J* = 8.3 Hz, 4H), 6.15 (d, *J* = 10.0 Hz, 4H), 6.07 (d, *J* = 10.0 Hz, 4H), 0.99 (t, *J* = 7.9 Hz, 18H), 0.98 (t, *J* = 7.9 Hz, 18H), 0.68 (q, *J* = 7.9 Hz, 12H), 0.66 (q, *J* = 7.9 Hz, 12H). ¹³C NMR (151 MHz, CDCl₃) δ 143.56, 142.92, 141.63, 140.33, 140.10, 132.46, 131.98, 129.16, 128.78, 127.09, 126.80, 126.68, 126.57, 124.89, 72.54, 72.35, 7.08, 7.06, 6.49.

HRMS (ESI-TOF) (m/z): $[M+H]^+$ calculated for $C_{66}H_{89}O_4Si_4$, 1057.5838; found, 1057.5869.

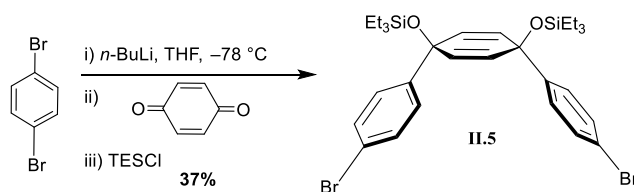


II.31. **II.14** (50 mg, 0.047 mmol, 1 equiv) was dissolved in tetrahydrofuran (1.2 mL) and a Tetra-*n*-butylammonium fluoride (0.21 mL, 0.28 mmol, 6 equiv, 1 M in tetrahydrofuran) was added. The reaction was stirred for 1 h at room temperature and quenched with water. Solvent was removed from this mixture under reduced pressure. Filtration afforded **II.31** as a white solid, which was washed with dichloromethane.

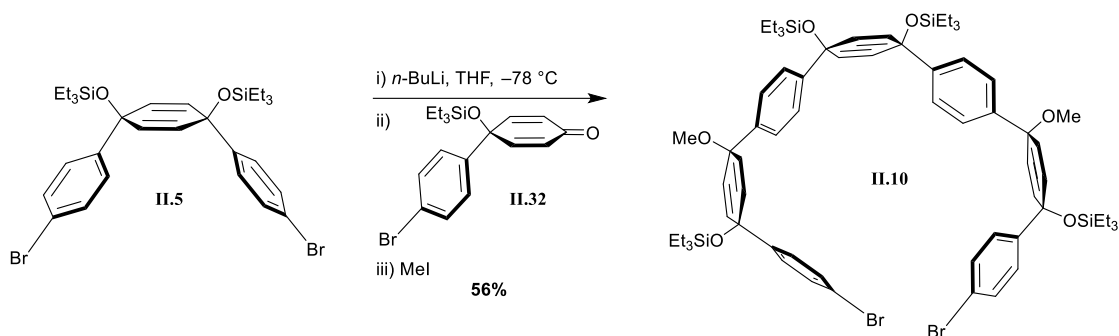


***m*[7]CPP.** Crude **II.31** was dissolved in minimal tetrahydrofuran and to it was added a solution of tin(II) dichloride monohydrate (23 mg, 100 μ mol, 2.1 eq) and concentrated aqueous hydrochloric acid (17 μ L, 200 μ mol, 4.2 eq) in THF (1 mL). The reaction was stirred at room temperature for 1 h and quenched with a 1 M aqueous solution of NaOH. This mixture was extracted with DCM and the combined extracts were dried over anhydrous sodium sulfate. The solvent was removed under reduced pressure and the material was purified by preparative thin layer chromatography on alumina (25% dichloromethane in hexanes) to yield ***m*[7]CPP** as a yellow fluorescent solid. (20 mg, 79%). IR (neat) 3020, 2922, 2850, 1581, 1480, 1261 cm^{-1} ; 1H NMR (600 MHz, Chloroform-*d*) δ 7.51 – 7.43 (m, 19H), 7.42 (d, $J = 8.5$ Hz, 4H), 7.21 (d, $J = 8.4$ Hz, 4H), 6.08 (t, $J = 1.9$ Hz, 1H). ^{13}C NMR (151 MHz, $CDCl_3$) δ 142.54, 141.91, 138.78, 137.57, 137.37, 137.30, 137.24, 136.58, 129.08, 128.90, 127.69, 127.51, 127.48, 127.43, 127.02,

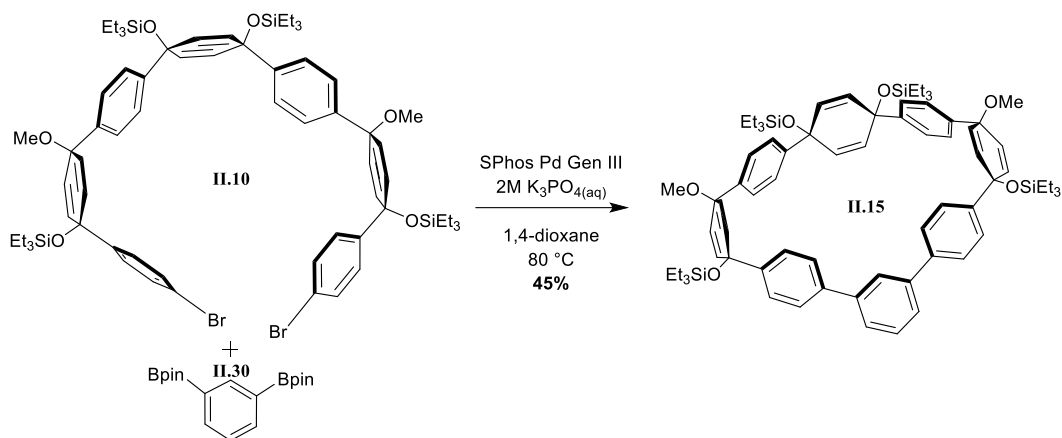
123.02. HRMS (ASAP-TOF) (m/z): $[M+H]^+$ calculated for $C_{42}H_{29}$, 533.2269; found, 533.2278.



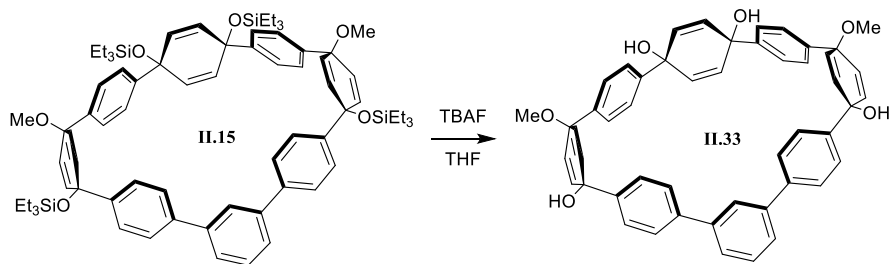
II.5. 1,4-dibromobenzene (5.00 g, 21.2 mmol, 2.8 equiv) was dissolved in tetrahydrofuran (125 mL) and cooled to $-78\text{ }^{\circ}\text{C}$. *n*-BuLi (8.2 mL, 20.4 mmol, 2.7 equiv, 2.5 M in hexanes) was added followed by 1,4-benzoquinone (818 mg, 7.57 mmol, 1 equiv), which was added in fifths. After each fifth, the reaction turned blue and the next fifth was not added until the reaction became yellow. When the last fifth was added, the reaction was stirred for 1 h, triethylsilyl chloride (4.4 mL, 4.0 g, 26 mmol, 3.5 equiv) was added and the reaction was warmed to room temperature overnight. The next day, the reaction was quenched with water (60 mL) and extracted with ethyl acetate (3 x 60 mL). The combined extracts were washed with brine (60 mL), dried over anhydrous sodium sulfate and solvent was removed to yield an oil. The product was purified by automated flash silica column chromatography (0% to 20% dichloromethane in hexanes) to yield a clear colorless oil. This was mixed with an equal amount of ethanol and let sit to yield large crystals, which were filtered and washed with ethanol, to yield **II.5** as a white solid (1.80 mg, 37%). IR (neat) 2952, 2871, 1477, 1400 cm^{-1} ; ^1H NMR (500 MHz, Chloroform-*d*) δ 7.38 (d, $J = 8.3$ Hz, 4H), 7.17 (d, $J = 8.3$ Hz, 4H), 5.95 (s, 4H), 0.92 (t, $J = 7.9$ Hz, 18H), 0.59 (q, $J = 8.0$ Hz, 12H). ^{13}C NMR (126 MHz, CDCl_3) δ 144.94, 131.39, 131.25, 127.60, 121.30, 71.09, 7.01, 6.41. HRMS (EI) (m/z): $[M]^+$ calculated for $C_{30}H_{42}Br_2O_2Si_2$, 648.1090; found, 648.1081.



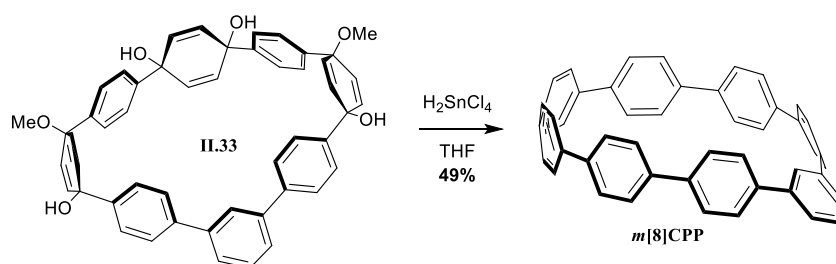
II.10. **II.5** (1.63 g, 2.50 mmol, 1 equiv) was dissolved in tetrahydrofuran (50 mL, 100 mM) and cooled to $-78\text{ }^{\circ}\text{C}$. *n*-BuLi (2.0 mL, 5.0 mmol, 2 equiv, 2.5 M in hexanes) was added followed immediately by **II.32** (1.5 mL, 1.9 g, 5 mmol, 2 equiv) and the reaction was stirred for 1 h at $-78\text{ }^{\circ}\text{C}$. It was quenched with methyl iodide (470 μL , 1.1 g, 7.5 mmol, 3 eq), warmed to room temperature and stirred overnight. The next day, water (20 mL) was added and the product was extracted with ethyl acetate (3 x 20 mL). The combined extracts were washed with brine (20 mL) and dried over anhydrous sodium sulfate. Solvent was removed under reduced pressure to yield an oil. The product was purified by automated flash silica column chromatography (20% to 80% dichloromethane in hexanes) to yield **II.10** as a white solid (1.8 g, 56%). ^1H NMR (600 MHz, Chloroform-*d*) δ 7.34 (d, $J = 8.6$ Hz, 4H), 7.30 (d, $J = 8.5$ Hz, 4H), 7.26 (d, $J = 8.5$ Hz, 4H), 7.16 (d, $J = 8.6$ Hz, 4H), 6.09 (d, $J = 10.2$ Hz, 4H), 5.99 (d, $J = 10.2$ Hz, 4H), 5.96 (s, 4H), 3.33 (s, 6H), 0.96 (t, $J = 7.9$ Hz, 18H), 0.92 (t, $J = 7.9$ Hz, 18H), 0.66 (q, $J = 7.9$ Hz, 12H), 0.60 (q, $J = 7.9$ Hz, 12H). ^{13}C NMR (151 MHz, CDCl_3) δ 145.68, 144.93, 141.99, 135.06, 131.40, 131.11, 129.35, 127.51, 126.02, 125.95, 121.07, 74.30, 71.68, 71.18, 52.06, 7.05, 6.49, 6.44. HRMS (ESI-TOF) (m/z): $[\text{M}+\text{Na}]^+$ calculated for $\text{C}_{68}\text{H}_{94}\text{Br}_2\text{NaO}_6\text{Si}_4$, 1299.4392; found, 1299.4379.



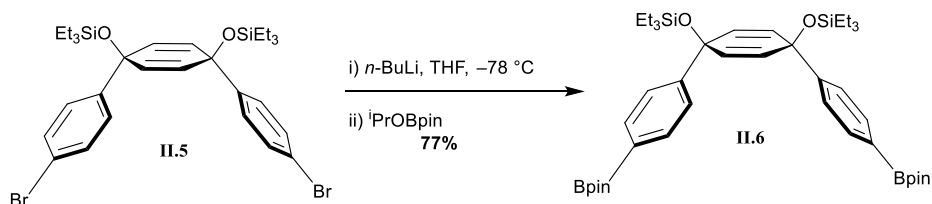
II.15. **II.30** (206 mg, 0.63 mmol, 1 equiv), **II.10** (800 mg, 0.63 mmol, 1 equiv), and Sphos Pd Gen III (49 mg, 0.063 mmol, 0.1 equiv) were dissolved in 1,4-dioxane (125 mL) and heated to 80 °C. K_3PO_4 (12.5 mL, 2 M in deionized water) was added and the reaction was stirred overnight. The reaction mixture was filtered through Celite[®], dried over sodium sulfate, and the solvent was removed under reduced pressure to yield a golden oil. The product was purified by automated flash silica column chromatography (20% to 80% dichloromethane in hexanes) to yield **II.15** as a white solid (340 mg, 45%). IR (neat) 2951, 2874, 1457, 1406 cm^{-1} ; 1H NMR (600 MHz, Chloroform-*d*) δ 7.65 (s, 1H), 7.58 (dd, $J = 7.6, 1.8$ Hz, 2H), 7.53 (d, $J = 8.4$ Hz, 4H), 7.51 (d, $J = 8.4$ Hz, 4H), 7.48 (d, $J = 7.5$ Hz, 1H), 7.45 (d, $J = 8.5$ Hz, 4H), 7.42 (d, $J = 8.3$ Hz, 4H), 6.15 (s, 4H), 6.12 (d, $J = 10.1$ Hz, 4H), 6.01 (d, $J = 10.2$ Hz, 4H), 3.29 (s, 6H), 1.01 (t, $J = 7.9$ Hz, 18H), 0.89 (t, $J = 8.0$ Hz, 18H), 0.72 (q, $J = 8.0$ Hz, 12H), 0.53 (q, $J = 8.0$ Hz, 12H). ^{13}C NMR (126 MHz, $CDCl_3$) δ 146.21, 145.04, 142.66, 141.06, 139.60, 135.49, 132.44, 131.12, 128.16, 127.82, 126.87, 126.31, 126.22, 125.87, 124.78, 73.80, 72.04, 69.76, 51.42, 7.12, 6.53. HRMS (ESI-TOF) (m/z): $[M+Na]^+$ calculated for $C_{74}H_{98}NaO_6Si_4$, 1217.6338; found, 1217.6381.



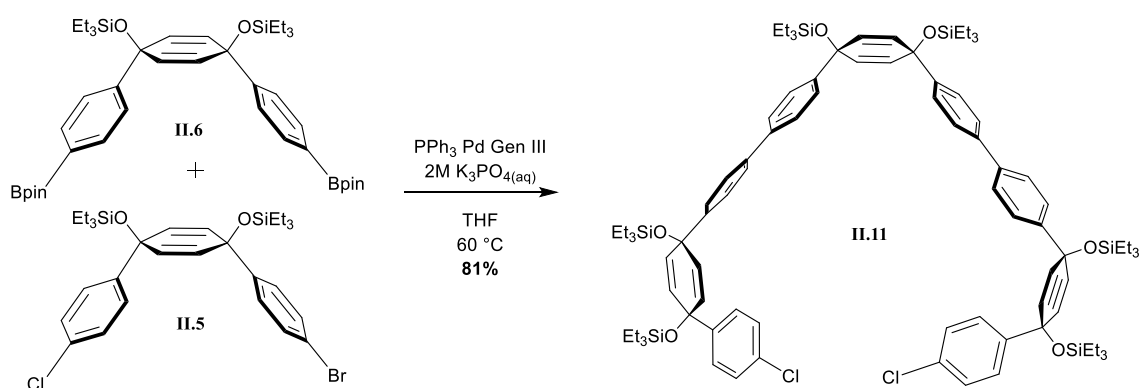
II.33. **II.15** (100 mg, 0.084 mmol, 1 equiv) was dissolved in tetrahydrofuran (2.1 mL) and Tetra-*n*-butylammonium fluoride (0.50 mL, 0.50 mmol, 6 equiv, 1 M in tetrahydrofuran) was added. The reaction was stirred for 1 h at room temperature and was quenched with water. Tetrahydrofuran was removed from this mixture under reduced pressure and filtration afforded **II.33** as a white solid, which was washed with dichloromethane. This crude material was used as is for the next reaction.



***m*[8]CPP.** Crude **II.33** was dissolved in minimal tetrahydrofuran and to it was added a solution of tin(II) dichloride monohydrate (62 mg, 280 μ mol, 3.3 eq) and concentrated aqueous hydrochloric acid (44 μ L, 530 μ mol, 6.3 eq) in THF (2.1 mL). The reaction was stirred at room temperature for 1 h and quenched with a 1 M aqueous solution of NaOH (1 mL). This mixture was extracted with dichloromethane (3 x 3 mL) and the combined extracts were dried over anhydrous sodium sulfate. The solvent was removed under reduced pressure and the product was purified by automated flash silica column chromatography (0% to 100% dichloromethane in hexanes) to yield ***m*[8]CPP** as a yellow solid (25 mg, 49%). IR (neat) 3022, 1586, 1481, 1388 cm^{-1} ; ^1H NMR (600 MHz, Chloroform-*d*) δ 7.56 (dt, $J = 7.7, 1.8$ Hz, 2H), 7.52 – 7.44 (m, 17H), 7.40 – 7.36 (m, 8H), 7.32 (d, $J = 8.2$ Hz, 4H), 6.36 (t, $J = 1.8$ Hz, 1H). ^{13}C NMR (151 MHz, CDCl_3) δ 142.42, 141.12, 139.45, 138.47, 138.00, 137.83, 137.57, 137.23, 135.86, 128.93, 128.51, 127.52, 127.49, 127.27, 127.24, 127.14, 123.24. HRMS (ASAP-TOF) (m/z): $[\text{M}+\text{H}]^+$ calculated for $\text{C}_{48}\text{H}_{33}$, 608.2582; found, 609.2585.

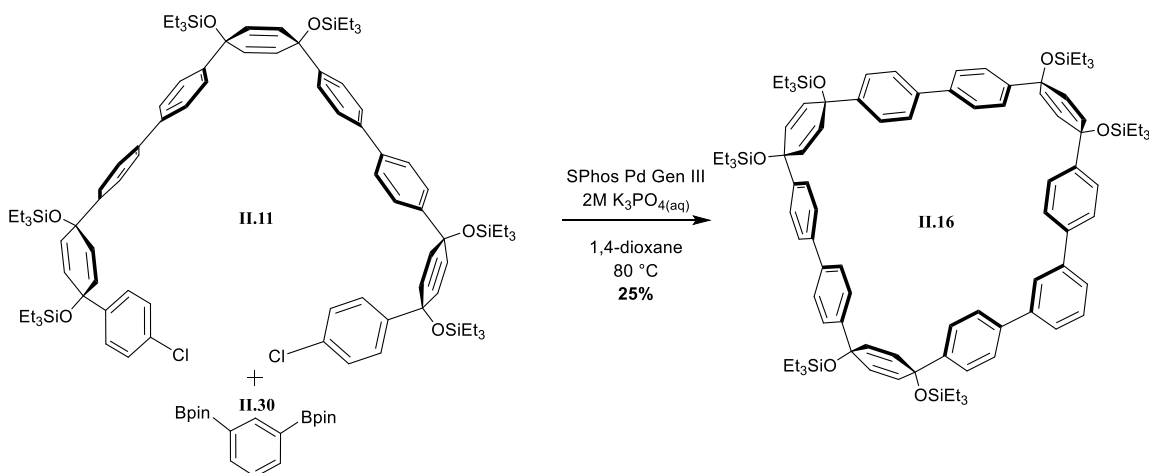


II.6. **II.5** (3.00 g, 4.61 mmol, 1 equiv) was dissolved in tetrahydrofuran (50 mL) and cooled to $-78\text{ }^{\circ}\text{C}$. *n*-BuLi (3.9 mL, 9.7 mmol, 2.1 equiv, 2.5 M in hexanes) was added followed immediately by 2-isopropoxy-4,4,5,5-tetramethyl-1,3,2-dioxaborolane (2.1 mL, 1.9 g, 10 mmol, 2.2 equiv). The reaction was stirred for 30 min and warmed to room temperature. The reaction was quenched with water (20 mL) and extracted with ethyl acetate (3 x 20 mL). The combined extracts were washed with brine (20 mL), dried over anhydrous sodium sulfate, and solvent was removed under reduced pressure to yield an oil. The oil was mixed with an equal amount of ethanol and placed in the freezer until crystals formed, which was filtered to yield **II.6** as a white crystalline powder (2.65 g, 77%). IR (neat) 2949, 2872, 1607, 1355 cm^{-1} ; ^1H NMR (500 MHz, Chloroform-*d*) δ 7.73 (d, $J = 7.6$ Hz, 4H), 7.37 (d, $J = 7.7$ Hz, 4H), 5.99 (s, 4H), 1.37 (s, 24H), 0.95 (t, $J = 7.8$ Hz, 18H), 0.62 (q, $J = 7.8$ Hz, 12H). ^{13}C NMR (126 MHz, CDCl_3) δ 149.08, 134.69, 131.41, 125.18, 83.72, 71.56, 24.89, 7.04, 6.45. HRMS (ESI-TOF) (m/z): $[\text{M}+\text{Na}]^+$ calculated for $\text{C}_{42}\text{H}_{66}\text{B}_2\text{NaO}_6\text{Si}_2$, 767.4482; found, 767.4514.

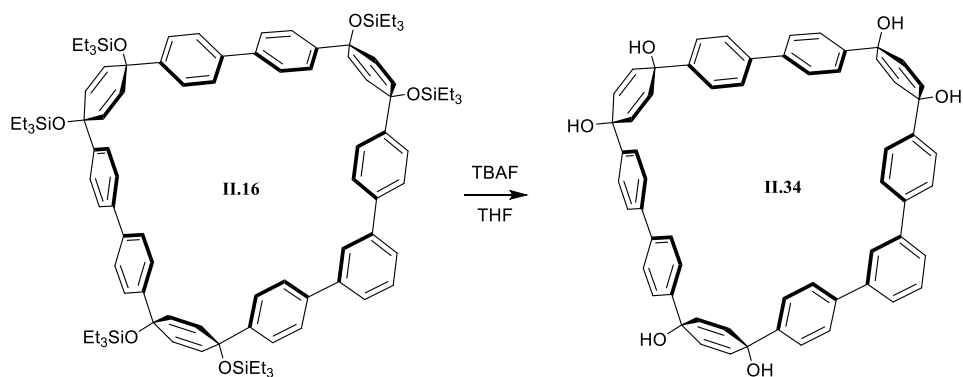


II.11. **II.6** (250 mg, 0.34 mmol, 1 equiv), **II.3** (407 mg, 0.67 mmol, 2 equiv), and PPh_3 Pd Gen III (11 mg, 0.017 mmol, 0.05 equiv) were dissolved in tetrahydrofuran (6.7 mL) and heated to $60\text{ }^{\circ}\text{C}$. K_3PO_4 (0.67 mL, 2 M in deionized water) was added and the reaction was left overnight. The next day, the reaction was cooled to room temperature, filtered through Celite[®] while rinsing with ethyl acetate (15 mL), and dried over anhydrous sodium sulfate. The solvent was removed under reduced pressure and the product was purified by automated flash silica column chromatography (0% to 50% dichloromethane in hexanes) to yield **II.11** as a white solid (421 mg, 81%). IR (neat) 2952, 2874, 1489, 1458, 1238 cm^{-1} ; ^1H NMR (500 MHz, Chloroform-*d*) δ 7.50 (d, $J = 8.2$

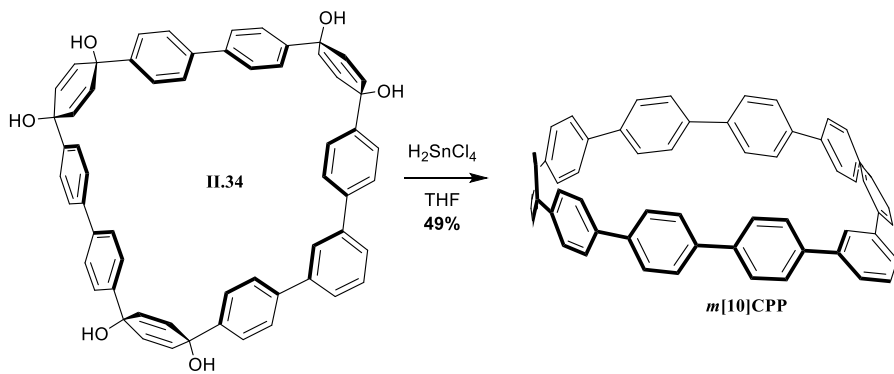
Hz, 8H), 7.42 (d, $J = 8.0$ Hz, 4H), 7.36 (d, $J = 7.9$ Hz, 4H), 7.28 (d, 4H), 7.22 (d, $J = 7.8$ Hz, 4H), 6.04 (s, 4H), 6.03 (d, $J = 8.8$ Hz, 4H), 5.95 (d, $J = 9.7$ Hz, 4H), 0.94 (q, $J = 8.3$ Hz, 54H), 0.67 – 0.57 (m, 36H). ^{13}C NMR (126 MHz, CDCl_3) δ 145.18, 144.83, 144.66, 139.70, 139.48, 132.99, 131.80, 131.52, 131.16, 128.23, 127.33, 126.78, 126.74, 126.33, 126.22, 71.38, 71.28, 71.18, 7.09, 7.06, 7.05, 6.51, 6.49, 6.45. HRMS (ESI-TOF) (m/z): $[\text{M}+\text{Na}]^+$ calculated for $\text{C}_{90}\text{H}_{126}\text{Cl}_2\text{NaO}_6\text{Si}_6$, 1563.7445; found, 1563.7485.



II.16. **II.11** (245 mg, 0.16 mmol, 1 equiv), **II.30** (52 mg, 0.16 mmol, 1 equiv), and SPhos Pd Gen III (12 mg, 0.016 mmol, 0.1 equiv) were dissolved in 1,4-dioxane (80 mL) and heated to 80 °C. K_3PO_4 (8 mL, 2M in deionized water) was added and the reaction was stirred for 3 h. The reaction mixture was filtered through Celite[®] and dried over anhydrous sodium sulfate. Solvent was removed to yield a brown oil, which was purified by automated flash silica column chromatography (0% to 100% dichloromethane in hexanes) to yield a white solid. The product was purified by recycling gel permeation chromatography (chloroform) to yield **II.16** as a white solid (62 mg, 25%). ^1H NMR (500 MHz, Chloroform- d) δ 7.74 (s, 1H), 7.58 – 7.52 (m, 6H), 7.52 – 7.46 (m, 9H), 7.46 – 7.39 (m, 8H), 7.35 (d, $J = 8.3$ Hz, 4H), 6.11 (d, $J = 9.8$ Hz, 4H), 6.04 – 5.97 (m, 7H), 1.03 – 0.87 (m, 54H), 0.71 – 0.53 (m, 36H). ^{13}C NMR (126 MHz, CDCl_3) δ 145.29, 145.22, 144.93, 141.64, 140.39, 139.46, 139.42, 131.80, 131.51, 131.36, 131.24, 129.12, 127.25, 126.75, 126.64, 126.51, 126.38, 126.13, 126.10, 71.57, 71.15, 71.11, 7.10, 7.07, 7.05, 6.49, 6.45. HRMS (ESI-TOF) (m/z): $[\text{M}+\text{Na}]^+$ calculated for $\text{C}_{96}\text{H}_{130}\text{NaO}_6\text{Si}_6$, 1569.8381; found, 1569.8341.

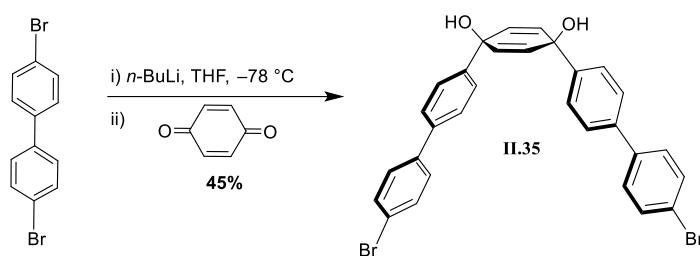


II.34. Tetrahydrofuran (1.3 mL) was added to **II.16** (20 mg, 13 μmol , 1 equiv) and the vial was equipped with a stir bar and septa. Tetra-*n*-butylammonium fluoride (120 μL , 1 mmol, 9 equiv, 1 M in tetrahydrofuran) was added to the reaction flask and stirred for 1 h at room temperature. The reaction was quenched with deionized water (1 mL) and the tetrahydrofuran was removed under reduced pressure. This mixture was filtered through a Büchner funnel, washed with deionized water and dichloromethane yielding **II.34** as a white solid. This solid was used as is for the next reaction.

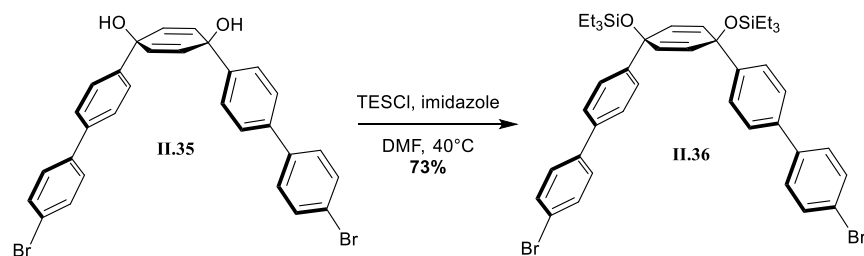


***m*[10]CPP.** Crude **II.34** (11 mg, 17 μmol , 1 eq) was dissolved in tetrahydrofuran (300 μL) and to it was added a solution of tin(II) dichloride monohydrate (9.5 mg, 42 μmol , 3.3 eq) and concentrated aqueous hydrochloric acid (6.7 μL , 80 μmol , 6.3 eq) in THF (320 μL). The reaction was stirred at room temperature for 1 h and quenched with a 1 M aqueous solution of NaOH (1 mL). This mixture was extracted with dichloromethane (3 x 3 mL) and the combined extracts were dried over anhydrous sodium sulfate. The solvent was removed under reduced pressure and the product was purified by preparative thin layer chromatography on alumina (50% dichloromethane in hexanes) to yield ***m*[10]CPP**

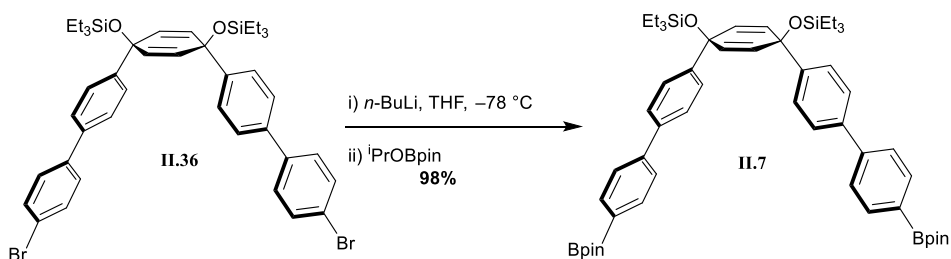
as a white solid (2 mg, 21%). IR (neat) 2918, 2849, 1672, 1480, 1463 cm^{-1} ; ^1H NMR (600 MHz, Chloroform-*d*) δ 7.62 (d, $J = 8.3$ Hz, 8H), 7.60 – 7.56 (m, 19H), 7.55 – 7.50 (m, 8H), 7.43 (d, $J = 7.9$ Hz, 4H), 6.86 (s, 1H). ^{13}C NMR (151 MHz, CDCl_3) δ 142.37, 141.12, 139.51, 139.22, 138.49, 138.32, 138.20, 138.13, 138.00, 137.93, 133.39, 129.03, 128.54, 127.65, 127.53, 127.49, 127.45, 127.44, 127.33, 127.24, 127.12, 124.26. LRMS (MALDI) (m/z): $[\text{M}]^+$ calculated for $\text{C}_{60}\text{H}_{40}$, 760.3125; found, 760.244.



II.35. 4,4'-Dibromobiphenyl (19 g, 0.061 mol, 3.3 equiv) was added to a 1000 mL round bottom flask equipped with a stir bar. The reaction flask was capped with a septa and the round bottom flask was evacuated and purged with nitrogen. Tetrahydrofuran (370 mL) was added to the reaction flask and cooled for 30 min at -78 °C. *n*-BuLi (24.1 mL, 0.11 mol, 1.05 equiv, 2.3 M in hexanes) was added to the reaction mixture dropwise over 25 min. The light brown solution was stirred for 15 min producing a white precipitate in a brown solution. *p*-benzoquinone (14.5 mL, 0.10 mol, 1 equiv) was added to a 9 mL test tube and capped with a septa in order to weigh due to pungent odor. This was added portion-wise by removing the septa from the reaction flask (while a large flow of nitrogen was still flowing into the flask). As the benzoquinone was added, the reaction mixture turns blue momentarily before returning to brown. Benzoquinone was added until the blue color remained (2.3 g total). The reaction was stirred at -78 °C for 3 h. The reaction was quenched with deionized water (160 mL) at -78 °C. The reaction mixture was warmed to room temperature. The product was extracted with ethyl acetate (3 x 200 mL) and washed with brine (3 x 100 mL). The organic layers were dried over sodium sulfate, decanted and concentrated to yield the crude product as a dark orange solid. This was purified by automated flash silica gel chromatography (10% to 60% ethyl acetate in hexanes). The crude product **II.35** was used as is for the next reaction.

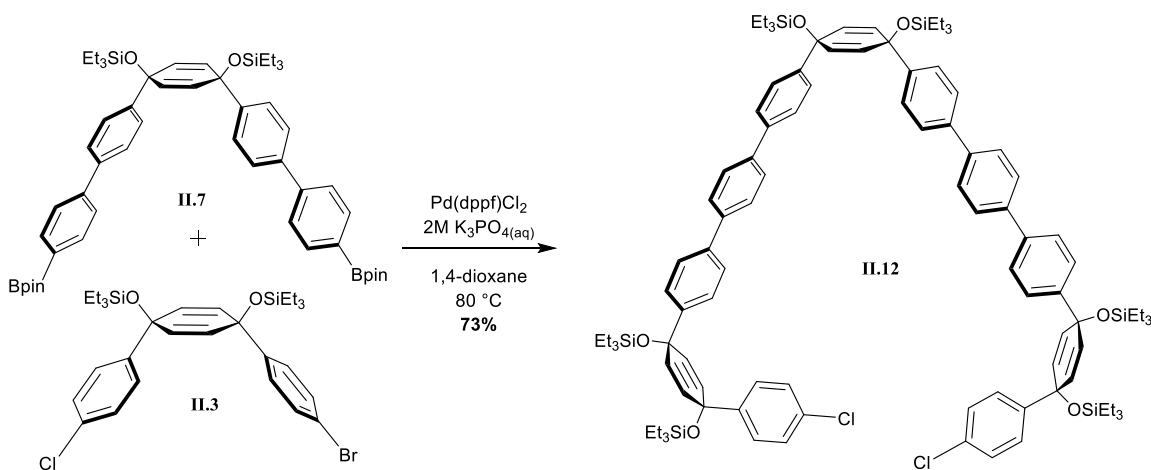


II.36. **II.35** (4.0 g, 7.0 mmol, 1 equiv) and imidazole (1.9 g, 28 mmol, 4 equiv) were added to a 250 mL round bottom flask equipped with a stir bar and septum. Dimethylformamide (35 mL) was added to the flask followed by triethylsilyl chloride (3.8 mL, 23 mmol, 1.2 equiv). The reaction mixture was heated to 40 °C in an oil bath and stirred overnight. The reaction mixture was cooled to room temperature and quenched with a saturated solution of sodium bicarbonate (30 mL). The product was extracted with ethyl acetate (3 x 100 mL) and washed with 5% lithium chloride solution in water (5 x 60 mL). The organic layers were dried over sodium sulfate and concentrated to yield the crude product as a brown solid. The product was purified by automated flash silica gel chromatography (0% to 10% ethyl acetate in hexanes) to give **II.36** as a pale yellow solid (4.10 g, 39% 2 steps). IR (neat) 2952, 2874, 1481, 1458 cm^{-1} ; ^1H NMR (600 MHz, Chloroform- d) δ 7.53 (d, $J = 8.4$ Hz, 4H), 7.47 – 7.41 (m, 12H), 6.04 (s, 4H), 0.95 (t, $J = 7.9$ Hz, 18H), 0.63 (q, $J = 7.9$ Hz, 12H). ^{13}C NMR (151 MHz, CDCl_3) δ 145.55, 139.66, 138.79, 131.83, 131.51, 128.62, 126.65, 126.45, 121.50, 71.32, 7.07, 6.46. LRMS (MALDI) (m/z): $[\text{M}]^+$ calculated for $\text{C}_{42}\text{H}_{50}\text{Br}_2\text{O}_2\text{Si}_2$, 802.17; found, 802.24.



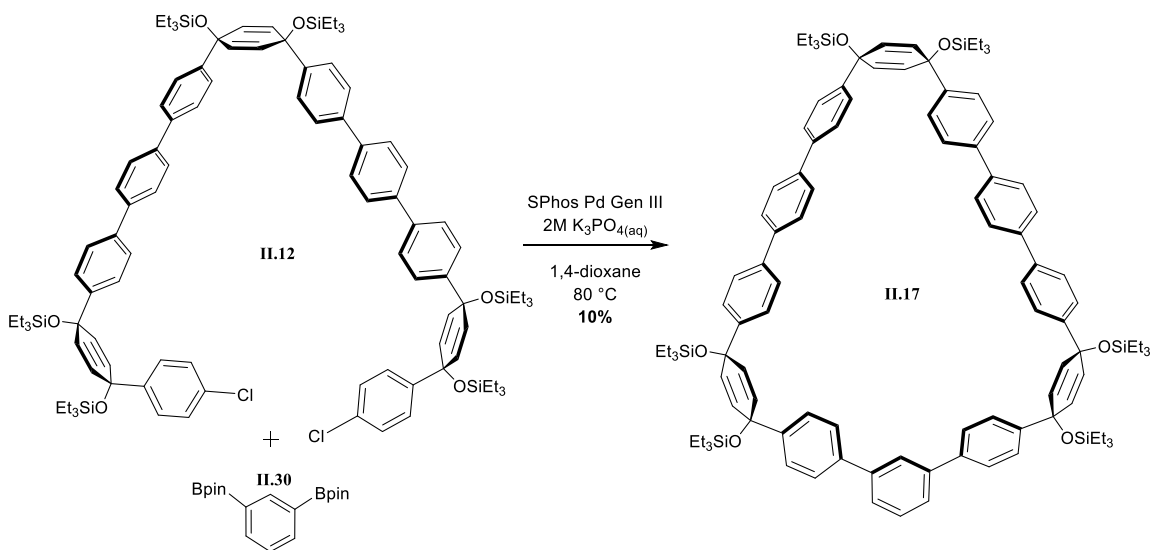
II.7. **II.36** (3.0 g, 3.74 mmol, 1.0 equiv) was added to a 100 mL round bottom flask equipped with a stir bar. The reaction flask was capped with a septa evacuated and refilled with nitrogen. Tetrahydrofuran (19 mL) was added to the reaction flask and the mixture was cooled for 30 min at -78 °C. $n\text{-BuLi}$ (3.4 mL, 8.2 mmol, 2.2 equiv, 2.4 M in hexanes) was added to the reaction mixture dropwise, followed by the dropwise addition

of 2-Isopropoxy-4,4,5,5-tetramethyl-1,3,2-dioxaborolane (3.0 mL, 14.9 mmol, 4 equiv) and the reaction was stirred at $-78\text{ }^{\circ}\text{C}$ for 1 h. The reaction was quenched with deionized water (30 mL) at $-78\text{ }^{\circ}\text{C}$ and warmed to room temperature. The product was extracted with ethyl acetate (3 x 50 mL) and washed with brine (3 x 20 mL). The organic layers were dried over sodium sulfate and concentrated to yield **II.7** as a yellow solid (3.3 g, 98%). IR (neat) 2954, 2875, 1609, 1359 cm^{-1} ; ^1H NMR (600 MHz, Chloroform- d) δ 7.87 (d, $J = 7.7$ Hz, 4H), 7.63 – 7.41 (m, 12H), 6.04 (s, 4H), 0.96 (t, $J = 7.8$ Hz, 18H), 0.64 (q, $J = 8.1$ Hz, 12H). ^{13}C NMR (151 MHz, CDCl_3) δ 145.52, 143.50, 139.86, 135.33, 131.59, 127.02, 126.41, 83.84, 71.43, 24.94, 24.88, 7.17, 6.56. HRMS (ESI-TOF) (m/z): $[\text{M}+\text{Na}]^+$ calculated for $\text{C}_{54}\text{H}_{74}\text{B}_2\text{O}_6\text{Si}_2$, 919.5108; found, 919.5129.



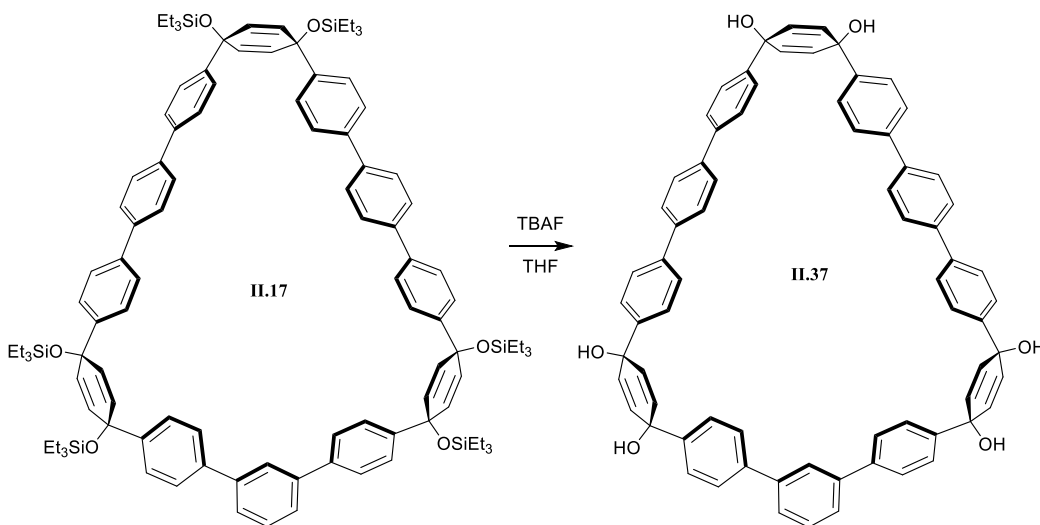
II.12. **II.7** (85.8 mg, 0.22 mmol, 1 equiv), **II.3** (270.3 mg, 0.45 mmol, 2 equiv) and $\text{Pd}(\text{dppf})_2\text{Cl}_2$ (25.5 mg, 0.031 mmol, 0.07 equiv) were added to a 10 mL round bottom flask equipped with a stir bar. The flask was evacuated (5 min) and purged with nitrogen 5 times. 1,4-dioxane and 2 M aqueous K_3PO_4 were sparged with nitrogen for at least 1 h prior to use. The round bottom flask was equipped with a septa and 1,4-dioxane (2.2 mL) was added to the round bottom flask. The round bottom flask was heated to $80\text{ }^{\circ}\text{C}$ over 5 min and K_3PO_4 (0.22 mL, 2 M in deionized water) was added. The reaction was stirred at $80\text{ }^{\circ}\text{C}$ overnight. The reaction mixture was cooled to room temperature and filtered through a fritted suction funnel filled with Celite[®]. The round bottom flask was rinsed with dichloromethane, which was filtered through the Celite[®] plug. The filtrate was added to a separatory funnel along with deionized water (20 mL) and the product was

extracted (3 x 20 mL) with dichloromethane. The organic layer was washed with brine (20 mL), dried over sodium sulfate and concentrated to yield the crude product as a brown solid. The product was purified by automated flash silica gel chromatography (5% to 25% dichloromethane in hexanes to yield **II.12** as a white solid (277 mg, 73%). IR (neat) 2952, 2874, 1485, 1457, 1401 cm^{-1} ; ^1H NMR (600 MHz, Chloroform-*d*) δ 7.65 (s, 8H), 7.55 (t, $J = 7.7$ Hz, 8H), 7.46 (d, $J = 8.1$ Hz, 4H), 7.39 (d, $J = 8.1$ Hz, 4H), 7.30 (s, 4H), 7.23 (d, $J = 8.4$ Hz, 4H), 6.09 – 6.02 (m, 8H), 5.97 (d, $J = 9.9$ Hz, 4H), 0.99 – 0.92 (m, 54H), 0.67 – 0.59 (m, 36H). ^{13}C NMR (151 MHz, CDCl_3) δ 145.26, 144.97, 144.68, 139.72, 139.61, 139.57, 139.48, 133.02, 131.82, 131.58, 131.21, 128.76, 128.28, 127.41, 127.38, 126.78, 126.76, 126.43, 126.32, 71.44, 71.32, 71.19, 18.66, 11.28, 7.14, 7.11, 7.09, 6.53, 6.51, 6.47, 6.34. LRMS (MALDI) (m/z): $[\text{M}]^+$ calculated for $\text{C}_{102}\text{H}_{134}\text{Cl}_2\text{O}_6\text{Si}_6$, 1693.82; found, 1694.838.



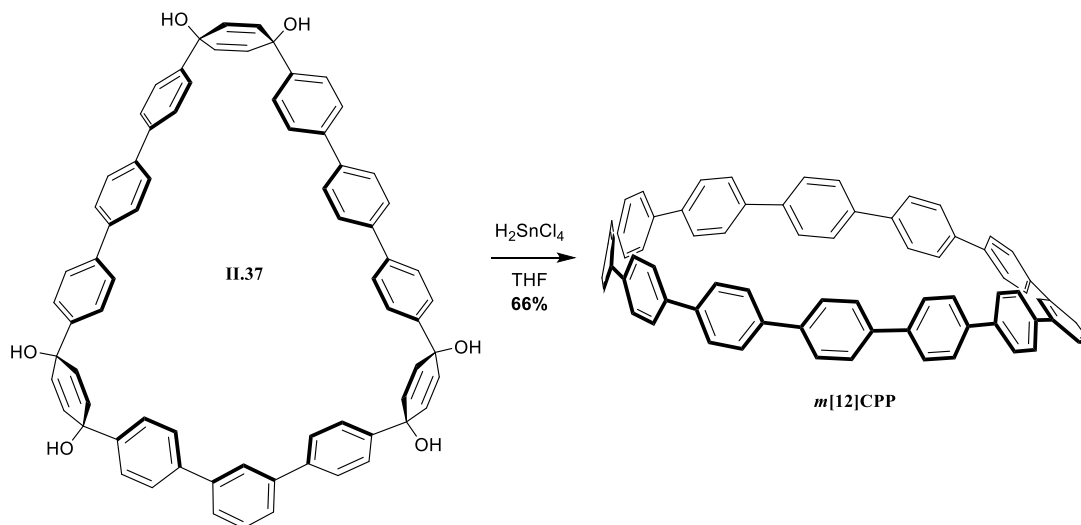
II.17. **II.30** (34.7 mg, 0.11 mmol, 1 equiv), **II.12** (101.3 mg, 0.054 mmol, 1.05 equiv) and Pd Sphos Gen III 3.6 mg, 0.0045 mmol, 0.1 equiv) were added to a 100 mL round bottom flask equipped with a stir bar. The flask was evacuated (5 min) and purged with nitrogen 5 times. 1,4-dioxane and aqueous 2 M K_3PO_4 were sparged for at least 1 h prior to use. The round bottom flask was equipped with a septum and 1,4-dioxane (33 mL) was added to the round bottom flask and the solution was sparged for 30 min. The round bottom flask was heated to 80 °C over 10 min and K_3PO_4 (0.33 mL, 2 M in deionized water) was added. The reaction was stirred at 80 °C overnight. The reaction mixture was

cooled to room temperature and filtered through a fritted suction funnel filled with Celite[®]. The round bottom flask was rinsed with dichloromethane, which was also filtered through the Celite[®] plug. The filtrate was added to a separatory funnel along with deionized water (30 mL) and the product was extracted (3 x 30 mL) with dichloromethane. The organic layer was washed with brine (40 mL), dried over sodium sulfate and concentrated to yield a brown oil. The product was purified by flash silica column chromatography (0% to 30% dichloromethane in hexanes) followed by recycling gel permeation chromatography yielding **II.17** as a white solid (18 mg, 10%). ¹H NMR (600 MHz, Chloroform-d) δ 7.77 (t, J = 1.7 Hz, 1H), 7.65 (d, J = 3.5 Hz, 2H), 7.62 – 7.45 (m, 25H), 7.36 (d, J = 8.1 Hz, 8H), 6.16 (d, J = 9.7 Hz, 4H), 6.05 (s, 4H), 6.00 (d, J = 9.8 Hz, 4H), 1.00 (t, J = 7.9 Hz, 18H), 0.97 (t, J = 7.9 Hz, 18H), 0.92 (t, J = 7.9 Hz, 18H), 0.71 (q, J = 7.9 Hz, 12H), 0.65 (q, J = 7.9 Hz, 12H), 0.57 (q, J = 7.9 Hz, 12H). ¹³C NMR (151 MHz, CDCl₃) δ 145.33, 145.06, 144.75, 141.82, 140.68, 139.63, 139.48, 139.42, 139.27, 132.07, 131.64, 131.10, 127.39, 127.37, 127.30, 127.28, 126.74, 126.61, 126.56, 126.53, 126.18, 71.80, 71.72, 71.01, 7.14, 7.10, 7.05, 6.50, 6.48. LRMS (MALDI) (m/z): [M+H]⁺ calculated for C₁₀₈H₁₃₉O₆Si₆, 1699.919; found, 1699.904.



II.37. Tetrahydrofuran (0.11 mL) was added to **II.17** (18.2 mg, 0.01 mmol, 1 equiv) and the vial was equipped with a stir bar and septa. Tetra-*n*-butylammonium fluoride (0.11 mL, 0.1 mmol, 10 equiv, 1 M in tetrahydrofuran) was added to the reaction flask and this was stirred for 2 h at room temperature. The reaction was quenched with deionized water

(5 mL) causing the product to precipitate. The resulting solution was filtered in a Büchner funnel, washed with deionized water and dichloromethane yielding **II.37** as a white solid. The crude product was used as is for the following reaction.



***m*[12]CPP**. $\text{SnCl}_2 \cdot \text{H}_2\text{O}$ (180.6 mg, 0.80 mmol) was added to a 100 mL round bottom flask equipped with a stir bar and septum. Tetrahydrofuran (20 mL) was added to the flask followed by hydrochloric acid (0.13 mL, 1.6 mmol, 12 M). This was stirred at room temperature for 30 min. H_2SnCl_2 solution (0.9 mL, 0.04 mmol, 3.3 equiv, 0.04 M) was added to the scintillation vial containing **II.37** (11.1 mg, 0.01 mmol, 1 equiv) and was stirred for 1 h at room temperature. The reaction was quenched with saturated sodium bicarbonate (5 mL). The filtrate was transferred to a separatory funnel and the product was extracted with ethyl acetate (3 x 7 mL). The organic layers were washed with brine (10 mL), dried over sodium sulfate and concentrated to give the crude product as a yellow solid. The product was purified by preparative thin layer chromatography on alumina (50% dichloromethane in hexanes) and recycling gel permeation chromatography to give ***m*[12]CPP** as a pale yellow solid (0.5 mg, 5% 2 steps).

***m*[12]CPP** is too insoluble to record a ^{13}C spectrum. IR (neat) 2924, 2853, 1483 cm^{-1} ; ^1H NMR (600 MHz, Chloroform-*d*) δ 7.68 – 7.56 (m, 40H), 7.56 – 7.53 (m, 3H), 7.51 (d, $J = 8.4$ Hz, 4H), 7.12 (t, $J = 1.8$ Hz, 1H). LRMS (MALDI) (m/z): $[\text{M}]^+$ calculated for $\text{C}_{72}\text{H}_{48}$, 912.3751; found, 912.329.

2.5.2 Photophysical Characterization

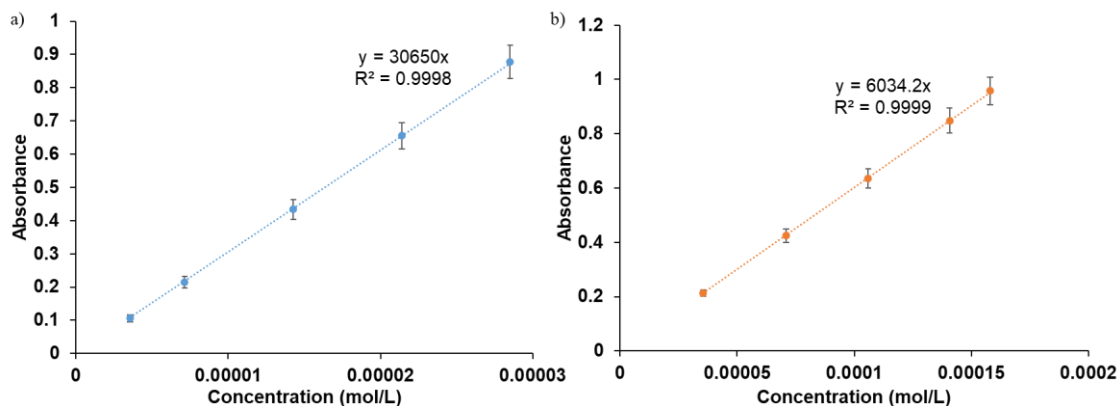


Figure 2.5. Extinction coefficient determination of *m*[5]CPP at the a) absorbance maxima and b) HOMO→LUMO transition.

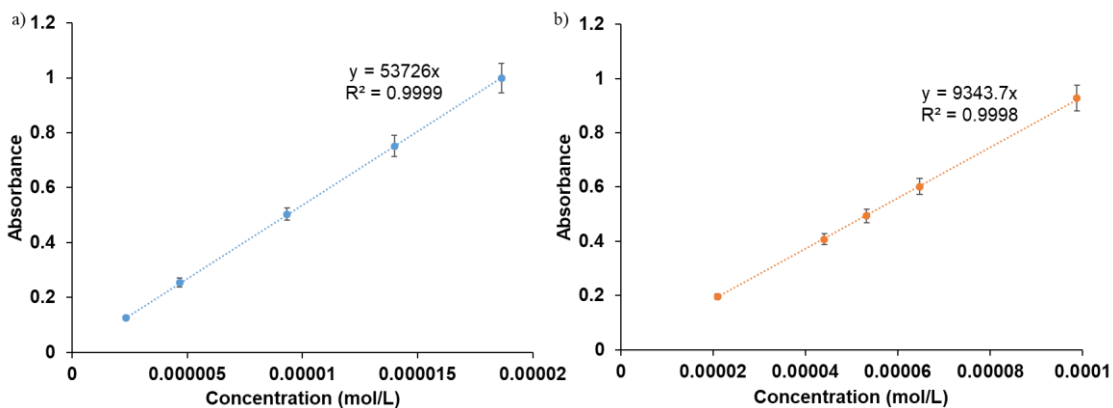


Figure 2.6. Extinction coefficient determination of *m*[6]CPP at the a) absorbance maxima and b) HOMO→LUMO transition.

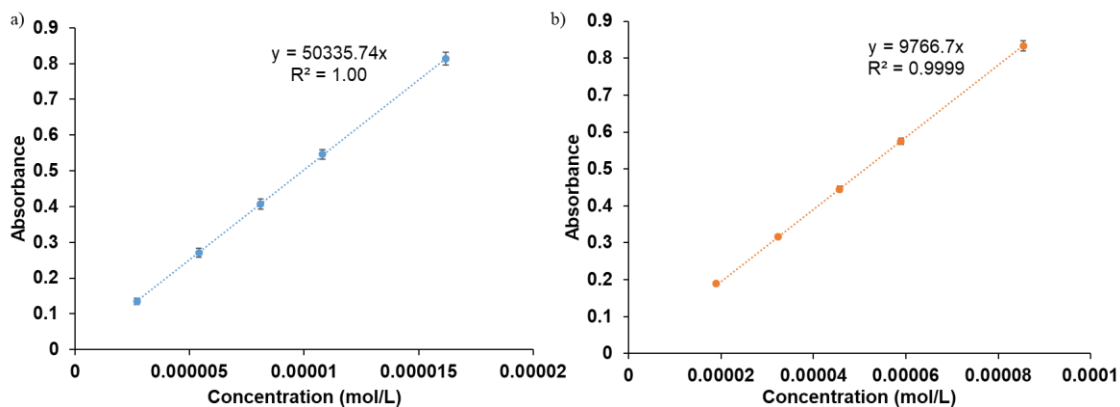


Figure 2.7. Extinction coefficient determination of *m*[7]CPP at the a) absorbance maxima and b) HOMO→LUMO transition.

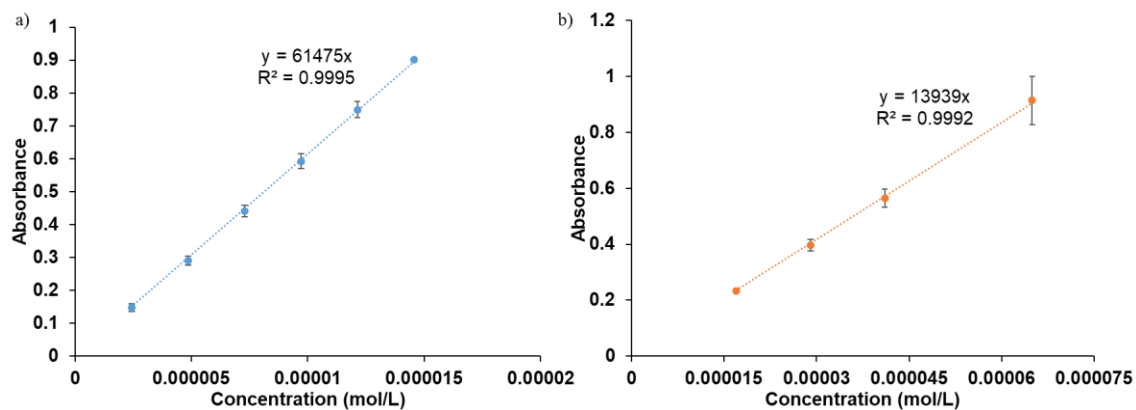


Figure 2.8. Extinction coefficient determination of *m*[8]CPP at the a) absorbance maxima and b) HOMO→LUMO transition.

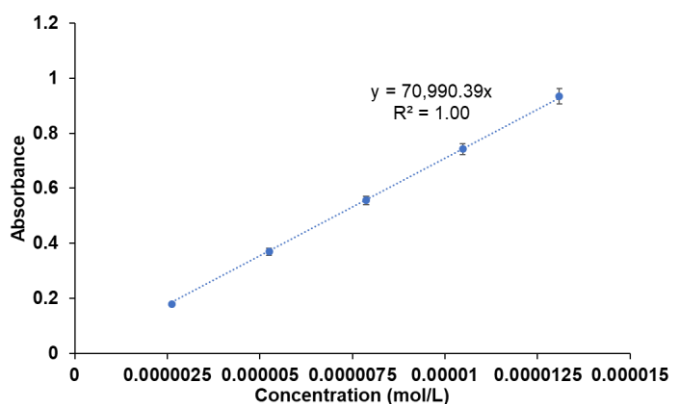


Figure 2.9. Extinction coefficient determination of *m*[10]CPP at the absorbance maxima.

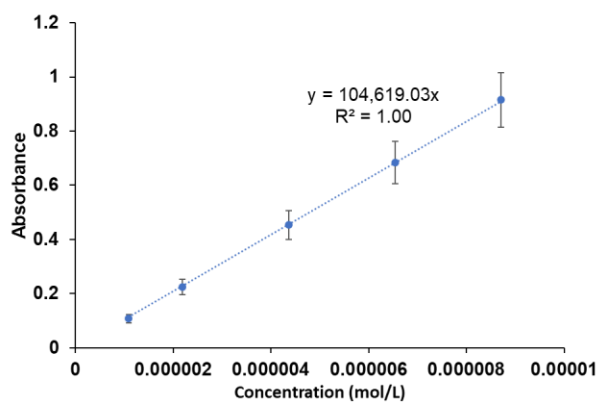


Figure 2.10. Extinction coefficient determination of *m*[12]CPP at the absorbance maxima.

Table 2.1. Triplicate quantum yield data, excited at the absorbance maxima.

<i>m[n]</i> CPP	Trial 1	Trial 2	Trial 3	$\Phi_{\text{Aver.}}$
5	0.013	0.014	0.014	0.014 ± 0.001
6	0.225	0.224	0.224	0.224 ± 0.001
7	0.453	0.445	0.451	0.450 ± 0.004
8	0.592	0.598	0.595	0.595 ± 0.003
10	0.726	0.729	0.722	0.726 ± 0.004
12	0.77	0.772	0.766	0.769 ± 0.003

Table 2.2. Triplicate quantum yield data, excited at HOMO→LUMO transition.

<i>m[n]</i> CPP	Trial 1	Trial 2	Trial 3	$\Phi_{\text{Aver.}}$
5	0.015	0.015	0.014	0.015 ± 0.001
6	0.246	0.232	0.234	0.237 ± 0.008
7	0.47	0.471	0.474	0.472 ± 0.002
8	0.608	0.612	0.608	0.609 ± 0.002

Table 2.3. HOMO→LUMO absorbance maxima and extinction coefficients.

<i>m[n]</i> CPP	H→L Absorbance (nm)	$\epsilon_{\text{H} \rightarrow \text{L}}$ ($\text{M}^{-1}\text{cm}^{-1}$)
5	428	$6.0 \times 10^3 \pm 0.3$
6	410	$9.4 \times 10^3 \pm 0.5$
7	394	$9.9 \times 10^3 \pm 0.08$
8	376	$1.4 \times 10^4 \pm 0.1$

Table 2.4. Fluorescence lifetimes and calculated decay rates.

<i>m[n]</i> CPP	Lifetime (ns)	Rate of radiative decay (10^8 s^{-1})	Rate of non-radiative decay (10^8 s^{-1})
5	1.05	0.133	9.36
6	2.68	0.834	2.89
7	3.56	1.26	1.54
8	3.41	1.45	1.48
10	2.45	2.96	1.12
12	1.78	4.32	1.30

2.5.3 Electrochemical Analysis

The oxidation of these molecules proceeds similar to that of CPPs with a decreasing oxidation potential with decreasing size. Two reversible oxidations are observed in the electrochemical window of DCM except for *m*[5]CPP which had a single irreversible oxidation event. As the size of the *m*[*n*]CPP increases, the separation between the oxidations becomes smaller and both oxidations shift to higher potential.

Table 2.5. Oxidation potentials of *m*[*n*]CPPs.

<i>m</i> [<i>n</i>]CPP	1 st Oxidation (V)	2 nd Oxidation (V)	Difference (V)
6	0.50	0.68	0.18
7	0.65	0.82	0.17
8	0.70	0.85	0.15
10	0.79	0.90	0.11
12	0.86	0.94	0.08

Table 2.6. First oxidation peak of $m[n]$ CPPs.

$m[n]$ CPP	1 st Oxidation Peak (V)
5	0.47
6	0.53
7	0.67
8	0.74
10	0.81
12	0.88

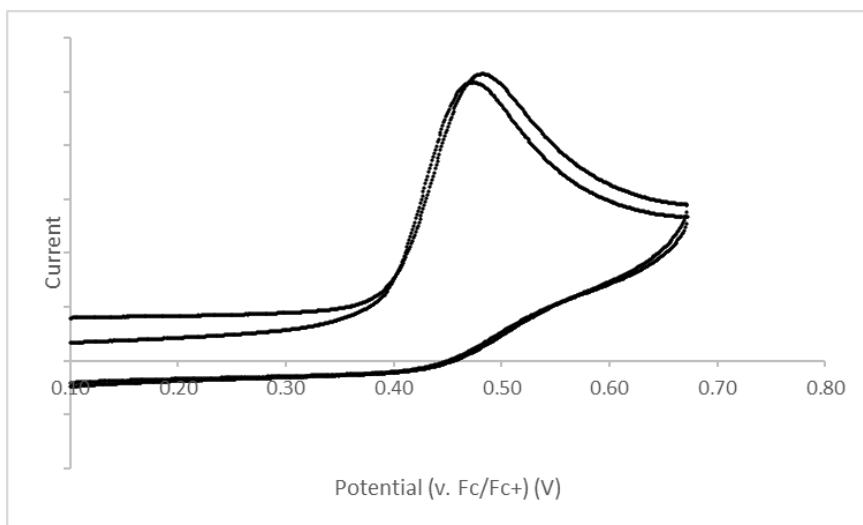


Figure 2.11. $m[5]$ CPP Single irreversible oxidation (DCM) $E = 0.47$ V.

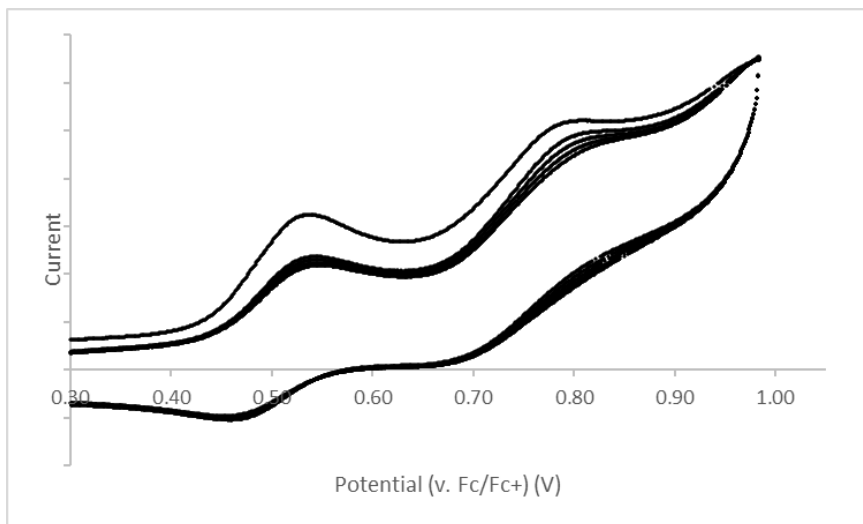


Figure 2.12. $m[6]$ CPP Oxidation (DCM) $E_{1/2} = 0.50$ V and 0.68 V.

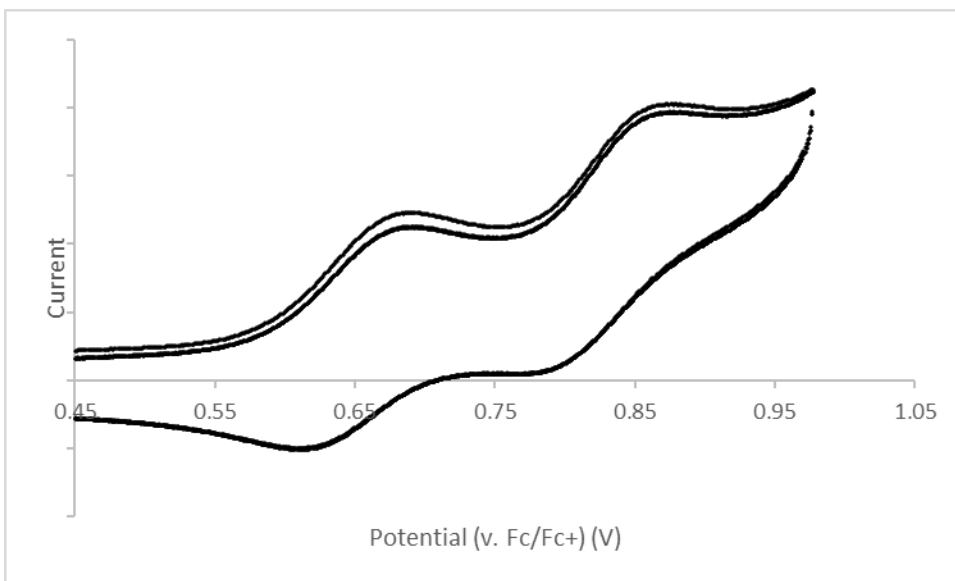


Figure 2.13. *m*[7]CPP Oxidation (DCM) $E_{1/2} = 0.65$ V and 0.81 V.

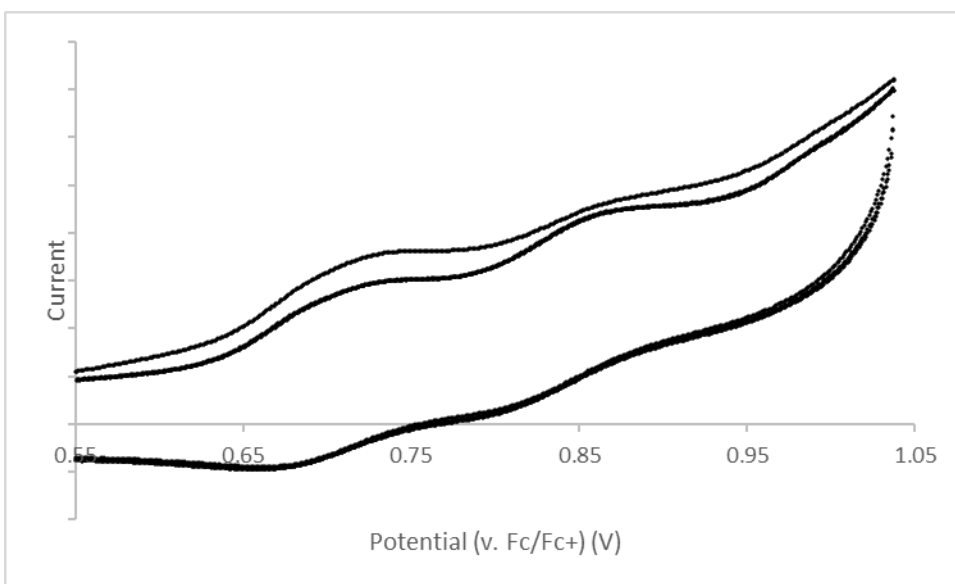


Figure 2.14. *m*[8]CPP Oxidation (DCM) $E_{1/2} = 0.69$ V and 0.85 V.

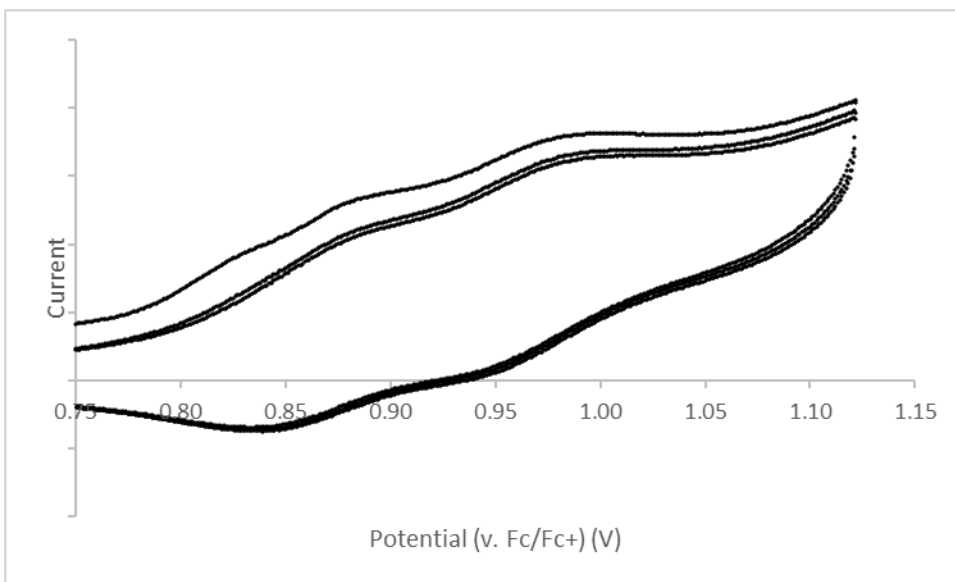


Figure 2.15. *m*[10]CPP Oxidation (DCM) $E_{1/2} = 0.80$ V and 0.91 V.

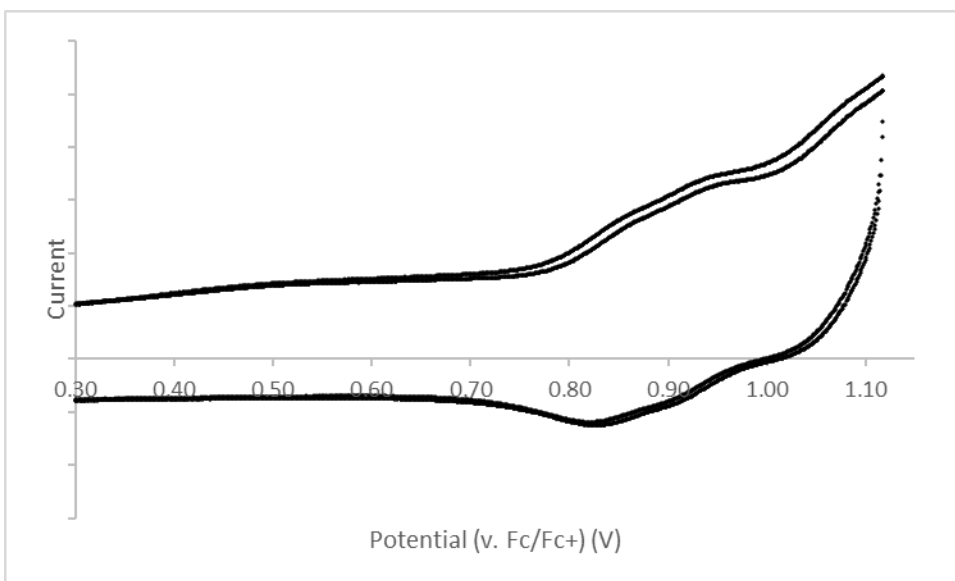


Figure 2.16. *m*[12]CPP Oxidation (DCM) $E_{1/2} = 0.86$ V and 0.95 V.

4. HOMO LUMO Level Calculations

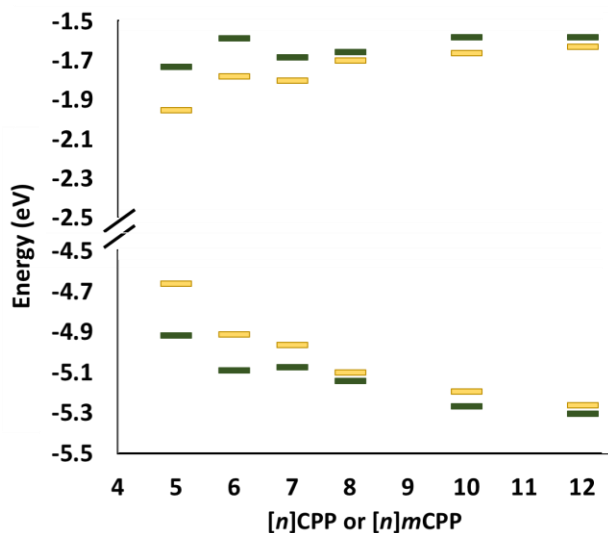


Figure 2.17. Comparison of HOMO and LUMO energy levels of $[n]$ CPPs (yellow) and $m[n]$ CPPs (green). Calculated using B3LYP/6-31G(d,p) level of theory.

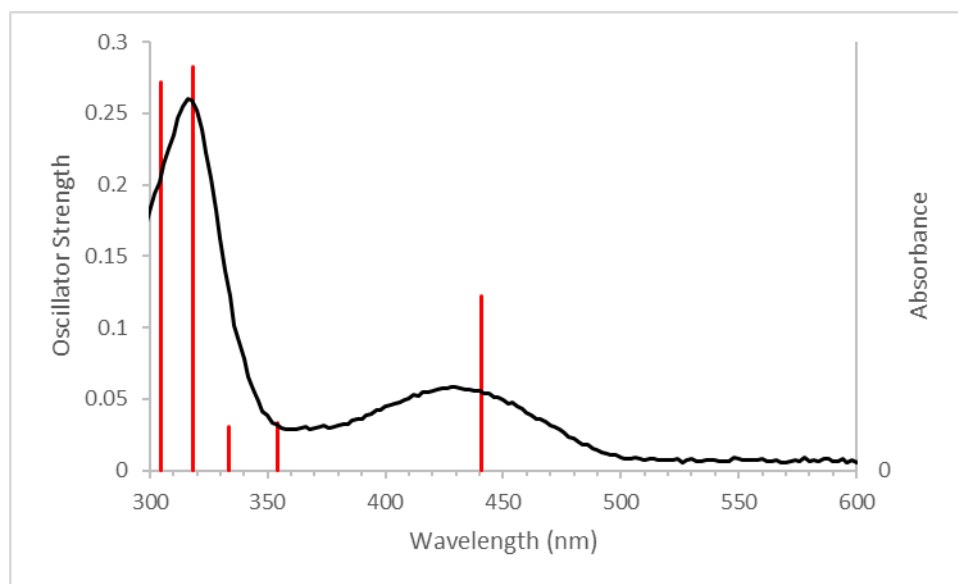
2.5.4 Calculations

Absorbance Calculations

Geometries optimized using Gaussian 09¹³⁷ with B3LYP/6-31G(d,p), then using the same basis, a time dependent calculation of 12 states was performed. The results were analyzed using GaussSum.

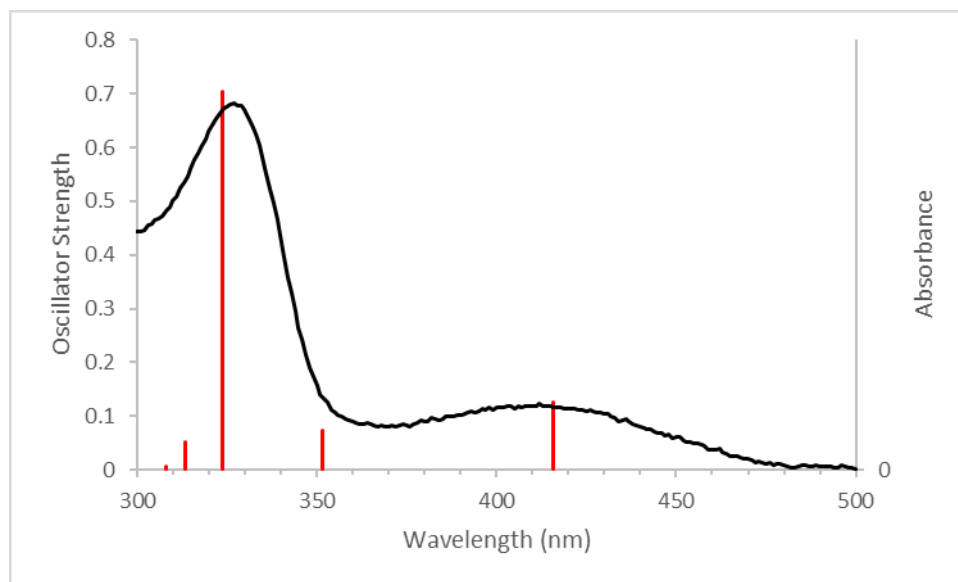
Table 2.7. Calculated HOMO→LUMO absorption for $m[n]$ CPPs.

$m[n]$ CPP	λ_{\max} (nm)	Oscillator strength	H→L Contribution (%)
5	441	0.122	98
6	416	0.126	97
7	404	0.172	97
8	397	0.176	95
10	388	0.227	91
12	383	0.281	86



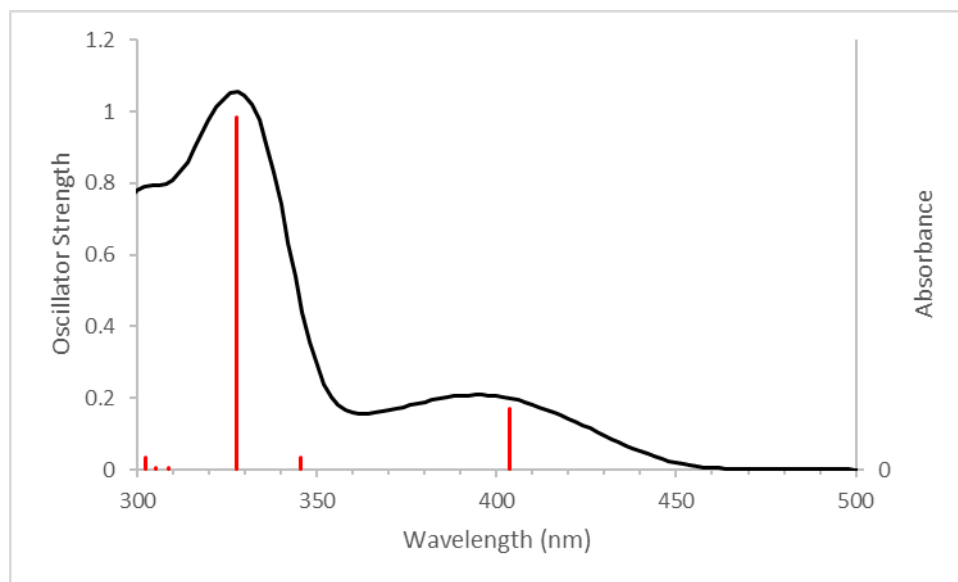
No.	Energy (cm ⁻¹)	Wavelength (nm)	Osc. Strength	Symmetry	Major contributing transitions
1	22677.08	440.9738	0.1217	Singlet-A	HOMO->LUMO (98%)
2	28232.63	354.2001	0.033	Singlet-A	H-1->LUMO (27%), HOMO->L+1 (71%)
3	29990.92	333.4343	0.0309	Singlet-A	H-1->LUMO (15%), HOMO->L+2 (70%)
4	31409.65	318.3735	0.2824	Singlet-A	H-1->LUMO (38%), HOMO->L+1 (17%), HOMO->L+2 (13%), HOMO->L+3 (24%)
5	32829.18	304.607	0.272	Singlet-A	H-1->LUMO (17%), HOMO->L+3 (51%)
6	34168.07	292.6709	0.0064	Singlet-A	H-2->LUMO (73%), H-1->L+1 (16%)
7	34314.05	291.4258	0.0007	Singlet-A	H-1->L+1 (37%), HOMO->L+4 (51%)
8	34995.59	285.7503	0.0523	Singlet-A	H-4->LUMO (10%), H-2->LUMO (12%), H-1->L+1 (20%), HOMO->L+4 (30%)
9	35145.61	284.5306	0.002	Singlet-A	H-4->LUMO (12%), H-3->LUMO (12%), HOMO->L+5 (33%), HOMO->L+6 (10%)
10	35563.4	281.1879	0.0103	Singlet-A	H-4->LUMO (23%), H-3->LUMO (14%), HOMO->L+6 (21%)
11	35806.18	279.2814	0.0019	Singlet-A	H-3->LUMO (37%), HOMO->L+6 (15%)
12	36343.34	275.1536	0.0588	Singlet-A	H-7->LUMO (23%), H-4->LUMO (23%), HOMO->L+8 (13%)

Figure 2.18. *m*[5]CPP Calculated absorption (red lines) compared to experimental absorption (black trace) results and table of calculated transitions.



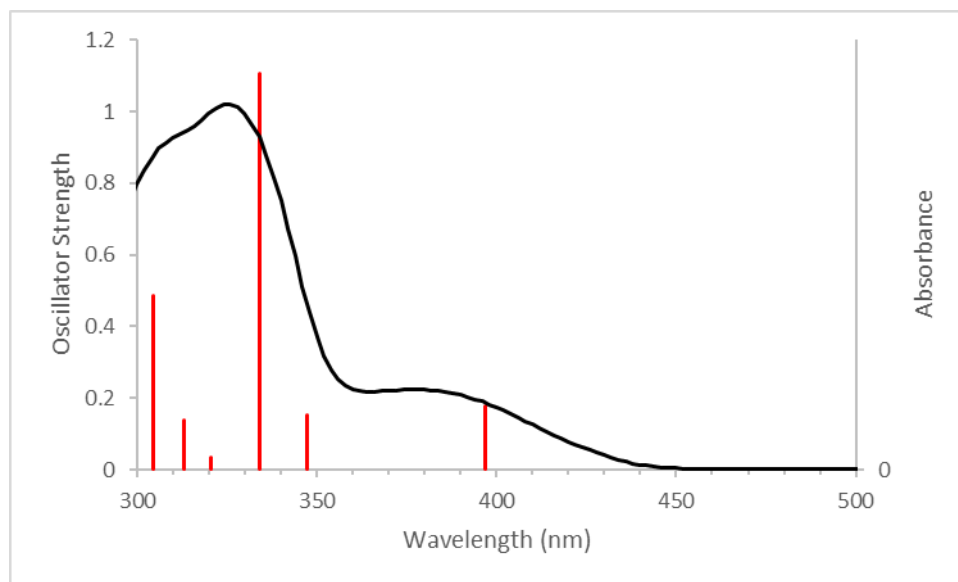
No.	Energy (cm ⁻¹)	Wavelength (nm)	Osc. Strength	Symmetry	Major contributing transitions
1	24054.68	415.7195	0.126	Singlet-A	HOMO->LUMO (97%)
2	28438.3	351.6384	0.0731	Singlet-A	H-1->LUMO (25%), HOMO->L+1 (74%)
3	30893.45	323.6932	0.7042	Singlet-A	H-1->LUMO (70%), HOMO->L+1 (22%)
4	31889.55	313.5824	0.0502	Singlet-A	HOMO->L+2 (79%)
5	32471.07	307.9664	0.0069	Singlet-A	H-2->LUMO (15%), H-1->L+1 (80%)
6	33162.29	301.5473	0.0005	Singlet-A	H-2->LUMO (30%), HOMO->L+3 (58%)
7	33675.26	296.9539	0.1059	Singlet-A	H-2->LUMO (36%), HOMO->L+4 (31%)
8	35029.47	285.474	0.2921	Singlet-A	H-2->LUMO (15%), HOMO->L+3 (27%), HOMO->L+4 (40%)
9	35264.17	283.5739	0.0218	Singlet-A	H-6->LUMO (18%), HOMO->L+5 (23%), HOMO->L+6 (37%)
10	36278.82	275.6429	0.0251	Singlet-A	H-3->LUMO (23%), HOMO->L+5 (40%), HOMO->L+6 (13%)
11	36550.63	273.5931	0.0082	Singlet-A	H-7->LUMO (27%), HOMO->L+7 (32%), HOMO->L+8 (21%)
12	36911.96	270.9149	0.0143	Singlet-A	H-8->LUMO (17%), H-3->LUMO (15%), H-2->L+1 (36%), HOMO->L+9 (13%)

Figure 2.19. *m*[6]CPP Calculated absorption (red lines) compared to experimental absorption (black trace) results and table of calculated transitions.



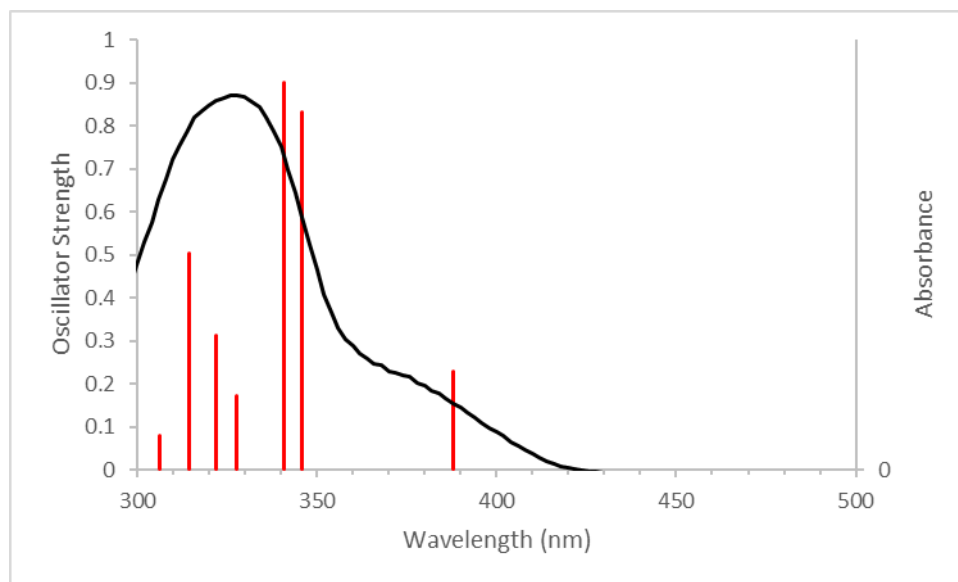
No.	Energy (cm-1)	Wavelength (nm)	Osc. Strength	Symmetry	Major contributing transitions
1	24781.38	403.5287	0.1718	Singlet-A	HOMO->LUMO (97%)
2	28944.01	345.4946	0.0342	Singlet-A	H-1->LUMO (32%), HOMO->L+1 (66%)
3	30529.7	327.5499	0.9834	Singlet-A	H-1->LUMO (66%), HOMO->L+1 (31%)
4	32396.87	308.6718	0.0062	Singlet-A	H-2->LUMO (12%), H-1->L+1 (83%)
5	32745.3	305.3873	0.0071	Singlet-A	H-2->LUMO (48%), HOMO->L+2 (45%)
6	33070.34	302.3857	0.0326	Singlet-A	H-4->LUMO (10%), HOMO->L+4 (74%)
7	33687.36	296.8473	0.2207	Singlet-A	H-2->LUMO (23%), HOMO->L+2 (23%), HOMO->L+3 (25%)
8	34174.52	292.6157	0.1759	Singlet-A	H-2->LUMO (12%), HOMO->L+2 (22%), HOMO->L+3 (44%)
9	35339.18	282.972	0.079	Singlet-A	HOMO->L+5 (43%)
10	35952.16	278.1474	0.0225	Singlet-A	H-2->L+1 (59%), H-1->L+2 (24%)
11	36171.55	276.4604	0.0569	Singlet-A	H-3->LUMO (24%), H-2->L+1 (10%), HOMO->L+3 (16%), HOMO->L+6 (12%)
12	36332.86	275.233	0.014	Singlet-A	H-10->LUMO (12%), H-3->LUMO (20%), HOMO->L+8 (20%)

Figure 2.20. *m*[7]CPP Calculated absorption (red lines) compared to experimental absorption (black trace) results and table of calculated transitions.



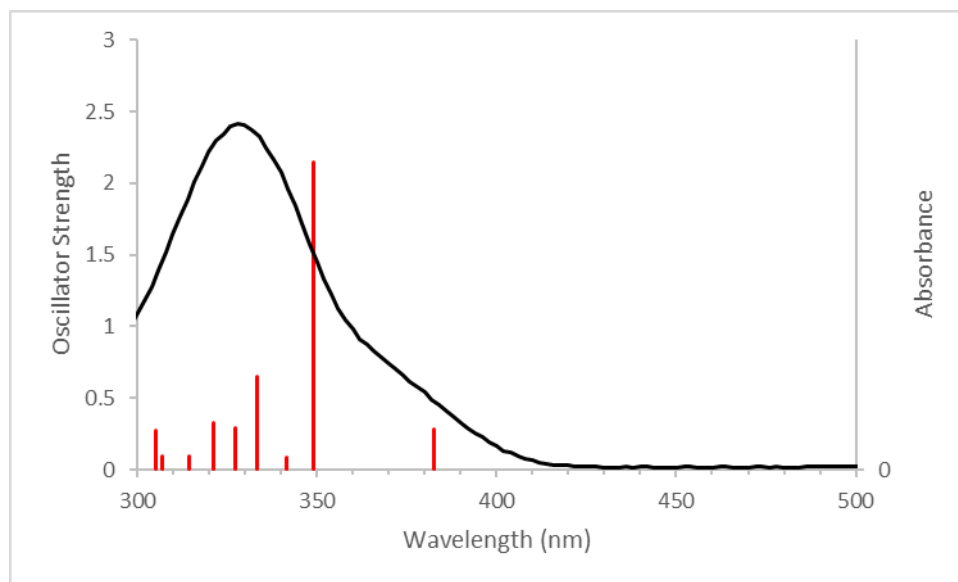
No.	Energy (cm-1)	Wavelength (nm)	Osc. Strength	Symmetry	Major contributing transitions
1	25186.28	397.0416	0.1764	Singlet-A	HOMO->LUMO (95%)
2	28785.12	347.4017	0.1531	Singlet-A	H-1->LUMO (18%), HOMO->L+1 (81%)
3	29923.98	334.1802	1.1065	Singlet-A	H-1->LUMO (80%), HOMO->L+1 (18%)
4	31187.85	320.6377	0.0351	Singlet-A	H-1->L+1 (85%)
5	31941.17	313.0756	0.1391	Singlet-A	H-2->LUMO (76%), HOMO->L+2 (14%)
6	32853.38	304.3827	0.4857	Singlet-A	H-2->LUMO (12%), HOMO->L+2 (78%)
7	33596.22	297.6525	0.0011	Singlet-A	H-5->LUMO (13%), HOMO->L+3 (19%), HOMO->L+4 (52%)
8	34197.1	292.4224	0.086	Singlet-A	H-2->L+1 (88%)
9	34645.55	288.6374	0.0318	Singlet-A	H-3->LUMO (12%), HOMO->L+3 (59%), HOMO->L+4 (18%)
10	34857.67	286.8809	0.0563	Singlet-A	HOMO->L+5 (55%)
11	35451.29	282.0772	0.0355	Singlet-A	H-3->LUMO (13%), H-1->L+2 (14%), HOMO->L+6 (29%)
12	35921.51	278.3847	0.2387	Singlet-A	H-3->LUMO (28%), H-1->L+2 (60%)

Figure 2.21. *m*[8]CPP Calculated absorption (red lines) compared to experimental absorption (black trace) results and table of calculated transitions.



No.	Energy (cm-1)	Wavelength (nm)	Osc. Strength	Symmetry	Major contributing transitions
1	25783.93	387.8384	0.2275	Singlet-A	HOMO->LUMO (91%)
2	28917.4	345.8126	0.8323	Singlet-A	HOMO->L+1 (98%)
3	29329.55	340.9531	0.9001	Singlet-A	H-1->LUMO (98%)
4	30510.34	327.7577	0.1709	Singlet-A	H-1->L+1 (88%)
5	31057.99	321.9783	0.3116	Singlet-A	H-2->LUMO (94%)
6	31807.28	314.3934	0.5032	Singlet-A	HOMO->L+2 (93%)
7	32663.84	306.1489	0.0805	Singlet-A	H-2->L+1 (89%)
8	33421.2	299.2113	0.0744	Singlet-A	H-3->LUMO (13%), HOMO->L+3 (78%)
9	33980.14	294.2896	0.2859	Singlet-A	H-1->L+2 (80%)
10	34545.53	289.473	0.0021	Singlet-A	H-6->LUMO (11%), H-3->LUMO (26%), HOMO->L+5 (37%)
11	34706.84	288.1276	0.054	Singlet-A	H-3->L+1 (10%), H-2->L+2 (48%), H-1->L+3 (27%)
12	34819.76	287.1932	0.0489	Singlet-A	H-3->LUMO (46%), HOMO->L+3 (13%), HOMO->L+5 (23%)

Figure 2.22. *m*[10]CPP Calculated absorption (red lines) compared to experimental absorption (black trace) results and table of calculated transitions.



No.	Energy (cm-1)	Wavelength (nm)	Osc. Strength	Symmetry	Major contribs
1	26136.4	382.6082	0.2811	Singlet-A	H-1->L+1 (10%), HOMO->LUMO (86%)
2	28658.49	348.9367	2.1502	Singlet-A	H-1->LUMO (30%), HOMO->L+1 (67%)
3	29285.99	341.4602	0.0886	Singlet-A	H-1->LUMO (66%), HOMO->L+1 (30%)
4	29996.57	333.3715	0.647	Singlet-A	H-1->L+1 (74%), HOMO->LUMO (10%)
5	30553.89	327.2905	0.2915	Singlet-A	H-2->LUMO (88%)
6	31134.61	321.1859	0.3285	Singlet-A	HOMO->L+2 (92%)
7	31779.86	314.6647	0.0906	Singlet-A	H-2->L+1 (91%)
8	32568.67	307.0436	0.0951	Singlet-A	H-3->LUMO (18%), HOMO->L+3 (70%)
9	32750.95	305.3347	0.2706	Singlet-A	H-1->L+2 (82%)
10	33423.62	299.1897	0.031	Singlet-A	H-2->L+2 (64%), H-1->L+3 (21%)
11	33493.79	298.5628	0.0572	Singlet-A	H-3->LUMO (73%), HOMO->L+3 (23%)
12	33971.27	294.3664	0.3944	Singlet-A	H-3->L+1 (34%), H-2->L+2 (23%), H-1->L+3 (32%)

Figure 2.23. *m*[12]CPP Calculated absorption (red lines) compared to experimental absorption (black trace) results and table of calculated transitions.

Strain Calculations

Strain calculated by comparison of single point energy of optimized geometries of the molecules in the theoretical homodesmotic reaction shown below. Geometries optimized using Gaussian 09¹³⁷ with B3LYP/6-31G(d,p).

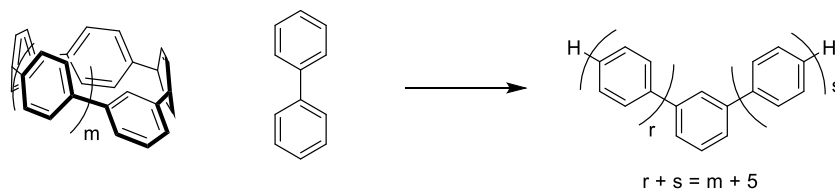


Table 2.8. Single point energies of compounds used in homodesmotic reactions and calculated strain.

$m[n]$ CPP	m	r	s	nanohoop	biphenyl	linear product	strain (hartrees)	strain (kcal/mol)
5	1	3	3	-1155.146	-463.3164	-1618.625	0.162858	102.2
6	2	4	3	-1386.234	-463.3164	-1849.674	0.123644	77.6
7	3	4	4	-1617.313	-463.3164	-2080.735	0.105867	66.4
8	4	5	4	-1848.389	-463.3164	-2311.795	0.090321	56.7
10	6	6	5	-2310.563	-463.3164	-2773.961	0.081901	51.4
12	8	7	6	-2772.704	-463.3164	-3236.089	0.068955	43.3

Table 2.9. Calculated strain energy in $m[n]$ CPPs, *ipso* carbon deviation, and dihedral angle. $[n]$ CPP values in brackets.¹³⁸ It is noted that the strain for each aryl ring in $m[n]$ CPPs are not equivalent due to asymmetry. *ipso* carbon deviations are for phenylenes opposite to the *meta* phenylene in the nanohoop.

$m[n]$ CPP	Strain energy (kcal/mol)	Strain per aryl ring (kcal/mol)	Phenylene <i>ipso</i> carbon deviation from planarity (°)	Dihedral angle (°)
5	102 (119)	20 (24)	17.0 (15.8)	23
6	78 (97)	13 (16)	14.1 (12.6)	25
7	66 (84)	9 (12)	12.0 (10.9)	28
8	57 (72)	7 (9)	10.6 (9.3)	30
10	51 (58)	5 (6)	8.4 (7.7)	31
12	43 (48)	4 (4)	7.0 (6.2)	34

2.6 Bridge to Chapter III

This chapter describes how to improve the quantum yield of smaller cycloparaphenylenes by up to 65 fold and how to unlock fluorescence in smaller hoops that were previously non-fluorescent. This is an important step towards the use of CPPs in biology. The next chapter describes how to further tune CPP optical properties for biological applications by expanding their fluorescence further into the red.

CHAPTER III

RED-SHIFTING THE FLUORESCENCE EMISSION OF CYCLOPARAPHENYLENES

From Lovell, T. C.; Garrison, Z. R.; Jasti, R. Synthesis, Characterization and Computational Investigation of Bright Orange-emitting Benzothiadiazole [10]Cycloparaphenylene. *Angew. Chem. Int. Ed.* **2020**, DOI: 10.1002/anie.202006350.

Conjugated aromatic macrocycles are attractive due to their unique photophysical and optoelectronic properties. In particular, the cyclic radially-oriented π -system of cycloparaphenylenes (CPPs) gives rise to photophysical properties unlike any other small molecule or carbon nanomaterial. CPPs have tunable emission, possess large extinction coefficients, wide effective Stokes shifts, and high quantum yields. However, accessing bright CPPs with emissions beyond 500 nm remains difficult. Herein, we present a novel and bright orange emitting CPP-based fluorophore showing a dramatic 105 nm red-shift in emission and striking 237 nm effective Stokes shift while retaining a large quantum yield of 0.59. We postulate, and experimentally and theoretically support, that the quantum yield remains large due to the lack of intramolecular charge transfer.

3.1 Introduction

Red-emitting fluorophores are desirable in biological applications because tissues scatter and absorb less light at longer wavelengths.⁶⁹ Longer wavelength (lower energy) light is also less damaging to cells. Additionally, a large Stokes shift will minimize self-quenching effects as well as increase signal-to-noise ratio for biological imaging.⁴ Large Stokes shifts also enable multicolor imaging, making it an important property to tune. Therefore, controllably manipulating the optical properties of fluorophores is crucial.

However, there remain inherent challenges with tuning the fluorescence of small molecules. Typically, the further red a fluorophore emits, the lower its quantum yield due to readily accessible non-radiative decay pathways. Additionally, increasing the conjugation of a system (a common strategy for inducing a red-shifting in emission)

generally results in a dramatic decrease in solubility, thus hampering its utility in materials or biological applications. Arguably the most difficult property to controllably and predictably tune is the Stokes shift, where there is a lack of reliable guidelines to follow.⁷¹ Cycloparaphenylenes (CPPs) have gained a lot of attention as novel fluorophores because they address some of these key issues. First, their unique structure results in an inherently large effective Stokes shift. Additionally, their curved architecture impedes the π - π stacking observed in their linear counterparts making them readily soluble in organic solvents.^{139,140} Finally, most CPPs are brighter than similar emitting small molecule fluorophores and CPPs retain their fluorescent properties in aqueous media owing to their attractiveness as novel fluorophores.^{5,66,68,141} However, bright CPPs with emissions beyond 500 nm have yet to be realized. CPP fluorescence red-shifts as the size of the nanohoop decreases. However, decreasing size leads to a dramatic decrease in quantum yield due to orbital symmetry rules.¹²⁰ For example, **[10]CPP** has a quantum yield of 0.46 or 0.65 (depending on report), compared to 0.007 for **[7]CPP** (**Figure 3.1**).^{119,132,133} Therefore, decreasing the size trades brightness for a red-shift in emission. Alternatively, one of the most successful approaches to influence the HOMO and LUMO energies (i.e. tune the fluorescence) of a molecule is incorporation of electron donor and acceptor units into the molecule.^{142–144} Simultaneously Jasti and Itami reported different donor-acceptor CPPs with electron acceptor units (**[10]CPTcaq** and **aza[8]CPP**, Figure 1).^{81,145} However, all of these molecules remain plagued by low quantum yields.

Herein, we present the first CPP where quantum yield is not sacrificed for red-shifting the emission. **BT[10]CPP** (**Figure 3.1**), a **[10]CPP** analog containing a single benzothiadiazole (BT) moiety, was synthesized and characterized. The inclusion of a BT unit into the CPP backbone dramatically red-shifts the **[10]CPP** emission profile by over 100 nm. The absorbance maximum of **BT[10]CPP** is virtually identical to the parent **[10]CPP**, resulting in a remarkable increase in effective Stokes shift (difference between the dominant absorption and emission maxima). Remarkably, the **BT[10]CPP** quantum yield is essentially unaffected. We investigate this phenomenon experimentally and computationally to gain an understanding of this outcome. Through this work, we establish **BT[10]CPP** as the brightest orange nanohoop in this rapidly growing class of molecules.

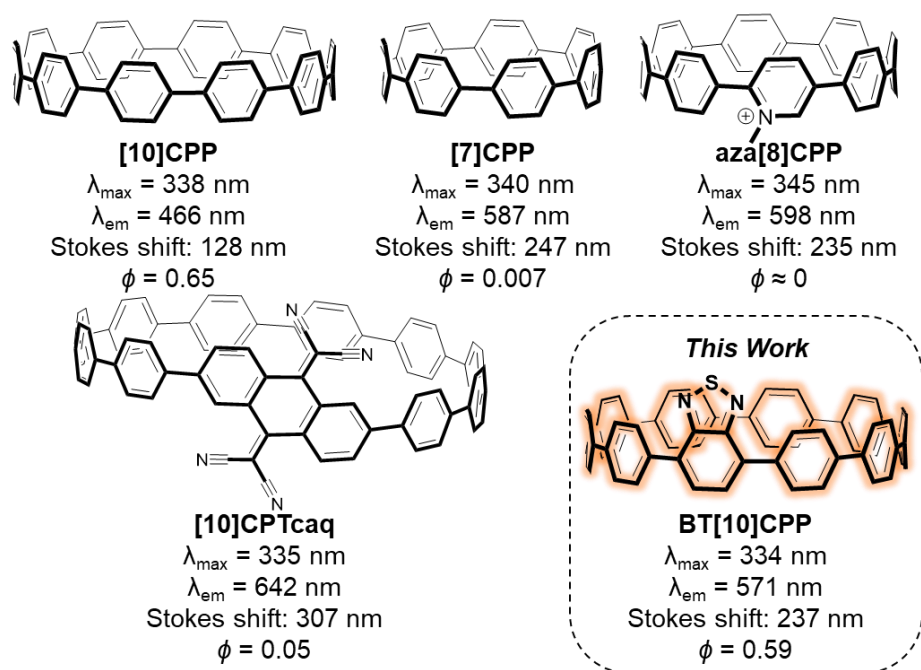


Figure 3.1. [10]CPP, furthest red-emitting nano hoops, and novel **BT[10]CPP**.

3.2 Synthesis

The strongly withdrawing BT moiety is well established to effectively red-shift the emission of conjugated polymers.^{146–148} Thus, we set out to determine if the nano hoop emission could be tuned through BT moiety incorporation. The BT unit was incorporated into a [10]CPP scaffold via Suzuki macrocyclization of **III.1** and 4,7-dibromobenzo[*c*]-1,2,5-thiadiazole to yield macrocycle **III.2a**. Triethylsilyl deprotection and mild reductive aromatization¹⁴⁹ afforded **BT[10]CPP**. A linear BT incorporated control, **III.3**, was synthesized for photophysical comparison through Suzuki coupling of 4,7-dibromobenzo[*c*]-1,2,5-thiadiazole and 4-methylphenylboronic acid pinacol ester. Synthesis of a smaller **BT[8]CPP** was also attempted. Macrocycle **III.4** was successfully synthesized in a similar fashion as **III.2a**, however, decomposition of **III.4** was observed. Additionally, multiple attempts to access the final **BT[8]CPP** through reductive aromatization were unsuccessful. We note that when H_2SnCl_4 solution was added to **III.4** a deep red color was observed, which quickly changed to orange. This color change may indicate formation of the desired **BT[8]CPP**, followed by rapid decomposition. We suspect that the instability of this molecule is the result of a high degree of strain in the smaller CPP (discussed below). **BT[10]CPP** and **III.3** were characterized by NMR (^1H

and ^{13}C), IR, and mass spectrometry, and further analyzed by UV-Vis, fluorescence and cyclic voltammetry.

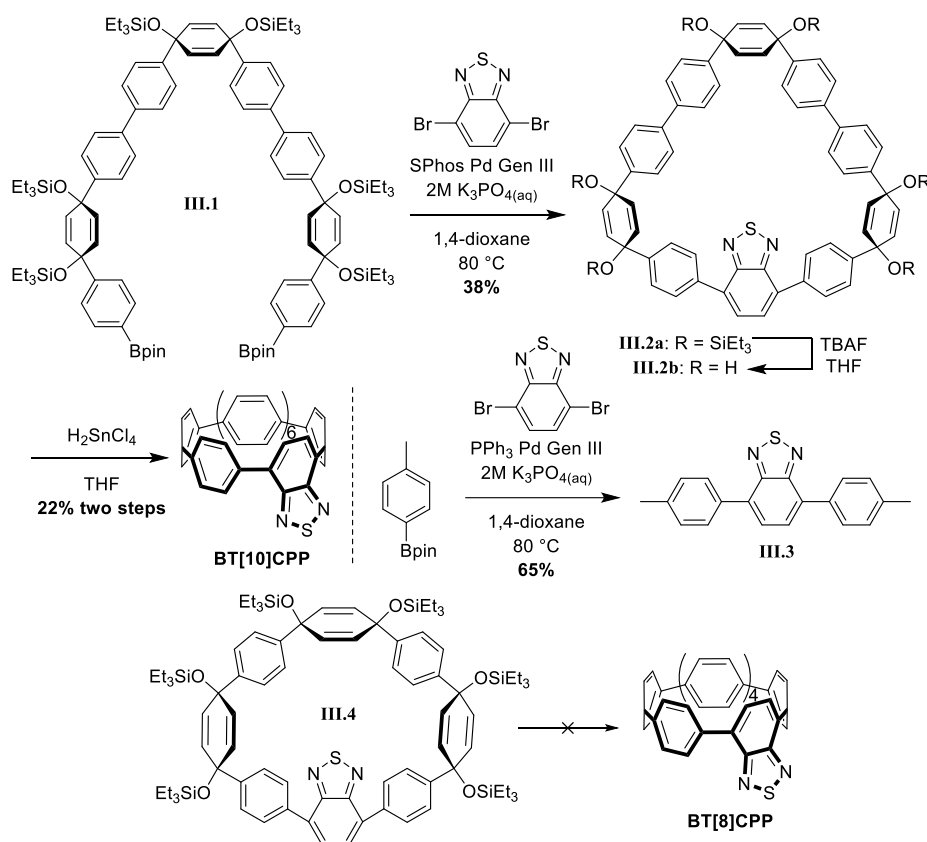


Figure 3.2. Synthesis of **BT[10]CPP**, linear BT system **III.3**, and attempted synthesis of **BT[8]CPP**.

We suspected that the instability of **BT[8]CPP** was the result of a high degree of strain in the smaller CPP. To quantify the strain energy in **BT[10]CPP** and **BT[8]CPP**, a strain analysis program (StrainViz) recently developed by our group was employed.¹⁵⁰ The total strain of each BT-containing CPP is almost identical to the analogous $[n]$ CPP (**Figure 3.17**). **[10]CPP** has a total strain of 57.4 kcal/mol versus 55.6 kcal/mol for **BT[10]CPP**. **[8]CPP** has a total strain of 70.5 kcal/mol versus 70.2 kcal/mol for **BT[8]CPP**. Notably, there is 58% more strain per phenylene in **BT[8]CPP** (8.77 kcal/mol) versus **BT[10]CPP** (5.56 kcal/mol). The significant (3.2 kcal/mol) increase in strain on the BT moiety of **BT[8]CPP** likely causes the observed decomposition. When compared to a typical CPP phenylene unit, the BT unit should have more diene character,

and thus the increased reactivity maybe another example of the effect of CPP ring size on strain-promoted reactions.^{151–153}

3.3 Photophysical properties

We next characterized the photophysical properties of **BT[10]CPP** to determine the consequences of incorporating a BT unit into the **[10]CPP** scaffold. The maximum absorption of **BT[10]CPP** was observed at 334 nm (**Figure 3.3a**), exhibiting a minor 4 nm blue-shift compared to the parent **[10]CPP**.¹⁵⁴ A similar small blue-shift in absorption is observed in other symmetry broken nanohoops.^{81,141} The extinction coefficient at the 334 nm absorbance maximum of **BT[10]CPP** ($5.4 \times 10^4 \text{ M}^{-1} \text{ cm}^{-1}$) was an order of magnitude higher than that of **III.3** ($7.6 \times 10^3 \text{ M}^{-1} \text{ cm}^{-1}$), but lower than **[10]CPP** ($1.3 \times 10^5 \text{ M}^{-1} \text{ cm}^{-1}$).¹¹⁹ The lower extinction coefficient relative to **[10]CPP** is unsurprising as it has been observed in the $m[n]$ CPPs, which also possess broken symmetry. Additionally, the broken symmetry of **BT[10]CPP** results in a second absorption band at 445 nm (**Figure 3.3a**), which correlates to a HOMO→LUMO transition (**Figure 3.12**) that is forbidden in the centrosymmetric all-hydrocarbon CPPs.^{120,141} The extinction coefficient of this second transition at 445 nm was found to be $8.6 \times 10^3 \text{ M}^{-1} \text{ cm}^{-1}$, far lower than the absorbance maximum at 334 nm. Time-dependent density-functional theory (TD-DFT) assigned the UV/Vis absorption bands. The calculations show the HOMO→LUMO absorption band is at 445 nm. The major absorption transition at 334 nm has contributions from the HOMO→LUMO+2, HOMO–4→LUMO and HOMO–4→LUMO (**Figure 3.12**).

In contrast to the relatively minor alterations in absorbance, BT unit insertion markedly affected the emission properties. **BT[10]CPP** emission maximum resides at 571 nm (**Figure 3.3a**), representing a remarkable 105 nm red shift in emission versus **[10]CPP** (466 nm).¹⁵⁴ As a result of this red shifted emission, **BT[10]CPP** exhibits a greatly increased effective Stokes shift (237 nm, 12427 cm^{-1}) compared to **[10]CPP** (128 nm, 7953 cm^{-1}). Despite this, **BT[10]CPP** has a quantum yield of 0.59, within the range of reported values of **[10]CPP** (0.46¹⁵⁵ and 0.65¹⁵⁶) and close to **III.3** (0.63). This was surprising considering other red-shifted nanohoops with electron accepting moieties have resulted in poor quantum yields. For example, **[10]CPTcaq** has a quantum yield of 0.05

and **aza[8]CPP** is almost non-emissive.^{81,145} Thus, **BT[10]CPP** currently represents the brightest orange nanohoop fluorophore. To deconvolute the BT moiety contributions to the **BT[10]CPP** photophysical properties, we also compared to control compound **III.3**. Fluorescence spectroscopy of **III.3** revealed an emission maximum at 505 nm, 66 nm less than that of **BT[10]CPP**. This suggests the curved nanohoop backbone contributes significantly to the observed emission of **BT[10]CPP**.

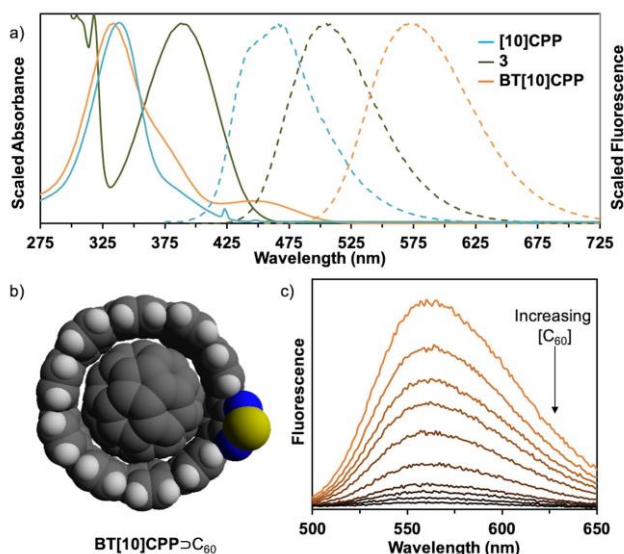


Figure 3.3. a) Experimental absorbance (solid line) and emission (dashed line) of **BT[10]CPP** and comparison to **[10]CPP** and **III.3** in dichloromethane. b) **BT[10]CPP⊃C₆₀** space filling model and c) **BT[10]CPP** fluorescence quenching by C₆₀.

One interesting property of **[10]CPP** is its ability to host C₆₀ with a high binding constant. A unique shape complementary host-guest interaction is formed where the intense fluorescence of **[10]CPP** is completely quenched by C₆₀ binding.¹¹³ We explored the host-guest properties of **BT[10]CPP** with C₆₀ by fluorescence-quenching experiments (**Figure 3.3b-c**). Although the fluorescence properties of the new **[10]CPP**-derivative have been drastically altered, the binding constant (k_a) for **BT[10]CPP** remains high at $(2.06 \pm 0.08) \times 10^6 \text{ L}^{-1} \text{ mol}^{-1}$. This work and others suggest that a wide variety of fullerene hosts can be designed from the basic **[10]CPP** scaffold.¹⁵⁷

3.4 Computational analysis

To further explore the novel photophysical properties of **BT[10]CPP**, time-dependent density-functional theory (TD-DFT) calculations were performed (using Gaussian 09 at the CAM-B3LYP/6-31G* level of theory with dichloromethane as the solvent) to analyze its electronic structure and absorption transition. The calculated frontier molecular orbitals of **BT[10]CPP**, **[10]CPP** and **[10]CPTcaq** are shown in **Figure 3.4**. The S_1 is the lowest lying excited state exhibited in CPPs, which shows exciton localization over seven phenylenes.¹²⁰ Both the S_1 (−1.92 eV) and HOMO (−6.53 eV) energies of **BT[10]CPP** were lower than those of **[10]CPP** (−1.14 and −6.47 eV, respectively). The significantly smaller S_1 →HOMO gap exhibited by **BT[10]CPP** determined by our calculations corroborates with the observed red-shifting in fluorescence. Interestingly, the HOMOs of both **[10]CPP** and **BT[10]CPP** are delocalized evenly around the hoop. However, the S_1 (and LUMO) of **BT[10]CPP** is localized on the benzothiadiazole moiety. The resulting HOMO-LUMO orbital separation results in an allowed HOMO→LUMO transition, which is observed at 445 nm in the UV-Vis spectrum of **BT[10]CPP**. The frontier molecular orbitals provide insight into the difference in quantum yields of **BT[10]CPP** and **[10]CPTcaq**.

As mentioned previously, a particularly anomalous discovery is the high quantum yield of **BT[10]CPP** despite a dramatically red-shifted emission. Based on experimental results and theoretical studies, we hypothesize that the high quantum yield is due to a lack of intramolecular charge transfer (ICT). Unlike **[10]CPP** and **BT[10]CPP**, the HOMO of **[10]CPTcaq** is localized on the phenylene backbone. The resultant HOMO and S_1 orbital separation indicates the **[10]CPTcaq** is a donor-acceptor molecule whereas **BT[10]CPP** and **[10]CPP** are not. Many donor-acceptor molecules exhibit ICT, which can decrease quantum yield.¹⁵⁸ Excited state TD-DFT calculations were used to analyze the fluorescence transitions of **[10]CPP**, **BT[10]CPP**, and **[10]CPTcaq**. The major fluorescence contribution of the S_1 → S_0 transition for **BT[10]CPP** and **[10]CPP** is dominated by LUMO→HOMO contributions (**Figure 3.14** and **3.15**). On the other hand, in **[10]CPTcaq** the major contribution is not from the LUMO→HOMO, but a mix of LUMO→HOMO, LUMO→HOMO−2 and LUMO→HOMO−1 contributions (**Figure 3.16**). This suggests that **BT[10]CPP** and **[10]CPP** fluoresce through a different

mechanism than **[10]CPTcaq**. This is supported experimentally with fluorescence lifetime analysis. The fluorescence lifetime of **BT[10]CPP** shows monoexponential decay with a lifetime of 7.4 ns, similar to **[10]CPP** (6.6 ns)¹⁵⁵, indicating fluorescence through a similar mechanism. Finally, solvatochromism studies show ICT as a fluorescence emission pathway in **[10]CPTcaq**.⁸¹ Charge transfer emissions undergo strong red-shifting with an increase of solvent polarity.^{159,160} In contrast, **BT[10]CPP** does not show solvatochromism (**Figure 3.5**), indicating no ICT. With the experimental and theoretical evidence given, it is concluded that the absence of ICT in this nanohoop retains the quantum yield.

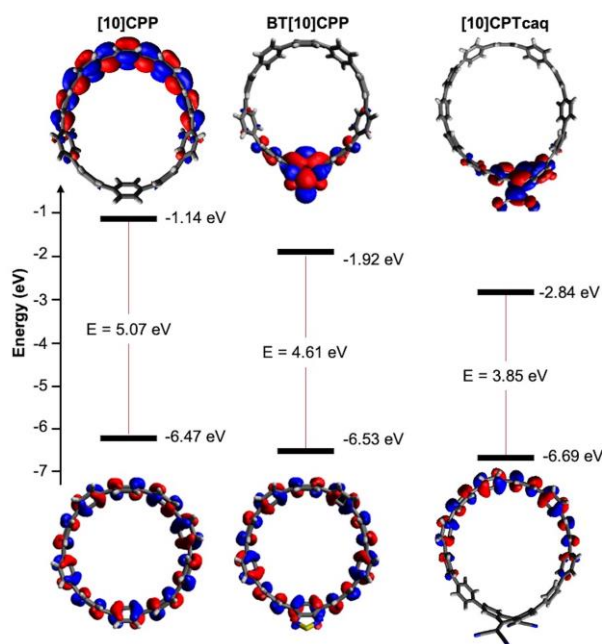


Figure 3.4. HOMO and S1' of **[10]CPP**, **BT[10]CPP** and **[10]CPTcaq** calculated at CAM-B3LP/6-31G* with dichloromethane as the solvent.

3.5 Conclusions

In summary, we show the incorporation of a BT unit into the **[10]CPP** backbone allows the marked red-shifting of emission while retaining the high quantum yield of the parent CPP, resulting in the brightest orange nanohoop synthesized to date. Theoretical calculations and experimental results elucidate that **BT[10]CPP** does not undergo ICT, rather it is more electronically similar to the parent **[10]CPP**. Given that the donor-acceptor nanohoos synthesized experience both ICT and a severe drop in quantum yield, we conclude that retaining the electronic structure of the parent CPP is critical in

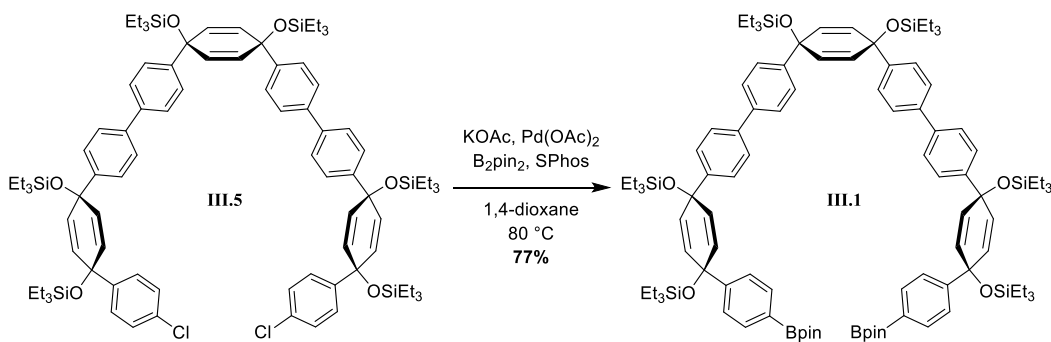
designing bright red-emitting nanohoops. Understanding and controlling these competing photophysical pathways is important for designing bright emitting nanohoops with a variety of emission wavelength. We anticipate these nanohoops will be especially useful as biological fluorophores and further studies will be reported in due time.

3.6 Experimental section

3.6.1 General experimental details and synthesis

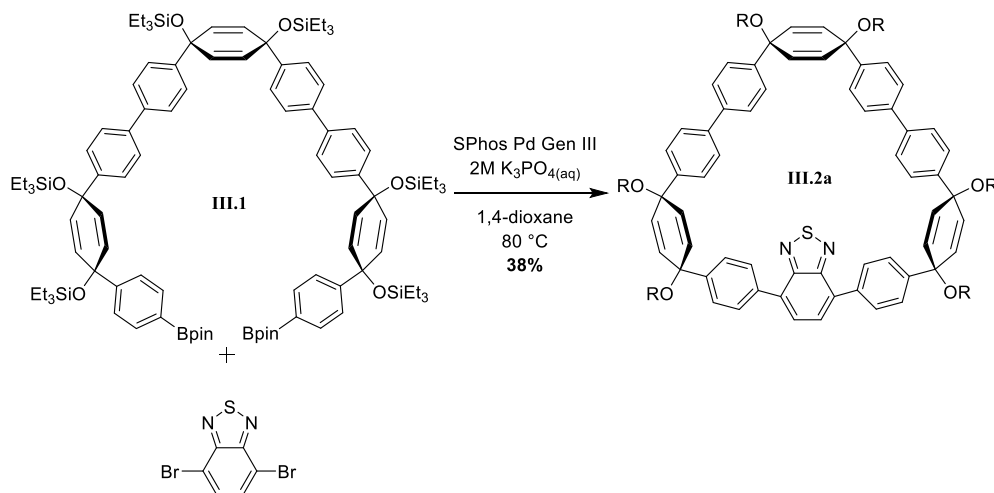
All glassware was flame dried and cooled under an inert atmosphere of nitrogen unless otherwise noted. Moisture sensitive reactions were carried out under nitrogen atmosphere using Schlenk and standard syringe/septa techniques. Tetrahydrofuran, dichloromethane, and 1,4-dioxane were dried by filtration through alumina according to the methods describes by Grubbs.¹³⁴ Silica column chromatography was conducted with Zeochem Zeoprep 60 Eco 40-63 μm silica gel. Automated flash chromatography was performed using a Biotage Isolera One. Recycling gel permeation chromatography (GPC) was performed using a Japan Analytical Industry LC-9101 preparative HPLC with JAIGEL-1H/JAIGEL-2H columns in series using CHCl_3 . Thin Layer Chromatography (TLC) was performed using Sorbent Technologies Silica Gel XHT TLC plates. Developed plates were visualized using UV light at wavelengths of 254 and 365 nm. ^1H NMR spectra were recorded at 500 MHz or 600 MHz on a Bruker Advance-III-HD NMR spectrometer. ^{13}C NMR spectra were recorded at 150 or 126 MHz on a Bruker Advance-III-HD NMR spectrometer. All ^1H NMR spectra were taken in CDCl_3 (referenced to TMS, δ 0.00 ppm). All ^{13}C NMR spectra were taken in CDCl_3 (referenced to chloroform, δ 77.16 ppm). Infrared absorption (IR) spectra were recorded on a Thermo Scientific Nicolet 6700 spectrometer equipped with a diamond crystal Smart ATR. Characteristic IR absorptions are reported in cm^{-1} . Mass spectra were obtained from the University of Oregon CAMCOR using ASAP. Absorbance and fluorescence spectra were obtained in a 1 cm Quartz cuvette with dichloromethane using an Agilent Cary 100 UV-Vis spectrometer and a Horiba Jobin Yvon Fluoromax-4 Fluorimeter. Fluorescent quantum yield of **BT[10]CPP** was measured in dichloromethane at room temperature using a Hamamatsu absolute PL quantum yield measurement system. Fluorescent quantum yield of **III.3** was measured in dichloromethane at room temperature as described by Jobin

Yvon Horiba with anthracene (ethanol) and quinine sulfate (0.1 M H₂SO₄) as standards. The integrated fluorescence region for **III.3** was 450-600. Fluorescence lifetimes were measured in dichloromethane using a Horiba Jobin Yvon TempPro Fluorescence Lifetime System. A LUDOX® prompt was used and decay curves were fit to a single exponential function. Electrochemical experiments were performed using a Biologic SP-50 potentiostat with a Ag wire reference electrode, Pt wire counter electrode, and glassy carbon working electrode under nitrogen atmosphere in 100 mM solutions of Bu₄NPF₆ in dichloromethane (DCM) with ferrocene reference. All reagents were obtained commercially unless otherwise noted. Compounds **III.5**¹⁴¹, **III.6**⁶⁶, PPh₃ Pd¹³⁶ Gen III and SPhos Pd Gen III¹³⁶ were prepared according to literature procedure.



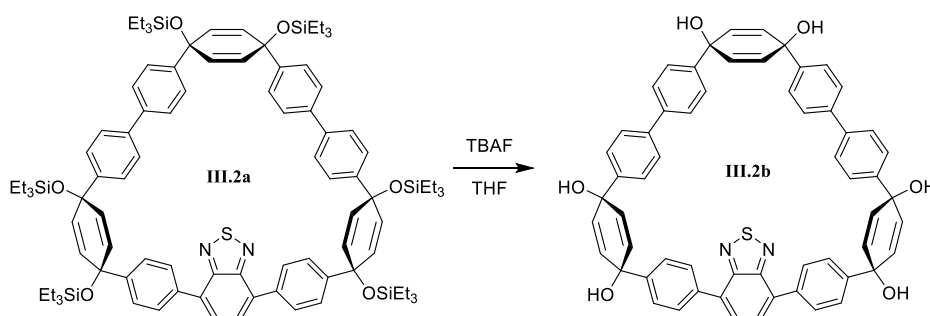
III.1. Oven-dried potassium acetate (390 mg, 4.0 mmol, 6.6 equiv) was added to a flame-dried 25 mL round bottom flask equipped with a stir bar. The KOAc and round bottom flask were flame-dried again under vacuum until all apparent moisture was removed. Pd(OAc)₂ (6.8 mg, 0.030 mmol, 0.05 equiv), SPhos (30.9 mg, 0.075 mmol, 0.125 equiv), B₂Pin₂ (611.4 mg, 2.4 mmol, 4 equiv) and **III.5** (0.9291 g, 0.60 mmol, 1 equiv) were added to the round bottom and the flask was put under vacuum for 2 hours. 1,4-dioxane (2.0 mL) was added and the reaction mixture was sparged for 20 minutes. It was then placed in a preheated oil bath at 80 °C and allowed to stir overnight. Ethyl acetate was added to the reaction mixture and it was sonicated. This was filtered through a fritted suction funnel filled with Celite, protected with filter paper. The round bottom was rinsed several times with ethyl acetate and sonicated. The filtrate was concentrated to yield the crude product. Ethanol (10 mL) was added and it was sonicated to yield the product, **III.1**, as white solid (795 mg, 77%). ¹H NMR (500 MHz, Chloroform-d) δ 7.74 (d, J = 7.6 Hz, 4H), 7.57 – 7.49 (m, 7H), 7.46 (d, J = 8.2 Hz, 4H), 7.43 – 7.38 (m, 8H), 6.09 – 6.01 (m, 11H), 1.34 (s, 24H), 0.97 (m, J = 7.9 Hz, 54H), 0.64 (m, J = 16.0, 11.0, 7.9 Hz,

36H). ^{13}C NMR (151 MHz, CDCl_3) δ 149.16, 145.07, 144.96, 139.60, 139.55, 134.70, 131.60, 131.48, 131.29, 126.80, 126.76, 126.25, 126.20, 125.23, 83.72, 71.53, 71.34, 24.85, 7.09, 7.07, 7.06, 6.46, 6.44. HRMS (ASAP) (m/z): $[\text{M}+\text{H}]$ calculated for $\text{C}_{102}\text{H}_{150}\text{B}_2\text{O}_{10}\text{Si}_6$, 1725.0031; found, 1726.0386. IR (neat) 2953.67, 2875.00, 1359.10, 1069.17, 1003.45, 725.96 cm^{-1} .

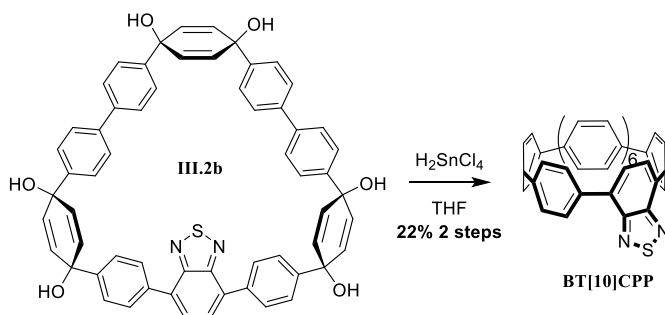


III.2a. 4,7-Dibromobenzo[c]-1,2,5-thiadiazole (124 mg, 0.42 mmol, 1 equiv), **III.1** (764.7 mg, 0.443 mmol, 1.05 equiv) and Sphos Pd Gen III (33.6 mg, 0.0422 mmol, 0.1 equiv) were added to a 250 mL round bottom flask equipped with a stir bar. The flask was evacuated (5 minutes) and purged with nitrogen 5 times. 1,4-dioxane and K_3PO_4 were sparged for at least 1 hour prior to use. The round bottom flask was equipped with a septa and 1,4-dioxane (141 mL) was added to the round bottom flask and the solution was sparged for 30 minutes. The round bottom flask was placed in a preheated oil bath (80 °C) for 10 minutes then K_3PO_4 (14 mL, 2 M in deionized water) was added. The reaction was allowed to stir at 80 °C overnight. The reaction mixture was allowed to cool to room temperature and was filtered through. The round bottom flask was rinsed with dichloromethane and filtered through the Celite plug. The filtrate was dried over sodium sulfate and concentrated. The product was purified by automated flash silica gel chromatography (0% to 60% dichloromethane in hexanes). The product was sonicated in acetone to yield the product **III.2a** as a yellow solid (257 mg, 38%). ^1H NMR (600 MHz, Chloroform-d) δ 7.88 (d, $J = 8.4$ Hz, 4H), 7.78 (s, 2H), 7.51 (dd, $J = 8.4, 3.2$ Hz, 8H), 7.45 (d, $J = 8.5$ Hz, 8H), 7.32 (d, $J = 8.4$ Hz, 4H), 6.11 (d, $J = 10.1$ Hz, 4H), 6.02 (d, $J =$

10.1 Hz, 4H), 6.01 (s, 5H), 0.99 (td, $J = 7.9, 5.8$ Hz, 40H), 0.95 – 0.89 (m, 33H), 0.68 (qd, $J = 7.9, 3.6$ Hz, 28H), 0.58 (q, $J = 7.9$ Hz, 19H). ^{13}C NMR (151 MHz, CDCl_3) δ 154.07, 145.80, 145.59, 144.71, 139.42, 136.40, 132.91, 131.70, 131.54, 131.50, 128.90, 128.23, 126.72, 126.51, 126.47, 126.32, 126.16, 71.85, 71.80, 70.57, 7.10, 7.07, 6.54, 6.50, 6.47, 6.3. HRMS (ASAP) (m/z): $[\text{M}+\text{H}]$ calculated for $\text{C}_{96}\text{H}_{128}\text{N}_2\text{O}_6\text{SSi}_6$, 1604.8109; found, 1605.8112. IR (neat) 2951.83, 2909.21, 2879.98, 1488.82, 1456.90, 1412.99, 731.36 cm^{-1} .

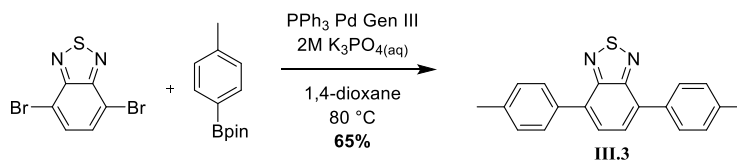


III.2b. Tetrahydrofuran (0.8 mL) was added to **III.2a** (120.6 mg, 0.080 mmol, 1 equiv) and the vial was equipped with a stir bar and septa. Tetra-*n*-butylammonium fluoride (0.8 mL, 0.8 mmol, 10 equiv, 1 M in tetrahydrofuran) was added to the reaction flask and this was allowed to stir for 1 h at room temperature. The reaction was quenched with deionized water (10 mL) causing the product to precipitate. The resulting solution was filtered with a Büchner funnel, washed with deionized water and dichloromethane yielding **III.2b** as a yellow solid. The crude product was used as is for the following reaction.



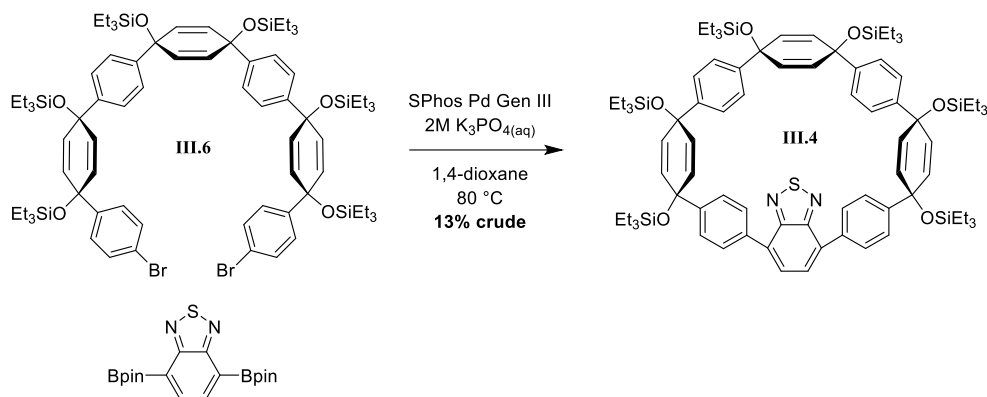
BT[10]CPP. $\text{SnCl}_2 \cdot \text{H}_2\text{O}$ (181 mg, 0.80 mmol) was added to a 100 mL round bottom flask equipped with a stir bar and septum. Tetrahydrofuran (20 mL) was added followed

by hydrochloric acid (0.13 mL, 1.6 mmol, 12 M). This was allowed to stir at room temperature for 30 minutes. **III.2b** (10 mg, 0.01 mmol, 1 equiv) was added to a 0.2-0.5 mL microwave vial equipped with a stir bar and septum and was purged with nitrogen. H₂SnCl₂ solution (0.9 mL, 0.04 mmol, 3.3 equiv, 0.04 M) was added to and the reaction was allowed to stir for 30 minutes at room temperature. The reaction was quenched with saturated sodium bicarbonate (20 mL) and the product was extracted with dichloromethane (3 x 10 mL). The organic layers were washed with brine (1 x 50 mL), dried over sodium sulfate and concentrated. The product was purified by alumina preparatory plate (100% dichloromethane) to give the product as an orange solid (10.3 mg, 22% 2 steps). NMR ¹H NMR (500 MHz, Chloroform-*d*) δ 7.95 (d, *J* = 8.4 Hz, 4H), 7.64 – 7.52 (m, 32H), 7.45 (s, 2H). ¹³C NMR (126 MHz, CDCl₃) δ 154.27, 139.62, 138.47, 138.24, 138.19, 138.17, 138.11, 137.84, 136.07, 130.95, 130.64, 128.11, 127.44, 127.40, 127.37, 127.34, 127.29, 127.08. HRMS (ASAP) (*m/z*): [M] calculated for C₆₀H₃₈N₂S, 818.2756; found, 818.2206. IR (neat) 2956.24, 2924.39, 2873.08, 2854.32, 1726.85, 1463.96, 738.43 cm⁻¹.



III.3. 4-tolylboronic acid pinacol ester (212.9 mg, 0.98 mmol, 2.05 equiv), 4,7-Dibromobenzo[*c*]-1,2,5-thiadiazole (140 mg, 0.48 mmol, 1 equiv) and PPh₃ Pd Gen III (30.1 mg, 0.048 mmol, 0.1 equiv) were added to a 100 mL round bottom flask equipped with a stir bar. The round bottom was evacuated (5 minutes) and backfilled with nitrogen 5 times. 1,4-dioxane and K₃PO₄ were sparged for at least 1 hour prior to use. The flask was equipped with a septum and 1,4-dioxane (40 mL) was added and the solution was sparged for 30 minutes. The flask was put in an oil bath at 80 °C for 10 minutes then K₃PO₄ (16 mL, 2 M in deionized water) was added. The reaction was allowed to stir for 5 min until the reaction mixture turned deep green. This was filtered through Celite® and sodium sulfate. The round bottom flask was rinsed with dichloromethane (50 mL) and filtered through the plug. The filtrate was dried over sodium sulfate and concentrated. The product was purified by gel permeation chromatography to yield **III.3** as a yellow-

green solid (98 mg, 65%). ^1H NMR (500 MHz, Chloroform-*d*) δ 7.84 (dd, $J = 8.1, 1.6$ Hz, 4H), 7.73 (s, 2H), 7.34 (d, $J = 7.9$ Hz, 4H), 2.44 (s, 6H). ^{13}C NMR (151 MHz, CDCl₃) δ 154.23, 138.29, 134.66, 133.09, 129.38, 129.13, 127.79, 21.35. HRMS (ASAP) (m/z): [M+1] calculated for C₂₀H₁₆N₂S, 316.1034; found, 317.1112. IR (neat) 3027.17, 2915.53, 2360.21, 1907.44, 1610.56, 737.00.



III.4. 2,1,3-benzothiadiazole-4,7-bis(boronic acid pinacol ester) (67 mg, 0.17 mmol, 1.05 equiv), **III.6** (243 mg, 0.16 mmol, 1 equiv) and Sphos Pd Gen III (13 mg, 0.016 mmol, 0.1 equiv) were added to a 100 mL round bottom flask equipped with a stir bar. The flask was evacuated (5 minutes) and purged with nitrogen 5 times. 1,4-dioxane and K₃PO₄ were sparged for at least 1 hour prior to use. The round bottom flask was equipped with a septa and 1,4-dioxane (55 mL) was added to the round bottom flask and the solution was sparged for 20 minutes. The round bottom flask was placed in a preheated oil bath (80 °C) for 10 minutes then K₃PO₄ (5.4 mL, 2 M in deionized water) was added. The reaction was allowed to stir at 80 °C overnight. The reaction mixture was allowed to cool to room temperature and was filtered through. The round bottom flask was rinsed with dichloromethane and filtered through the Celite plug. The filtrate was dried over sodium sulfate and concentrated. The product was purified by automated flash silica gel chromatography (0% to 60% dichloromethane in hexanes) and gel permeation chromatography (chloroform). The product was not able to be isolated as a pure product due to decomposition (30 mg, 13% crude). ^1H NMR (600 MHz, Chloroform-*d*) δ 7.77 (d, $J = 8.3$ Hz, 4H), 7.65 (s, 2H), 7.31 (d, $J = 8.2$ Hz, 4H), 7.14 (d, $J = 8.2$ Hz, 4H), 6.96 (d, $J = 8.2$ Hz, 5H), 6.06 (d, $J = 9.8$ Hz, 4H), 6.04 (s, 4H), 5.95 (d, $J = 10.1$ Hz, 5H), 0.99 (td, $J = 7.9, 4.8$ Hz, 34H), 0.91 (dt, $J = 12.9, 7.9$ Hz, 40H), 0.70 – 0.65 (m, 21H), 0.58 (q, $J =$

7.9 Hz, 16H), 0.51 (q, $J = 8.0$ Hz, 13H). ^{13}C NMR (151 MHz, CDCl_3) δ 154.25, 145.98, 145.32, 144.08, 136.68, 133.31, 132.21, 132.10, 132.07, 131.84, 131.71, 131.60, 129.80, 129.19, 128.32, 128.09, 126.79, 126.71, 126.32, 126.26, 125.90, 125.78, 125.51, 125.24, 71.85, 71.82, 71.56, 71.51, 71.39, 69.50, 7.19, 7.08, 7.06, 7.02, 6.60, 6.58, 6.53, 6.50, 6.48, 6.47, 6.44, 6.34, 4.99 (decomposition product observed in ^{13}C NMR, cannot differentiate from product peaks).

3.6.2 Photophysical characterization

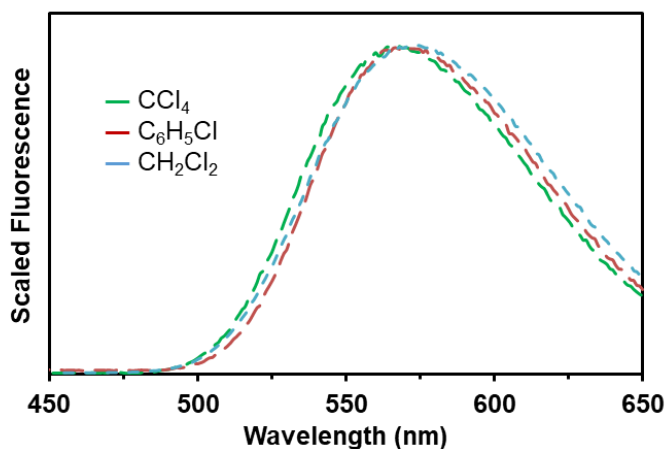


Figure 3.5. Fluorescence of BT[10]CPP in various solvents, excited at 334 nm.

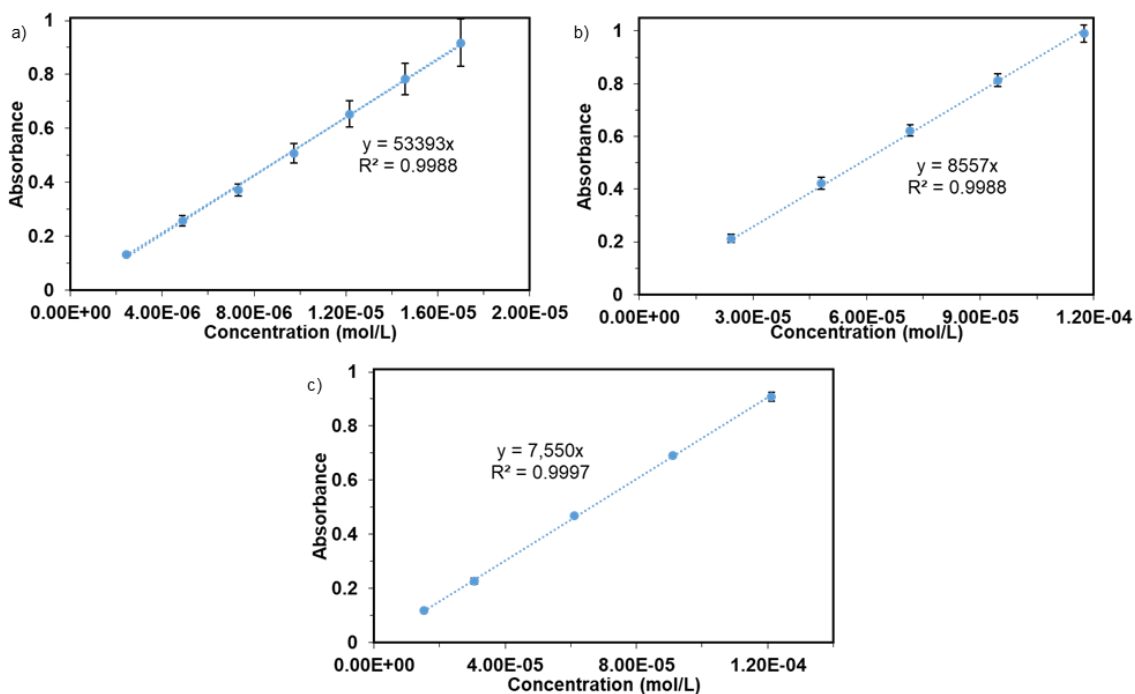


Figure 3.6. Absorbance versus concentration for extinction coefficient determination of **BT[10]CPP** at the a) absorbance maximum and b) HOMO→LUMO transition and c) extinction coefficient of **III.3**.

Table 3.1. Average extinction coefficient and error of **BT[10]CPP** at absorbance maximum and HOMO→LUMO transition and **III.3**.

Compound	Extinction Coefficient ($M^{-1}cm^{-1}$)
BT[10]CPP (λ_{max})	$(5.4 \pm 0.4) \times 10^4$
BT[10]CPP ($\lambda_{HOMO \rightarrow LUMO}$)	$(8.6 \pm 0.3) \times 10^3$
3	$(7.6 \pm 0.9) \times 10^3$

Table 3.2. Triplicate quantum yields, average quantum yield and error of **BT[10]CPP** and **III.3**.

Compound	Trial 1	Trial 2	Trial 3	ϕ
BT[10]CPP	0.594	0.596	0.588	0.593 ± 0.004
III.3	0.628	0.628	0.626	0.627 ± 0.001

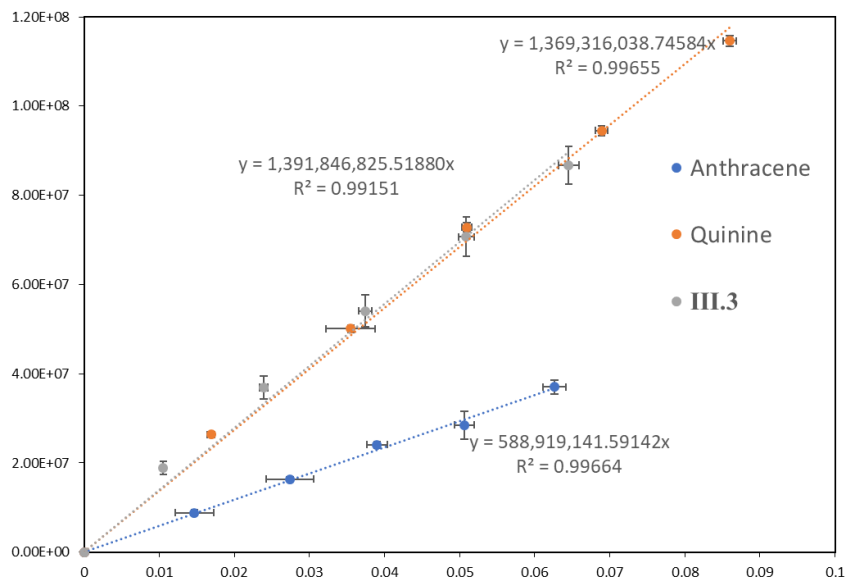


Figure 3.7. Experimental (circles) and fitted (dashed lines) triplicate data of the integrated fluorescence intensity vs absorbance of compound **III.3** (grey) and standards anthracene (blue) and quinine sulfate (orange) used to determine quantum yield.

Table 3.3. Fluorescence lifetimes of **BT[10]CPP** and **III.3** and calculated decay rates⁸⁷ of **BT[10]CPP**.

Compound	Lifetime (ns)	Rate of radiative decay (10⁷ s⁻¹)	Rate of non-radiative decay (10⁷ s⁻¹)
BT[10]CPP	7.40	8.01	5.50
III.3	10.9	5.78	3.39

3.6.3 C₆₀ Binding Constant

Fluorescence titration experiments were carried out in triplicate, a stock solution of C₆₀ in toluene was added to solutions of [10]CPP and BT[10]CPP in toluene at 25 °C. Both molecules were excited at 340 nm. Emission spectra were collected and the fluorescence signal was measured at 470 nm for [10]CPP and 571 nm for **BT[10]CPP**. The fluorescence enhancement (F/F₀) as a function of host concentration was studied. This data was then used to extract the binding constant based on the complexation model shown below. A 1:1 host:guest complexation was assumed based on previous work.¹¹³

$$\frac{F}{F_0} = \frac{1 + Ak[G]}{1 + k[G]}$$

F is the fluorescence intensity at each concentration of guest addition, F₀ is the fluorescence of the host without guest addition, [G] is guest concentration, A is a ratio of proportionality constants and k is the binding constant. A and k are treated as parameters and determined by Origin using non-linear curve fitting with the least squares method.^{113,161}

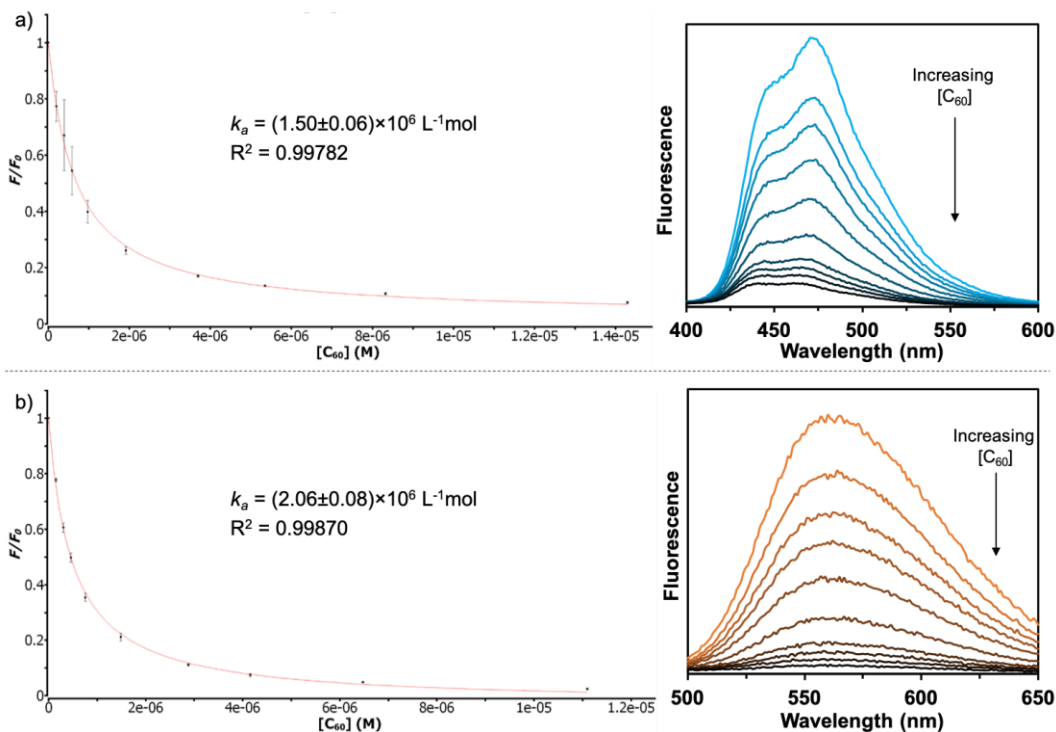


Figure 3.8. Fluorescence titration and binding curve of C_{60} and **[10]CPP** or **BT[10]CPP** in toluene. a) **[10]CPP** (5.52×10^{-7} mol/L) in the presence of C_{60} (5.00×10^{-5} mol/L) and b) **BT[10]CPP** (3.91×10^{-7} mol/L) in the presence of C_{60} (3.89×10^{-5} mol/L).

3.6.4. Electrochemical Analysis

BT[10]CPP has one reversible oxidation with an oxidation potential of 0.78 V and **III.3** has one reversible oxidation with an oxidation potential of 1.14 V and one reversible reduction with a reduction potential of -2.00 V in the electrochemical window of DCM. **BT[10]CPP** is expected to show a reduction within the electrochemical window of DCM similar to that seen with the test system. A possible reduction can be seen at -1.7 V (**Figure 3.9**), but a scan from which the reduction could be calculated was unable to be attained.

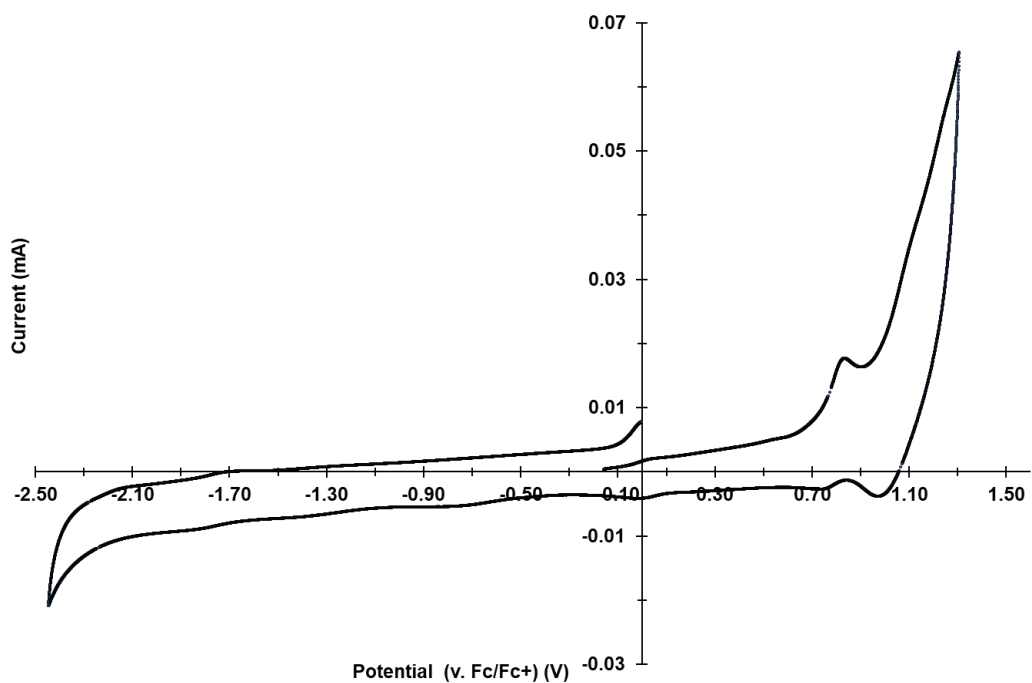


Figure 3.9. BT[10]CPP single reversible oxidation (DCM) $E = 0.78$ V.

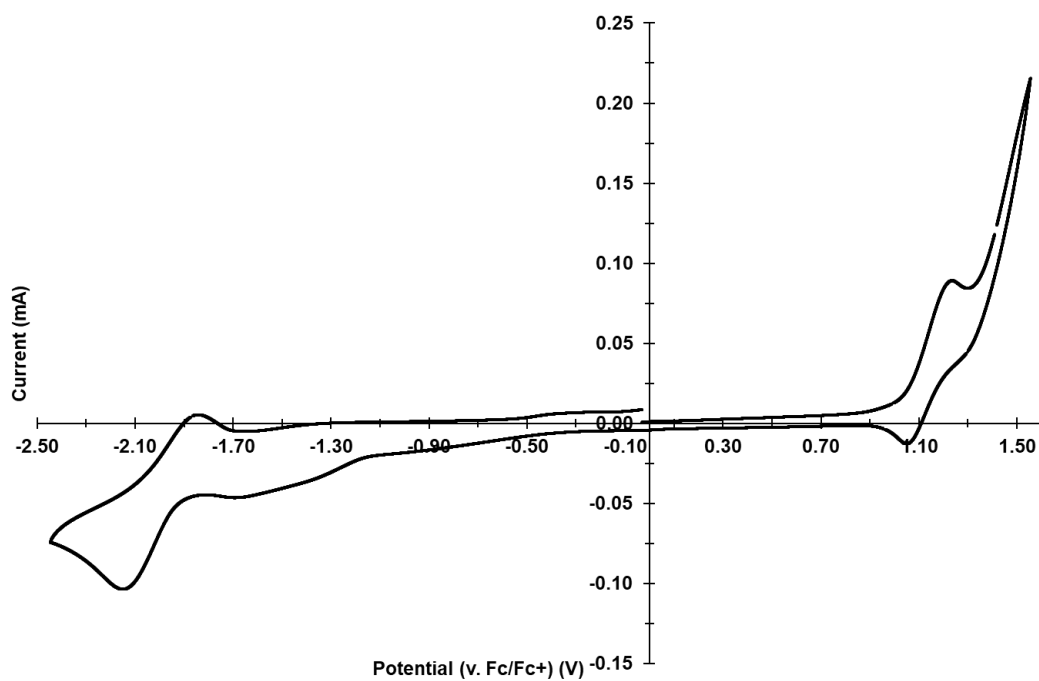


Figure 3.10. III.3 single reversible oxidation (DCM) $E = 1.14$ V and reduction (DCM) $E = -2.00$ V.

3.6.5. Computational Calculations

Geometries were optimized using Gaussian 09 (Frisch, M. J.; Trucks, G. W.; Schlegel, H. B.; Scuseria, G. E.; Robb, M. A.; Cheeseman, J. R.; Scalmani, G.; Barone, V.; Mennucci, B.; Petersson, G. A.; et al. Gaussian 09, Revision E.01. Gaussian, Inc.: Wallingford CT, 2013.). Geometry optimizations for absorbance calculations were done using the B3LYP functional and 6-31G* basis set. Geometry optimizations for HOMO and S_1 orbitals and fluorescence calculations were done using the CAM-B3LYP functional and 6-31G* basis sets and the effect of solvent was included by the polarizable continuum model (PCM) using dichloromethane as the solvent.

HOMO orbitals were analyzed from the CAM-B3LYP/6-31G* geometry optimization calculations. Using these optimized structures, a time dependent optimization was performed to determine the excited state geometry optimized structures (S_1 orbitals) using the CAM-B3LYP functional and 6-31G* basis sets and the effect of solvent was included by the polarizable continuum model (PCM) using dichloromethane as the solvent.

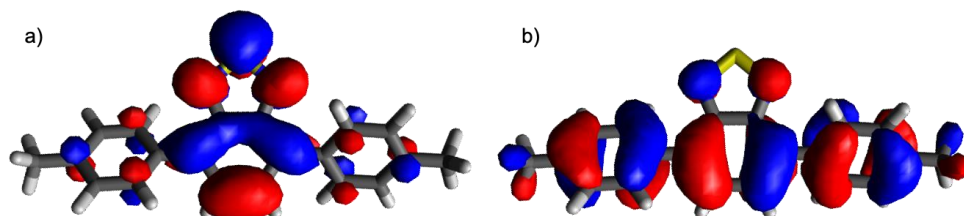
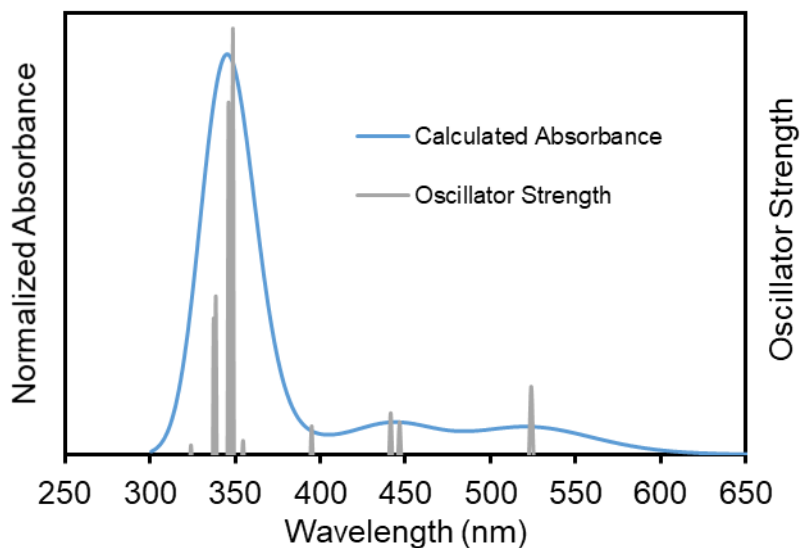


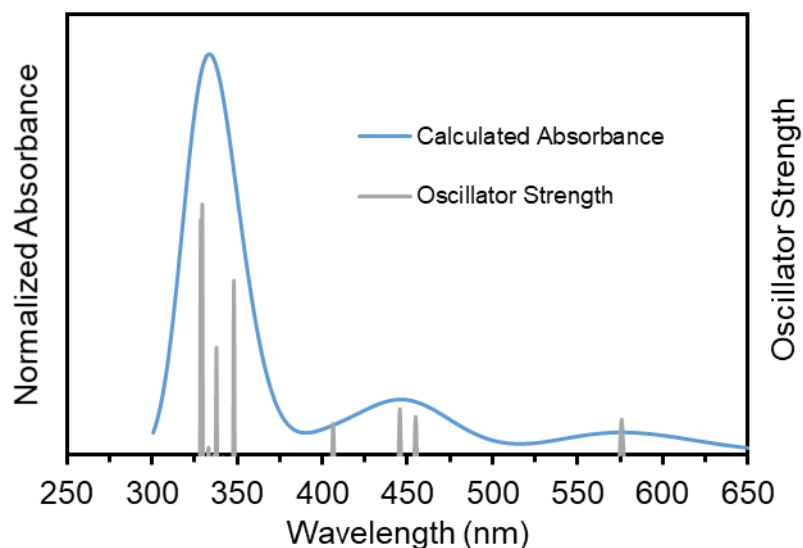
Figure 3.11. Calculated a) LUMO (-1.22 eV) and b) HOMO (-7.01 eV) orbitals of **III.3**.

UV/Vis spectra of **BT[10]CPP** and **BT[8]CPP** were calculated using the geometry optimized structures. Then, using B3LYP/6-31G(d,p) a time dependent calculation of 12 states was performed. The results were analyzed using GaussSum.



No	Energy (cm^{-1})	Wavelength (nm)	Osc. Strength	Major Contributions
1	19103.3736	523.46775	0.1941	HOMO→LUMO (93%)
2	22400.5909	446.416796	0.0986	H-1→LUMO (93%)
3	22634.4933	441.803573	0.123	H-2→LUMO (98%)
4	25337.2758	394.675421	0.0877	HOMO→L+1 (90%)
5	28198.9507	354.623124	0.0008	H-3→LUMO (95%)
6	28198.9507	354.623124	0.0484	H-4→LUMO (86%)
7	28712.7294	348.277583	1.1585	HOMO→L+2 (87%)
8	28938.5662	345.559622	0.9594	H-1→L+1 (90%)
9	29566.0699	338.225541	0.4376	H-2→L+1 (93%)
10	29666.8899	337.076115	0.3785	HOMO→L+3 (84%)
11	30939.6416	323.20995	0.0365	H-11→LUMO (18%), H-9→LUMO (10%), H-7→LUMO (38%), H-1→L+2 (18%)
12	31025.9435	322.310907	0.0048	H-12→LUMO (13%), H-10→LUMO (41%), H-8→LUMO (22%), H-6→LUMO (18%)

Figure 3.12. Calculated absorption spectrum and electronic transitions for **BT[10]CPP**.

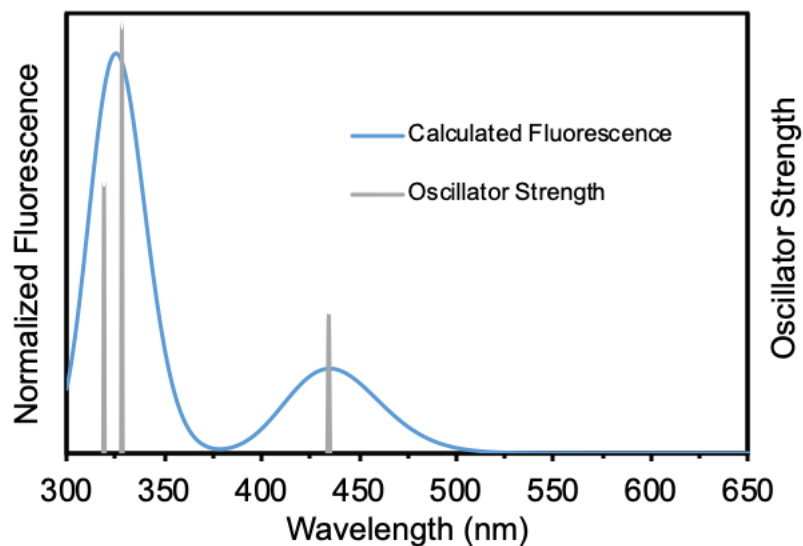


No.	Energy (cm ⁻¹)	Wavelength (nm)	Osc. Strength	Major contributions
1	17368.34	575.7602	0.1049	HOMO→LUMO (97%)
2	21997.97	454.5875	0.1125	H-1→LUMO (97%)
3	22448.83	445.4575	0.1333	H-2→LUMO (98%)
4	24620.88	406.1593	0.0939	HOMO→L+1 (95%)
5	28762.54	347.6745	0.4816	HOMO→L+2 (89%)
6	29248.08	341.9027	0.0022	H-8→LUMO (10%), H-6→LUMO (20%), H-3→LUMO (67%)
7	29606.19	337.7672	0.3003	H-1→L+1 (93%)
8	29741.69	336.2283	0.0087	H-7→LUMO (53%), H-5→LUMO (22%)
9	30032.05	332.9776	0.0296	H-8→LUMO (19%), H-6→LUMO (44%), H-3→LUMO (29%)
10	30051.41	332.7631	0.0023	H-4→LUMO (79%)
11	30388.55	329.0713	0.688	H-2→L+1 (84%)
12	30451.46	328.3915	0.6461	HOMO→L+3 (90%)

Figure 3.13. Calculated absorption spectrum and electronic transitions for **BT[8]CPP**.

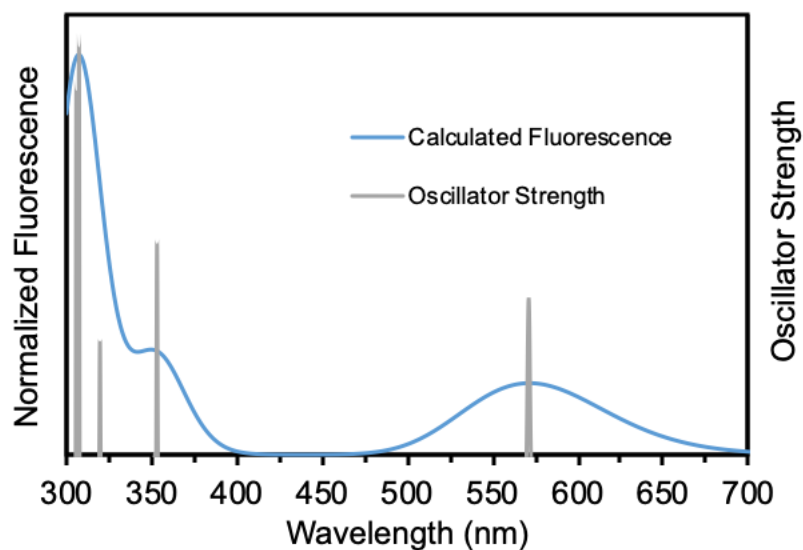
5. d) Fluorescence Calculations

Fluorescence spectra of **[10]CPP**, **BT[10]CPP** and **[10]CPTcaq** were calculated using the excited state geometry optimized structures. Using the CAM-B3LYP functional and 6-31G* basis sets a time dependent calculation of 12 states was performed and the effect of solvent was included by the PCM using dichloromethane as the solvent. The results were analyzed using GaussSum.



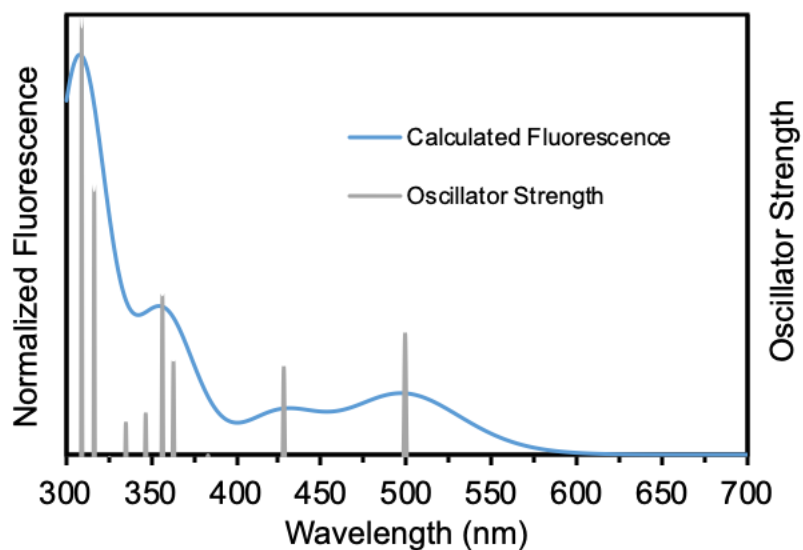
No.	Energy (cm-1)	Wavelength (nm)	Osc. Strength	Major contributions
1	22992.4471	434.925432	0.7212	HOMO→LUMO (85%)
2	30422.4265	328.704878	2.1996	H-2→LUMO (43%), HOMO→L+2 (39%)
3	31254.7907	319.950951	1.3828	H-1→LUMO (23%), H-1→L+1 (32%), HOMO→L+1 (21%)
4	34491.4936	289.926557	0.0011	H-2→LUMO (33%), HOMO→L+2 (36%)
5	34771.368	287.592942	0.0045	H-5→LUMO (10%), HOMO→L+5 (35%)
6	36343.3426	275.153558	0.1176	H-1→L+1 (20%)
7	36560.3057	273.520689	0.05	H-1→LUMO (17%), HOMO→L+6 (12%)
8	36578.0499	273.388002	0.1826	H-3→LUMO (15%), H-2→L+1 (23%), H-1→L+2 (24%), HOMO→L+3 (14%)
9	36998.2648	270.282946	0.0074	H-1→LUMO (28%), HOMO→L+1 (36%)
10	37743.5211	264.946134	0.0111	H-2→L+6 (14%)
11	38562.1738	259.32148	0.0067	H-13→LUMO (14%)
12	38658.1538	258.67764	0.0059	H-14→LUMO (10%), H-1→L+7 (21%)

Figure 3.14. Calculated fluorescence spectrum and electronic transitions for [10]CPP.



No.	Energy (cm-1)	Wavelength (nm)	Osc. Strength	Major contributions
1	17498.1983	571.487407	0.5054	HOMO→LUMO (92%)
2	28324.5784	353.050268	0.6758	H-4→LUMO (16%), H-2→LUMO (75%)
3	28397.1683	352.147787	0.0199	HOMO→L+1 (39%), HOMO→L+3 (23%)
4	31228.9809	320.21538	0.3671	H-1→LUMO (59%), HOMO→L+3 (14%)
5	32507.3697	307.622551	1.2968	H-2→L+1 (13%), HOMO→L+2 (54%)
6	32676.7461	306.028022	1.1598	H-1→L+1 (41%), HOMO→L+3 (14%)
7	33680.0998	296.911234	0.2172	H-16→LUMO (16%), H-12→LUMO (13%), H-7→LUMO (24%)
8	34732.6534	287.913506	0.0019	H-13→LUMO (27%), H-10→LUMO (13%), H-8→LUMO (16%), H-6→LUMO (18%)
9	35519.8505	281.532716	0.0026	H-19→LUMO (10%), H-14→LUMO (10%), H-3→LUMO (43%), H-1→LUMO (14%)
10	35612.6043	280.799459	0.1894	H-16→LUMO (43%), H-7→LUMO (14%)
11	36252.2019	275.845313	0.0016	H-15→LUMO (11%), H-4→LUMO (46%), H-2→LUMO (13%)
12	36387.7031	274.818116	0.0006	H-20→LUMO (10%), H-19→LUMO (52%), H-3→LUMO (13%)

Figure 3.15. Calculated fluorescence spectrum and electronic transitions for **BT[10]CPP**.

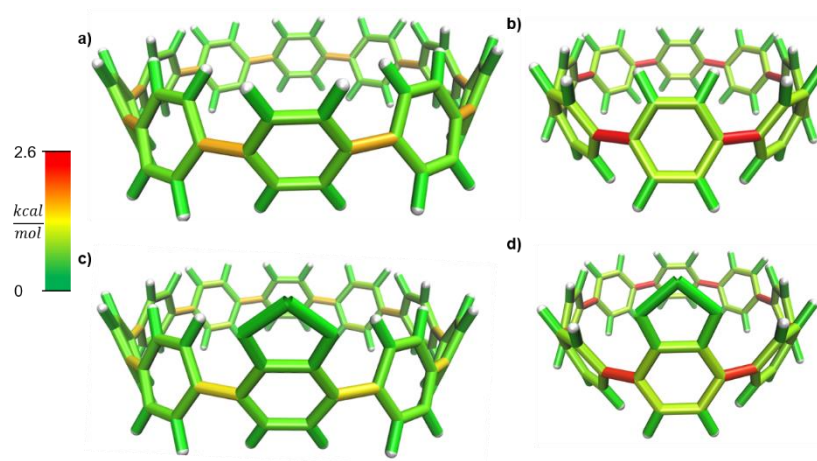


No.	Energy (cm-1)	Wavelength (nm)	Osc. Strength	Major contributions
1	20056.589	498.589267	0.4764	H-2→LUMO (25%), H-1→LUMO (28%), HOMO→LUMO (26%)
2	23382.0129	427.679176	0.3479	H-4→LUMO (12%), H-3→LUMO (22%), H-2→LUMO (17%), H-1→LUMO (31%)
3	26108.9734	383.01008	0.0141	H-2→LUMO (10%), HOMO→LUMO (69%)
4	27535.7682	363.16401	0.3662	H-5→LUMO (37%), H-3→LUMO (20%), H-1→LUMO (12%)
5	28030.1861	356.758245	0.6162	H-2→L+1 (15%), H-1→L+1 (21%), HOMO→L+1 (18%)
6	28887.5534	346.169849	0.1707	H-17→LUMO (61%)
7	29842.5139	335.092414	0.1358	H-19→LUMO (15%), H-3→LUMO (12%), H-2→LUMO (10%), H-1→LUMO (11%)
8	30682.137	325.922539	0.0052	H-14→LUMO (10%), H-4→LUMO (29%), H-2→LUMO (29%)
9	31555.6355	316.900606	1.0156	H-3→L+1 (14%), H-1→L+1 (16%), H-1→L+3 (11%), HOMO→L+3 (17%)
10	32360.5768	309.017978	1.6413	H-4→L+1 (10%), H-2→L+1 (18%), HOMO→L+2 (15%), HOMO→L+4 (11%)
11	33725.2669	296.513591	0.5809	H-21→LUMO (14%), H-19→LUMO (16%), H-5→LUMO (16%), H-3→LUMO (18%)
12	33904.322	294.947647	0.7147	H-5→L+1 (10%), H-3→L+1 (11%), H-1→L+2 (17%), HOMO→L+3 (12%)

Figure 3.16. Calculated fluorescence spectrum and electronic transitions for [10]CPTcaq.

3.6.7 StrainViz calculations

Details for running calculations found at <https://github.com/CurtisColwell/StrainViz>. 10 fragments were used for [10]CPP and BT[10]CPP and 8 fragments for [8]CPP and BT[8]CPP, each with one missing phenylene. Calculations were run at the B3LYP/6-31G* level of theory.



Strain Type (kcal/mol)	[8]CPP	BT[8]CPP	[10]CPP	BT[10]CPP
Total	70.49	70.17	57.41	55.57
Bond	1.60	1.91	2.50	6.01
Angle	4.04	4.11	5.60	2.77
Dihedral	64.84	64.15	48.92	46.78
Strain per phenylene	8.81	8.77	5.74	5.56

Figure 3.17. Strain-Viz calculations of a) **BT[10]CPP**, b) **BT[8]CPP**, c) **[10]CPP** and d) **[8]CPP**.

3.7 Bridge to Chapter IV

In this chapter the first example of a dramatically red-shifted CPP that retains its brightness is described. In the next chapter, now that we have a firm understanding of how to manipulate the photophysical properties of nanohoops, we explore their use in intracellular targeted *in vivo* imaging.

CHAPTER IV

IN-VIVO IMAGING OF AN INTRACELLULAR TARGETED CYCLOPARAPHENYLENE

This chapter includes unpublished co-authored material. The excerpts were written by myself with assistance from Sarah G. Bolton. The experimental work included was performed by myself with assistance from Sarah G. Bolton and Dr. Yu Zhao. Professor Ramesh Jasti and Professor Michael D. Pluth provided experimental input.

Advances in small molecule dye technology are typically structural modifications of scaffolds discovered over half a century ago. These scaffolds often suffer from chemical instability, low brightness, photo-instability and are cell impermeable. Carbon nanohoops are a new type of nanostructure that possess ideal characteristics of nanomaterials while having the tunability and precise synthesis of small molecules, therefore nanohoops are promising candidates to fulfill stringent fluorophore requirements. Herein, we report the first intracellular targeted nanohoop. This fluorophore is bright, does not suffer from intermolecular fluorescent quenching, is non-cytotoxic and cell permeable.

4.1 Introduction

New classes of fluorescent probes and sensors allow observation of complex biological processes in living systems.¹⁻³ A wide variety of fluorescent probes are available including small molecule organic dyes and nanomaterials like nanoparticles, polymers, and carbon nanotubes (CNTs).^{5,162,163} Nanomaterials such as quantum dots are useful imaging agents due to their solubility, brightness, photostability, and emission tunability.^{164,165} However, they are limited by cell impermeability and toxicity to cells and production personale.^{166,167} CNTs are promising potential cell-compatible fluorophores due to their low toxicity and near-infrared excitation wavelengths.¹⁶⁸⁻¹⁷⁰ However, they are not soluble in aqueous media and their optical properties are a direct result of their molecular structure, which cannot be synthesized with atomic

precision.^{171,172} In particular, the functionalization, length, CNT type, and purity are extremely difficult to control.^{171–177} Due to the tunability and synthetic control of small molecule fluorophores, they are currently favored for biological imaging.

Advances in small molecule dye technology are typically structural modifications of scaffolds discovered over half a century ago, such as the fluorone core used to make fluorescein, rhodamine, Janelia Fluor® dyes and their many derivatives (**Figure 4.1**).^{5,35,93} While this approach has been fruitful, there are several drawbacks with the common scaffolds. For example, the fluorescence of fluorescein scaffolds are pH sensitive,¹⁷⁸ fluorescein and cyanine dyes have low photostability,^{131,179} and coumarin dyes have low brightness.⁵ Lastly, most of these fluorophores are not water soluble without additional solubilizing groups. Sulfonation using fuming sulfuric acid is the most common method to instill solubility.⁹⁶ While this provides solubility, it proceeds in low yields, is incompatible with several important functional groups and results in cell impermeable fluorophores.^{93,180} Therefore, the design of new small molecule fluorophores must to be carefully considered to be (i) synthesized controllably with easy functionalization, (ii) bright and retain its fluorescent properties in a cellular context, (iii) non-cytotoxic, (iv) cell permeable, and (v) photostable.

Carbon nanohoops are a new type of nanostructure that possess ideal characteristics of nanomaterials while having the tunability and precise synthesis of small molecules, therefore are promising candidates to fulfill the stringent fluorophore requirements. In their simplest form, carbon nanohoops are [*n*]cycloparaphenylenes ([*n*]CPPs) where “*n*” phenylene units are bent into an all-*para* linked macrocycle resembling a short slice of a CNT (**Figure 4.1**). Unlike common small molecule fluorophores, nanohoops are chemically robust. They are stable between pH 3–12⁶⁶, in presence of harsh oxidants (DDQ)¹⁸¹, and even strongly electrophilic Br₂¹⁵³. Additionally, their curved architecture impedes the π - π stacking observed in linear oligophenylenes rendering CPPs readily soluble, even in polar solvents like dimethyl sulfoxide.^{139,140} Due to the unique structure of the nanohoops, all size nanohoops share a common absorption (350 nm), while the emission red-shifts as the size of the hoop decreases, producing huge effective Stokes shifts of 110–250 nm in comparison to other commercial dyes (6–110 nm).^{5,68} The extinction coefficients of the nanohoops are on the order of 10⁵ M⁻¹cm⁻¹,

which is larger than common fluorophores such as DAPI, Rhodamine 110 and BODIPY-FL.⁵ CPP quantum yields (ϕ) reach up to 0.80 for [12]CPP, though are lower for the smaller sizes due to Laport forbidden emission.^{120,141} However, by tuning the symmetry of CPPs we can enhance the fluorescence of the smaller sizes. Recently, we synthesized *meta*[*n*]CPPs where the symmetry of CPPs is broken simply by shifting one bond by one atom (Figure 1). With this minor change, the quantum yields were increased up to 65 fold and effectively turned-on the fluorescence for previously non-emissive sizes.¹⁴¹ Moreover, the emission may be tuned while maintaining brightness through introduction of electron poor aromatic units.⁶⁴ [10]CPP emits at 466 nm and incorporation of a benzothiadiazole moiety (BT[10]CPP) shifts the fluorescence by more than 100 nm to 575 nm. All these characteristics position them as promising fluorescent scaffolds for biological applications.

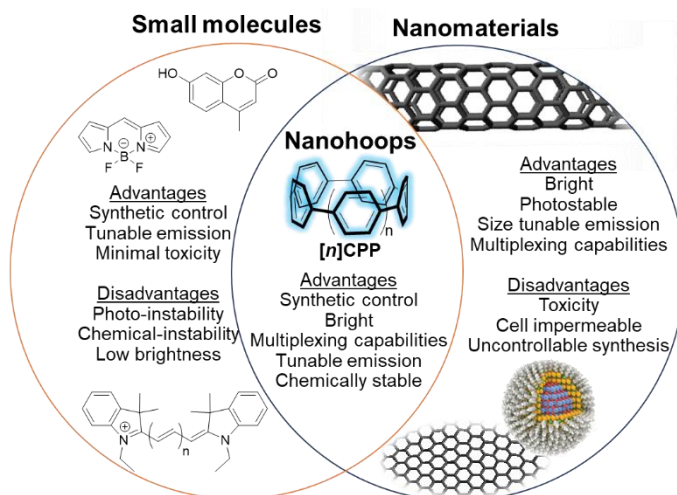


Figure 4.1. Advantages and challenges with common small molecules fluorophores and carbon nanomaterials. CPPs as a promising novel fluorescent scaffold at the intersection of small molecules and nanomaterials.

There are very few reports of CPPs being used in a biological context due to the novelty of this scaffold. A notable example is the use of a sulfonated [8]CPP, which retains its brightness in aqueous buffer. This nano hoop was effectively taken into the cytosol of HeLa cells, and was non-toxic up to concentrations of 10 μ M.⁶⁶ While a folic acid-functionalized [8]CPP was successfully targeted to folate receptors on the cell surface of HeLa cells, no CPP-based fluorophores have yet been targeted to specific

intracellular locales. Additionally, this molecule was difficult to synthesize, and the mechanism of its surprising uptake into live cells is unknown. To further explore the potential of nanohoops as biological imaging agents, it is necessary to (i) improve the CPP synthesis for targeting or bioconjugation purposes, (ii) understand the uptake mechanism, and (iii) evaluate their performance relative to commercial dyes in a cellular context.

Building on this prior work, in this chapter, we report our development of novel synthetic methods to create CPPs optimized for more specific biological applications. We prepared a lysosome targeted CPP to address challenges of imaging the acidic lysosome microenvironment.¹⁸² Herein, we present the first intracellular targeted CPP and compared its performance to the commonly used LysoTrackerTM Deep Red. A CPP-based lysosome targeted probe was synthesized, which retains its brightness and is non-cytotoxic in HeLa cells up to 50 μ M. Colocalization studies determine the nanohoop localizes to the lysosome.

4.2 Synthesis

An alkyne was incorporated into a *m*[6]CPP through macrocyclization of **IV.1** and **IV.2**. Deprotection of the silyl protecting groups (**IV.3a**) and mild reductive aromatization (**IV.3b**) afforded **alkyne-*m*[6]CPP, IV.4**. Click reaction of azido-PEG₄-morpholine (**IV.5**) and **alkyne-*m*[6]CPP** afforded the lysosome targeted CPP **IV.6** as desired.¹⁸² We also synthesized an NHS ester derivative (**IV.8**) to act as a control compound. Characterization by NMR (¹H and ¹³C), IR and mass spectrometry confirmed structural assignment. Over the years we have tried using many different functional groups to yield biocompatible CPPs.⁶⁶ Azide-alkyne click chemistry seemed like a suitable method to install the functionality and solubility needed. The advantage of using a silyl protected alkyne in the CPP synthesis is no additional deprotection step is needed because the alkyne protecting group is removed during the deprotection of the alcohols. Additionally, there would only be one high yielding reaction after the formation of the CPP. Lastly, the click partner could contain a large variety of functional groups providing a very modular synthetic approach. This new synthetic approach fulfills the fluorophore design requirement of a controllable synthesis with ability to be easily functionalized.

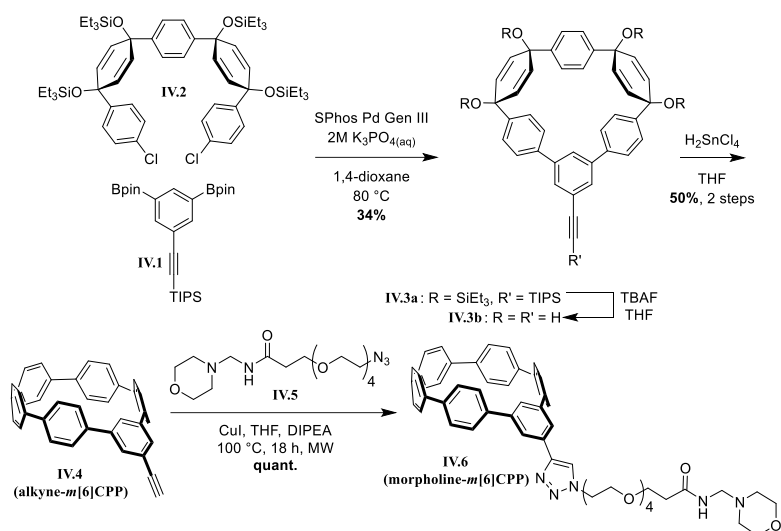


Figure 4.2. Synthesis of lysosome targeted nanohoop.

4.3 Photophysical Properties

The photophysical properties are similar to unfunctionalized *m*[6]CPP.¹⁴¹ The absorbance maximum of **alkyne-*m*[6]CPP** and **morpholine-*m*[6]CPP** is 330 nm, similar to *m*[6]CPP at 328 nm. The extinction coefficients at the 330 nm absorbance maximum of the nanohoops were similar to that of the parent *m*[6]CPP. Importantly, the fluorescence properties of **morpholine-*m*[6]CPP** are retained in relevant imaging media such as PBS ($\lambda_{em} = 519$ nm) and FluoroBrite™ DMEM ($\lambda_{em} = 515$ nm). The effective Stokes shift of 189 nm is much larger than the average fluorophores. The quantum yield of alkyne-*m*[6]CPP in DMSO is the same as *m*[6]CPP in dichloromethane (Table 1). Furthermore, the *m*[6]CPP scaffold that we chose to do this initial feasibility work on (due to synthetic ease) is one of the dimmest nanohoops available. Therefore, the larger brighter nanohoops available may significantly outperform commercial fluorophores in their emission range. Importantly, the second fluorophore requirement of bright probes that retain its fluorescent properties in a cellular context is fulfilled. Furthermore, we can use the brightness properties of the basic nanohoop scaffolds to estimate how they will perform in aqueous media since they retain their photophysical properties. This is contrary to other fluorophores like coumarin and fluorescein which exhibit environment sensitivity by factors like pH and solvent polarity.^{131,183,184}

Table 4.1. Photophysical properties of **alkyne-*m*[6]CPP** and **morpholine-*m*[6]CPP** in DMSO and comparison to parent *m*[6]CPP in CH₂Cl₂.

	λ_{Abs} (nm)	λ_{em} (nm)	ϵ (M ⁻¹ cm ⁻¹)	ϕ
alkyne-<i>m</i>[6]CPP	330	519	5.2×10^4	0.22
morpholine-<i>m</i>[6]CPP	330	519	1.7×10^4	0.12
<i>m</i>[6]CPP	328	510	5.4×10^4	0.22

Self-quenching is largely problematic at high dye concentrations or with protein labeling when dye molecule are in close proximity resulting in the formation of non-fluorescent dimers or larger aggregates.¹³¹ One hypothesis regarding the curved architecture of the CPPs is they exhibit less aggregation induced quenching, but this has not been tested experimentally. We tested this hypothesis by looking at the concentration dependent fluorescence of Alexa FluorTM 488, AMC, BODIPY-FL, and sulfo-Cy3 versus **morpholine-*m*[6]CPP**. BODIPY-FL fluorescence increases, but begins to decrease around 70 μM . BODIPYs are known to show a decrease in fluorescence at with increasing concentrations due to dye-dye interactions. When the concentration of Alexa FluorTM 488 and Cy3 are increased there is an initial increase in fluorescence, which levels off around 100 μM . Alexa FluorTM and sulfonated cyanine dyes are designed to minimize self-quenching through electrostatic repulsion of sulfonic acid groups. Gratifyingly, the nanohoop fluorescence continually increases up to the maximum measurable optical density.

4.4 Cytotoxicity and *in-vivo* Imaging

To determine CPP utility as probes for *in vivo* imaging we analyzed their cytotoxicity. Live HeLa cells were treated with 1, 5, 20 and 50 μM solutions of **morpholine-*m*[6]CPP** and NHS-*m*[6]CPP for 1 hour. Cell death was measured using CCK-8 cell assay (**Figure 4.3**). **morpholine-*m*[6]CPP** demonstrated no cytotoxicity even at high concentrations of 50 μM . NHS-*m*[6]CPP demonstrated minimal toxicity. These results indicate that both CPPs are cell-compatible, and we moved onto imaging experiments.

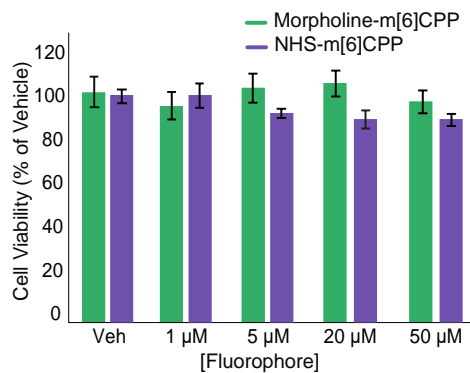


Figure 4.3. Cytotoxicity studies of **morpholine-*m*[6]CPP** and NHS-*m*[6]CPP in HeLa cells over 1 hour. Neither CPP compound shows significant cytotoxicity up to 50 μ M.

We next sought to determine the cell permeability of the nano hoops in HeLa cells. HeLa cells were treated with a 100 nM solution of **morpholine-*m*[6]CPP** or 1 μ M NHS-*m*[6]CPP in FBS free DMEM with 0.5% DMSO vehicle for 45 minutes. When incubated with LysoTracker™ Deep Red, NHS-*m*[6]CPP was taken up by the cells and appeared to be throughout the cytosol, demonstrating bright fluorescence, but showing little colocalization with LysoTracker™ (Figure 4.4g-4.4i). This is consistent with the previous reports of *in vivo* imaging of CPPs.^{66,185} **Morpholine-*m*[6]CPP** on the other hand, localizes in a specific cellular areas as sharp puncta (Figure 4.4a, 4.4d). When coincubated with LysoTracker™ DeepRed, **morpholine-*m*[6]CPP** shows strong colocalization (Figure 4.4a-4.4c). Pearson's coefficients of **morpholine-*m*[6]CPP** and LysoTracker™ Deep Red of 0.83 indicate that it is localized in the lysosome as desired. Furthermore, colocalization of **morpholine-*m*[6]CPP** and MitoTracker™ Deep Red (Figure 4.4d-4.4f), a mitochondria-targeted fluorophore, shows minimal colocalization with a Pearson's coefficient 0.57. The Pearson's coefficient of 0.44 for NHS-*m*[6]CPP and LysoTracker™ Deep Red demonstrates a lack of colocalization and indicate that the morpholine moiety is responsible for localization to the lysosome. This proves that we have altered the nano hoop structure and controllably targeted a specific intracellular location. Gratifyingly, there are no significant changes in cell morphology after incubation with the hoops, confirming the absence of cytotoxicity.

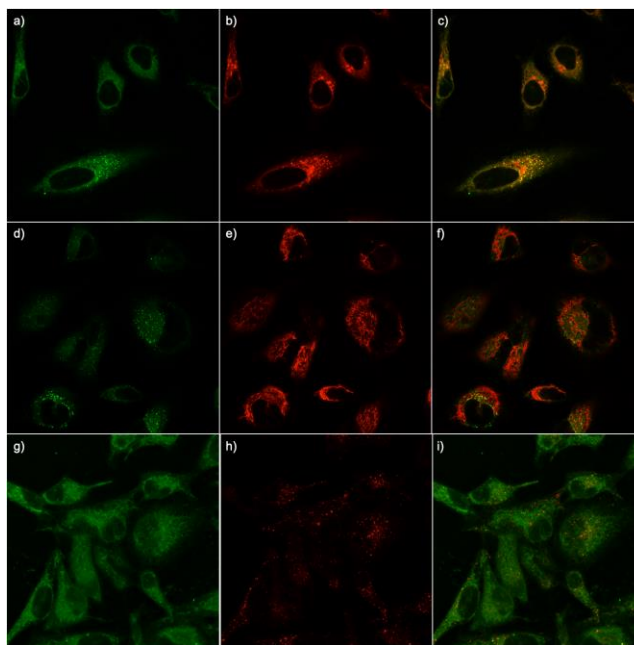


Figure 4.4. Colocalization of **morpholine-*m*[6]CPP** and NHS-*m*[6]CPP in live HeLa cells. a) **morpholine-*m*[6]CPP**, b) LysoTracker™ Deep Red, c) overlay. d) **morpholine-*m*[6]CPP**, e) MitoTracker™, f) overlay. g) NHS-*m*[6]CPP b) LysoTracker™ Deep Red, c) overlay.

The internalization mechanism of nanohoop fluorophores has not yet been studied. Understanding the mechanism by which the fluorophores are taken up can help direct design principles and understand functionality tolerance. Endocytosis is a likely mechanism due to the size and charge.^{186–188} To test this, HeLa cells were incubated with **morpholine-*m*[6]CPP** at 4, 27 and 37 °C for 45 minutes, and visualized by fluorescence microscopy. Lowering the temperature of the cellular incubation should lower the uptake of the nanohoops if the uptake is due to active transport mechanisms rather than passive transport. **Figure 4.5** shows a temperature-dependent uptake of **morpholine-*m*[6]CPP**. There is little intracellular fluorescence observed at 4 °C, in contrast to that observed at 27 or 37 °C. This indicates uptake is through an energy-dependent mechanism, such as endocytosis.¹⁸⁸

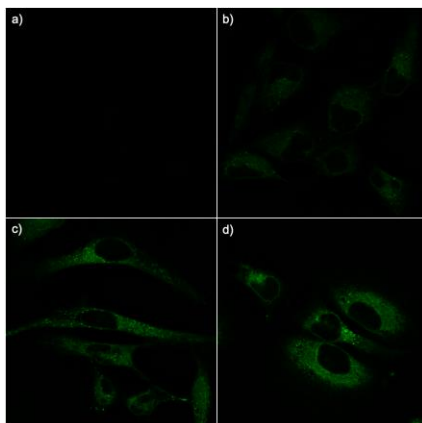


Figure 4.5. HeLa cell uptake of **morpholine-*m*[6]CPP** at 4, 27 and 37 °C to investigate uptake mechanism. Uptake is strongly hindered at 4°C incubation, demonstrating an energy dependent mechanism of nanohoop uptake into cells.

4.5 Conclusions

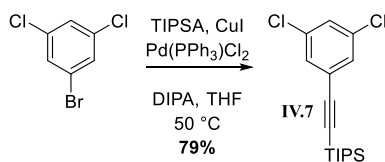
In summary, we synthesized the first cycloparaphenylene-based organelle targeted fluorescent probe. This carbon-based curved molecular structure is unlike other fluorophores used for cellular imaging. This structure results in bright fluorescent molecules with enhanced aqueous solubility. The novel fluorophore is non-cytotoxic, even at high concentrations (50 μ M). Cellular uptake mechanistic studies indicate that the fluorophore is taken up through endocytosis, but more studies have to be done to determine the exact pathway. The synthetic methods described in this work opens doors to many biocompatible CPP probe structures that were previously unattainable. The synthesis allows functionalization with an unlimited number of linkers with different functionality. The nanohoop structure offers optical properties unlike any other small molecule, cell permeability and lack of cytotoxicity. Furthermore, the nanohoops are poised for multiplexed and multimodal imaging making it an intriguing novel scaffold for fluorescent probe development.

4.6 Experimental Section

4.6.1 General experimental details and synthesis

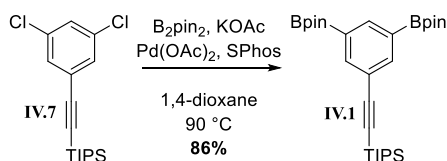
All glassware was flame dried and cooled under an inert atmosphere of nitrogen unless otherwise noted. Moisture sensitive reactions were carried out under nitrogen atmosphere using Schlenk and standard syringe/septa techniques. Tetrahydrofuran, dichloromethane,

and 1,4-dioxane were dried by filtration through alumina according to the methods describes by Grubbs.¹³⁴ Silica column chromatography was conducted with Zeochem Zeoprep 60 Eco 40-63 μm silica gel. Automated flash chromatography was performed using a Biotage Isolera One. Recycling gel permeation chromatography (GPC) was performed using a Japan Analytical Industry LC-9101 preparative HPLC with JAIGEL-1H/JAIGEL-2H columns in series using CHCl_3 . Thin Layer Chromatography (TLC) was performed using Sorbent Technologies Silica Gel XHT TLC plates. Developed plates were visualized using UV light at wavelengths of 254 and 365 nm. ^1H NMR spectra were recorded at 500 MHz or 600 MHz on a Bruker Advance-III-HD NMR spectrometer. ^{13}C NMR spectra were recorded at 150 or 126 MHz on a Bruker Advance-III-HD NMR spectrometer. All ^1H NMR spectra were taken in CDCl_3 (referenced to TMS, δ 0.00 ppm). All ^{13}C NMR spectra were taken in CDCl_3 (referenced to chloroform, δ 77.16 ppm). Mass spectra were obtained from the University of Oregon CAMCOR using ASAP. Absorbance and fluorescence spectra were taken with Tecan Spark® in a Nunc® 96-well plate. Fluorescent quantum yields were measured in a 1 cm Quartz cuvette with dimethyl sulfoxide at room temperature using an Agilent Cary 100 UV-Vis spectrometer and a Horiba Jobin Yvon Fluoromax-4 Fluorimeter. HeLa cells (ATCC CCL-2) were purchased from ATCC and the CCK-8 cell viability kit was purchased from Dojindo Molecular Technologies Inc. Cell viability was measured using a BioTek Synergy 2 plate reader. Cell imaging experiments were performed on a Zeiss LSM 880 fluorescence microscope. All reagents were obtained commercially unless otherwise noted. Compounds **IV.2**¹⁴¹, and SPhos Pd Gen III¹³⁶ were prepared according to literature procedure.



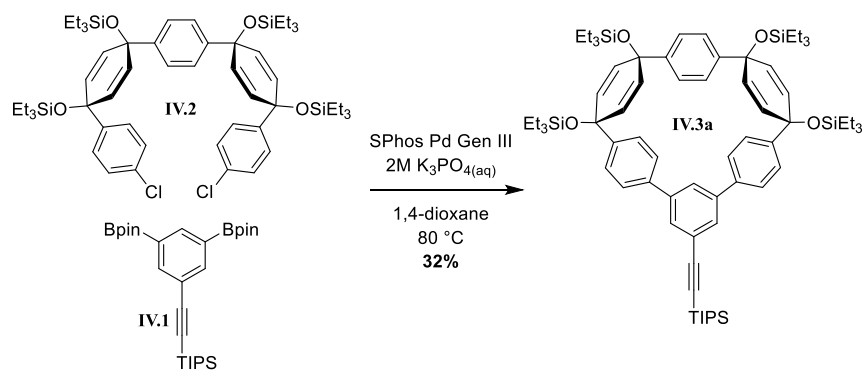
IV.7. 1-bromo-3,5-dichlorobenzene (15 g, 66.4 mmol, 1 equiv), CuI (632.3 mg, 3.3 mmol, 0.05 equiv) and $\text{Pd}(\text{PPh}_3)_2\text{Cl}_2$ (466.1 mg, 0.664 mmol, 0.01 equiv) were added to a 500 mL round bottom flask equipped with a stir bar. The flask was put under vacuum for 30 minutes. Diisopropyl amine (67 mL) and tetrahydrofuran (132 mL) were added to a 250

mL round bottom flask and sparged for an hour. The reaction flask was equipped with a septum, the DIPA/THF mixture was added and the reaction mixture was sparged for 5 minutes. Triisopropylsilylacetylene (16.5 mL, 73.0 mmol, 1.1 equiv) was added and the round bottom flask was placed in a preheated oil bath and allowed to stir at 50 °C overnight. The reaction was allowed to cool to room temperature and was quenched with ammonium chloride. The product was extracted (3 x 20) with ethyl acetate, washed with water (2 x 20 mL) and brine (1 x 20 mL), dried over sodium sulfate and concentrated to yield the crude product. The crude product was purified by automated flash silica gel chromatography (hexanes) to yield **IV.7** as a light yellow oil (19 g, 79%). ¹H NMR (600 MHz, Chloroform-*d*) δ 7.33 (d, *J* = 1.9 Hz, 2H), 7.30 (t, *J* = 1.9 Hz, 1H), 1.12 (d, *J* = 2.9 Hz, 21H). ¹³C NMR (151 MHz, CDCl₃) δ 134.76, 130.18, 128.65, 126.24, 103.97, 94.03, 18.61, 11.21. HRMS (ASAP) (m/z): [M] calculated for C₁₇H₂₄SiCl₂, 326.1024; found, 326.0672.



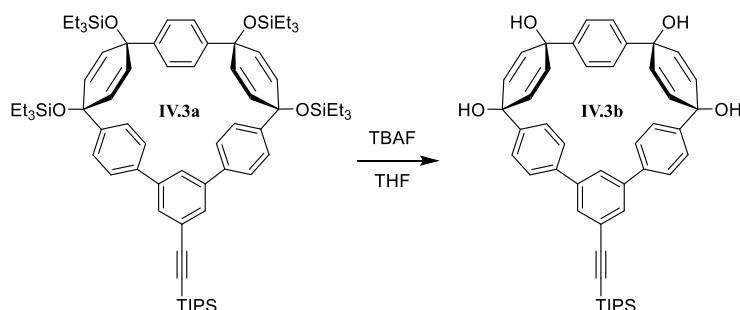
IV.1. Oven-dried potassium acetate (11.9 g, 121 mmol, 6.6 equiv) was added to a flame-dried 100 mL round bottom flask equipped with a stir bar. The KOAc and round bottom flask were flame-dried again under vacuum until all apparent moisture was removed. Pd(OAc)₂ (20.6 mg, 0.092 mmol, 0.005 equiv), SPhos (941 mg, 2.3 mmol, 0.125 equiv), B₂Pin₂ (18.6 g, 73.3 mmol, 4 equiv) and **IV.7** (0.9291 g, 0.60 mmol, 1 equiv) were added to the round bottom and the flask was evacuated (5 minutes) and purged with nitrogen 5 times. 1,4-dioxane (61 mL) that had been sparged for an hour was added and the reaction mixture and was sparged for 5 minutes. It was then placed in a preheated oil bath at 90 °C and allowed to stir overnight. Ethyl acetate was added to the reaction mixture and it was sonicated. This was filtered through a fritted suction funnel filled with Celite. The round bottom was rinsed several times with ethyl acetate and sonicated. The filtrate was concentrated to yield the crude product as a yellow solid. This was rinsed with ethanol to yield **IV.1** as white solid (8.03 g, 86%). ¹H NMR (500 MHz, Chloroform-*d*) δ 8.19 (t, *J* = 1.3 Hz, 1H), 7.99 (d, *J* = 1.3 Hz, 2H), 1.34 (s, 24H), 1.12 (s, 21H). ¹³C NMR (126 MHz,

CDCl₃) δ 140.88, 140.80, 122.69, 106.91, 90.19, 83.98, 24.87, 18.72, 11.36. HRMS (ASAP) (m/z): [M] calculated for C₂₉H₄₉B₂O₄Si, 511.3586; found, 511.3611.

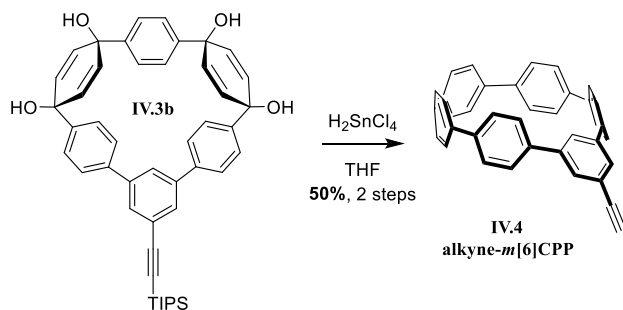


IV.3a. **IV.1** (501.8 mg, 0.98 mmol, 1.2 equiv), **IV.2** (800.0 mg, 0.82 mmol, 1 equiv) and Sphos Pd Gen III (65.2 mg, 0.082 mmol, 0.1 equiv) were added to a 500 mL round bottom flask equipped with a stir bar. The flask was evacuated (5 minutes) and purged with nitrogen 5 times. 1,4-dioxane and K₃PO₄ were sparged for at least 1 hour prior to use. The round bottom flask was equipped with a septa and 1,4-dioxane (273 mL) was added to the round bottom flask and the solution was sparged for 30 minutes. The round bottom flask was placed in a preheated oil bath (80 °C) for 10 minutes then K₃PO₄ (27 mL, 2 M in deionized water) was added. The reaction was allowed to stir at 80 °C overnight. The reaction mixture was allowed to cool to room temperature. It was then filtered through a fritted suction funnel of Celite. The round bottom flask was rinsed with dichloromethane and filtered through the Celite plug. The filtrate was added to a separatory funnel along with deionized water (20 mL) and the product was extracted (3 x 100 mL) with dichloromethane. The organic layers were dried over sodium sulfate and concentrated to yield the crude product as a brown solid. The product was purified by automated flash silica gel chromatography (0% to 20% dichloromethane in hexanes) to give **IV.3a** as a white solid (390 mg, 34%). ¹H NMR (500 MHz, Chloroform-*d*) δ 7.67 (d, *J* = 1.8 Hz, 2H), 7.45 (d, *J* = 8.4 Hz, 4H), 7.27 (d, *J* = 8.4 Hz, 4H), 6.92 (s, 4H), 6.13 (d, *J* = 10.2 Hz, 4H), 5.72 (d, *J* = 10.1 Hz, 4H), 1.18 (s, 22H), 0.97 (t, *J* = 7.9 Hz, 19H), 0.92 (t, *J* = 7.9 Hz, 20H), 0.68 (q, *J* = 7.9 Hz, 14H), 0.57 (q, *J* = 7.9 Hz, 14H). ¹³C NMR (126 MHz, CDCl₃) δ 145.17, 144.74, 142.35, 142.29, 141.69, 131.53, 131.37, 128.76, 126.17, 126.04, 125.31, 123.77, 107.39, 90.50, 71.16, 70.52, 18.73, 11.39, 7.11, 6.99, 6.58, 6.41,

6.17. HRMS (ASAP) (m/z): [M] calculated for C₇₁H₁₀₅O₄Si₅, 1161.6859; found, 1161.7059.

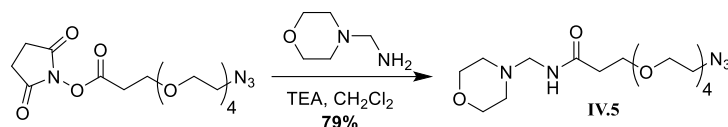


IV.3b. Tetrahydrofuran (2.7 mL) was added to the 20 mL scintillation vial containing **IV.3a** (307.5 mg, 0.26 mmol, 1 equiv) and the vial was equipped with a stir bar and septa. Tetra-*n*-butylammonium fluoride (2.7 mL, 2.6 mmol, 10 equiv, 1 M in tetrahydrofuran) was added to the reaction flask and this was allowed to stir for 2 hours at room temperature. Deionized water (10 mL) was added and the organic solvent was removed via rotovap. The solid was collected by suction filtration and rinsed with dichloromethane to yield **IV.3b** as a white solid. The crude product was used as is for the following reaction.

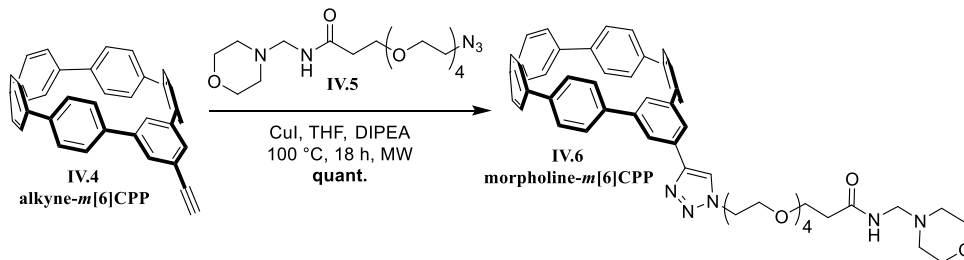


IV.4. SnCl₂•H₂O (181 mg, 0.80 mmol) was added to a 100 mL round bottom flask equipped with a stir bar and septum. Tetrahydrofuran (20 mL) was added followed by hydrochloric acid (0.13 mL, 1.6 mmol, 12 M). This was allowed to stir at room temperature for 30 minutes. H₂SnCl₂ solution (15 mL, 0.58 mmol, 2.2 equiv, 0.04 M) was added to the scintillation vial containing **IV.3b** (145.2 mg, 0.26 mmol, 1 equiv) and the reaction was allowed to stir for 1 hour at room temperature. The reaction was quenched with saturated sodium bicarbonate (20 mL) and the product was extracted with

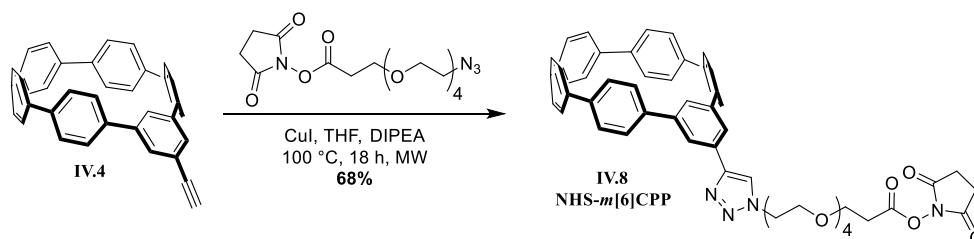
dichloromethane (3 x 20 mL). The organic layers were washed with brine (1 x 50 mL), dried over sodium sulfate and concentrated to give the crude product as a yellow solid. The product was purified by automated flash alumina gel chromatography (0% to 30% dichloromethane in hexanes) to give the product as a yellow solid (63 mg, 50% two steps). ^1H NMR (600 MHz, Chloroform-*d*) δ 7.57 (d, J = 1.8 Hz, 2H), 7.46 – 7.36 (m, 16H), 7.13 (d, J = 8.6 Hz, 4H), 5.59 (t, J = 1.8 Hz, 1H), 3.13 (s, 1H). ^{13}C NMR (151 MHz, CDCl_3) δ 142.75, 141.65, 140.15, 139.38, 137.52, 136.40, 136.21, 129.41, 128.09, 127.86, 127.58, 127.23, 126.00. HRMS (ASAP) (m/z): [M] calculated for $\text{C}_{38}\text{H}_{25}$, 481.1956; found, 481.1745.



IV.5. 4-morpholinemethanamine (87 mg, 0.75 mmol, 3 equiv), Azido-PEG₄-NHS ester (97 mg, 0.25 mmol, 1 equiv) and TEA (0.10 mL) and were added to a 10 mL round bottom equipped with a stir bar and septa. Dichloromethane (7.49 mL) was added and the mixture was allowed to stir overnight at room temperature. Water was added and the product was extracted with dichloromethane (3 x 5 mL). The organic layers were washed with brine (1 x 5 mL), dried over sodium sulfate and concentrated to yield the crude product. The product was purified by gel permeation chromatography to yield a clear oil (74 mg, 79%). ^1H NMR (500 MHz, Chloroform-*d*) δ 6.73 (s, 1H), 3.74 (t, J = 5.9 Hz, 2H), 3.71 (t, J = 4.7 Hz, 4H), 3.69 – 3.63 (m, 13H), 3.39 (t, 2H), 3.36 (t, 2H), 2.50 – 2.44 (m, 7H). ^{13}C NMR (126 MHz, CDCl_3) δ 171.46, 70.63, 70.61, 70.54, 70.48, 70.34, 70.25, 69.98, 67.29, 66.84, 57.25, 53.38, 50.63, 36.96, 35.78. HRMS (ASAP) (m/z): [M+H] calculated for $\text{C}_{102}\text{H}_{150}\text{B}_2\text{O}_{10}\text{Si}_6$, 1725.0031; found, 1726.0386.



IV.6. IV.4 (4.7 mg, 0.0098 mmol, 1 equiv), copper iodide (0.2 mg, 0.001 mmol, 0.1 equiv) and **IV.5** (3.7 mg, 0.0098 mmol, 1 equiv) were added to an oven dried 0.2-0.5 mL microwave vial equipped with a stir bar. The vial was equipped with a septum and was evacuated and purged with nitrogen. Dry diisopropylethyl amine (0.1 mL, 0.58 mmol, 53 equiv) and tetrahydrofuran (0.4 mL) were added to the vial, which was then sealed and heated to 100 °C in the microwave for 18 hours. The reaction mixture was concentrated to remove the DIPEA. The product was dissolved in dichloromethane and added to water to remove the copper. The product was extracted with dichloromethane (3 x 5 mL), dried over sodium sulfate and concentrated to yield **IV.6** as a green solid (8.5 mg, quant.). ¹H NMR (500 MHz, Chloroform-*d*) δ 8.09 (s, 1H), 7.93 (d, *J* = 1.6 Hz, 2H), 7.42 (q, *J* = 9.8, 9.4 Hz, 16H), 7.19 (d, *J* = 8.3 Hz, 4H), 6.56 (s, 1H), 5.58 (t, *J* = 2.0 Hz, 1H), 4.63 (t, *J* = 5.0 Hz, 2H), 3.95 (t, *J* = 5.0 Hz, 2H), 3.74 (t, *J* = 5.7 Hz, 2H), 3.72 – 3.60 (m, 21H), 3.57 (s, 4H), 3.36 (dq, *J* = 21.6, 5.5 Hz, 4H), 2.49 – 2.42 (m, 10H). ¹³C NMR (126 MHz, CDCl₃) δ 171.31, 147.75, 143.24, 142.31, 139.29, 139.22, 137.47, 136.41, 136.29, 131.69, 129.45, 128.08, 127.85, 127.57, 127.23, 121.36, 119.64, 70.73, 70.70, 70.64, 70.61, 70.59, 70.56, 70.41, 70.33, 70.26, 70.06, 69.57, 67.34, 67.31, 66.95, 66.92, 57.23, 53.42, 50.70, 50.46, 37.04, 37.00, 35.78, 29.71. HRMS (ASAP) (*m/z*): [M] calculated for C₅₄H₅₆N₅O₆, 870.4231; found, 870.3938.



IV.8. IV.4 (4.3 mg, 0.0090 mmol, 1 equiv), copper iodide (0.2 mg, 0.001 mmol, 0.1 equiv) and azido-PEG₄-NHS ester (3.5 mg, 0.0090 mmol, 1 equiv) were added to an oven dried 0.2-0.5 mL microwave vial equipped with a stir bar. The vial was equipped with a septum and was evacuated and purged with nitrogen. Dry diisopropylethyl amine (0.1 mL, 0.58 mmol, 65 equiv) and tetrahydrofuran (0.4 mL) were added to the vial, which was then sealed and heated to 100 °C in the microwave for 18 hours. The reaction mixture was concentrated to remove the DIPEA. The product was dissolved in

dichloromethane and added to water to remove the copper. The product was extracted with dichloromethane (3 x 5 mL), dried over sodium sulfate and concentrated to yield the crude product. The product was purified by recycling gel permeation chromatography in chloroform to give **IV.8** as a green solid (5.3 mg, 68%). ^1H NMR (500 MHz, Chloroform-*d*) δ 8.10 (s, 1H), 7.93 (d, $J = 1.7$ Hz, 2H), 7.46 – 7.39 (m, 18H), 7.20 (d, $J = 8.6$ Hz, 4H), 5.58 (t, $J = 1.8$ Hz, 1H), 4.63 (t, $J = 5.0$ Hz, 2H), 3.95 (t, $J = 5.0$ Hz, 2H), 3.79 (t, $J = 6.4$ Hz, 2H), 3.69 – 3.60 (m, 14H), 3.59 (s, 4H), 2.85 (t, $J = 6.4$ Hz, 2H), 2.79 (s, 4H). ^{13}C NMR (126 MHz, CDCl_3) δ 168.92, 166.73, 143.23, 142.38, 139.18, 137.45, 136.41, 136.33, 131.76, 129.47, 128.08, 127.85, 127.57, 127.22, 121.39, 119.66, 77.28, 77.02, 76.77, 70.70, 70.67, 70.65, 70.62, 70.54, 70.50, 69.55, 65.70, 53.42, 50.46, 32.17, 29.71, 25.58, 0.00. HRMS (ASAP) (m/z): [M] calculated for $\text{C}_{53}\text{H}_{48}\text{N}_4\text{O}_8$, 868.3472; found, 868.3278.

4.6.2 Photophysical characterization

The extinction coefficients were measured in DMSO using a Tecan Spark® in a Nunc® 96-well plate. The volume used was 100 μL and the pathlength was determined to be 0.278 cm based on the 96-well plate dimensions.

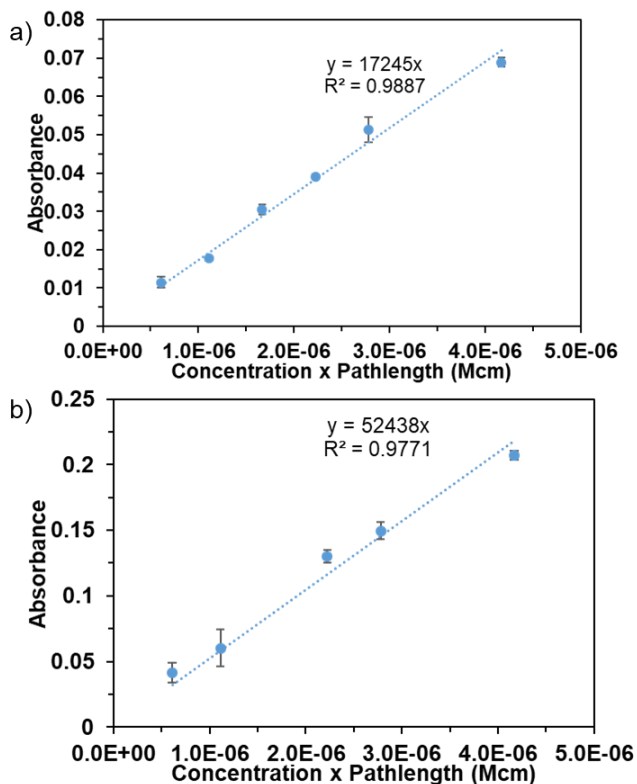


Figure 4.6. Absorbance versus concentration×pathlength for extinction coefficient determination of a) **morpholine-*m*[6]CPP** and b) **alkyne-*m*[6]CPP** in DMSO.

Table 4.2. Average extinction coefficient and error of **morpholine-*m*[6]CPP** and **alkyne-*m*[6]CPP**.

Compound	Extinction Coefficient (M ⁻¹ cm ⁻¹)
morpholine-<i>m</i>[6]CPP	$(1.7 \pm 0.03) \times 10^4$
alkyne-<i>m</i>[6]CPP	$(5.2 \pm 0.2) \times 10^4$

Table 4.3. Triplicate quantum yields, average quantum yield and error of **morpholine-*m*[6]CPP** and **alkyne-*m*[6]CPP**.

Compound	Trial 1	Trial 2	Trial 3	ϕ
alkyne-<i>m</i>[6]CPP	0.222	0.223	0.223	0.223 ± 0.0006

4.6.3 Cell Imaging Experiments

HeLa cells (ATCC CCL-2) were cultured in high glucose Dulbecco’s modified Eagle’s medium (DMEM) supplemented with 10% fetal bovine serum (FBS) and 1% penicillin/streptomycin at 37 °C under 5% CO₂. HeLa cells were then plated and incubated at 37 °C under 5% CO₂ overnight before performing experiments.

Colocalization Studies

HeLa cells were plated in poly-D-lysine coated glass bottom dishes (MatTek) containing 2.00 mL of 10% FBS DMEM. The next day, adherent cells were washed 2X with FBS-free DMEM. Cells were then incubated in 2 mL FBS-free DMEM containing either 60 nM LysoTracker Deep Red (Invitrogen) or 150 nM MitoTracker Deep Red (Invitrogen) for 30 minutes at 37°C. After this incubation, the media was aspirated, and cells were again rinsed 2X with FBS-free DMEM. Cells were then incubated with morpholine-*m*[6]CPP in FBS-free DMEM for 30 minutes at 37°C. The media was again aspirated, and cells were rinsed 2X with DMEM and then imaged in FluoroBrite DMEM (Gibco) on a Zeiss LSM 880 confocal microscope.

Cytotoxicity Studies

HeLa cells were plated at 20,000 cells/well in plastic 96 well plates. The next day, media was removed, and cells were rinsed once with FBS-free DMEM. Cells were incubated again in FBS-free DMEM containing either morpholine-m[6]CPP or NHS-PEG4-m[6]CPP as a control for 1 hour at 37°C. After the incubation, media was removed and replaced with FBS-free DMEM containing 10% CCK-8 cytotoxicity reagent (Dojindo). Plates were incubated again for one hour and read on a plate reader (BioTek Synergy 2) at 450 nm.

Uptake Studies

HeLa cells were plated in poly-D-lysine coated glass bottom dishes (MatTek) containing 2.00 mL of 10% FBS DMEM. The next day, adherent cells were washed 2X with FBS-free DMEM. Cells were then incubated in 2 mL FBS-free DMEM containing morpholine-m[6]CPP in either 37°C, 27°C, or 4°C for 45 minutes. The media was removed, and cells were rinsed 2X in DMEM and then imaged in FluoroBrite DMEM (Gibco) on a Zeiss LSM 880 confocal microscope.

4.7 Bridge to Chapter V

In this chapter, we synthesized the first intracellular targeted nanohoop and showed its use in one- and two-photon fluorescence imaging. The next chapter describes step towards broadening the use of nanohoops in biological applications through attaching these novel fluorophores to biological entities.

CHAPTER V

BIOCONJUGATION OF CYCLOPARAPHENYLENES TO BIOMOLECULES FOR IMMUNOCHEMISTRY AND *IN VITRO* IMAGING

This chapter includes unpublished co-authored material. The excerpts were written by myself with editorial assistance from Professor Ramesh Jasti. The experimental work included was performed by myself with assistance from Julia Shangguan, Dr. Fehmi Civitci, Dr. John Kenison, and Randall Armstrong. Experimental guidance was provided by Professor Xiaolin Nan and Professor Ramesh Jasti.

Bioconjugation is utilized in an endless number of applications and has allowed the discovery of new biomolecules and elucidation of complex biological processes. Therefore, an important step towards broadening the utility of nanohoop fluorophores is the efficient conjugation of these structures to biological entities without disruption of function. Herein, for the first time we describe the synthesis of a nanohoop with a bioconjugation handle and efforts towards its conjugation to DNA and proteins. Furthermore, with these conjugates we explore the two-photon fluorescence imaging of CPPs.

5.1 Introduction

Bioconjugation is an imperative tool at the interface of chemistry and biology. It entails the linkage of a biomolecule with another material or molecule used to interrogate a biological system. Bioconjugation is utilized in an endless number of applications and has enabled the discovery of new biomolecules and understand of complex biological processes.¹⁸⁹ Consequently, an important step towards utilizing nanohoop-based fluorophores for a broad array of biological applications is the efficient conjugation of these structures to biological entities without disruption of function. There are many strategies and functional groups used for the linkage of biomolecules to a reporter molecule such as azide-alkyne click chemistry, sulfhydryl-reactive groups and amine reactive groups (**Figure 5.1**). The most common reactive functional groups are amine-

reactive, such as N-hydroxysuccinimide esters (NHS esters) and isocyanates. These react with primary amines of proteins at the N-terminus of a polypeptide or a lysine residue and amine-functionalized DNA. The most commonly used amine reactive group is an NHS ester, therefore this was the initial functional handle targeted.

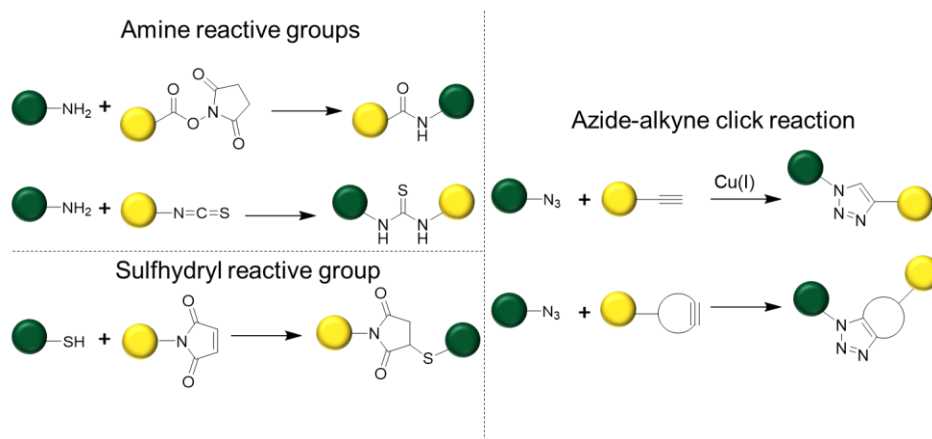


Figure 5.1. Different functional groups used for conjugation of biomolecules and reporter molecules.

5.2 Synthesis of a CPP with conjugation handle

To install the reactive handle, we sought to carry a protected alcohol through the CPP synthesis, as was done previously.^{66,190} However, in previous synthetic efforts, the *tert*-butyldimethylsilyl protecting group was too labile and was unintentionally removed during the CPP synthesis. Therefore, the use of a methoxymethyl protecting group was explored. Macrocycle **V.3** was synthesized through macrocyclization of **V.1** and **V.2** followed by a deprotection of the triethylsilyl protecting groups affording **V.4**. Using standard aromatization conditions, CPP **V.5** was afforded in low yields (26%, **Figure 5.1**). The low yield is thought to be interference of the MOM oxygens with the tin complex.¹⁹¹ Deprotection of the alcohol resulted in decomposition giving the desired product **V.6** in only trace amounts. Furthermore, the alcohol must be oxidized to a carboxylic acid then converted to an NHS ester indicating this was an impractical route to a bioconjugatable NHS ester CPP.

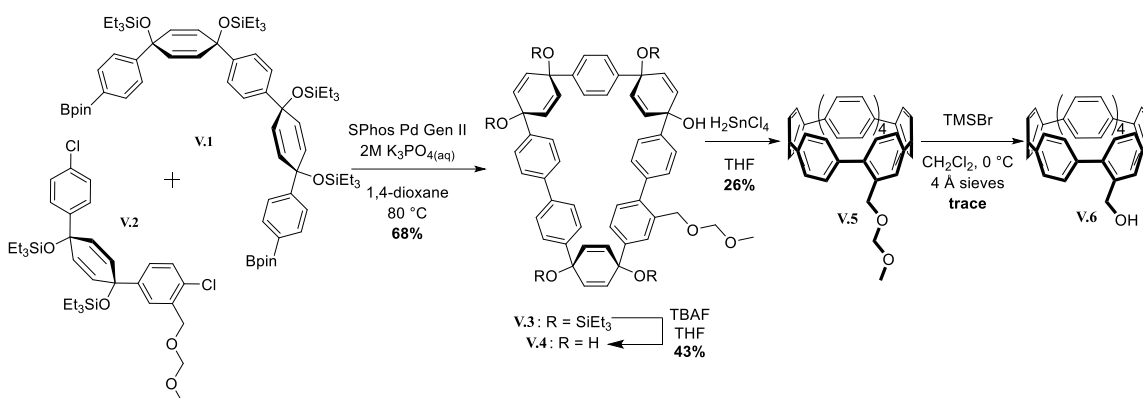


Figure 5.2. Synthesis of benzyl alcohol functionalized CPP towards an NHS ester-CPP for bioconjugation.

Next, a more labile ethyl ester protecting group was explored, which would require less post CPP modification to afford an NHS ester CPP. Macrocyclization of **V.7** and **V.8** afforded the ethyl ester macrocyclic precursor **V.9** in good yields. Deprotection of the triethyl silyl groups and aromatization afforded **V.10**, a CPP with a protected ester. The ester was quantitatively saponified to the carboxylic acid **V.11** then converted to the desired NHS ester CPP **V.12**. With the desired bioconjugation handle, we tested the utility of the nano hoop in flow cytometry in collaboration with Randall Armstrong at Oregon Health Science University. A large variety of conjugation conditions were explored to attach the nano hoop to a CD8 antibody, but conjugation was not achieved. It is hypothesized that since the NHS-ester is directly on the hoop it may be too sterically hindered for reaction with a large biomolecule like an antibody. Additionally, we thought the CPP might not be soluble enough for conjugation, thus a more soluble and accessible NHS-ester nano hoop was synthesized.

Recent work in our lab yielded CPPs functionalized with protected alkynes for novel conjugated polymers.⁶³ This allowed the opportunity to utilize azide-alkyne “click” chemistry, an ideal method to install the functionality and solubility needed. Click chemistry not only reduces the amount of post-aromatization reactions, but the azide coupling partner could contain a large variety of functional groups allowing access to a variety of biologically relevant structures. Finally, an additional deprotection step is not needed because the alkyne protecting group would be removed during the pre-aromatization alcohol deprotection. Alkyne[12]CPP **V.13** was synthesized in a similar

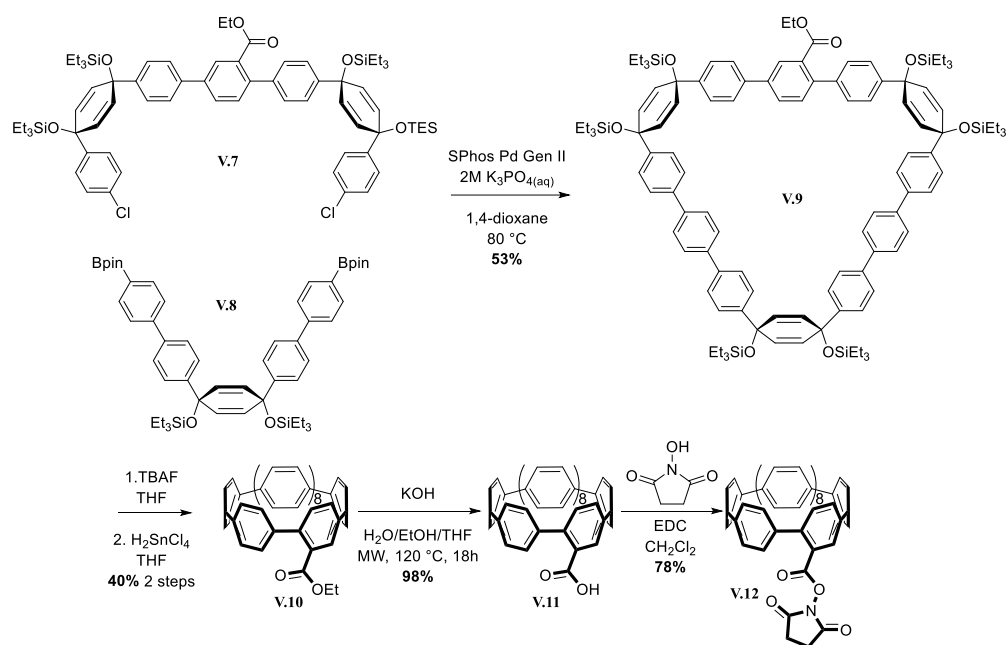


Figure 5.3. Synthesis of NHS ester-CPP for bioconjugation.

manner to **V.10**, then an azido-PEG₄-NHS ester is clicked on in high yields (**Figure 5.4**). This strategy was employed to make NHS ester versions of *m*[6]CPP, *m*[8]CPP, *m*[10]CPP, [8]CPP and [10]CPP. Additionally, *m*[6]CPP versions with varying PEG_x linker lengths (x = 4, 12, 24) was synthesized, further highlighting the versatility of this approach.

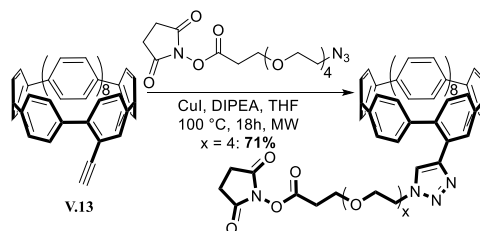


Figure 5.4. Synthesis of NHS-PEG₄-[12]CPP for bioconjugation.

5.3 Conjugation of NHS-PEG_x-CPPs to amine functionalized DNA

Single stranded DNA (ssDNA) was labelled, as part of a collaboration with OHSU, to analyze nano hoop performance in two-photon fluorescence microscopy using a DNA labelling technique. 45 μL of 0.1 M sodium bicarbonate buffer (pH 8.3) was mixed with 5 μL 1 mM amine-ssDNA (IS1) followed by a 10 mole excess of the nano hoop. Different length PEG linkers were tested to see if there was a difference in

conjugation efficiency, but denaturing polyacrylamide gel electrophoresis analysis revealed no nanohoop conjugation using this method (**Figure 5.5**, OHSU Conditions). However, the Cy3 control did achieve high conjugation efficiency. Following a Thermo Fisher protocol, 5 μ L of 1 mM DNA was mixed with 1 M sodium bicarbonate buffer followed by the nanohoops with different PEG linkers. The conjugation efficiency was greater, but a significant amount of free ssDNA was observed by methylene blue stain (**Figure 5.5**, Thermo Conditions). No difference was observed between the PEGx linkers. Notably, the final concentration of DNA and nanohoop in solution is higher for the protocol that afforded better conjugation, therefore, these were the next parameters tested.

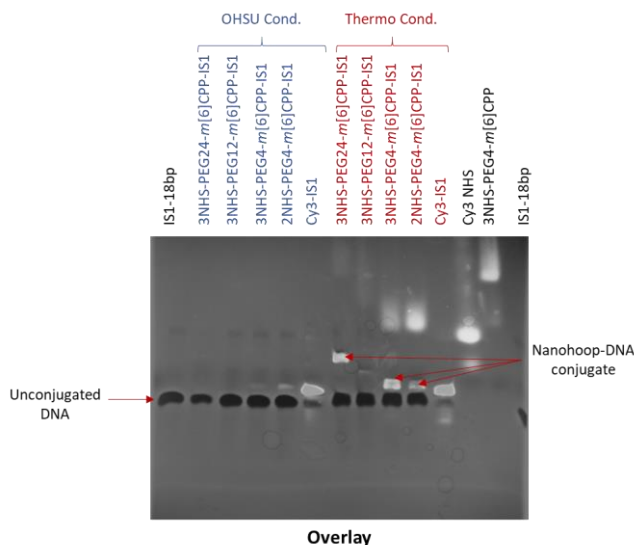


Figure 5.5. Gel analysis of nanohoop-DNA conjugates.

The molar ratio of the nanohoop was varied while either keeping the final concentration of DNA or nanohoop constant. All reactions done with varying molar ratio of hoop at a constant final hoop concentration of 5 mM showed conjugation of 90% or greater (**Figure 5.6a**). Reactions with final DNA concentration of 1.9 mM and varying equivalence of nanohoop showed less effective conjugation efficiency. Conjugation above 80% was not reached until a 30 mole excess of nanohoop was used and 99% conjugation was achieved at 40 mole excess. This study indicates the final nanohoop concentration is a key parameter when trying to achieve effective conjugation, though this has only been studied at 5 mM, so further exploration is required.

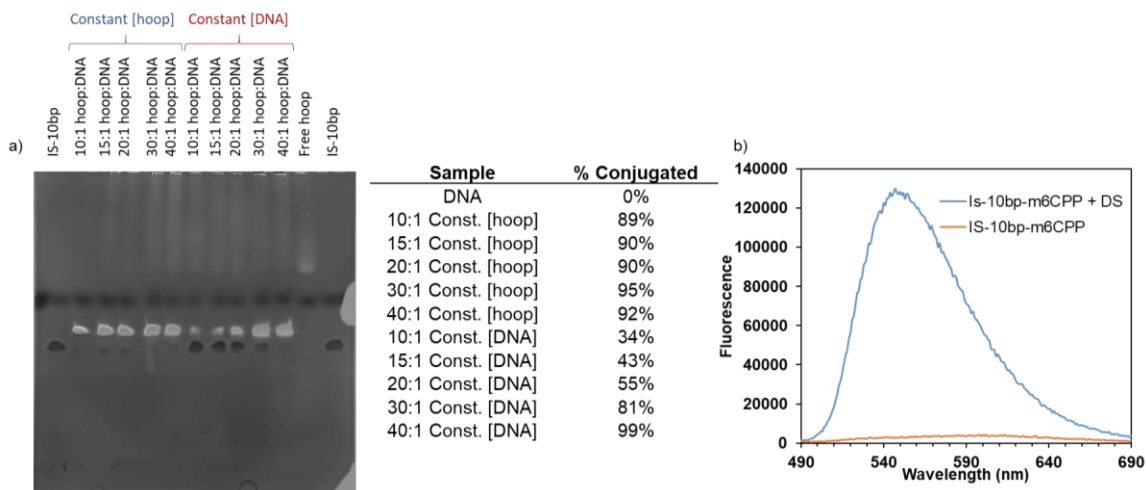


Figure 5.6. a) Gel analysis of nanohoop-DNA conjugations with constant hoop final concentration or constant DNA concentration. b) analysis of duplex formation of nanohoop-ssDNA conjugate and complementary ssDNA.

Next, we utilized SYBR green I (SG) to determine if the nanohoop-ssDNA conjugate could still form a duplex with a complementary ssDNA strand. When SG interacts with double stranded DNA (dsDNA) the fluorescence increases by greater than 1000 fold. Minimal SG fluorescence is observed when mixed with just the nanohoop-ssDNA conjugate as expected (**Figure 5.6b**, orange). However, when the complementary ssDNA is added, the SG fluorescence increases significantly (**Figure 5.6b**, blue). This indicates that the nanohoop is not interfering with the DNA duplex formation.

The conjugates were then utilized in two-photon fluorescence (TPF) imaging. TPF is advantageous it uses lower energy excitation, which is less harmful to cell samples. U2OS cells were fixed, permeabilized, and immunofluorescence was done using secondary detection. Microtubules were labelled with beta-tubulin monoclonal antibody, then samples were incubated with donkey anti-mouse secondary antibody that was modified with the complementary ssDNA. Conjugates were added to the labelled cells and were imaged using a Zeiss LSM 880 Laser-Scanning Confocal Microscope. Images from two different nanohoop-ssDNA conjugates are shown in **Figure 5.7**. Large fluorescent aggregates are observed and the TPF signal is relatively dim. One possibility for the low signal could be because the binding of the short ssDNA strands (10bp) is reversible. Therefore, we decided to conjugate the nanohoops to proteins to eliminate the possibility of reversible binding.

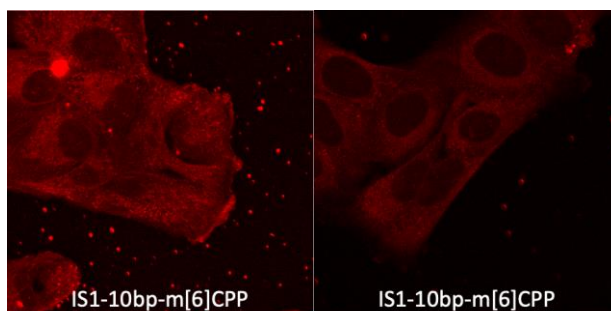


Figure 5.7. TPF imaging of DNA-nanohoop conjugates.

5.3 Conjugation of NHS-PEG_x-CPPs to proteins

Conjugation to anti-IgG was attempted with NHS-PEG₄-*m*[6]CPP, NHS-PEG₁₂-*m*[6]CPP, NHS-PEG₂₄-*m*[6]CPP and NHS-PEG₄[12]CPP in sodium bicarbonate buffer. Reactions were purified either by 50K centrifuge filters or P-30 spin columns. The protein fractions from both purifications were fluorescent under UV-irradiation, indicating that the antibody was labelled, however analysis of the conjugates by fluorescence microscopy did not show any signal. It is hypothesized that the nanohoop is interfering with the antibody binding. To investigate this, we turned to a protein that would be easier to label.

Concanavalin A (Con A) binds to α -glucopyranosyl residues and is a widely used lectin in cell biology. This protein is easier to label because the structure and active site are protected during the conjugation reaction through the presence of a sugar. Con A was dissolved in carbonate-bicarbonate buffer (pH 9) and 0.9% sodium chloride. α -methyl-D-mannopyranoside was added to protect the binding sites, then the NHS-PEG₄-nanohoop was added.¹⁹² The conjugates were purified by 10 K centrifuge filters.

These conjugates were analyzed by TPF imaging and only the *m*[6]CPP conjugates showed signal (**Figure 5.8**). It was thought that since the larger hoops did not show signal solubility could be the issue. Additional imaging in DMSO and Tween buffer still showed no signal for the larger hoops. To determine if the signal was low because the larger nanohoops were dimmer TPF fluorophores we analyzed the conjugates with one-photon imaging (**Figure 5.9**). HeLa cells were fixed and permeabilized followed by incubation with the Con A conjugates. Again, the *m*[6]CPP-Con A conjugate was the only conjugate that showed cell structure, while the *m*[8]CPP and [8]CPP conjugates

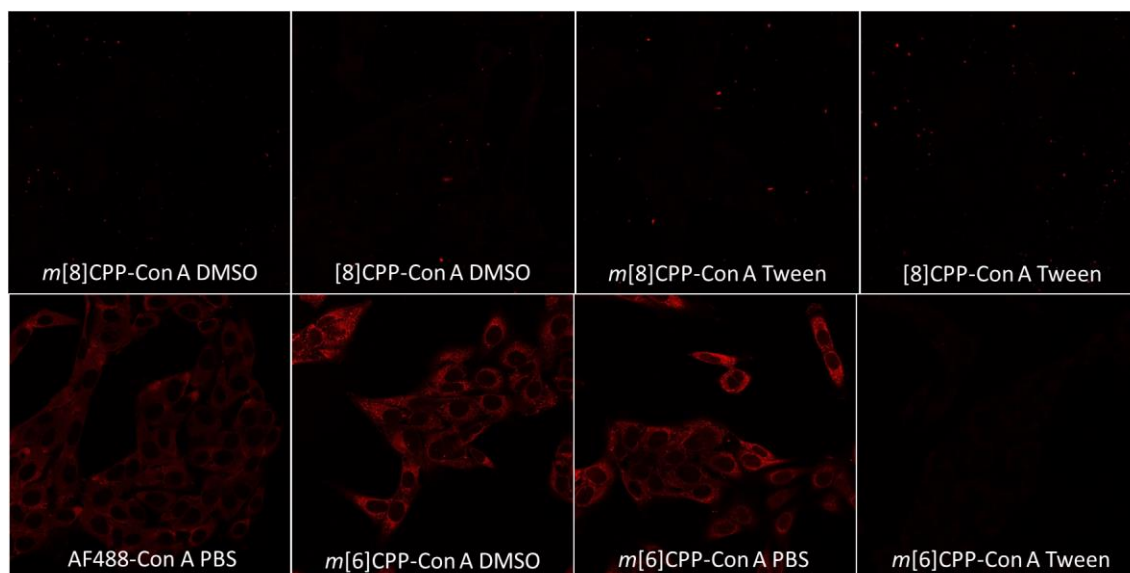


Figure 5.8. TPF imaging of Con A-nanohoop conjugates in different media.

showed large fluorescent aggregates. Furthermore, analyzing the degree of labeling for these conjugates showed inefficient conjugation (**Figure 5.9**). The optimal conjugation conditions and degree of labelling (DOL) have yet to be determined and the solubility of the larger hoops may have to be increased.

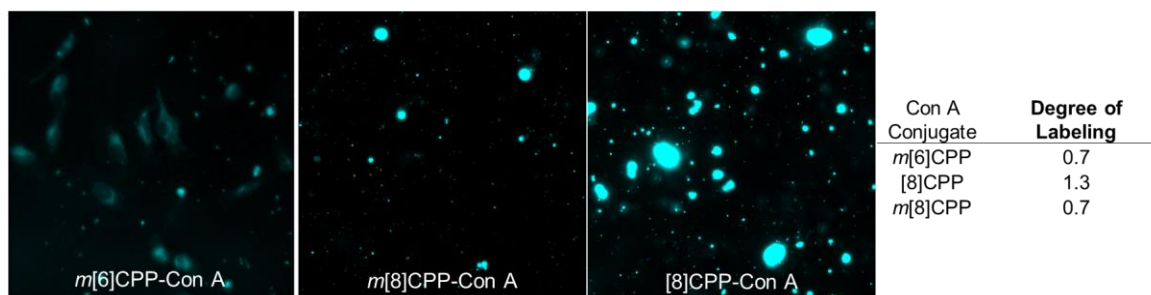


Figure 5.9. One-photon fluorescence imaging of Con A-nanohoop conjugates and degree of labelling.

5.4 Synthesis of biotin-CPP and antibody labeling

An alternative approach to directly labeling proteins such as antibodies without disrupting their function is to take advantage of the biotin-streptavidin host-guest binding. Using the alkyne *m*[6]CPP described above, a biotin linker was clicked on to make a streptavidin reactive probe. U2OS cells were fixed and permeabilized and

immunofluorescence staining was done using secondary detection. Microtubules were labelled with beta-tubulin monoclonal anti-body, then samples were incubated with a biotinylated donkey anti-mouse secondary antibody, followed by treatment with Streptavidin then addition of biotin-nanohoop conjugate. There was a greater signal from this method compared to the Con A conjugates, however questions remain regarding solubility issues with larger hoops.

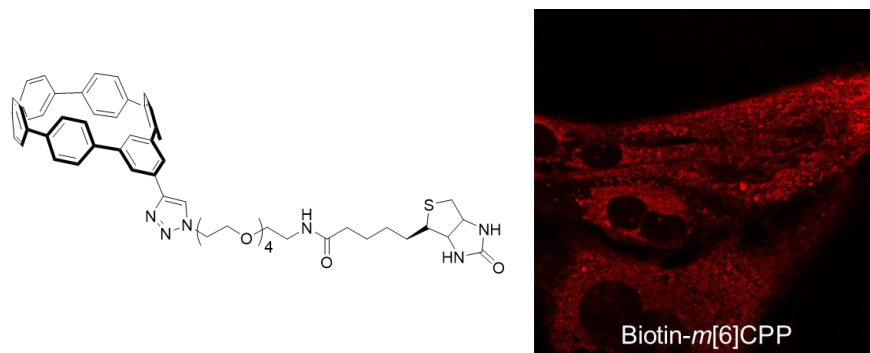


Figure 5.10. Synthesis and TPF imaging of biotin-nanohoop.

5.5 Conclusions and future work

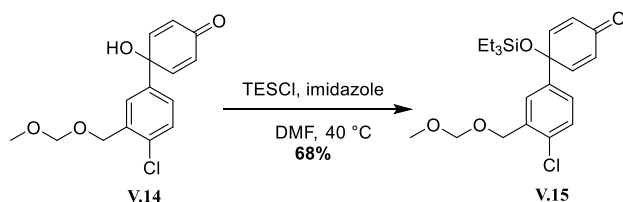
The optimal conjugation conditions have yet to be worked out, however great strides have been made in the use of nanohoops as biomolecular labels. For the first time, we demonstrate the covalent linkage of the novel nanohoop fluorophores to multiple different biomolecules. This was a necessary feat for the broader application of this novel scaffold. Furthermore, with the conjugates prepared we report the first TPF imaging of nanohoops.

Our future work is to test a more soluble derivative of the NHS-PEG₄-m[6]CPP, a sulfo-NHS ester. The sulfonate should increase the initial solubility of the hoop and in turn lead to improved conjugation efficiency.¹⁸⁹ Furthermore, we are working on synthesizing TriCEP linkers that will incorporate both additional solubility and functionality needed (ie. sulfonation and conjugation handle).¹⁹³

5.6 Experimental detail

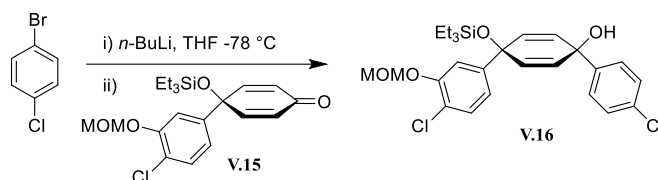
5.6.1 Synthesis and general experimental detail

All glassware was flame dried and cooled under an inert atmosphere of nitrogen unless otherwise noted. Moisture sensitive reactions were carried out under nitrogen atmosphere using Schlenk and standard syringe/septa techniques. Tetrahydrofuran, dichloromethane, dimethylformamide and 1,4-dioxane were dried by filtration through alumina according to the methods describes by Grubbs.¹³⁴ Silica column chromatography was conducted with Zeochem Zeoprep 60 Eco 40-63 μm silica gel. Automated flash chromatography was performed using a Biotage Isolera One. Recycling gel permeation chromatography (GPC) was performed using a Japan Analytical Industry LC-9101 preparative HPLC with JAIGEL-1H/JAIGEL-2H columns in series using CHCl_3 . Thin Layer Chromatography (TLC) was performed using Sorbent Technologies Silica Gel XHT TLC plates. Developed plates were visualized using UV light at wavelengths of 254 and 365 nm. ^1H NMR spectra were recorded at 500 MHz or 600 MHz on a Bruker Advance-III-HD NMR spectrometer. ^{13}C NMR spectra were recorded at 150 or 126 MHz on a Bruker Advance-III-HD NMR spectrometer. All ^1H NMR spectra were taken in CDCl_3 (referenced to TMS, δ 0.00 ppm). All ^{13}C NMR spectra were taken in CDCl_3 (referenced to chloroform, δ 77.16 ppm). Infrared absorption (IR) spectra were recorded on a Thermo Scientific Nicolet 6700 spectrometer equipped with a diamond crystal Smart ATR. Characteristic IR absorptions are reported in cm^{-1} . Mass spectra were obtained from the University of Oregon CAMCOR using ASAP. Compounds **V.1**¹⁴¹, **V.8**¹⁴¹, **V.19**¹⁴¹, Alkyne-m[6]CPP, $\text{PPh}_3 \text{Pd}^{136}$ Gen III and SPhos Pd Gen III¹³⁶ were prepared according to literature procedure.

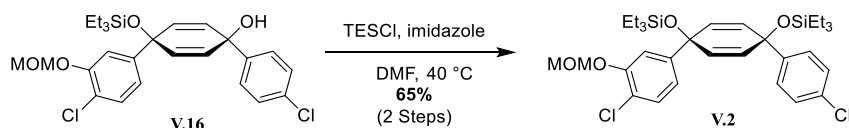


V.15. **V.14** was left by former postdoctoral researcher Evan Jackson and was confirmed by NMR. ^1H NMR (500 MHz, Chloroform-*d*) δ 7.57 (d, J = 1.9 Hz, 1H), 7.34 – 7.32 (m, 2H), 6.83 – 6.77 (m, 3H), 6.23 (d, J = 10.1 Hz, 2H), 4.75 (s, 3H), 4.66 (s, 3H), 3.41 (s, 4H). S9 (5 g, 17 mmol, 1 equiv) and imidazole (4.6 g, 68 mmol, 4 equiv) were added to a 250 mL round bottom flask and was equipped with a stir bar and septum. Dimethylformamide (85 mL) was added to the flask followed by triethylsilylchloride

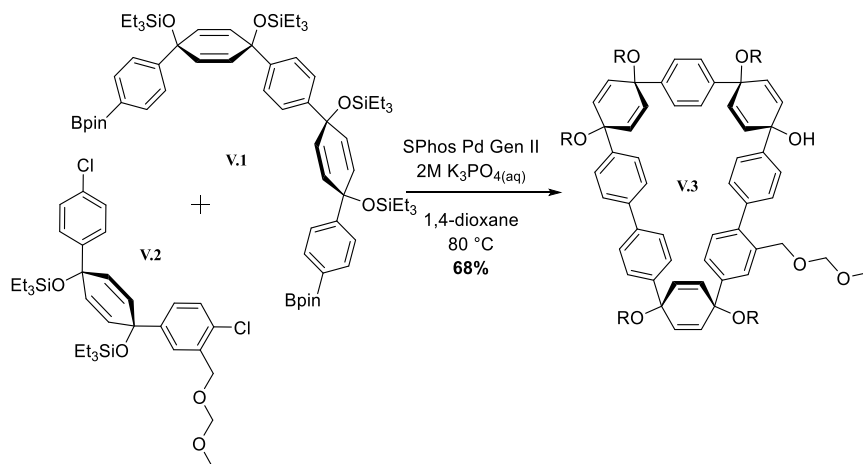
(8.54 mL, 51 mmol, 3 equiv) was added to the flask. The reaction mixture was heated to 40 °C in an oil bath and stirred for 3 hours. The reaction mixture was cooled to room temperature and quenched with a saturated solution of sodium bicarbonate (30 mL). The product was extracted with ethyl acetate (3 x 50 mL) and washed with 5% lithium chloride solution in water (1 x 20 mL) and brine (1 x 20 mL). The organic layers were then dried over sodium sulfate and concentrated to yield the crude product as a yellow oil. The product was purified by silica gel chromatography (0% to 20% ethyl acetate in hexanes) to give S10 as a slightly yellow oil (4.7 g, 68%). ¹H NMR (500 MHz, Chloroform-*d*) δ 7.57 (d, *J* = 1.9 Hz, 1H), 7.34 – 7.32 (m, 2H), 6.83 – 6.77 (m, 3H), 6.23 (d, *J* = 10.1 Hz, 2H), 4.75 (s, 3H), 4.66 (s, 3H), 3.41 (s, 4H), 0.98 (t, *J* = 7.9 Hz, 9H), 0.66 (q, *J* = 7.9 Hz, 6H).



V.16. 1-bromo-4-chlorobenzene (1.0 g, 5.3 mmol, 1.1 equiv) was added to a 100 mL one-neck round bottom flask equipped with a stir bar and septa. The flask was evacuated and filled with nitrogen. Tetrahydrofuran (27 mL) was added to the round bottom flask and was cooled for 30 minutes at –78 °C with an IPA/dry ice bath. *n*-BuLi (2.1 mL, 16 mmol, 1.05 equiv, 2.5 M in hexanes) was added dropwise over 3 minutes. **V.15** (2 g, 5 mmol, 1 equiv) added to the reaction flask dropwise and the reaction was allowed to stir for an hour at –78 °C. The reaction was quenched with deionized water (10 mL) while at –78 °C and deionized water (5 mL) was added again when the ice bath was removed. The product was extracted with ethyl acetate (3 x 20 mL) and washed with brine (3 x 20). The organic layers were dried over sodium sulfate and concentrated to yield the crude product S11 as a yellow oil. The product was not purified.

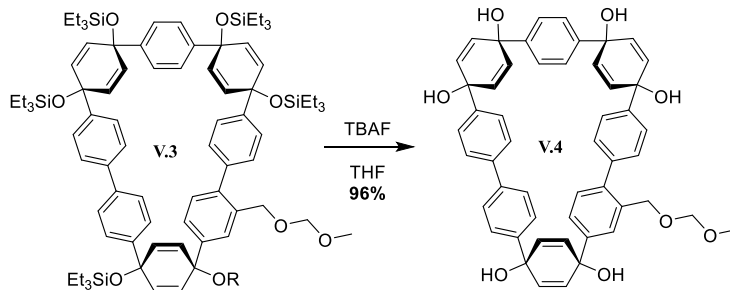


V.2. Crude **V.16** and imidazole (1.3 g, 20 mmol, 4 equiv) were added to a 250 mL round bottom flask and was equipped with a stir bar and septum. Dimethylformamide (24 mL) was added to the flask followed by triethylsilylchloride (1.2 mL, 7.3 mmol, 1.5 equiv) was added to the flask. The reaction mixture was heated to 40 °C in an oil bath and stirred overnight. The reaction mixture was cooled to room temperature and quenched with a saturated solution of sodium bicarbonate (20 mL). The product was extracted with ethyl acetate (3 x 30 mL) and washed with 5% lithium chloride solution in water (1 x 20 mL) and brine (1 x 20 mL). The organic layers were then dried over sodium sulfate and concentrated to yield the crude product as a yellow oil. The product was purified by automated flash silica gel chromatography (0% to 10% ethyl acetate in hexanes) to give **7** as a clear oil (2 g, 65% 2 steps). ¹H NMR (500 MHz, Chloroform-*d*) δ 7.40 (d, *J* = 2.2 Hz, 1H), 7.26 (d, *J* = 4.7 Hz, 2H), 7.24 – 7.20 (m, 2H), 7.19 (d, *J* = 2.3 Hz, 0H), 5.96 (d, *J* = 1.0 Hz, 4H), 4.68 (s, 2H), 4.59 (s, 2H), 0.93 (td, *J* = 8.0, 5.0 Hz, 18H), 0.63 – 0.56 (m, 13H). ¹³C NMR (126 MHz, Chloroform-*d*) δ 144.76, 144.47, 135.43, 133.00, 131.95, 131.49, 131.40, 129.05, 128.29, 127.32, 126.94, 126.18, 96.21, 77.26, 77.01, 76.76, 71.15, 71.02, 66.70, 55.40, 14.12, 7.01, 6.42.



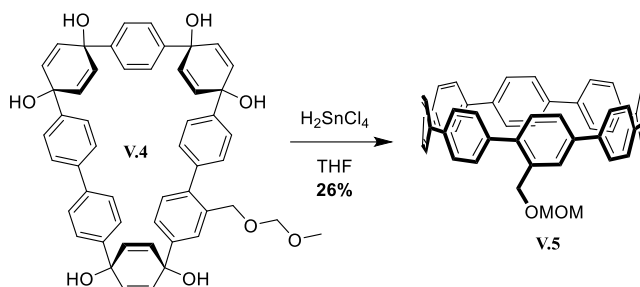
V.3. **V.1** (219 mg, 0.19 mmol, 1.2 equiv), **V.2** (100 mg, 0.16 mmol, 1 equiv) and SPhos Gen-II (11 mg, 0.016 mmol, 0.1 equiv) were added to a 100 mL round bottom flask equipped with a stir bar. The flask was evacuated (5 minutes) and purged with nitrogen 5 times. 1,4-dioxane and K₃PO₄ were sparged for at least 1 hour prior to use. The round bottom flask was equipped with a septa and 1,4-dioxane (53 mL) was added. This

solution was sparged with nitrogen for 30 minutes. The round bottom flask was placed in a preheated oil bath (80 °C) for 5 minutes then K₃PO₄ (5.2 mL, 0.03 equiv, 2 M in deionized water) was added. The reaction was allowed to stir at 80 °C overnight. The reaction mixture was allowed to cool to room temperature and filtered through a fritted suction funnel filled with Celite. The RBF was rinsed with dichloromethane and filtered through the Celite plug. The filtrate was added to a separatory funnel along with deionized water (50 mL) and the product was extracted (2 x 70) with dichloromethane. The organic layer was washed with brine (1 x 50 mL), dried over sodium sulfate and concentrated. The product was purified by automated flash silica chromatography (0% to 10% ethyl acetate in hexanes) and gel permeation size exclusion chromatography to give **V.3** (190 mg, 68%). ¹H NMR (600 MHz, Chloroform-*d*) δ 7.47 – 7.45 (m, 5H), 7.44 – 7.38 (m, 7H), 7.28 (d, *J* = 8.4 Hz, 2H), 7.25 (s, 1H), 7.03 (t, *J* = 7.9 Hz, 3H), 6.93 (dd, *J* = 8.1, 1.9 Hz, 1H), 6.18 (d, *J* = 10.0 Hz, 2H), 6.09 – 6.02 (m, 6H), 5.95 (d, *J* = 10.1 Hz, 2H), 5.90 (d, *J* = 10.1 Hz, 2H), 4.47 (s, 2H), 4.37 (s, 2H), 3.15 (s, 3H), 0.98 (dt, *J* = 7.9, 6.7 Hz, 40H), 0.93 (td, *J* = 7.9, 6.0 Hz, 22H), 0.67 (ddt, *J* = 23.8, 9.8, 7.7 Hz, 29H), 0.55 (p, *J* = 8.0 Hz, 14H). (*m/z*): [M]⁺ calcd. for C₈₇H₁₃₀O₈Si₆, 1470.84; found, 1492 ([M]⁺+Na).

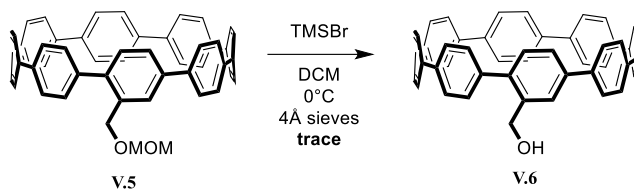


V.4. Tetrahydrofuran (6 mL) was added to a 25 mL round bottom flask containing **V.3** (8.2 mg, 0.56 mmol, 1 equiv), which was equipped with a stir bar and septa. Tetra-*n*-butylammonium fluoride (5.6 mL, 5.6 mmol, 10 equiv, 1 M in tetrahydrofuran) was added to the reaction flask and this was allowed to stir for 2 hours at room temperature. The reaction was quenched with deionized water (3 mL) and was concentrated to remove the tetrahydrofuran. The reaction mixture was filtered through a Buchner funnel, washed with deionized water yielding **V.4** as a white solid (422 mg, 96%). ¹H NMR (600 MHz,

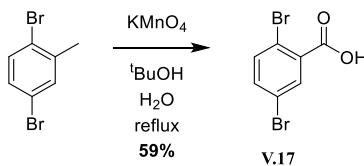
DMSO-*d*₆) δ 7.57 (d, *J* = 8.2 Hz, 2H), 7.48 (d, *J* = 8.2 Hz, 2H), 7.45 (d, *J* = 8.3 Hz, 2H), 7.42 – 7.40 (s, 6H), 7.40 (d, *J* = 2.0 Hz, 3H), 7.32 (dd, *J* = 7.8, 6.0 Hz, 3H), 7.11 (d, *J* = 8.3 Hz, 2H), 7.04 (d, *J* = 7.9 Hz, 1H), 7.03 – 7.00 (m, 1H), 6.10 (d, *J* = 9.9 Hz, 2H), 6.03 (d, *J* = 9.9 Hz, 2H), 5.88 – 5.81 (m, 9H), 5.58 (d, *J* = 10.7 Hz, 2H), 4.42 (s, 2H), 4.29 (s, 2H), 3.04 (s, 3H).



V.5. SnCl₂•H₂O (180 mg, 0.80 mmol) was added to a 100 mL round bottom flask equipped with a stir bar and septum. Tetrahydrofuran (20 mL) was added to the RBF followed by hydrochloric acid (0.13 mL, 1.6 mmol, 12 M) to make a H₂SnCl₂ solution. This was allowed to stir at room temperature for 30 minutes. **V.4** (9.5 mg, 0.01 mmol, 1 equiv) was added to a 5 mL round bottom flask that was equipped with a stir bar and septum. The flask was evacuated and refilled with nitrogen. H₂SnCl₂ solution (1 mL, 0.28 mmol, 3.3 equiv, 0.04 M) was added and the reaction was allowed to stir for an hour at room temperature. It was quenched with saturated sodium bicarbonate (2 mL) and filtered through a fritted suction funnel with a celite plug. The filtrate was transferred to a separatory funnel, deionized water (5 mL) was added and the product was extracted with dichloromethane (3 x 5 mL). The organic layers were washed with brine (2 x 5 mL), dried over sodium sulfate and concentrated to give a yellow solid. The product was purified by silica gel chromatography (preparatory plate, dichloromethane) to give **V.5** as a yellow solid (2.1 mg, 26%). ¹H NMR (600 MHz, Chloroform-*d*) δ 7.83 (d, 1H), 7.52 (d, *J* = 8.9 Hz, 4H), 7.49 (d, *J* = 9.8 Hz, 4H), 7.46 (d, *J* = 5.4 Hz, 11H), 7.44 (d, *J* = 4.5 Hz, 2H), 7.42 (d, *J* = 8.2 Hz, 2H), 7.37 (d, *J* = 8.4 Hz, 2H), 7.31 (d, *J* = 8.6 Hz, 2H), 7.08 (d, 1H), 7.01 (d, *J* = 7.8 Hz, 1H), 6.84 (d, *J* = 8.4 Hz, 1H), 4.89 (s, 2H), 4.81 (s, 2H), 3.47 (s, 3H). (*m/z*): [M]⁺ calcd. for C₅₁H₃₈O₂, 682.29; found, 682.

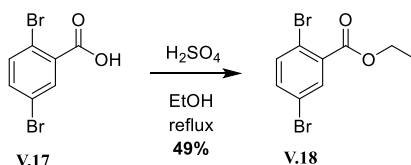


V.6. 4Å molecular sieves were added to 15 mL round bottom flask equipped with a stir bar. The round bottom flask was put under vacuum and the sieves and round bottom flask were flame-dried again to ensure the sieves were activated. **V.5** (6.2 mg, 0.009 mmol, 1 equiv) was added to the flask, followed by dichloromethane (1 mL). The round bottom flask was evacuated and filled with nitrogen. The RBF and was placed in an ice bath and allowed to stir for 15 minutes. Trimethylsilyl bromide (0.04 mL, 0.2 mmol, 20 equiv) was added to the reaction mixture. The reaction was allowed to stir at 0 °C for one hour. The reaction was quenched with deionized water (1 mL) at 0 °C and deionized water (1 mL) was added once the septa was removed. The product was extracted (3 x 5 mL) with dichloromethane and the combined organic layers were washed 1x with brine, dried over sodium sulfate and concentrated to yield the crude product as a yellow solid. The product was purified by silica gel chromatography (preparatory plate, 50% dichloromethane in hexanes) to yield **V.6** as a yellow solid in trace amounts. $^1\text{H NMR}$ (600 MHz, Chloroform-*d*) δ 7.88 (d, $J = 2.0$ Hz, 1H), 7.56 – 7.36 (m, 28H), 6.96 (dd, $J = 8.5, 2.0$ Hz, 1H), 6.78 (d, $J = 8.4$ Hz, 1H), 4.89 (s, 2H). (m/z): $[\text{M}]^+$ calcd. for $\text{C}_{49}\text{H}_{34}\text{O}$, 638.26; found, 638.

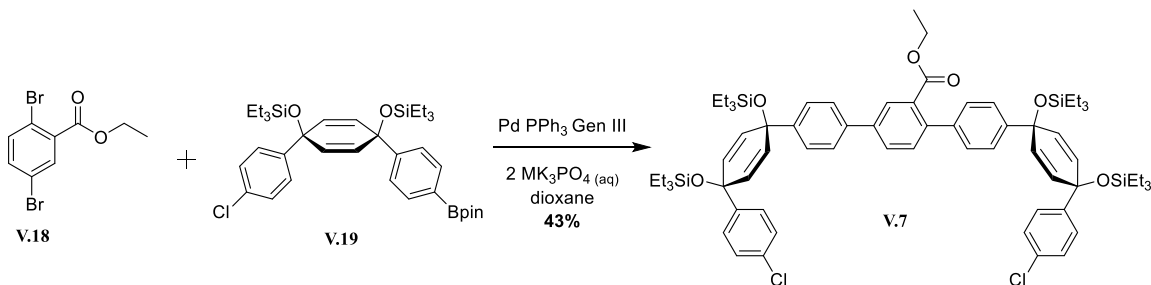


V.17. KMnO_4 (42 g 0.35 mol, 4.4 equiv), 2,5-dibromotoluene (11 mL, 0.08 mol, 1 equiv), deionized water (105 mL) and tert butyl alcohol (105 mL) were put in a 500 mL round bottom flask (not flame-dried) equipped with a stir bar. The round bottom flask was equipped with a water condenser and refluxed in an oil bath, open to air, at 85 °C over 2 nights. The reaction mixture was filtered through a fritted suction funnel filled with Celite that was protected with filter paper on the top. The round bottom flask was rinsed with deionized water and filtered through the Celite plug. The filtrate was acidified with 2 M

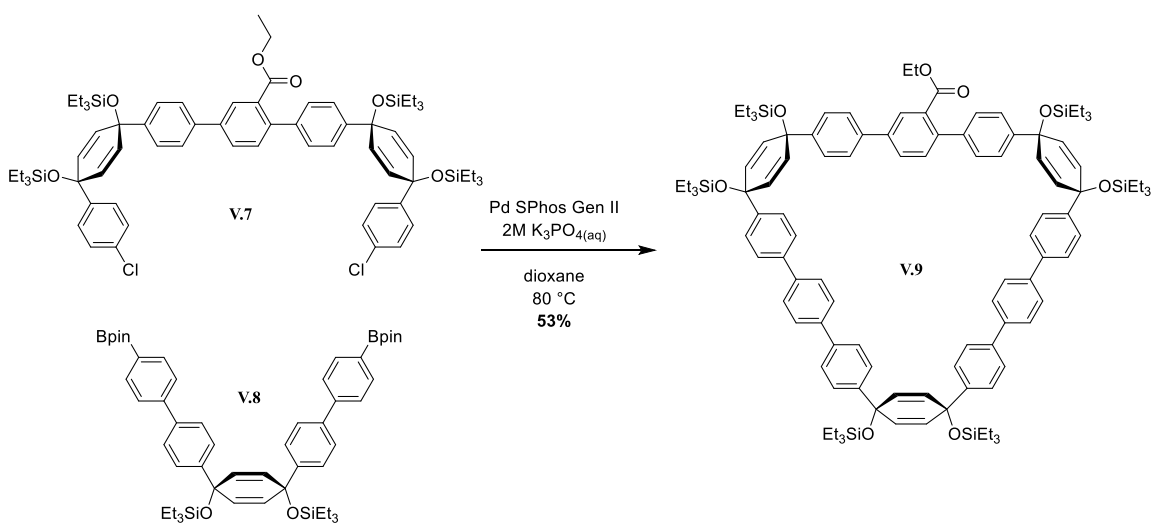
hydrochloric acid until there was a large amount of white precipitate. The solution was filtered with a fritted suction funnel. The filtrate was acidified again, resulting in more white precipitate, which was filtered. The product was heated under vacuum to remove any water, yielding **S21** as a white solid (13.3 g, 59%). $^1\text{H NMR}$ (500 MHz, $\text{DMSO-}d_6$) δ 13.72 (s, 1H), 7.88 (d, $J = 2.4$ Hz, 1H), 7.67 (d, $J = 8.5$ Hz, 1H), 7.63 (dd, $J = 8.6, 2.3$ Hz, 1H).



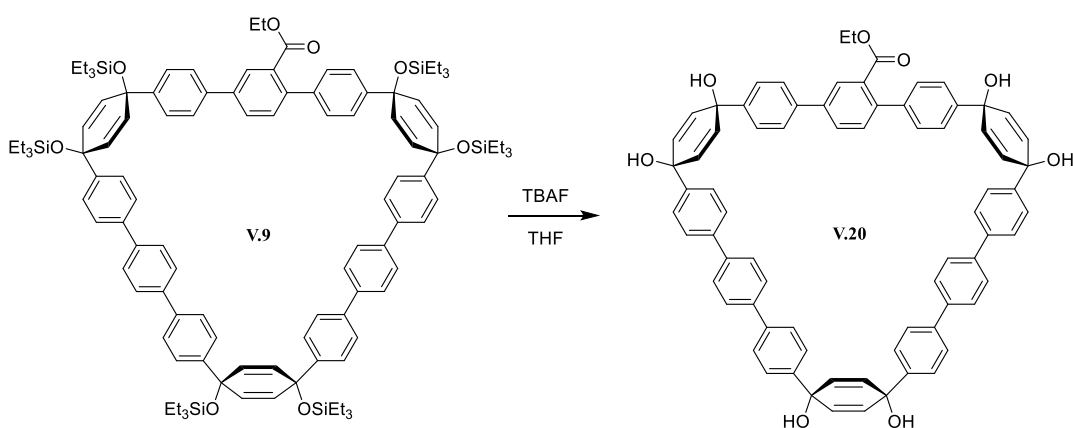
V.18. **V.17** (1.01 g, 3.6 mmol, 1 equiv) was added to a 50 mL round bottom flask (not flame-dried) equipped with a stir bar and dissolved in ethanol (22 mL). Concentrated sulfuric acid (0.38 mL, 7.1 mmol, 2 equiv) was added to the reaction mixture. The solution was turbid and became clear and colorless upon heating. The reaction was refluxed at 100 °C for 3 days. The reaction mixture was allowed to cool to room temperature. Dichloromethane was added and the solution was transferred to a separatory funnel. Deionized water (10 mL) was added and the product was extracted with dichloromethane (3 x 20 mL). The organic layers were washed with brine (1 x 10), dried over sodium sulfate and concentrated to yield a clear oil. The product was purified by silica chromatography (dichloromethane) to yield **V.18** as a clear colorless oil (542 mg, 49%). $^1\text{H NMR}$ (500 MHz, $\text{Chloroform-}d$) δ 7.90 (d, $J = 2.5$ Hz, 1H), 7.52 (d, $J = 8.5$ Hz, 1H), 7.44 (dd, $J = 8.5, 2.4$ Hz, 1H), 4.40 (q, $J = 7.2$ Hz, 2H), 1.41 (t, $J = 7.1$ Hz, 3H). $^{13}\text{C NMR}$ (151 MHz, $\text{Chloroform-}d$) δ 164.87, 135.69, 135.36, 134.03, 134.00, 120.99, 120.36, 77.24, 77.03, 76.82, 62.07, 53.44, 14.19.



V.7, **V.18** (100 mg, 0.325 mmol, 1 equiv), **V.19** (466.6 mg, 0.714 mmol, 2.2 equiv) and Pd(dppf)₂Cl₂ (14 mg, 0.016 mmol, 0.05 equiv) were added to a 15 mL round bottom flask equipped with a stir bar. The flask was evacuated (5 minutes) and purged with nitrogen 5 times. 1,4-dioxane and K₃PO₄ were sparged for at least 1 hour prior to use. The round bottom flask was equipped with a septa and 1,4-dioxane (1.6 mL) was added to the round bottom flask. This solution was sparged with nitrogen for 5 minutes. The round bottom flask was placed in a preheated oil bath (80 °C) for 5 minutes then K₃PO₄ (0.16 mL, 2 M in deionized water) was added. The reaction was allowed to stir at 80 °C overnight. The reaction mixture was allowed to cool to room temperature. It was then filtered through a fritted suction funnel with Celite. The round bottom flask was rinsed with dichloromethane and filtered through the Celite plug. The filtrate was added to a separatory funnel along with deionized water (50 mL) and the product was extracted (2 x 20) with dichloromethane. The organic layer was washed with brine (1 x 20 mL), dried over sodium sulfate and concentrated. The product was purified by automated flash silica gel chromatography (0% to 10% ethyl acetate in hexanes) to yield **V.7** as white bubbles (371.4 mg, 43%). ¹H NMR (500 MHz, Chloroform-*d*) δ 8.01 (d, *J* = 2.0 Hz, 1H), 7.73 (dd, *J* = 8.0, 2.0 Hz, 1H), 7.56 (d, *J* = 8.5 Hz, 2H), 7.42 (dd, *J* = 12.6, 8.2 Hz, 4H), 7.35 (d, *J* = 8.4 Hz, 2H), 7.30 – 7.26 (m, 5H), 7.23 (d, *J* = 8.6 Hz, 4H), 6.04 (d, *J* = 10.1 Hz, 4H), 5.97 (dd, *J* = 10.2, 6.6 Hz, 4H), 4.10 (q, *J* = 7.1 Hz, 1H), 1.54 (s, 3H), 0.99 (d, *J* = 7.1 Hz, 2H), 0.95 (tdd, *J* = 7.9, 4.9, 2.7 Hz, 36H), 0.66 – 0.59 (m, 24H).

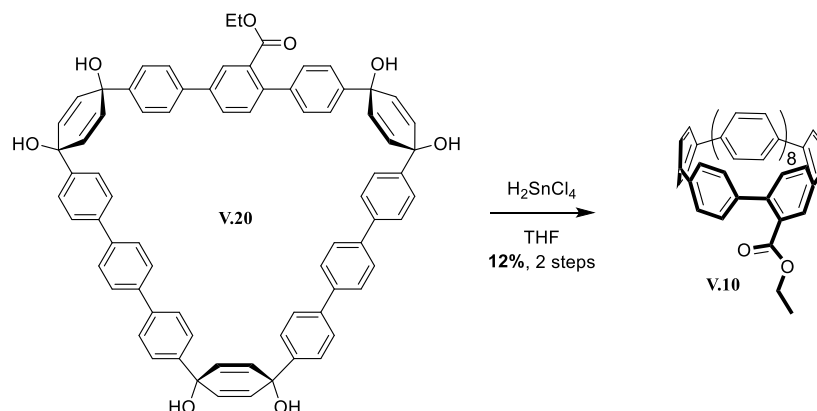


V.9. **V.7** (50 mg, 0.0416 mmol, 1 equiv), **V.8** (44.8 mg, 0.0500 mmol, 1.2 equiv) and Pd Sphos Gen III (3.3 mg, 0.00416 mmol, 0.1 equiv) were added to a 50 mL round bottom flask equipped with a stir bar. The flask was evacuated (5 minutes) and purged with nitrogen 5 times. 1,4-dioxane and K_3PO_4 were sparged for at least 1 hour prior to use. The round bottom flask was equipped with a septa and 1,4-dioxane (13.9 mL) was added to the round bottom flask. The round bottom flask was placed in a preheated oil bath (80 °C) for 5 minutes then K_3PO_4 (1.4 mL, 2 M in deionized water) was added. The reaction was allowed to stir at 80 °C overnight. The reaction was cooled to room temperature and filtered through a fritted suction funnel filled with Celite. The round bottom flask was rinsed with dichloromethane and filtered through the Celite plug. The filtrate was added to a separatory funnel along with deionized water (20 mL) and the product was extracted (3 x 20) with dichloromethane. The organic layer was washed with brine (1 x 20 mL), dried over sodium sulfate and concentrated to yield the crude product as an orange oil. The product was purified by automated flash silica gel chromatography (0% to 10% ethyl acetate in hexanes) to yield a clear oil. Acetone (5 mL) was added to the oil and sonicated to yield **V.9** as a pale yellow solid. 1H NMR (600 MHz, Chloroform-*d*) δ 8.03 (s, 1H), 7.76 (d, $J = 7.9$ Hz, 4H), 7.69 (d, $J = 9.4$ Hz, 6H), 7.63 – 7.57 (m, 7H), 7.48 (ddd, $J = 14.7, 11.6, 8.2$ Hz, 13H), 7.32 (d, $J = 8.1$ Hz, 4H), 6.07 (d, $J = 3.7$ Hz, 12H), 4.10 (q, $J = 7.1$ Hz, 2H), 1.37 (s, 3H), 0.99 (qd, $J = 9.0, 8.2, 3.8$ Hz, 75H), 0.72 – 0.62 (m, 39H).



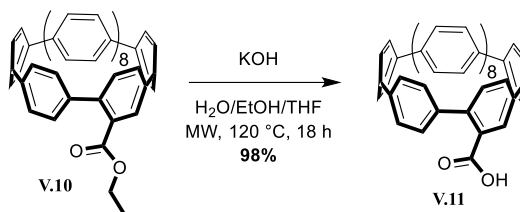
V.20. Tetrahydrofuran (0.28 mL) was added to a 5 mL round bottom flask containing **V.9** (50 mg, 0.03 mmol, 1 equiv), which was equipped with a stir bar and septa. Tetra-*n*-butylammonium fluoride (0.28 mL, 0.30 mmol, 10 equiv, 1 M in tetrahydrofuran) was

added to the reaction flask and this was allowed to stir for 2 hours at room temperature. The reaction was quenched with deionized water (5 mL). The reaction mixture was filtered through a Buchner funnel, washed with deionized water yielding crude **V.20** as a white solid. The product was not purified further before use in subsequent reaction.

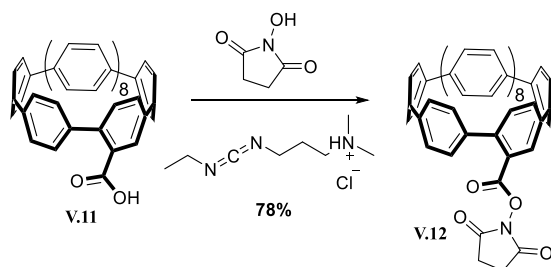


V.10. $\text{SnCl}_2 \cdot \text{H}_2\text{O}$ (181 mg, 0.80 mmol) was added to a 100 mL RBF equipped with a stir bar and septum. Tetrahydrofuran (20 mL) was added to the RBF followed by hydrochloric acid (0.13 mL, 1.6 mmol, 12 M). This was allowed to stir at room temperature for 30 minutes. TCL300 (200 mg, 0.18 mmol, 1 equiv) was added to a 25 mL RBF that was equipped with a stir bar and septum. The flask was evacuated and refilled with nitrogen. H_2SnCl_2 solution (15.2 mL, 0.61 mmol, 3.3 equiv, 0.04 M) was added and the reaction was allowed to stir for an hour at room temperature. The reaction was quenched with saturated sodium bicarbonate (5 mL). The filtrate was transferred to a separatory funnel and the product was extracted with dichloromethane (3 x 20 mL). The organic layers were washed with brine (1 x 20 mL), dried over sodium sulfate and concentrated to give the crude product as a yellow solid. The product was purified by alumina preparatory plate (70/30 dichloromethane/hexanes) to give **V.10** as a white solid (22.2 mg, 12%). ^1H NMR (600 MHz, Chloroform-*d*) δ 8.40 (d, $J = 2.0$ Hz, 1H), 7.66 (d, $J = 9.2$ Hz, 41H), 7.57 (d, $J = 8.3$ Hz, 2H), 7.46 (dd, $J = 8.3, 2.1$ Hz, 1H), 7.37 (d, $J = 8.3$ Hz, 2H), 7.17 (d, $J = 8.3$ Hz, 1H), 4.37 (q, $J = 7.2$ Hz, 2H), 1.28 (t, $J = 7.1$ Hz, 4H). ^{13}C NMR (151 MHz, CDCl_3) δ 168.34, 141.01, 140.38, 138.88, 138.80, 138.70, 138.63, 138.61, 138.56, 138.54, 138.49, 138.45, 138.38, 138.20, 137.92, 133.36, 131.57, 129.81,

128.83, 127.65, 127.60, 127.49, 127.47, 127.41, 127.39, 127.36, 127.32, 127.31, 127.28, 127.25, 127.21, 127.14, 61.28, 31.93, 13.98, 6.81, 6.42, 1.02.

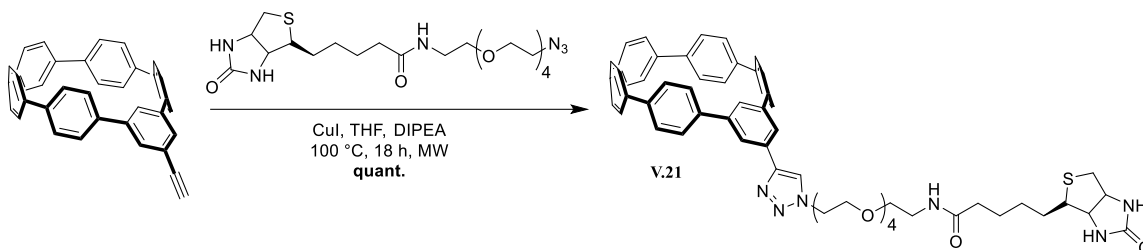


V.11. **V.10** (9.5 mg, 0.01 mmol, 1 equiv), KOH (22 mg, 0.4 mmol, 40 equiv), water (0.08 mL), ethanol (1 mL) and tetrahydrofuran (1 mL) were added to a 2-5 mL microwave vial equipped with a stir bar. The vial was capped and the reaction was run at 120 °C for 18 hours on very high. The reaction mixture was acidified with concentrated hydrochloric acid and the product was extracted with ethyl acetate (3 x 20). The organic layer was washed with brine (1 x 20 mL), dried over sodium sulfate and concentrated to yield **V.11** as a yellow solid (9 mg, 98%). ¹H NMR (600 MHz, Chloroform-*d*) δ 8.49 (d, *J* = 2.0 Hz, 1H), 7.62 (d, *J* = 10.4 Hz, 39H), 7.55 (d, *J* = 8.2 Hz, 2H), 7.47 (dd, *J* = 8.4, 2.0 Hz, 2H), 7.39 (d, *J* = 8.2 Hz, 2H), 7.14 (d, *J* = 8.2 Hz, 1H).



V.12. **V.11** (6 mg, 0.01 mmol, 1 equiv), N-hydroxysuccinimide (1.1 mg, 0.009 mmol, 1.5 equiv) and 1-Ethyl-3-(3-dimethylaminopropyl)carbodiimide (2.4 mg, 0.013 mmol, 2 equiv) were added to a 5 mL flame-dried RBF equipped with a stir bar and septum. The RBF was purged with nitrogen and 1 mL of DCM was added. The reaction was allowed to stir overnight. The reaction was diluted with deionized water (4 mL) and transferred to a separatory funnel. The product was extracted with dichloromethane (3 x 10 mL), washed with brine (1 x 10 mL) and dried over sodium sulfate. This was decanted and concentrated to yield a yellow solid. The product was purified by silica chromatography (preparatory plate, dichloromethane, yellow middle spot) to give **V.12** as a yellow solid

(5 mg, 78%). ^1H NMR (600 MHz, Chloroform-*d*) δ 8.54 (d, $J = 2.1$ Hz, 1H), 7.68 (d, $J = 8.4$ Hz, 3H), 7.62 (d, $J = 39.5$ Hz, 36H), 7.53 (dd, $J = 8.3, 2.1$ Hz, 1H), 7.48 (d, $J = 8.5$ Hz, 2H), 7.21 (d, $J = 8.4$ Hz, 1H), 2.88 (d, $J = 12.7$ Hz, 4H).



V.21. IV.4 (3.2 mg, 0.0067 mmol, 1 equiv), copper iodide (0.2 mg, 0.0001 mmol, 0.1 equiv), and azido-PEG4-biotin (3.3 mg, 0.0067 mmol, 1 equiv) were added to a 0.2-0.5 mL microwave vial. The vial was equipped with a stir bar, septum and was evacuated and purged with nitrogen. Tetrahydrofuran (0.4 mL) was added to the vial followed by dry DIPEA (dried over sieves) (0.1 mL, 0.45 mmol, 87 equiv), which was then sealed and heated to 100 °C in the microwave for 18 hours. The reaction mixture was transferred to a scintillation vial and was concentrated to remove DIPEA. The product was dissolved in dichloromethane and water was added to remove the copper. The product was extracted with dichloromethane (3 x 5 mL), dried over sodium sulfate and concentrated to yield product as a green solid (6.5 mg, quant.). ^1H NMR (500 MHz, Chloroform-*d*) δ 8.13 (s, 1H), 7.93 (d, $J = 1.6$ Hz, 1H), 7.42 (q, $J = 9.4$ Hz, 9H), 7.19 (d, $J = 8.2$ Hz, 3H), 6.67 – 6.61 (m, 1H), 5.58 (s, 1H), 5.36 (s, 1H), 4.65 (t, $J = 5.0$ Hz, 2H), 4.60 (s, 1H), 4.49 – 4.45 (m, 1H), 4.31 – 4.27 (m, 1H), 3.96 (t, $J = 5.0$ Hz, 2H), 3.69 – 3.59 (m, 8H), 3.56 (s, 3H), 3.41 (s, 2H), 3.16 – 3.10 (m, 2H), 2.90 (dd, $J = 12.9, 5.1$ Hz, 2H), 2.70 (t, $J = 13.2$ Hz, 2H), 2.18 (q, $J = 6.9$ Hz, 2H), 1.42 (q, $J = 7.6$ Hz, 3H). ^{13}C NMR (126 MHz, CDCl_3) δ 173.09, 143.26, 142.30, 139.31, 139.24, 137.49, 136.41, 136.28, 131.69, 129.47, 128.09, 127.86, 127.58, 127.25, 121.44, 119.63, 70.60, 70.56, 70.49, 70.43, 70.08, 69.93, 69.56, 61.76, 60.11, 55.37, 50.45, 40.59, 39.16, 35.83, 30.93, 29.71, 28.08, 25.49. HRMS (ASAP) (m/z): [M] calculated for $\text{C}_{58}\text{H}_{61}\text{N}_6\text{O}_6\text{S}$, 969.4373; found, 969.4468.

5.6.2 Cell Studies

One-Photon Imaging

HeLa cells (ATCC CCL-2) were cultured in high glucose Dulbecco's modified Eagle's medium (DMEM) supplemented with 10% fetal bovine serum (FBS) and 1% penicillin/streptomycin at 37 °C under 5% CO₂. HeLa cells were then plated and incubated at 37 °C under 5% CO₂ overnight before performing experiments. HeLa cells were plated in poly-D-lysine coated glass bottom dishes (MatTek) containing 2.00 mL of 10% FBS DMEM. The next day, adherent cells were washed 2X with PBS. 1 mL of 4% formaldehyde solution was added and cells were incubated for 15 minutes at room temperature. The fixing solution was removed and the cells were rinsed 3x with PBS. 1 mL of 0.5% Triton®X-100 solution was added and incubated for 15 minutes at room temperature. The permeabilization solution was removed and the cells were washed 2x with PBS. 1.5 mL of 3% bovine serum albumin solution was added and incubated for 60 minutes at room temperature. The blocking solution was removed and the cells were rinsed 2x with PBS. Cells were then incubated in 2 mL PBS containing Con A-nanohoop conjugates or Alexa Fluor 488-Con A control for 30 minutes at room temperature. After this incubation, the media was aspirated, and cells were again rinsed 2X with PBS and imaged in PBS on a Zeiss LSM 880 confocal microscope.

Two-Photon Imaging

U2OS cells (ATCC HTB-96)) were cultured in high glucose Dulbecco's modified Eagle's medium (DMEM, ThermoFisher, 11995073) supplemented with 10% fetal bovine serum (FBS, Fisher Scientific, 26-140-079) at 37 °C under 5% CO₂. Cells were then plated and incubated at 37 °C under 5% CO₂ overnight before performing experiments. U2OS cells were plated on Lab-Tek® II eight-well chambered coverglasses (ThermoFisher, 155360) containing 10% FBS DMEM. The next day, adherent cells were washed 1x with PBS. 250 µL of 3.7% formaldehyde solution with 0.1% glutaraldehyde (Millipore Sigma, G6257) was added and cells were incubated for 20 minutes at room temperature. The fixing solution was removed and the cells were rinsed 2x with PBS. 350 µL of 0.2% Triton®X-100 (Sigma, X100) +3% BSA (Fisher Scientific, BP1600) solution was added and incubated for 30 minutes at room temperature. The permeabilization/blocking solution was removed and the cells were washed 2x with PBS. Cells were then incubated with beta-tubulin monoclonal antibody (1:200, ThermoFisher

Scientific, 32-2600) in 3% BSA solution and incubated for 50 minutes at room temperature. The staining solution was removed and the cells were washed 3x with PBS, 5 minutes per wash. Cells were then incubated with donkey anti-Mouse secondary antibody conjugated to a 32-mer DNA oligo (~8 ug/ml, made via DBCO-azide click chemistry)) in 3% BSA + 5% salmon sperm DNA (ThermoFisher Scientific, 32-2600) in PBS and incubated for 45 minutes at room temperature. The staining solution was removed and the cells were washed 3x with PBS, 5 minutes per wash, and then post-fixed for 10 minutes. Prior to imaging, 100 nM of a 10-mer oligo-nanohoop conjugate in 200 mM NaCl in PBS was added. Samples were imaged on a Zeiss LSM 880 Laser-Scanning Confocal Microscope.

5.7 Concluding Remarks

Cycloparaphenylenes have great promise as novel fluorescent scaffolds for interrogating biological systems. Innovations such as improving the brightness of small easily accessible nanohoops, synthesizing bright orange emitting derivatives, creation of intracellular targeted nanohoops and connection of these molecules to biological entities greatly expands the utility of cycloparaphenylenes in biology. With this thesis, and other works, there have been significant advances in using cycloparaphenylenes as novel fluorescent probes for biological applications.

REFERENCES CITED

- (1) Coons, A. H.; Creech, H. J.; Jones, R. N.; Berliner, E. The Demonstration of Pneumococcal Antigen in Tissue by the Use of Fluorescent Antibody. *J. Immunol.* **1949**, *45*, 159–170.
- (2) Herschel, J. F. W. On a Case of Superficial Colour Presented by a Homogeneous Liquid Internally Colorless. *Philos. Trans.* **1845**, 143–145.
- (3) Stokes, G. G. On the Change of Refrangibility of Light. *Philos. Trans.* **1852**, *142*, 463–562.
- (4) Lakowicz, J. R. *Fluorophores*, 3rd ed.; Springer US: Boston, MA, 2006.
- (5) Lavis, L. D.; Raines, R. T. Bright Ideas for Chemical Biology. *ACS Chem. Biol.* **2008**, *3*, 142–155.
- (6) Lakowicz, J. R. Introduction to Fluorescence. In *Principles of Fluorescence Spectroscopy*; Springer US: Boston, MA, 2006; pp 1–26.
- (7) Vogel, A. Darstellung von Benzoesäure Aus Der Tonka-Bohne Und Aus Den Meliloten - Oder Steinklee - Blumen. *Ann. der Phys. und der Phys. Chemie* **1820**, *64*, 161–166.
- (8) Guibourt, N. J.-B. G. *Histoire Abrégée Des Drogues Simples*; Paris : Paris, 1820.
- (9) Salem, M. A.; Helal, M. H.; Gouda, M. A.; Ammar, Y. A.; A El-Gaby, M. S.; Abbas, S. Y. An Overview on Synthetic Strategies to Coumarins. *Synth. Commun.* **2018**, *48*, 1534–1550.
- (10) Sun, W.-C.; Gee, K. R.; Haugland, R. P. Synthesis of Novel Fluorinated Coumarins: Excellent UV-Light Excitable Fluorescent Dyes. *Bioorg. Med. Chem. Lett.* **1998**, *8*, 3107–3110.
- (11) Lavis, L. D.; Raines, R. T. Bright Building Blocks for Chemical Biology. *ACS Chem. Biol.* **2014**, *9*, 855–866.
- (12) Young, D. M.; Welker, J. J. C.; Doxsee, K. M. Green Synthesis of a Fluorescent Natural Product. *J. Chem. Educ.* **2011**, *88*, 319–321.
- (13) Holden, M. S.; Crouch, R. D. The Pechmann Reaction. *J. Chem. Educ.* **1998**, *75*, 1631.

- (14) Salem, M. A.; Helal, M. H.; Gouda, M. A.; Ammar, Y. A.; A El-Gaby, M. S.; Abbas, S. Y. An Overview on Synthetic Strategies to Coumarins. *Synth. Commun.* **2018**, *48*, 1534–1550.
- (15) Nizamov, S.; Willig, K. I.; Sednev, M. V.; Belov, V. N.; Hell, S. W. Phosphorylated 3-Heteroaryl coumarins and Their Use in Fluorescence Microscopy and Nanoscopy. *Chem. Eur. J.* **2012**, *18*, 16339–16348.
- (16) Jin, X.; Uttamapinant, C.; Ting, A. Y. Synthesis of 7-Aminocoumarin by Buchwald-Hartwig Cross Coupling for Specific Protein Labeling in Living Cells. *Chembiochem* **2011**, *12*, 65–70.
- (17) Sednev, M. V.; Belov, V. N.; Hell, S. W. Fluorescent Dyes with Large Stokes Shifts for Super-Resolution Optical Microscopy of Biological Objects: A Review. *Methods Appl. Fluoresc.* IOP Publishing Ltd December 1, 2015.
- (18) Mojzych, M.; Henary, M. Heterocyclic Polymethine Dyes. *Top. Heterocycl. Chem.* **2008**, *14*, 1–9.
- (19) Musso, H. The Pigments of Fly Agaric, Amanita Muscaria. *Tetrahedron* **1979**, *35*, 2843–2853.
- (20) Lee, L. G.; Chen, C.-H.; Chiu, L. A. Thiazole Orange: A New Dye for Reticulocyte Analysis. *Cytometry* **1986**, *7*, 508–517.
- (21) Ryel, H.; Yue, S.; Wemmer, D. E.; Quesada, M. A.; Haugland, R. P.; Mathies, R. A.; Glazer, A. N. Stable Fluorescent Complexes of Double-Stranded DNA with Bis-Intercalating Asymmetric Cyanine Dyes: Properties and Applications. *Nucleic Acids Res.* *20*, 2803–2812.
- (22) Mujumdar, R. B.; Ernst, L. A.; Mujumdar, S. R.; Lewis, C. J.; Waggoner, A. S. Cyanine Dye Labeling Reagents: Sulfoindocyanine Succinimidyl Esters. *Bioconjug. Chem.* **1993**, *4*, 105–111.
- (23) Mujumdar, S. R.; Mujumdar, R. B.; Grant, C. M.; Waggoner, A. S. Cyanine-Labeling Reagents: Sulfo benzindocyanine Succinimidyl Esters. *Bioconjug. Chem.* **1996**, *7*, 356–362.
- (24) El-Shishtawy, R. M.; Almeida, P. A New Vilsmeier-Type Reaction for One-Pot Synthesis of pH Sensitive Fluorescent Cyanine Dyes. *Tetrahedron* **2006**, *62*, 7793–7798.
- (25) Bouteiller, C.; Clavé, G.; Bernardin, A.; Chipon, B.; Massonneau, M.; Renard, P.-Y.; Anthony Romieu. Novel Water-Soluble Near-Infrared Cyanine Dyes: Synthesis, Spectral Properties, and Use in the Preparation of Internally Quenched Fluorescent Probes. *Bioconjugate Chem.* **2007**, *18*, 1303–1317.

- (26) Chipon, B.; Clavé, G.; Bouteiller, C.; Massonneau, M.; Renard, P.-Y.; Romieu, A. Synthesis and Post-Synthetic Derivatization of a Cyanine-Based Amino Acid. Application to the Preparation of a Novel Water-Soluble NIR Dye. *Tetrahedron Lett.* **2006**, *47*, 8279–8284.
- (27) Waggoner, A. Covalent Labeling of Proteins and Nucleic Acids with Fluorophores. *Method Enzym.* **1995**, *246*, 362–373.
- (28) Baeyer, A. Über Ein Neue Klasse von Farbstoffen. *Berichte der Dtsch. Chem. Gesellschaft zu Berlin* **1871**, *4*, 555–558.
- (29) Sun, W.-C.; Gee, K. R.; Klaubert, D. H.; Haugland, R. P. Synthesis of Fluorinated Fluoresceins. *J. Org. Chem.* **1997**, *62*, 6469–6475.
- (30) Haugland, R. P. *Handbook of Fluorescent Probes and Research Chemicals; Molecular Probes*: Eugene, OR, 1992.
- (31) Ceresole, M. Production of New Red Coloring-Matter. US377349, 1888.
- (32) Khanna, P. L.; Ullman, E. F. 4',5'-Dimethoxy-6-Carboxyfluorescein: A Novel Dipole-Dipole Coupled Fluorescence Energy Transfer Acceptor Useful for Fluorescence Immunoassays. *Anal. Biochem.* **1980**, *108*, 156–161.
- (33) Grimm, J. B.; Lavis, L. D. Synthesis of Rhodamines from Fluoresceins Using Pd-Catalyzed C-N Cross-Coupling. *Org. Lett.* **2011**, *13*, 6354–6357.
- (34) Dwight, S. J.; Levin, S. Scalable Regioselective Synthesis of Rhodamine Dyes. *Org. Lett.* **2016**, *18*, 5316–5319.
- (35) Lavis, L. D. Teaching Old Dyes New Tricks: Biological Probes Built from Fluoresceins and Rhodamines. *Annu. Rev. Biochem.* **2017**, *86*, 825–843.
- (36) Zhou, X.; Lai, R.; Beck, J. R.; Li, H.; Stains, C. I. Nebraska Red: A Phosphate-Based near-Infrared Fluorophore Scaffold for Chemical Biology Applications. *Chem. Commun.* **2016**, *52*, 12290–12293.
- (37) Treibs, A.; Kreuzer, F.-H. Difluorboryl-Komplexe von Di- Und Tripyrrylmethenen. *Liebigs Ann. Chem.* **1968**, *718*, 208–223.
- (38) Richard P. Haugland; Kang, H. C. Chemically Reactive Dipyrrometheneboron Difluoride Dyes. US4774339A, August 10, 1987.
- (39) Li, Z.; Mintzer, E.; Bittman, R. First Synthesis of Free Cholesterol-BODIPY Conjugates. *J. Org. Chem.* **2006**, *71*, 1718–1721.

- (40) Loudet, A.; Burgess, K. BODIPY Dyes and Their Derivatives: Syntheses and Spectroscopic Properties. *Chem. Rev.* **2007**, *107*, 4891–4932.
- (41) Wagner, R. W.; Lindsey, J. S. Boron-Dipyrromethene Dyes for Incorporation in Synthetic Multi-Pigment Light-Harvesting Arrays. *Pure Appl. Chem.* **1996**, *68*, 1373–1380.
- (42) Lee, J.-S.; Kang, N.-Y.; Kim, Y. K.; Samanta, A.; Feng, S.; Kim, H. K.; Vendrell, M.; Park, J. H.; Chang, Y.-T. Synthesis of a BODIPY Library and Its Application to the Development of Live Cell Glucagon Imaging Probe. *J. Am. Chem. Soc.* **2009**, *131*, 10077–10082.
- (43) Jiao, L.; Yu, C.; Liu, M.; Wu, Y.; Cong, K.; Meng, T.; Wang, Y.; Hao, E. Synthesis and Functionalization of Asymmetrical Benzo-Fused BODIPY Dyes. *J. Org. Chem.* **2010**, *75*, 6035–6038.
- (44) Zhao, N.; Vicente, M. G. H.; Fronczek, F. R.; Smith, K. M. Synthesis of 3,8-Dichloro-6-Ethyl-1,2,5,7-Tetramethyl-BODIPY from an Asymmetric Dipyrroketone and Reactivity Studies at the 3,5,8-Positions. *Chem. Eur. J.* **2015**, *21*, 6181–6192.
- (45) Schmitt, A.; Hinkeldey, B.; Wild, M.; Jung, G. Synthesis of the Core Compound of the BODIPY Dye Class: 4,4'-Difluoro-4-Bora-(3a,4a)-Diaza-s-Indacene. *J. Fluoresc.* **2009**, *19*, 755–758.
- (46) Arroyo, I. J.; Hu, R.; Merino, G.; Zhong Tang, B.; Pe, E.; Alta, N. S. The Smallest and One of the Brightest. Efficient Preparation and Optical Description of the Parent Borondipyrromethene System. *J. Org. Chem.* **2009**, *74*, 5719.
- (47) Tram, K.; Yan, H.; Jenkins, H. A.; Vassiliev, S.; Bruce, D. The Synthesis and Crystal Structure of Unsubstituted 4,4-Difluoro-4-Bora-3a,4a-Diaza-s-Indacene (BODIPY). *Dye. Pigment.* **2009**, *82*, 392–395.
- (48) Tao, J.; Sun, D.; Sun, L.; Li, Z.; Fu, B.; Liu, J.; Zhang, L.; Wang, S.; Fang, Y.; Xu, H. Tuning the Photo-Physical Properties of BODIPY Dyes: Effects of 1, 3, 5, 7-Substitution on Their Optical and Electrochemical Behaviours. *Dye. Pigment.* **2019**, *168*, 166–174.
- (49) Huang, C.; Barlow, S.; Marder, S. R. Perylene-3,4,9,10-Tetracarboxylic Acid Diimides: Synthesis, Physical Properties, and Use in Organic Electronics. *J. Org. Chem.* **2011**, *76*, 2386–2407.
- (50) Heinz, L. Cyclic Carboxylic Imide Structures as Structure Elements of High Stability. Novel Developments in Perylene Dye Chemistry. *Heterocycles* **1995**, *40*, 477.

- (51) Qu, J.; Kohl, C.; Pottek, M.; Müllen, K. Ionic Perylenetetracarboxydiimides: Highly Fluorescent and Water-Soluble Dyes for Biolabeling. *Angew. Chemie Int. Ed.* **2004**, *43*, 1528–1531.
- (52) Nowak-Król, A.; Würthner, F. Progress in the Synthesis of Perylene Bisimide Dyes. *Org. Chem. Front.* **2019**, *6*.
- (53) Peneva, K.; Hermann, A.; Mullen, K. Water-Soluble Rylene Dyes, Methods for Preparing the Same and Uses Thereof as Fluorescent Labels for Biomolecules. WO2009065508A3, 2011.
- (54) Peneva, K.; Mihov, G.; Nolde, F.; Rocha, S.; Hotta, J.; Braeckmans, K.; Hofkens, J.; Uji-i, H.; Herrmann, A.; Müllen, K. Water-Soluble Monofunctional Perylene and Terrylene Dyes: Powerful Labels for Single-Enzyme Tracking. *Angew. Chemie Int. Ed.* **2008**, *47*, 3372–3375.
- (55) Peneva, K.; Mihov, G.; Herrmann, A.; Zarrabi, N.; Börsch, M.; Duncan, T. M.; Müllen, K. Exploiting the Nitrilotriacetic Acid Moiety for Biolabeling with Ultrastable Perylene Dyes. *J. Am. Chem. Soc.* **2008**, *130*, 5398–5399.
- (56) Bai, Q.; Gao, B.; Ai, Q.; Wu, Y.; Ba, X. Core-Extended Terrylene Diimide on the Bay Region: Synthesis and Optical and Electrochemical Properties. *Angew. Chem., Int. Ed.* **2011**, *13*, 1789.
- (57) Jasti, R.; Bhattacharjee, J.; Neaton, J. B.; Bertozzi, C. R. Synthesis, Characterization, and Theory of [9]-, [12]-, and [18]Cycloparaphenylene: Carbon Nanohoop Structures. *J. Am. Chem. Soc.* **2008**, *130*, 17646–17647.
- (58) Yamago, S.; Watanabe, Y.; Iwamoto, T. Synthesis of [8]Cycloparaphenylene from a Square-Shaped Tetranuclear Platinum Complex. *Angew. Chemie Int. Ed.* **2010**, *49*, 757–759.
- (59) Omachi, H.; Matsuura, S.; Segawa, Y.; Itami, K. A Modular and Size-Selective Synthesis of [n]Cycloparaphenylenes: A Step toward the Selective Synthesis of [n,n] Single-Walled Carbon Nanotubes. *Angew. Chemie Int. Ed.* **2010**, *49*, 10202–10205.
- (60) Patel, V. K.; Kayahara, E.; Yamago, S. Practical Synthesis of [n]Cycloparaphenylenes (N=5, 7-12) by H₂SnCl₄-Mediated Aromatization of 1,4-Dihydroxycyclo-2,5-Diene Precursors. *Chem. - A Eur. J.* **2015**, *21*, 5742–5749.
- (61) Darzi, E. R.; White, B. M.; Loventhal, L. K.; Zakharov, L. N.; Jasti, R. An Operationally Simple and Mild Oxidative Homocoupling of Aryl Boronic Esters To Access Conformationally Constrained Macrocycles. *J. Am. Chem. Soc.* **2017**, *139*, 3106–3114.

- (62) Sisto, T. J.; Golder, M. R.; Hirst, E. S.; Jasti, R. Selective Synthesis of Strained [7]Cycloparaphenylene: An Orange-Emitting Fluorophore. *J. Am. Chem. Soc.* **2011**, *133*, 15800–15802.
- (63) Peters, G. M.; Grover, G.; Maust, R. L.; Colwell, C. E.; Bates, H.; Edgell, W. A.; Jasti, R.; Kertesz, M.; Tovar, J. D. Linear and Radial Conjugation in Extended π -Electron Systems. *J. Am. Chem. Soc.* **2020**, *142*, 2293–2300.
- (64) Lovell, T. C.; Garrison, Z. R.; Jasti, R. Synthesis, Characterization and Computational Investigation of Bright Orange-emitting Benzothiadiazole [10]Cycloparaphenylene. *Angew. Chem. Int. Ed* **2020**, DOI: 10.1002/anie.202006350.
- (65) Leonhardt, E. J.; Van Raden, J. M.; Miller, D.; Zakharov, L. N.; Alemán, B.; Jasti, R. A Bottom-Up Approach to Solution-Processed, Atomically Precise Graphitic Cylinders on Graphite. *Nano Lett.* **2018**, *18*, 7991–7997.
- (66) White, B. M.; Zhao, Y.; Kawashima, T. E.; Branchaud, B. P.; Pluth, M. D.; Jasti, R. Expanding the Chemical Space of Biocompatible Fluorophores: Nano hoops in Cells. *ACS Cent. Sci.* **2018**, *4*, 1173–1178.
- (67) Van Raden, J. M.; Leonhardt, E. J.; Zakharov, L. N.; Pérez-Guardiola, A.; Pérez-Jiménez, A. J.; Marshall, C. R.; Brozek, C. K.; Sancho-García, J. C.; Jasti, R. Precision Nanotube Mimics via Self-Assembly of Programmed Carbon Nano hoops. *J. Org. Chem.* **2019**, acs.joc.9b02340.
- (68) Darzi, E. R.; Jasti, R. The Dynamic, Size-Dependent Properties of [5]-[12]Cycloparaphenylenes. *Chem. Soc. Rev.* **2015**, *44*, 6401–6410.
- (69) Smith, A. M.; Mancini, M. C.; Nie, S. Bioimaging: Second Window for in Vivo Imaging. *Nat. Nanotechnol.* **2009**, *4*, 710–711.
- (70) Roncali, J. Molecular Engineering of the Band Gap of π -Conjugated Systems: Facing Technological Applications. *Macromol. Rapid Commun.* **2007**, *28*, 1761–1775.
- (71) Liu, X.; Xu, Z.; Cole, J. M. Molecular Design of UV–vis Absorption and Emission Properties in Organic Fluorophores: Toward Larger Bathochromic Shifts, Enhanced Molar Extinction Coefficients, and Greater Stokes Shifts. *J. Phys. Chem. C* **2013**, *117*, 16584–16595.
- (72) Albright, T. A.; Burdett, J. K.; Whangbo, M.-H. *Orbital Interactions in Chemistry*; John Wiley & Sons, Inc.: Hoboken, NJ, USA, 2013.

- (73) Mao, Y.; Head-Gordon, M.; Shao, Y. Unraveling Substituent Effects on Frontier Orbitals of Conjugated Molecules Using an Absolutely Localized Molecular Orbital Based Analysis. *Chem. Sci.* **2018**, *9*.
- (74) Besson, T.; Coudert, G.; Guillaumet, G. Synthesis and Fluorescent Properties of Some Heterobifunctional and Rigidized 7-Aminocoumarins. *J. Heterocycl. Chem.* **1991**, *28*, 1517–1523.
- (75) Alabugin, I. V.; Gilmore, K. M.; Peterson, P. W. Hyperconjugation. *WIREs Comput. Mol. Sci.* **2011**, *1*, 109–141.
- (76) Ramanan, C.; Smeigh, A. L.; Anthony, J. E.; Marks, T. J.; Wasielewski, M. R. Competition between Singlet Fission and Charge Separation in Solution-Processed Blend Films of 6,13-Bis(Triisopropylsilylethynyl)-Pentacene with Sterically-Encumbered Perylene-3,4:9,10-Bis(Dicarboximide)s. *J. Am. Chem. Soc.* **2012**, *134*.
- (77) Fron, E.; Schweitzer, G.; Osswald, P.; Würthner, F.; Marsal, P.; Beljonne, D.; Müllen, K.; De Schryver, F. C.; Van der Auweraer, M. Photophysical Study of Bay Substituted Perylenediimides. *Photochem. Photobiol. Sci.* **2008**, *7*, 1509.
- (78) Shibano, Y.; Imahori, H.; Adachi, C. Organic Thin-Film Solar Cells Using Electron-Donating Perylene Tetracarboxylic Acid Derivatives. *J. Phys. Chem. C* **2009**, *113*, 15454–15466.
- (79) Ahn, M.; Kim, M.-J.; Wee, K.-R. Electron Push–Pull Effects in 3,9-Bis(p-(R)-Diphenylamino)Perylene and Constraint on Emission Color Tuning. *J. Org. Chem.* **2019**, *84*, 12050–12057.
- (80) Battagliarin, G.; Zhao, Y.; Li, C.; Müllen, K. Efficient Tuning of LUMO Levels of 2,5,8,11-Substituted Perylenediimides via Copper Catalyzed Reactions. *Org. Lett.* **2011**, *13*, 339–3401.
- (81) Kuwabara, T.; Orii, J.; Segawa, Y.; Itami, K. Curved Oligophenylenes as Donors in Shape-Persistent Donor-Acceptor Macrocycles with Solvatofluorochromic Properties. *Angew. Chem. Int. Ed.* **2015**, *54*, 9646–9649.
- (82) Tasior, M.; Kim, D.; Singha, S.; Krzeszewski, M.; Ahn, K. H.; Gryko, D. T. P-Expanded Coumarins: Synthesis, Optical Properties and Applications. *J. Mater. Chem. C* **2015**, *3*, 1421–1446.
- (83) Lee, L. G.; Berry, G. M.; Chen, C.-H. Vita Blue: A New 633 Nm Excitable Fluorescent Dye for Cell Analysis. *Cytometry* **1989**, *10*, 151–164.
- (84) Sibrian-Vazquez, M.; Escobedo, J. O.; Lowry, M.; Strongin, R. M. Progress toward Red and Near-Infrared (NIR) Emitting Saccharide Sensors. *Pure Appl. Chem.* **2012**, *84*, 2443–2456.

- (85) Li, G.; Otsuka, Y.; Matsumiya, T.; Suzuki, T.; Li, J.; Takahashi, M.; Yamada, K. A Straightforward Substitution Strategy to Tune BODIPY Dyes Spanning the Near-Infrared Region via Suzuki-Miyaura Cross-Coupling. *Materials (Basel)*. **2018**, *11*, 1297–1308.
- (86) Swavey, S.; Quinn, J.; Coladipietro, M.; Cox, K. G.; Brennaman, M. K. Tuning the Photophysical Properties of BODIPY Dyes through Extended Aromatic Pyrroles. *RSC Adv.* **2017**, *7*, 173–179.
- (87) Segawa, Y.; Fukazawa, A.; Matsuura, S.; Omachi, H.; Yamaguchi, S.; Irle, S.; Itami, K. Combined Experimental and Theoretical Studies on the Photophysical Properties of Cycloparaphenylenes. *Org. Biomol. Chem.* **2012**, *10*, 5979–5984.
- (88) Karlsson, J. K. G.; Harriman, A. Origin of the Red-Shifted Optical Spectra Recorded for Aza-BODIPY Dyes. *J. Phys. Chem. A* **2016**, *120*, 2537–2546.
- (89) Gershoni-Poranne, R.; Rahalkar, A. P.; Stanger, A. The Predictive Power of Aromaticity: Quantitative Correlation between Aromaticity and Ionization Potentials and HOMO–LUMO Gaps in Oligomers of Benzene, Pyrrole, Furan, and Thiophene. *Phys. Chem. Chem. Phys.* **2018**, *20*, 14808–14817.
- (90) Vogel, P.; Houk, K. N. *Organic Chemistry: Theory, Reactivity and Mechanisms in Modern Synthesis*; WILEY-VCH: Weinheim, GER, 2019.
- (91) Jia, K.; Wan, Y.; Xia, A.; Li, S.; Gong, F.; Yang, G. Characterization of Photoinduced Isomerization and Intersystem Crossing of the Cyanine Dye Cy3. *J. Phys. Chem. A* **2007**, *111*, 1593–1597.
- (92) Waggoner, A. S. Rigidized Trimethine Cyanine Dyes. WO99/31181, 1999.
- (93) Grimm, J. B.; English, B. P.; Chen, J.; Slaughter, J. P.; Zhang, Z.; Revyakin, A.; Patel, R.; Macklin, J. J.; Normanno, D.; Singer, R. H.; et al. A General Method to Improve Fluorophores for Live-Cell and Single-Molecule Microscopy. *Nat. Methods* **2015**, *12*, 244–250.
- (94) Panchuk-Voloshina, N.; Haugland, R. P.; Bishop-Stewart, J.; Bhalgat, M. K.; Millard, P. J.; Mao, F.; Leung, W.-Y.; Haugland, R. P. Alexa Dyes, a Series of New Fluorescent Dyes That Yield Exceptionally Bright, Photostable Conjugates. *J. Histochem. Cytochem.* **1999**, *47*, 1179–1188.
- (95) Mujumdar, R. B.; Ernst, L. A.; Mujumdar, S. R.; Waggoner, A. S. Cyanine Dye Labeling Reagents Containing Isothiocyanate Groups. *Cytometry* **1989**, *1*, 11–19.
- (96) Wang, H.-Y.; Leung, W.-Y.; Mao, F. Sulfonated Derivatives of 7-Aminocoumarin. US005696157A, December 9, 1997.

- (97) Sato, E.; Matsuhisa, A.; Sakashita, M.; Kanaoka, Y. New Water-Soluble Fluorogenic Amine. 7-Aminocoumarin-4-Methanesulfonic Acid (ACMS) and Related Substrates for Proteinases. *Chem. Pharm. Bull. (Tokyo)*. **1988**, *36*, 3496–3502.
- (98) Woronoff, G.; Harrak, A. El; Mayot, E.; Schicke, O.; Miller, O. J.; Soumillion, P.; Griffiths, A. D.; Ryckelynck, M. New Generation of Amino Coumarin Methyl Sulfonate-Based Fluorogenic Substrates for Amidase Assays in Droplet-Based Microfluidic Applications. *Anal. Chem* **2011**, *83*, 2852–2857.
- (99) Weers, J. G.; Rathman, J. F.; Axe, F. U.; Crichlow, C. A.; Poland, L. D.; Scheuing, D. R.; Wiersema, R. J.; Zielske, A. G. Effect of the Intramolecular Charge Separation Distance on the Solution Properties of Betaines and Sulfobetaines. *Langmuir* **1991**, *7*, 854–867.
- (100) Kratzer, D.; Barner, L.; Friedmann, C.; Bräse, S.; Lahann, J. A Synthetic Route to Sulfobetaine Methacrylates with Varying Charge Distance. *European J. Org. Chem.* **2014**, *2014*, 8064–8071.
- (101) Rao Renikuntla, B.; Rose, H. C.; Eldo, J.; Waggoner, A. S.; Armitage, B. A. Improved Photostability and Fluorescence Properties through Polyfluorination of a Cyanine Dye. *Org. Lett.* **2004**, *6*, 909–912.
- (102) Zheng, Q.; Lavis, L. D. Development of Photostable Fluorophores for Molecular Imaging. *Curr. Opin. Chem. Biol.* **2017**, *39*, 32–38.
- (103) Rasnik, I.; McKinney, S. A.; Ha, T. Nonblinking and Long-Lasting Single-Molecule Fluorescence Imaging. *Nat. Methods* **2006**, *3*, 891–893.
- (104) Altman, R. B.; Terry, D. S.; Zhou, Z.; Zheng, Q.; Geggier, P.; Kolster, R. A.; Zhao, Y.; Javitch, J. A.; Warren, J. D.; Blanchard, S. C. Cyanine Fluorophore Derivatives with Enhanced Photostability. *Nat. Methods* **2012**, *9*, 68–71.
- (105) Dave, R.; Terry, D. S.; Munro, J. B.; Blanchard, S. C. Mitigating Unwanted Photophysical Processes for Improved Single-Molecule Fluorescence Imaging. *Biophys. J.* **2009**, *96*, 2371–2381.
- (106) Spitalsky, Z.; Tasis, D.; Papagelis, K.; Galiotis, C. Carbon Nanotube-Polymer Composites: Chemistry, Processing, Mechanical and Electrical Properties. *Prog. Polym. Sci.* **2010**, *35*, 357–401.
- (107) Hong, G.; Diao, S.; Antaris, A. L.; Dai, H. Carbon Nanomaterials for Biological Imaging and Nanomedicinal Therapy. *Chem. Rev.* **2015**, *115*, 10816–10906.

- (108) Titirici, M. M.; White, R. J.; Brun, N.; Budarin, V. L.; Su, D. S.; Del Monte, F.; Clark, J. H.; MacLachlan, M. J. Sustainable Carbon Materials. *Chem. Soc. Rev.* **2015**, *44*, 250–290.
- (109) Jariwala, D.; Sangwan, V. K.; Lauhon, L. J.; Marks, T. J.; Hersam, M. C. Carbon Nanomaterials for Electronics, Optoelectronics, Photovoltaics, and Sensing. *Chem. Soc. Rev.* **2013**, *42*, 2824–2860.
- (110) Wen, L.; Li, F.; Cheng, H. M. Carbon Nanotubes and Graphene for Flexible Electrochemical Energy Storage: From Materials to Devices. *Adv. Mater.* **2016**, *28*, 4306–4337.
- (111) Ball, M.; Zhong, Y.; Fowler, B.; Zhang, B.; Li, P.; Etkin, G.; Paley, D. W.; Decatur, J.; Dalsania, A. K.; Li, H.; et al. Macrocyclization in the Design of Organic N-Type Electronic Materials. *J. Am. Chem. Soc.* **2016**, *138*, 12861–12867.
- (112) Kayahara, E.; Sun, L.; Onishi, H.; Suzuki, K.; Fukushima, T.; Sawada, A.; Kaji, H.; Yamago, S. Gram-Scale Syntheses and Conductivities of [10]Cycloparaphenylene and Its Tetraalkoxy Derivatives. *J. Am. Chem. Soc.* **2017**, *139*, 18480–18483.
- (113) Iwamoto, T.; Watanabe, Y.; Sadahiro, T.; Haino, T.; Yamago, S. Size-Selective Encapsulation of C₆₀ by [10]Cycloparaphenylene: Formation of the Shortest Fullerene-Peapod. *Angew. Chemie Int. Ed.* **2011**, *50*, 8342–8344.
- (114) Della Sala, P.; Talotta, C.; Capobianco, A.; Soriente, A.; De Rosa, M.; Neri, P.; Gaeta, C. Synthesis, Optoelectronic, and Supramolecular Properties of a Calix[4]Arene-Cycloparaphenylene Hybrid Host. *Org. Lett.* **2018**, *20*, 37.
- (115) Della Sala, P.; Talotta, C.; Caruso, T.; De Rosa, M.; Soriente, A.; Neri, P.; Gaeta, C. Tuning Cycloparaphenylene Host Properties by Chemical Modification. *J. Org. Chem.* **2017**, *82*, 9885–9889.
- (116) Evans, P. J.; Darzi, E. R.; Jasti, R. Efficient Room-Temperature Synthesis of a Highly Strained Carbon Nanohoop Fragment of Buckminsterfullerene. *Nat. Chem.* **2014**, *6*, 404–408.
- (117) Kayahara, E.; Patel, V. K.; Yamago, S. Synthesis and Characterization of [5]Cycloparaphenylene. *J. Am. Chem. Soc.* **2014**, *136*, 2284–2287.
- (118) Xia, J.; Jasti, R. Synthesis, Characterization, and Crystal Structure of [6]Cycloparaphenylene. *Angew. Chemie Int. Ed.* **2012**, *51*, 2474–2476.
- (119) Iwamoto, T.; Watanabe, Y.; Sakamoto, Y.; Suzuki, T.; Yamago, S. Selective and Random Syntheses of [n]Cycloparaphenylenes (n = 8–13) and Size Dependence of Their Electronic Properties. *J. Am. Chem. Soc.* **2011**, *133*, 8354–8361.

- (120) Adamska, L.; Nayyar, I.; Chen, H.; Swan, A. K.; Oldani, N.; Fernandez-Alberti, S.; Golder, M. R.; Jasti, R.; Doorn, S. K.; Tretiak, S. Self-Trapping of Excitons, Violation of Condon Approximation, and Efficient Fluorescence in Conjugated Cycloparaphenylenes. *Nano Lett.* **2014**, *14*, 6539–6546.
- (121) Franklin-Mergarejo, R.; Alvarez, D. O.; Tretiak, S.; Fernandez-Alberti, S. Carbon Nanorings with Inserted Acenes: Breaking Symmetry in Excited State Dynamics. *Sci. Rep.* **2016**, *6*, 31253.
- (122) Della Sala, P.; Capobianco, A.; Caruso, T.; Talotta, C.; De Rosa, M.; Neri, P.; Peluso, A.; Gaeta, C. An Anthracene-Incorporated [8]Cycloparaphenylene Derivative as an Emitter in Photon Upconversion. *J. Org. Chem.* **2018**, *83*, 220–227.
- (123) Della Sala, P.; Buccheri, N.; Sanzone, A.; Sassi, M.; Neri, P.; Talotta, C.; Rocco, A.; Pinchetti, V.; Beverina, L.; Brovelli, S.; et al. First Demonstration of the Use of Very Large Stokes Shift Cycloparaphenylenes as Promising Organic Luminophores for Transparent Luminescent Solar Concentrators. *Chem. Commun.* **2019**, *55*, 3160–3163.
- (124) Ball, M.; Zhang, B.; Zhong, Y.; Fowler, B.; Xiao, S.; Ng, F.; Steigerwald, M.; Nuckolls, C. Conjugated Macrocycles in Organic Electronics. *Acc. Chem. Res.* **2019**, *52*, 1068–1078.
- (125) Kayahara, E.; Sun, L.; Onishi, H.; Suzuki, K.; Fukushima, T.; Sawada, A.; Kaji, H.; Yamago, S. Gram-Scale Syntheses and Conductivities of [10]Cycloparaphenylene and Its Tetraalkoxy Derivatives. *J. Am. Chem. Soc.* **2017**, *139*, 18480–18483.
- (126) Jackson, E. P.; Sisto, T. J.; Darzi, E. R.; Jasti, R. Probing Diels-Alder Reactivity on a Model CNT Sidewall. *Tetrahedron* **2016**, *72*, 3754–3758.
- (127) Li, P.; Sisto, T. J.; Darzi, E. R.; Jasti, R. The Effects of Cyclic Conjugation and Bending on the Optoelectronic Properties of Paraphenylenes. *Org. Lett.* **2014**, *16*, 182–185.
- (128) Lai, R. Y.; Fleming, J. J.; Merner, B. L.; Vermeij, R. J.; Bodwell, G. J.; Bard, A. J. Electrogenated Chemiluminescence. 74. Photophysical, Electrochemical, and Electrogenated Chemiluminescent Studies of Selected Nonplanar Pyrenophanes. *J. Phys. Chem. A* **2004**, *108*, 376–383.
- (129) Cosa, G.; Focsaneanu, K.-S.; McLean, J. R. N.; McNamee, J. P.; Scaiano, J. C. Photophysical Properties of Fluorescent DNA-Dyes Bound to Single- and Double-Stranded DNA in Aqueous Buffered Solution. *Photochem. Photobiol.* **2001**, *73*, 585–599.

- (130) Hard, T.; Fan, P.; Kearns, D. R. A Fluorescence Study of the Binding of HOECHST 33258 and DAPI to Halogenated DNAs. *Photochem. Photobiol.* **1990**, *51*, 77–86.
- (131) Johnson, I. D. Practical Considerations in the Selection and Application of Fluorescent Probes. In *Handbook of Biological Confocal Microscopy: Third Edition*; Pawley, J. B., Ed.; Springer US: Boston, MA, 2006; pp 353–367.
- (132) Darzi, E. R.; Sisto, T. J.; Jasti, R. Selective Syntheses of [7]-[12]Cycloparaphenylenes Using Orthogonal Suzuki-Miyaura Cross-Coupling Reactions. *J. Org. Chem.* **2012**, *77*, 6624–6628.
- (133) Sisto, T. J.; Golder, M. R.; Hirst, E. S.; Jasti, R. Selective Synthesis of Strained [7]Cycloparaphenylene: An Orange-Emitting Fluorophore. *J. Am. Chem. Soc.* **2011**, *133*, 15800–15802.
- (134) Pangborn, A. B.; Giardello, M. A.; Grubbs, R. H.; Rosen, R. K.; Timmers, F. J. Safe and Convenient Procedure for Solvent Purification. *Organometallics* **1996**, *15*, 1518–1520.
- (135) Pelter, A.; Elgendy, S. Phenolic Oxidation with (Diacetoxyiodo)Benzene. *Tetrahedron Lett.* **1988**, *29*, 677–680.
- (136) Bruno, N. C.; Tudge, M. T.; Buchwald, S. L. Design and Preparation of New Palladium Precatalysts for C–C and C–N Cross-Coupling Reactions. *Chem. Sci.* **2013**, *4*, 916–920.
- (137) Frisch, M. J.; Trucks, G. W.; Schlegel, H. B.; Scuseria, G. E.; Robb, M. A.; Cheeseman, J. R.; Scalmani, G.; Barone, V.; Mennucci, B.; Petersson, G. A.; et al. Gaussian 09, Revision E.01. Gaussian, Inc.: Wallingford CT, 2013.
- (138) Darzi, E. R.; Jasti, R. The Dynamic, Size-Dependent Properties of [5]-[12]Cycloparaphenylenes. *Chem. Soc. Rev.* **2015**, *44*, 6401–6410.
- (139) Li, P.; Sisto, T. J.; Darzi, E. R.; Jasti, R. The Effects of Cyclic Conjugation and Bending on the Optoelectronic Properties of Paraphenylenes. *Org. Lett.* **2014**, *16*, 182–185.
- (140) Meerholz, K.; Heinze, J. Electrochemical Solution and Solid-State Investigations on Conjugated Oligomers and Polymers of the α -Thiophene and the p-Phenylene Series. *Electrochim. Acta* **1996**, *41*, 1839–1854.
- (141) Lovell, T. C.; Colwell, C. E.; Zakharov, L. N.; Jasti, R. Symmetry Breaking and the Turn-on Fluorescence of Small, Highly Strained Carbon Nanohoops. *Chem. Sci.* **2019**, *10*, 3786–3790.

- (142) Tarkuç, S.; Eelkema, R.; Grozema, F. C. The Relationship between Molecular Structure and Electronic Properties in Dicyanovinyl Substituted Acceptor-Donor-Acceptor Chromophores. *Tetrahedron* **2017**, *73*, 4994–5004.
- (143) Roquet, S.; Cravino, A.; Leriche, P.; Alévêque, O.; Frère, P.; Roncali, J. Triphenylamine-Thienylenevinylene Hybrid Systems with Internal Charge Transfer as Donor Materials for Heterojunction Solar Cells. *J. Am. Chem. Soc.* **2006**, *128*, 3459–3466.
- (144) Gao, C.; Wang, L.; Li, X.; Wang, H. Rational Design on D-A Conjugated P(BDT-DTBT) Polymers for Polymer Solar Cells. *Polym. Chem.* **2014**, *5*, 5200–5210.
- (145) Darzi, E. R.; Hirst, E. S.; Weber, C. D.; Zakharov, L. N.; Lonergan, M. C.; Jasti, R. Synthesis, Properties, and Design Principles of Donor-Acceptor Nanohoops. *ACS Cent. Sci.* **2015**, *1*, 335–342.
- (146) Karikomi, M.; Kitamura, C.; Tanaka, S.; Yamashita, Y. New Narrow-Bandgap Polymer Composed of Benzobis(1,2,5-Thiadiazole) and Thiophenes. *J. Am. Chem. Soc.* **1995**, *117*, 6791–6792.
- (147) Hou, J.; Chen, H. Y.; Zhang, S.; Li, G.; Yang, Y. Synthesis, Characterization, and Photovoltaic Properties of a Low Band Gap Polymer Based on Silole-Containing Polythiophenes and 2,1,3-Benzothiadiazole. *J. Am. Chem. Soc.* **2008**, *130*, 16144–16145.
- (148) Li, M.; An, C.; Pisula, W.; Müllen, K. Cyclopentadithiophene–Benzothiadiazole Donor–Acceptor Polymers as Prototypical Semiconductors for High-Performance Field-Effect Transistors. *Acc. Chem. Res.* **2018**, *51*, 1196–1205.
- (149) Patel, V. K.; Kayahara, E.; Yamago, S. Practical Synthesis of [n]Cycloparaphenylenes (N=5, 7-12) by H₂SnCl₄-Mediated Aromatization of 1,4-Dihydroxycyclo-2,5-Diene Precursors. *Chem. Eur. J.* **2015**, *21*, 5742–5749.
- (150) Colwell, C. E.; Price, T. W.; Stauch, T.; Jasti, R. Strain Visualization for Strained Macrocycles. *Chem. Sci.* **2020**, *11*, 3923–3930.
- (151) Schaub, T. A.; Margraf, J. T.; Zakharov, L.; Reuter, K.; Jasti, R. Strain-Promoted Reactivity of Alkyne-Containing Cycloparaphenylenes. *Angew. Chemie Int. Ed.* **2018**, *57*, 16348–16353.
- (152) Li, P.; Wong, B. M.; Zakharov, L. N.; Jasti, R. Investigating the Reactivity of 1,4-Anthracene-Incorporated Cycloparaphenylene. *Org. Lett.* **2016**, *18*, 1574–1577.
- (153) Kayahara, E.; Qu, R.; Yamago, S. Bromination of Cycloparaphenylenes: Strain-Induced Site-Selective Bis-Addition and Its Application for Late-Stage Functionalization. *Angew. Chemie Int. Ed.* **2017**, *56*, 10428–10432.

- (154) Jasti, R.; Bhattacharjee, J.; Neaton, J. B.; Bertozzi, C. R. Synthesis, Characterization, and Theory of [9]-, [12]-, and [18]Cycloparaphenylene: Carbon Nanohoop Structures. *J. Am. Chem. Soc.* **2008**, *130*, 17646–17647.
- (155) Fujitsuka, M.; Cho, D. W.; Iwamoto, T.; Yamago, S.; Majima, T. Size-Dependent Fluorescence Properties of [n]Cycloparaphenylenes (n = 8-13), Hoop-Shaped π -Conjugated Molecules. *Phys. Chem. Chem. Phys.* **2012**, *14*, 14585–14588.
- (156) Darzi, E. R.; Sisto, T. J.; Jasti, R. Selective Syntheses of [7]–[12]Cycloparaphenylenes Using Orthogonal Suzuki–Miyaura Cross-Coupling Reactions. *J. Org. Chem.* **2012**, *77*, 6624–6628.
- (157) Xu, Y.; Wang, B.; Kaur, R.; Minameyer, M. B.; Bothe, M.; Drewello, T.; Guldi, D. M.; von Delius, M. A Supramolecular [10]CPP Junction Enables Efficient Electron Transfer in Modular Porphyrin–[10]CPP \Rightarrow Fullerene Complexes. *Angew. Chemie Int. Ed.* **2018**, *57*, 11549–11553.
- (158) Lakowicz, J. R. Mechanisms and Dynamics of Fluorescence Quenching. In *Principles of Fluorescence Spectroscopy*; Springer: Baltimore; pp 331–351.
- (159) Grabowski, Z. R.; Rotkiewicz, K.; Rettig, W. Structural Changes Accompanying Intramolecular Electron Transfer: Focus on Twisted Intramolecular Charge-Transfer States and Structures. *Chem. Rev.* **2003**, *103*, 3899–4031.
- (160) Reichardt, C. Solvatochromic Dyes as Solvent Polarity Indicators. *Chem. Rev.* **1994**, *94*, 2319–2358.
- (161) Thordarson, P. Determining Association Constants from Titration Experiments in Supramolecular Chemistry. *Chem. Soc. Rev.* **2011**, *40*, 1305.
- (162) Mcquade, D. T.; Pullen, A. E.; Swager, T. M. Conjugated Polymer-Based Chemical Sensors. *Chem. Rev.* **2000**, *100*, 2537–2574.
- (163) Hong, G.; Diao, S.; Antaris, A. L.; Dai, H. Carbon Nanomaterials for Biological Imaging and Nanomedicinal Therapy. *Chem. Rev.* **2015**, *115*, 10816–10906.
- (164) Chan, W. C. W.; Nie, S. Quantum Dot Bioconjugates for Ultrasensitive Nonisotopic Detection. *Science (80-.)*. **1998**, *281*, 2016–2018.
- (165) Bruchez, M.; Moronne, M.; Gin, P.; Weiss, S.; Alivisatos, A. P. Semiconductor Nanocrystals as Fluorescent Biological Labels. *Science (80-.)*. **1998**, *281*, 2013–2016.

- (166) Bradburne, C. E.; Delehanty, J. B.; Boeneman Gemmill, K.; Mei, B. C.; Mattoussi, H.; Susumu, K.; Blanco-Canosa, J. B.; Dawson, P. E.; Medintz, I. L. Cytotoxicity of Quantum Dots Used for in Vitro Cellular Labeling: Role of QD Surface Ligand, Delivery Modality, Cell Type, and Direct Comparison to Organic Fluorophores. *Bioconjug. Chem.* **2013**, *24*, 1570–1583.
- (167) Derfus, A. M.; Chan, W. C. W.; Bhatia, S. N. Intracellular Delivery of Quantum Dots for Live Cell Labeling and Organelle Tracking. *Adv. Mater.* **2004**, *16*, 961–966.
- (168) Panwar, N.; Soehartono, A. M.; Chan, K. K.; Zeng, S.; Xu, G.; Qu, J.; Coquet, P.; Yong, K. T.; Chen, X. Nanocarbons for Biology and Medicine: Sensing, Imaging, and Drug Delivery. *Chem. Rev.* **2019**, *119*, 9559–9656.
- (169) Zhu, S.; Yang, Q.; Antaris, A. L.; Yue, J.; Ma, Z.; Wang, H.; Huang, W.; Wan, H.; Wang, J.; Diao, S.; et al. Molecular Imaging of Biological Systems with a Clickable Dye in the Broad 800-to 1,700-Nm near-Infrared Window. *PNAS* **2017**, *114*, 962–967.
- (170) Wang, H.; Wang, Z.; Ye, M.; Zong, S.; Li, M.; Chen, P.; Ma, X.; Cui, Y. Optically Encoded Nanoprobes Using Single Walled Carbon Nanotube as the Building Scaffold for Magnetic Field Guided Cell Imaging. *Talanta* **2014**, *119*, 144–150.
- (171) Ohfuchi, M.; Miyamoto, Y. Optical Properties of Oxidized Single-Wall Carbon Nanotubes. *Carbon N. Y.* **2017**, *114*, 418–423.
- (172) Ghosh, S.; Weisman, R. B. Advanced Sorting of Single-Walled Carbon Nanotubes by Nonlinear Density-Gradient Ultracentrifugation. *Nat Nanotechnol* **2010**, *5*, 443–450.
- (173) Endo, M.; Strano, M. S.; Ajayan, P. M. Potential Applications of Carbon Nanotubes. In *Carbon Nanotubes*; 2007; pp 13–62.
- (174) Yang, F.; Wang, X.; Zhang, D.; Yang, J.; Luo, D.; Xu, Z.; Wei, J.; Wang, J. Q.; Xu, Z.; Peng, F.; et al. Chirality-Specific Growth of Single-Walled Carbon Nanotubes on Solid Alloy Catalysts. *Nature* **2014**, *510*, 522–524.
- (175) He, M.; Jiang, H.; Liu, B.; Fedotov, P. V.; Chernov, A. I.; Obraztsova, E. D.; Cavalca, F.; Wagner, J. B.; Hansen, T. W.; Anoshkin, I. V.; et al. Chiral-Selective Growth of Single-Walled Carbon Nanotubes on Lattice-Mismatched Epitaxial Cobalt Nanoparticles. *Sci. Rep.* **2013**, *3*.
- (176) Sanchez-Valencia, J. R.; Dienel, T.; Gröning, O.; Shorubalko, I.; Mueller, A.; Jansen, M.; Amsharov, K.; Ruffieux, P.; Fasel, R. Controlled Synthesis of Single-Chirality Carbon Nanotubes. *Nature* **2014**, *512*, 61–64.

- (177) Green, A. A.; Hersam, M. C. Progress towards Monodisperse Single-Walled Carbon Nanotubes. *Nat. Nanotechnol.* **2008**, *3*, 387–394.
- (178) Lavis, L. D.; Rutkoski, T. J.; Raines, R. T. Tuning the PKa of Fluorescein to Optimize Binding Assays. *Anal. Chem* **2007**, *79*, 6775–6782.
- (179) Dempsey, G. T.; Vaughan, J. C.; Chen, K. H.; Bates, M.; Zhuang, X. Evaluation of Fluorophores for Optimal Performance in Localization-Based Super-Resolution Imaging. *Nat. Methods* **2011**, *8*, 1027–1036.
- (180) Liu, Z.; Lavis, L. D.; Betzig, E. Imaging Live-Cell Dynamics and Structure at the Single-Molecule Level. *Mol. Cell* **2015**, *58*, 644–659.
- (181) Cheung, K. Y.; Gui, S.; Deng, C.; Liang, H.; Xia, Z.; Liu, Z.; Chi, L.; Miao, Q. Synthesis of Armchair and Chiral Carbon Nanobelts. *Chem* **2019**, *5*, 838–847.
- (182) Gao, P.; Pan, W.; Li, N.; Tang, B. Fluorescent Probes for Organelle-Targeted Bioactive Species Imaging. *Chem. Sci.* **2019**, *10*, 6035–6071.
- (183) Jones, G.; Jackson, W. R.; Choi, C.; Bergmark, W. R. Solvent Effects on Emission Yield and Lifetime for Coumarin Laser Dyes. Requirements for a Rotatory Decay Mechanism. *J. Phys. Chem* **1985**, *89*, 294–300.
- (184) Sjöback, R.; Nygren, J.; Kubista, M. Absorption and Fluorescence Properties of Fluorescein. *Spectrochim. Acta Part A Mol. Biomol. Spectrosc.* **1995**, *51*, L7–L21.
- (185) Tang, H.; Gu, Z.; Li, C.; Li, Z.; Wu, W.; Jiang, X. Nanoscale Vesicles Assembled from Non-Planar Cyclic Molecules for Efficient Cell Penetration. *Biomater. Sci.* **2019**, *7*, 2552–2558.
- (186) Yang, N. J.; Hinner, M. J. Getting across the Cell Membrane: An Overview for Small Molecules, Peptides, and Proteins. *Methods Mol. Biol.* **2015**, *1266*, 29–53.
- (187) Wagner, J.; Li, L.; Simon, J.; Landfester, K.; Mailänder, V.; Müllen, K.; Ng, D. Y. W.; Wu, Y.; Weil, T.; Krutzke, L. Amphiphilic Polyphenylene Dendron Conjugates for Surface Remodeling of Adenovirus 5. *Angew. Chemie Int. Ed.* **2020**, *59*, 2–11.
- (188) Stangenberg, R.; Wu, Y.; Hedrich, J.; Kurzbach, D.; Wehner, D.; Weidinger, G.; Kuan, S. L.; Jansen, M. I.; Jelezko, F.; Luhmann, H. J.; et al. A Polyphenylene Dendrimer Drug Transporter with Precisely Positioned Amphiphilic Surface Patches. *Adv. Healthc. Mater.* **2015**, *4*, 377–384.
- (189) Hermanson, G. T. *Bioconjugate Techniques: Third Edition*; Elsevier Inc., 2013.

- (190) Golder, M. R.; Colwell, C. E.; Wong, B. M.; Zakharov, L. N.; Zhen, J.; Jasti, R. Iterative Reductive Aromatization/Ring-Closing Metathesis Strategy toward the Synthesis of Strained Aromatic Belts. *J. Am. Chem. Soc.* **2016**, *138*, 6577–6582.
- (191) Marshall, J. L.; Lehnher, D.; Lindner, B. D.; Tykwinski, R. R. Reductive Aromatization/De aromatization and Elimination Reactions to Access Conjugated Polycyclic Hydrocarbons, Heteroacenes, and Cumulenes. *Chempluschem* **2017**, *82*, 967–1001.
- (192) Roth, J.; Binder, M.; Gerhard, U. J. Conjugation of Lectins with Fluorochromes: An Approach to Histochemical Double Labeling of Carbohydrate Components. *Histochemistry* **1978**, *56*, 265–273.
- (193) Frei, A. P.; Jeon, O. Y.; Kilcher, S.; Moest, H.; Henning, L. M.; Jost, C.; Plückthun, A.; Mercer, J.; Aebersold, R.; Carreira, E. M.; et al. Direct Identification of Ligand-Receptor Interactions on Living Cells and Tissues. *Nat. Biotechnol.* **2012**, *30*, 997–1001.